Carbon Nitride Supported Nanostructured Materials: Catalysts for Fuel Cell Reactions and Organic Reactions

By

Tanmay Bhowmik

CHEM 11201204007

National Institute of Science Education and Research

(NISER) Bhubaneswar, Odisha – 752050

A thesis submitted to the
Board of Studies in Chemical Sciences
In partial fulfillment of requirements

for the Degree of

DOCTOR OF PHILOSOPHY

of

HOMI BHABHA NATIONAL INSTITUTE

July, 2018

Version approved during the meeting of Standing Committee of Deans held during 29-30 Nov 2013

Homi Bhabha National Institute[1]

Recommendations of the Viva Voce Committee

As members of the Viva Voce Committee, we certify that we have read the dissertation prepared by **Tanmay Bhowmik** entitled **"Carbon Nitride Supported Nanostructured Materials: Catalysts for Fuel Cell Reactions and Organic Reactions"** and recommend that it may be accepted as fulfilling the thesis requirement for the award of Degree of Doctor of Philosophy.

Chairman - **Date:** 4.3.19

Prof. A. Srinivasan

Guide Sudip Barman **Date:** 04.03.19

Dr. Sudip Barman

Examiner – KKNanda **Date:** 04/03/2019

Prof. Karuna Kar Nanda

Member 1- Prasenjit Mal **Date:** 04.03.2019

Dr. Prasenjit Mal

Member 2- Nagendra **Date:** 04.03.19

Dr. Nagendra K. Sharma

Member 3- **Date:** 04.03.19

Dr. Abdur Rahaman

Final approval and acceptance of this thesis is contingent upon the candidate's submission of the final copies of the thesis to HBNI.

I/We hereby certify that I/we have read this thesis prepared under my/our direction and recommend that it may be accepted as fulfilling the thesis requirement.

Date: 04.03.19

Place: NISER

Sudip Barman

Co-guide (if applicable) **Guide**

---

[1] This page is to be included only for final submission after successful completion of viva voce.

STATEMENT BY AUTHOR

This dissertation has been submitted in partial fulfillment of requirements for an advanced degree at Homi Bhabha National Institute (HBNI) and is deposited in the Library to be made available to borrowers under rules of the HBNI.

Brief quotations from this dissertation are allowable without special permission, provided that accurate acknowledgement of source is made. Requests for permission for extended quotation from or reproduction of this manuscript in whole or in part may be granted by the Competent Authority of HBNI when in his or her judgment the proposed use of the material is in the interests of scholarship. In all other instances, however, permission must be obtained from the author.

Tanmay Bhowmik

…………Tanmay Bhowmik

DECLARATION

I, hereby declare that the investigation presented in the thesis has been carried out by me. The work is original and has not been submitted earlier as a whole or in part for a degree / diploma at this or any other Institution / University.

Tanmay Bhowmik

……….Tanmay Bhowmik

List of Publications

1. **“**Palladium Nanoparticle-Graphitic Carbon Nitride Porous Synergistic Catalyst for Hydrogen Evolution-Oxidation Reactions over a Broad Range of pH and Correlation of Its Catalytic Activity with Measured Hydrogen Binding Energy” **Bhowmik, T.**; Kundu, M. K.; Barman, S., *ACS Catal.*, **2016,** *6*, 1929–1941.

2. **“**Growth of One-Dimensional RuO_2 Nanowires on g-Carbon Nitride- An Active and Stable Bifunctional Electrocatalyst for Hydrogen and Oxygen Evolution Reactions at All pH Values” **Bhowmik, T.**; Kundu, M. K.; Barman, S., *ACS Appl. Mater. Interfaces*, **2016**, *8*, 28678-28688.

3. “Highly efficient electrocatalytic oxidation of formic acid on palladium nanoparticles-graphitic carbon nitride composite” **Bhowmik, T.**; Kundu, M. K.; Barman, S., *Int. J Hydrogen Energy,* **2017,** 42, 212-217.

4. **“**CoFe Layered Double Hydroxide Supported on Graphitic Carbon Nitrides: An Efficient and Durable Bifunctional Electrocatalyst for Oxygen Evolution and Hydrogen Evolution Reactions” **Bhowmik, T.**; Kundu, M. K.; Barman, S.,
ACS Appl. Energy Mater. **2018,** *1*, 1200-1209.

5. “Highly active and durable Pd nanoparticles-porous graphitic carbon nitride composite for electrocatalytic oxygen reduction reaction”. **Bhowmik, T.**; Kundu, M. K.; Barman, S., *Int. J Hydrogen Energy*, **2016**, 41, 14768-14777.

6. “Ultrasmall gold nanoparticles-graphitic carbon nitride composite- an efficient catalyst for ultrafast reduction of 4-nitrophenol and removal of organic dyes from water” **Bhowmik, T.**#; Kundu, M. K.#; Barman, S., *RSC Adv***.**, **2015**, 5, 38760-38773.
(# equal contribution)

7. “Facile synthesis of carbon quantum dots and thin graphene sheets for non-enzymatic sensing of hydrogen peroxide”. Sadhukhan, M.#; **Bhowmik, T.#**; Kundu, M. K.; Barman, S., *RSC Adv.*, **2014**, 4, 4998-5005. **(# equal contribution)**

8. “Gold aerogel supported on graphitic carbon nitride- an efficient electrocatalyst for oxygen reduction reaction and hydrogen evolution reaction”Kundu,M. K.; **Bhowmik, T.**; Barman, S., *J. Mater. Chem. A*, **2015**, 3, 23120-23135.

9. “Highly dispersed platinum nanoparticles on graphitic carbon nitride: A highly active and durable electrocatalyst for oxidation of methanol, formic acid and formaldehyde” Sadhukhan, M.; Kundu, M. K.; **Bhowmik, T.;** Barman, S. *Inter. J. Hydrogen Energy,* **2017**, *42*, 9371-9383.

10.“Pt Nanostructures/N-Doped Carbon hybrid, an Efficient Catalyst for Hydrogen Evolution/Oxidation Reactions: Enhancing its Base Media Activity through Bifunctionality of the Catalyst“ Kundu, M. K.; **Bhowmik, T.;** Mishra, R.; Barman, S.*ChemSusChem*, **2018**,11, 2388-2401.

11. “Rhodium metal–rhodium oxide (Rh–Rh_2O_3) nanostructures with Pt-like or better activity towards hydrogen evolution and oxidation reactions (HER, HOR) in acid and base: correlating its HOR/HER activity with hydrogen binding energy and oxophilicity of the catalyst” Kundu, M. K.#; Mishra, R.#; **Bhowmik, T.;** Barman, S. *J. Mater. Chem. A*, **2018**, 6, 23531-23541. **(# equal contribution).**

Manuscript under preparation:

1. **“**Highly Dispersed Palladium Nanoparticles Supported on Graphitic Carbon Nitride for Selective Hydrogenation of Nitro Compounds and Ullmann Coupling Reaction“. **Bhowmik, T.;** Sadhukhan, M.; Barman, S.

2. “$Co_1Al_2(OH)_m$ LDH and g-carbon nitride composite nanostructure: An Efficient Electrocatalyst for Water Oxidation Reactions in Alkaline Electrolyte”.**Bhowmik, T.;** Kundu, M. K.; Barman, S.

Conferences:

1. **Poster Presentation: “**Electrocatalytic Hydrogen Evolution and Oxidation Reactions on Palladium Nanoparticle-Graphitic Carbon Nitride Porous Composite Over Broad Range of pH” in 20th Chemical Research Society of India (CRSI) National Symposium in Chemistry on 3rd -5th February, 2017 organized at Gauhati University.

2. **Poster Presentation:** “One Dimensional RuO_2 Nanowires Supported on g-carbon nitride: An Active and Stable Bifunctional Electrocatalyst for Hydrogen and Oxygen Evolution Reactions at all pH Values” in International Conference on Recent Advances in Material Chemistry on 24th -26th February, 2017 at Utkal University.

3. **Poster Presentation:** “Highly active and durable Pd nanoparticles-porous graphitic carbon nitride composite for electrocatalytic oxygen reduction reaction” in Inter IISER and NISER Chemistry Meet (IINCM-2017) on 22th -24th December, 2017 organized at School of Chemical Sciences, National Institute of Science Education & Research, Bhubaneswar.

4. 11th CRSI-RSC Symposium on 2nd February, 2017, organized at Gauhati University.

5. Indo French Symposium on “Functional Metal-Organics: Applications in Materials and Catalysis” on 24th – 26th February, 2014, organized at School of Chemical Sciences, National Institute of Science Education & Research, Bhubaneswar.

Tanmay Bhowmik

…………Tanmay Bhowmik

Dedicated To My Parents

&

To The Memories of My Grandfather

(Late Kamalendu Purkait)

ACKNOWLEDGEMENTS

It is high time to convey my gratitude in this humble acknowledgement to all of the people who have supported me continuously to reach at this stage that I could be able to write a thesis.

Firstly, I would like to express my sincere gratitude and regards to my supervisor **Dr. Sudip Barman** for his constant help, valuable guidance, and continuous support during my research work. His everlasting enthusiasm towards solving a mystery rather than publishing yet another paper and the openness for new ideas have always been a source of great inspiration to me.

I am thankful to my doctorial committee members **Prof. Alagar Srinivasan, Dr. Prasenjit Mal, Dr. Nagendra k. Sharma and Dr. Abdur Rahaman (Biological sciences).** I wish to extend my warmest thanks to other faculty members in School of Chemical Sciences, NISER for their constant support and valuable suggestions during carrying out various experiments of my thesis work.

I would like to acknowledge the Homi Bhabha National Institute (HBNI), India for my academic registration, Department of Atomic Energy (DAE), India for financial support (fellowship) and **National Institute of Science Education and Research (NISER), Bhubaneswar,** for providing me all types of research facilities and excellent academic atmosphere. I extend my heartfelt thanks to director-NISER **Prof. Sudhakar Panda** for providing me infrastructure to carry out my research work. I also thanks to **Prof. T. K. Chandrashekar**, founder Director-NISER and **Prof. V. Chandrashekhar**, Ex-Director-NISER.

I would like to express my special thanks to my past lab members **Dr. Mriganka Sadthukhan, Dr. Susanta Kr. Bera, Amit kumar patel, Sarat kanrar, Ranjan Behera,** and present lab members **Manas K. Kundu, Ranjit Mishra, Amal K. Vinod,**

Shubham Sahoo, Dr. Asish Das for their continuous help offered during my research work. Their encouragements and useful discussions helped me to overcome various difficulties during my research work.

I express my thanks to all of my NISER friends especially **Sourav, Arindam, Somnath, Subhyan, Sajal**, **Somnath Banerjee** and seniors **Dr. Tapas Kumar Achar, Dr. Milan barman, Dr. Saikat maity, Dr. Prasit sahoo and Dr. Basujit Chatterjee** for making my Ph.D life the memorable.

There are some people without whom I would not have been the person I am today. I wish to express my deep gratitude to NISER senior, **Dr. Tapas Kumar Achar,** for his valuable advice and suggestions during my initial research work.

Above all, I would like to express my sincere gratitude to my grandfather **Late Kamalendu Purkait** and grandmother **Rekha Purkait** for their affectionate blessings, endless supports and constant encouragements. My grandfather would have been the happiest person, if he had been alive today. I express my deep regards and love to my family especially my father **Amal Kanta Bhowmik** and mother **Sumita Bhowmik** for their affectionate blessings, unconditional love, endless support and constant encouragement throughout the course of this work. Whatever I am and whatever I intend to be my life is because of their never ending love and bless. I would also like express my deepest gratitude to my younger brother **Mrinmoy Bhowmik** and sister-in-law **Dipika Bhowmik** for their constant support.

Finally, I thank a lot to the almighty for all those things which made my life full of happiness and prosperity till date.

CONTENTS

Homi Bhabha National Institute

SYNOPSIS OF Ph. D. THESIS

1. **Name of the Student:** Tanmay Bhowmik

2. **Name of the Constituent Institution:** National Institute of Science Education and Research (NISER), Bhubaneswar

3. **Enrolment No. :** CHEM11201204007

4. **Title of the Thesis:** Carbon Nitride Supported Nanostructured Materials: Catalysts for Fuel Cell Reactions and Organic Reactions

5. **Board of Studies:** School of Chemical Sciences

Introduction:

With increasing concern over rapid depletion of fossil fuels and negative impact on the environment due to excessive use of fossil fuels, there is urgent need of renewable energy resource and storage techniques alternative to the fossil fuels[1]. The regenerative fuel cell (RFCs) is a potential device for electrochemical energy storage and conversion system[2]. The RFCs built up with two stacks[3]: (i) Electrolyser stack where fuel is produced from a renewable resource and stores the electrical energy in the form of chemical energy and (ii) Fuel cell stack where electricity is produced from chemical energy. Among various processes, the electrochemical energy/environmental H_2-O_2-H_2O cycle is one of the leading building blocks for viable energy and fuel production in aqueous electrolyte system. The electrochemical energy/environmental H_2-O_2-H_2O cycle mainly consists of four half-cell reactions; namely hydrogen oxidation reaction (HOR), oxygen reduction reaction (ORR) in fuel cell stack and hydrogen evolution reaction (HER), oxygen evolution reaction (OER) in water electrolyzer stack. All these processes have a sluggish kinetics without suitable catalyst. The best choices of the electrocatalyst for fuel cells and electrolyser applications are the supported NPs having very high surface areas. The main advantages of these supported NPs catalyst are its larger electrochemically active surface area (ECSA) of the NPs with the minimal use of metal, greater efficiency and lower cost. But one of the major limitations for carbon supported catalyst is its lower electrocatalytic stability arises due to the rapid degradation of carbon. In this regard it should be mentioned that the graphitic carbon nitride[4], a two dimension (2D) graphene like carbon materials has gained impetus attentions as supported materials for NPs because of its higher thermal and chemical stability. Moreover, the carbon nitride supported different nanocomposite[5] has potential applications towards electrochemical fuel cell reactions, sensing, heterogeneous organic transformation, and photocatalysis applications.

Scope and Organization of the Present Thesis

In this thesis, attempts have been made to introduce facile synthesis of graphitic carbon nitride supported various nano composites to evaluate their various catalytic activities for both organic reactions and electrochemical reactions occurred in fuel cells. Additionally, our efforts were extended to understand the mechanistic aspects and reaction kinetics of various catalytic reactions. The present thesis contains nine chapters and the contents of the chapter have been summarized as follows:

Chapter 1: Nanocomposite for Electrochemical Energy Conversion and Organic Reaction.

In chapter 1, we have reviewed the current and future energy demands and explored the importance of renewable energy conversions and storage techniques. The history and development of fuel cell as well as water electrolyser are highlighted. The main concern of this chapter was on the general description of different fuel cell reactions such as hydrogen oxidation reaction (HOR), oxygen reduction reaction (ORR) and water electrolyser reaction namely hydrogen evolution reaction (HER), oxygen evolution reaction (OER). The reaction steps, mechanisms and kinetics of these processes are discussed. A brief description of theoretical backgrounds to develop the efficient electro catalysts for different renewable process has been demonstrated. This chapter also records an account of current literatures pertaining to different nanocarbon materials graphene,[6] carbon nanotube (CNTs),[7] carbon nitride based[5] precious and non-precious metal nanostructure materials, used for various fuel cell reactions. The layered double hydroxides (LDHs) are considered as promising materials due its layered open structure and densely distributed active sites. LDH is an anionic clay consisted of mixed metal cations hydroxide layers; separated by hydrated charge balancing anions[8] and their general formula is $[M^{2+}_{1-x}\ M^{3+}_{x}\ (OH)_2]^{x+}[A^{n-}_{(x/n)}.\ mH_2O]^{x}$. Different synthesis methods, properties and electrochemical applications of transition metals LDH based composite materials were disscused. Moreover, NPs based heterogeneous[9] catalyst for various organic conversions has been briefly discussed in the last section of this chapter.

Chapter 2: General Experimental Methods and Techniques

This chapter describes a brief description of various instrumental techniques, exclusively used for this present thesis work. The working principle of powder X-ray diffraction (p-XRD), UV-Visible spectroscopy, Fourier transform infra-red spectroscopy (FT-IR), X-ray photoelectron spectroscopy (XPS) and other microscopic techniques such as TEM SEM have been discussed. Basic principle of different voltammetry such as linear sweep voltammetry (LSV), cyclic voltammetry (CV), and potential step voltammetry (Chronometric) has been discussed. The detailed description of experimental electrochemical setup and electrode preparation procedure is included. The materials details and synthetic procedure of graphitic carbon nitride is also demonstrated.

Chapter 3 Palladium Nanoparticle-Graphitic Carbon Nitride Porous Composite: Synthesis and Its Application in HER/HOR at all pH Values

(**Ref:** T. Bhowmik, M. K. Kundu, S. Barman; *ACS Catal.* 2016, 6, 1929–1941)

The hydrogen reduction reaction (HER/HRR) and hydrogen oxidation reaction (HOR) in aqueous medium are the two fundamental reactions for the development of a non-fossil fuel based energy storage and conversion devices. HOR is anodic process in fuel cells where chemical energy in hydrogen is converted to the electrical energy whereas HER, a cathodic process stores the energy in chemical form by liberating the hydrogen. Commercial carbon supported platinum (comm. Pt/C) catalyst has been universally considered as the best catalyst for both cathode and anode. This chapter deals with the synthesis of porous palladium nanoparticles-carbon nitride composite (Pd-CN_x) for its superior activity and high durability towards HER in both acidic and alkaline media.

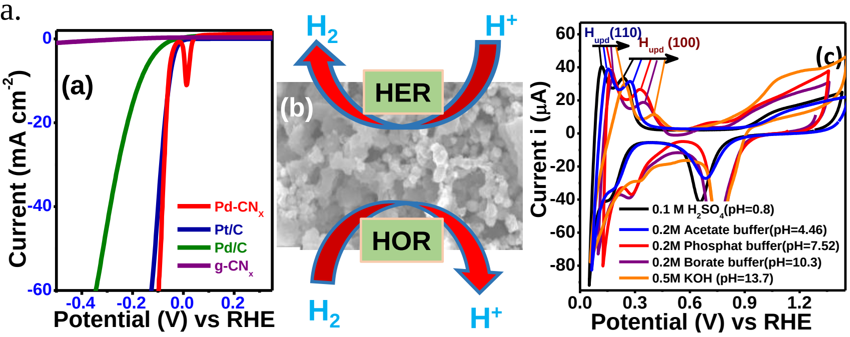

Figure 1. (a) HER LSV curve in 0.5 M H_2SO_4 electrolyte. (b) Morphology of Pd-CN_x. (c) CVs curve of Pd-CN_x in different pH electrolyte.

The Pd-CN_x composites exhibited excellent catalytic activity for hydrogen evolution in acidic media with small onset potential of -12 mV and a Tafel slope of 35 mV dec^{-1}. At a small Pd loading of 0.043 mg cm^{-2}, this catalyst exhibits a current density of 10 mA cm^{-2} at a low overpotential of -55 mV with an excellent stability. The HER activity on Pd-CN_x composite is slightly better or comparable with comm. Pt/C in acid media. Furthermore, this catalyst has displayed superior HOR activity, measured by rotating disk experiment with a broad range of pH (0-14) in different buffer solution. The HER /HOR activity of porous Pd-CN_x composite in different buffer solution were correlated by hydrogen binding energy (HBE) of catalyst surface. HER/HOR activity gradually decreases with increasing the HBE as solution pH increases. The superior HER/HOR activities and very high durability at porous Pd-CN_x composite are due to strong bonding between Pd and carbon (Pd-C bond), porous morphology, the synergistic interactions between Pd-NPs and CN_x support.

Chapter 4. Electrocatalytic Oxygen Reduction Reaction on Pd Nanoparticles-Porous Graphitic Carbon Nitride Composite

(**Ref:** T. Bhowmik, M. K. Kundu, S. Barman; *Int. J Hydrogen Energy*, 2016, 41, 14768-14777)

The electrochemical oxygen reduction reaction (ORR) is one of the most important cathodic redox reactions for the development of proton or /and anion exchange membrane fuel cells (PEMFCs and AEMFCs) as well as direct liquid fuel cells (DLFCs). The commercial carbon supported platinum (Pt/C) catalyst is generally used as potential catalyst for ORR. However, the insufficient electrocatalytic stability, low abundance and low energy efficiency of precise Pt metal are the main technical drawbacks associated with ORR.

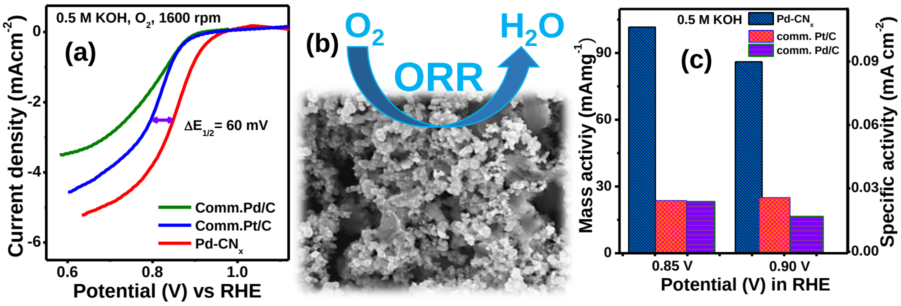

Figure 2. (a) ORR LSV curves of different catalyst. (b) FE-SEM image of Pd-CN$_x$. (c) Comparison of MA and SA.

Chapter 4 describes the superior electrocatalytic ORR activity of palladium nanoparticles-carbon nitride (Pd-CN$_x$) composite in both alkaline and acidic medium. The ORR activity on Pd-CN$_x$ catalyst is better (half wave potential $E_{1/2}$ of 60mV more positive) than that of Pt/C in 0.5 M KOH solution and is almost comparable in acid media. Moreover, this porous composite displays excellent methanol tolerance and has better long term durability than that of commercial Pt/C in both acidic and alkaline media. Only 4 and 6 mV positive shift of $E_{1/2}$ after 1,500 potential cycles in basic medium and acid medium respectively, further proves the excellent durability of this catalyst. The superior electrocatalytic activity and excellent stability of porous Pd-CN$_x$ composite can be attributed to the unique synergistic interaction between CN$_x$ support and Pd nanoparticles (Pd-NPs), lower the d-band centre of Pd, easy mass transport, and surface structure of Pd-NPs.

Chapter 5. One Dimensional RuO_2 Nanowires on g-Carbon Nitride for Hydrogen and Oxygen Evolution Reactions at All pH Values

(**Ref:** T. Bhowmik, M. K. Kundu, S. Barman; *ACS Appl. Mater. Interfaces*, 2016, *8*, 28678-28688)

Development of highly efficient and durable bifunctional electrocatalyst for hydrogen and oxygen evolution reactions (HER and OER) is essential for the efficient overall water splitting reaction in electrolyzer devices. The commercial Pt/C and RuO_2 are highly active towards HER and OER respectively; but their poor stability under different operating conditions is the main obstacle for their commercialization. This chapter demonstrates the growth of one dimensional highly crystalline RuO_2 nanowires on carbon nitride (1D-RuO_2-CN_x) for their applications in HER and OER over all pH values. The 1D-RuO_2-CN_x, as an OER catalyst, exhibits low onset overpotential of ~ 200 mV in both acidic and basic media whereas Tafel slopes are 52 and 56 mV/dec respectively. This catalyst requires low overpotential of 250 mV and 260 mV to drive the current density of 10 $mAcm^{-2}$ in acidic and basic media respectively.

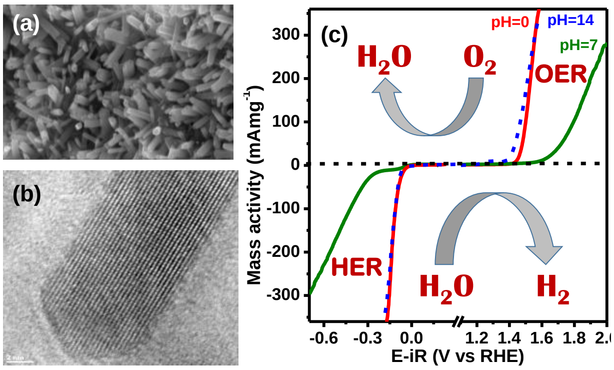

Figure 3. (a) FE-SEM, (b) HRTEM image and (c) LSV polarization curve for HER as well as OER.

The mass activity of 1D-RuO_2-CN_x catalyst is 352 mA mg^{-1} which is ~14 time higher than that of comm. RuO_2. Most importantly, the 1D-RuO_2-CN_x catalyst has remarkably higher stability in compare to comm. RuO_2 and IrO_2. This catalyst also exhibits superior HER activity with current density of 10 $mAcm^{-2}$ at ~93 and 95 mV in acidic and basic media. The HER Tafel slopes of this catalyst are 40 mV/dec in acidic condition and 70 mV/dec in basic condition. The HER activity of this catalyst is slightly lower than Pt/C in acid media whereas in basic media the activity is comparable or even better than that of Pt/C at higher over-potentials. The catalysis is also important in neutral medium due to its low cost and better safety as compared to the others. 1D-RuO_2-CN_x composite showed improved HER and OER activity as compared to the state-of-the-art catalyst in 0.1 M PBS buffer electrolyte.

Chapter 6 Formic Acid oxidation on Palladium Nanoparticles- Graphitic Carbon Nitride

(**Ref:** T. Bhowmik, M. K. Kundu, S. Barman; *Int. J Hydrogen Energy,* 2017, 42, 212-217)

The difficulties in hydrogen storage and transportation are the main limitations associated with the practical applications of hydrogen fuel cells whereas methanol cross over, toxicity of methanol are the main obstacles for direct methanol fuel cells (DMFCs) as compare to the Direct Formic Acid Fuel Cells (DFAFCs). The electro-oxidation of formic acid on solid surfaces is known to occur via two different paths – (1) dehydrogenation process, the direct-path involves oxidation of formic acid to carbon dioxide ($HCOOH = CO_2 + 2H^+ + 2e^-$) and (2) the indirect-path (dehydration path) occurs via intermediate formation, oxidation of adsorbed CO species ($HCOOH = CO_{ads} + H_2O = CO_2 + 2H^+ + 2e^-$). The main challenge of DFAFCs catalyst is to reduce the possibility of dehydration path over direct-path way as CO poisoning of the catalyst which further reduces its activity. The comm. Pt/C catalyst follows the indirect-path for FAO reaction. Therefore, it is not suitable catalyst for DFAFCs. This chapter reports the electrocatalytic activity of palladium nanoparticles-carbon nitride composite (PdNPs/CN_x) towards the formic acid oxidation (FAO) with high mass activity (1640 $mAmg_{Pd}^{-1}$) in acid electrolyte. The PdNPs/CN_x catalyst has 70 mV more negative peak potential and 7.2 times higher mass activity than commercial Pd/C catalyst for FAO reaction in 0.5 M H_2SO_4 electrolyte. In addition, at 0.4 V (RHE) (the typical working voltage in DFAFC) the current density of PdNPs/CN_x catalyst for FAO is ~7.6 times and ~36 times higher than that of the commercial Pd/C and Pt/C catalyst respectively. The mass activity of this catalyst is 23 times higher than commercial Pd/C even after 1000 CV cycles demonstrating the outstanding stability of PdNPs/CN_x catalyst.

Chapter 7. CoFe Layered Double Hydroxide Supported on Graphitic Carbon Nitrides as a Bi-functional Electrocatalyst

(**Ref:** T. Bhowmik, M. K. Kundu, S. Barman; *ACS Appl. Energy Mater.* 2018, *1*, 1200-1209)

Finding non-precious metal based highly active and durable bi-functional electrocatalysts for overall water-splitting is essential for the development of various renewable energy storage and conversion technologies. Generally, most of the HER catalysts are active in acidic environment whereas most of the nonprecious OER catalysts are active under alkaline environment. Therefore, there is always a pH mismatch associated with the development of non-precious metal based highly active and durable bi-functional electrocatalyst. This present chapter reports the synthesis of cobalt iron layered double hydroxide ($Co_{1-\delta}Fe_{\delta}$ LDH) and g-carbon nitride composite ($Co_{1-\delta}Fe_{\delta}$ LDH/g-CN_x) for overall water electrolysis in alkaline electrolyte.

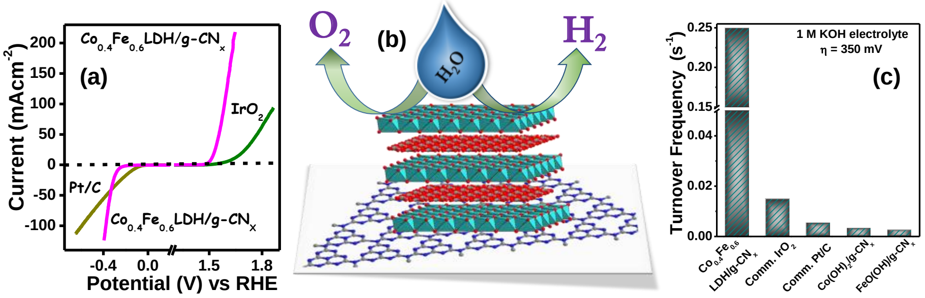

Figure 4. (a) HER and OER LSV curve different catalyst. (b) Schematic representation of $Co_{1-\delta}Fe_{\delta}$ LDH supported on g-CN_x and HER, OER. (c) Comparison of TOF values of different catalyst.

The thin $Co_{1-\delta}Fe_{\delta}$ LDH nano-sheets are successfully impregnated on graphitic carbon nitride surface by one pot co-precipitation method at ambient temperature. The optimal composite, $Co_{0.4}Fe_{0.6}$ LDH/g-CN_x exhibited superior OER activity in 1 M KOH electrolyte with a small overpotential of 0.28 V for 10 $mAcm^{-2}$, low Tafel slope of 29 mV/dec, 100% faradic efficiency and high TOF of 0.25 s^{-1} which is superior than the comm. IrO_2. Furthermore, the $Co_{0.4}Fe_{0.6}$ LDH/g-CN_x composite exhibited remarkable HER activity in alkaline media and its HER activity is slightly lower than that of comm. Pt/C at low overpotential but it out-performs Pt/C at high overpotential. This catalyst requires a potential of 1.61 V to obtain current density of 10 mA cm^{-2} for overall water splitting in the alkaline electrolyte. Furthermore, the catalyst demonstrated its long term durability and higher stability for HER and OER under alkaline environment.

Chapter 8. $Co_1Al_2(OH)_m$ LDH and g-Carbon Nitride Composite Nanostructure for Water Oxidation Reaction

(**Ref:** T. Bhowmik, M. K. Kundu, S. Barman; manuscript under preparation)

Water oxidation is the fundamental process for the development of promising energy conversion technologies including integrated solar water-splitting devices, water electrolyzers, and rechargeable Li-air batteries. Electrocatalytic water oxidation is the evaluation of molecular O_2 via multi proton/electron-coupled steps from intermittent sources such as water (H_2O). The oxygen evolution reaction (OER) is the bottleneck process in overall water splitting reaction. Therefore, the development of a superior electrocatalyst for OER is a daunting task.

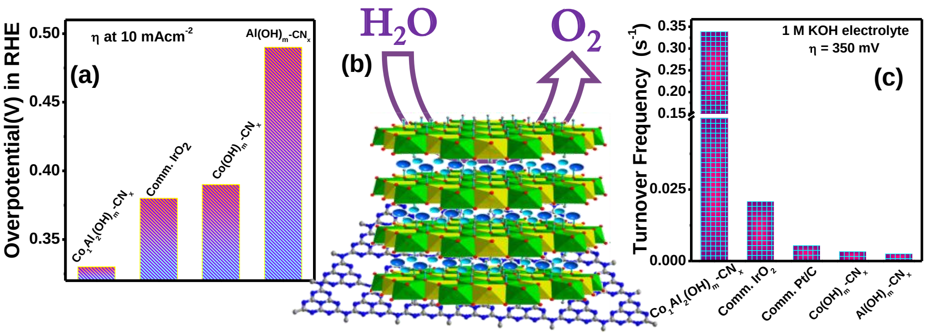

Figure 5. (a) Comparison of overpotential of different catalyst. (b) Schematic representation of $Co_1Al_δ(OH)_m$ supported on CN_x and OER. (c) Comparison of TOF values for different catalyst.

Chapter 8 demonstrates the synthesis of composite of cobalt aluminium layered double hydroxide-carbon nitride ($Co_1Al_δ(OH)_m$-CN_x) by simple microwave heating method and their applications towards water oxidation reaction in alkaline electrolyte. A series of $Co_1Al_δ(OH)_m$-CN_x composite materials was synthesised by varying the amount of Co and Al precursors. Among those different compositions, highest catalytic activity was observed for $Co_1Al_2(OH)_x$-CN_x composite materials with a small overpotentials of 0.31 V to achieve 10 mA cm^{-2} current density, low Tafel slope of 36 mV/dec and ~99% Faradic efficiency. The $Co_1Al_2(OH)_x$-CN_x composite showed the very high intrinsic activity with TOF value of 0.34 s^{-1}at 0.35 V which is 17 times higher as compared to comm. IrO_2 (0.021s^{-1}). The catalyst displayed very high stability and long term durability under OER conditions in alkaline environment. The supperior OER activty as well as higher stability may be attributed due to the strong synergestic effect betwwen support and $Co_1Al_δ(OH)_m$ LDH or improved ECSA of the composite materials.

Chapter 9. Selective Hydrogenation of Nitro Compounds and Ullmann Coupling Reaction by Palladium Nanoparticles Supported on Graphitic Carbon Nitride.

(**Ref:** T. Bhowmik, M. Sadhukhan, S. Barman; **manuscript under preparation**)

Improved catalytic activity with enhanced stability, size-shape dependent selectivity and reactivity makes the heterogenious nanocatalyst as a versatile tool for organic transformation. Chapter 9 deals with a facile synthesis of highly dispersed palladium nanoparticles embedded on graphitic carbon nitride (Pd@CN$_x$) by ultrasound assisted method without aid of any external reducing agent and its effective catalytic activity towards easy dehydrogenation of sodium borohydride ($NaBH_4$) and ammonia borane (AB) in aqueous medium.

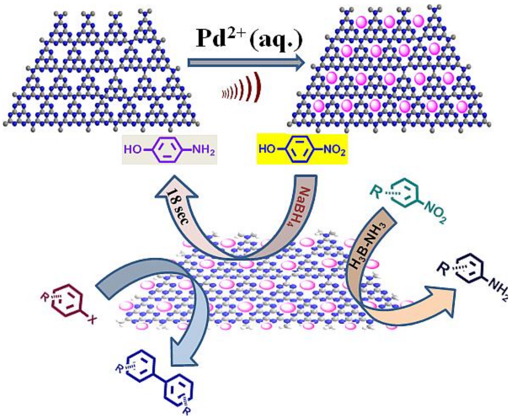

Figure 6. Schematic representation of synthesis and application of Pd@CN$_x$ composite towards nitro reduction and ullmann coupling reaction.

This mentioned catalyst displayed highly selective reduction towards nitro groups in presence of other reducible groups with good stability. Furthermore, the catalyst exhibits superior catalytic activity towards ullmann coupling reaction of different aryl halides with broad range of substrates scope.

References:

1. Stamenkovic, V. R.; Strmcnik, D.; Lopes, P. P.; Markovic, N. M., *Nat. Mater.* **2017,** *16*, 57-69.
2. Ng, J. W. D.; Gorlin, Y.; Hatsukade, T.; Jaramillo, T. F., A , *Adv. Energy Mater.* **2013,** *3*, 1545-1550.
3. Jiao, Y.; Zheng, Y.; Jaroniec, M.; Qiao, S. Z., *Chem. Soc. Rev.* **2015,** *44*, 2060-2086.
4. Wang, Y.; Wang, X.; Antonietti, M., *Angew. Chem. Int. Ed.* **2012,** *51*, 68-89.
5. Wen, J.; Xie, J.; Chen, X.; Li, X., *Appl. Surf. Sci.* **2017,** *391*, 72-123.
6. Chen, D.; Tang, L.; Li, J., *Chem. Soc. Rev.* **2010,** *39*, 3157-3180.
7. Schnorr, J. M.; Swager, T. M., *Chem. Mater.* **2011,** *23*, 646-657.
8. Long, X.; Wang, Z.; Xiao, S.; An, Y.; Yang, S., *Mater. Today* **2016,** *19*, 213-226.
9. Astruc, D.; Lu, F.; Aranzaes, J. R., *Angew. Chem. Int. Ed.* **2005,** *44*, 7852-7872.

Publications in Refereed Journal:

a. Published

*1. **Bhowmik, T.**; Kundu, M. K.; Barman, S., *Palladium Nanoparticle-Graphitic Carbon Nitride Porous Synergistic Catalyst for Hydrogen Evolution-Oxidation Reactions over a Broad Range of pH and Correlation of Its Catalytic Activity with Measured Hydrogen Binding Energy. ACS Catal.*, **2016,** *6*, 1929–1941.

*2. **Bhowmik, T.**; Kundu, M. K.; Barman, S., *Growth of One-Dimensional RuO2 Nanowires on g-Carbon Nitride- An Active and Stable Bifunctional Electrocatalyst for Hydrogen and Oxygen Evolution Reactions at All pH Values. ACS Appl. Mater. Interfaces*, **2016**, *8*, 28678-28688.

*3. **Bhowmik, T.**; Kundu, M. K.; Barman, S., *Highly efficient electrocatalytic oxidation of formic acid on palladium nanoparticles-graphitic carbon nitride composite. Int. J Hydrogen Energy*, **2017,** 42, 212-217.

*4. **Bhowmik, T.**; Kundu, M. K.; Barman, S., *CoFe Layered Double Hydroxide Supported on Graphitic Carbon Nitrides: An Efficient and Durable Bifunctional Electrocatalyst for Oxygen Evolution and Hydrogen Evolution Reactions. ACS Appl. Energy Mater.* **2018,** *1*, 1200-1209.

*5. **Bhowmik, T.**; Kundu, M. K.; Barman, S., *Highly active and durable Pd nanoparticles-porous graphitic carbon nitride composite for electrocatalytic oxygen reduction reaction.Int. J Hydrogen Energy*, **2016**, 41, 14768-14777.

6. **Bhowmik, T.**[#]; Kundu, M. K.[#]; Barman, S., *Ultra small gold nanoparticles-graphitic carbon nitride composite- an efficient catalyst for ultrafast reduction of 4-nitrophenol and removal of organic dyes from water.RSC Adv.*, **2015**, 5, 38760-38773. **(# equal contribution)**

7. Sadhukhan, M.[#]; **Bhowmik, T.**[#]; Kundu, M. K.; Barman, S., *Facile synthesis of carbon quantum dots and thin graphene sheets for non-enzymatic sensing of hydrogen peroxide. RSC Adv.*, **2014**, 4, 4998-5005. **(# equal contribution)**

8. Kundu, M. K.; **Bhowmik, T.**; Barman, S., *Gold aerogel supported on graphitic carbon nitride- an efficient electrocatalyst for oxygen reduction reaction and hydrogen evolution reaction. J. Mater. Chem. A*, **2015**, 3, 23120-23135.

9. Sadhukhan, M.; Kundu, M. K.; **Bhowmik, T.;** Barman, S., *Highly dispersed platinum nanoparticles on graphitic carbon nitride: A highly active and durable electrocatalyst for oxidation of methanol, formic acid and formaldehyde. Inter. J. Hydrogen Energy*, **2017**, *42*, 9371-9383.

10. Kundu, M. K.; **Bhowmik, T.;** Mishra, R.; Barman, S., *Pt Nanostructures/N-Doped Carbon hybrid, an Efficient Catalyst for Hydrogen Evolution/Oxidation Reactions: Enhancing its Base Media Activity through Bifunctionality of the Catalyst. ChemSusChem*, **2018**, *11*, 2388-2401.

11. Kundu, M.K. [#]; Mishra, R. [#]; **Bhowmik, T.**; Barman, S., *Rhodium metal–rhodium oxide ($Rh–Rh_2O_3$) nanostructures with Pt-like or better activity towards hydrogen evolution and*

oxidation reactions (HER, HOR) in acid and base: correlating its HOR/HER activity with hydrogen binding energy and oxophilicity of the catalyst. J. Mater. Chem. A, **2018**, *6*, 23531-23541 (#equal contribution)

b. Manuscript under preparation:

*1. **Bhowmik, T.;** Sadhukhan, M.; Barman, S., *Highly Dispersed Palladium Nanoparticles Supported on Graphitic Carbon Nitride for Selective Hydrogenation of Nitro Compounds and Ullmann Coupling Reaction.*

*2. **Bhowmik, T.;** Kundu, M. K.; Barman, S., $Co_1Al_2(OH)_m$ *LDH and g-carbon nitride composite nanostructure: An Efficient Electrocatalyst for Water Oxidation Reactions in Alkaline Electrolyte.*

***Pertaining to thesis**

Other Publications:

a. Conference/Symposium

1. **Poster Presentation: "**Electrocatalytic Hydrogen Evolution and Oxidation Reactions on Palladium Nanoparticle-Graphitic Carbon Nitride Porous Composite Over Broad Range of pH" in 20th Chemical Research Society of India (CRSI) National Symposium in Chemistry on 3rd -5th February, 2017 organized at Gauhati University.

2. **Poster Presentation:** "One Dimensional RuO_2 Nanowires Supported on g-carbon nitride: An Active and Stable Bifunctional Electrocatalyst for Hydrogen and Oxygen Evolution Reactions at all pH Values" in International Conference on Recent Advances in Material Chemistry on 24th -26th February, 2017 at Utkal University.

3. **Poster Presentation:** "Highly active and durable Pd nanoparticles-porous graphitic carbon nitride composite for electrocatalytic oxygen reduction reaction" in Inter IISER and NISER Chemistry Meet (IINCM-2017) on 22th -24th December, 2017 organized at School of Chemical Sciences, National Institute of Science Education & Research, Bhubaneswar.

4. 11th CRSI-RSC Symposium on 2nd February, 2017, organized at Gauhati University.

5. Indo French Symposium on "Functional Metal-Organics: Applications in Materials and Catalysis" on 24th – 26th February, 2014, organized at School of Chemical Sciences, National Institute of Science Education & Research, Bhubaneswar.

Tanmay Bhowmik
Signature of Student:

Date: 16.05.2018

Doctoral Committee:

S. No.	Name	Designation	Signature	Date
1.	**Prof. A. Srinivasan**	Chairman		16 · 05 · 2018
2.	**Dr. Sudip Barman**	Guide/ Convener		16 · 05 · 2018
3.		Co-guide (if any)		
4.	**Dr. Prasenjit Mal**	Member	Prasenjit Mal	16 · 05 · 2018
5.	**Dr. Nagendra K. Sharma**	Member	Sharma	16 · 05 · 2018
6.	**Dr. Abdur Rahaman**	Member		16 · 05 · 2018

List of Figure Caption

List of Table Caption

List of Abbreviations

0D	Zero dimension
1D	one dimension
2D	Two dimension
3D	Three dimension
XPS	X-ray Photoelectron Spectroscopy
p-XRD	Powder X-ray Diffraction
TGA	Thermogravimetric Analysis
UV-VIS	Ultra Violet and Visible
TEM	Transmission Electron Microscopy
FE-SEM	Field Emission Scanning Electron Microscopy
SAED	Selected Area Electron Diffraction
rGO	Reduced graphene oxide
PBS	Phosphate buffer solution
NP	Nanoparticle
JCPDS	Joint Committee on Powder Diffraction Standards
HRTEM	High Resolution Transmission Electron Microscopy
FWHM	Full width at half maxima
FTIR	Fourier Transform Infrared Spectroscopy
EDS	Energy Dispersive X-ray spectroscopy
CV	Cyclic-voltammetry
LSV	Linear Sweep Voltammetry
BE	Binding Energy
GO	Graphene oxide
Comm.	Commercial
g-CN$_x$	Graphitic Carbon Nitride
GO	Graphene oxide
CNT	Carbon nanotube
NC	Nitrogen doped carbon.
ICP-OES	Inductively coupled plasma optical emission spectrometry
PEM	Proton Exchange Membrane
AEM	Anion Exchange Membrane
FCs	Fuel cell
WEs	Water Electrolyser

RFCs	Regenerative Fuel Cell
HER	Hydrogen Evolution Reaction
HOR	Hydrogen Oxidation reaction
ORR	Oxygen Reduction Reaction
OER	Oxygen Evolution Reaction
FAO	Formic Acid Oxidation
GC	Glassy Carbon
AB	Ammonium Borane
NP	Nitro phenol
AP	Amino Phenol
EtOH	Ethanol
ECSA	Electrochemical surface Area
EIS	Electrochemical Impedance Spectra
Rct	Charge Transfer Resistance
MA	Mass Activity
SA	Specific Activity
TOF	Turn Over Frequency
TON	Turn Over Number
MW	Microwave
US	Ultrasound
a.u.	Arbitrary unit
RRD	Rotating Disk Electrode
RHE	Reversible Hydrogen Electrode
nm	Nanometer
cm	Centimeter
Eq.	Equation
XPS	X-ray photoelectron spectroscopy
DI water	De-ionised water
wt.%	Weight percentage
LDH	Layered Double Hydroxide
EIA	Energy Information Administration
TWh	Terawatt hour
HBE	Hydrogen Binding Energy
PGMs	Platinum Group Metal

Chapter 1

Nanocomposite for Electrochemical Energy Conversions and Organic Reactions

1.1 Abstract

In this present thesis, we have reviewed the current and future energy demands and explored the importance of renewable energy conversions and storage techniques. The history and development of fuel cells as well as water electrolysers are being highlighted. The main concern of this chapter was the general descriptions, reaction steps, mechanisms and kinetics of different fuel cell reactions such as hydrogen oxidation reaction (HOR), oxygen reduction reaction (ORR) and water electrolyser reaction namely hydrogen evolution reaction (HER), oxygen evolution reaction (OER). Brief descriptions of theoretical backgrounds for the development of various efficient electro catalysts for different renewable processes have been exploited. This chapter also records an account of current literatures pertaining to different nanocarbon materials graphene, carbon nanotube (CNTs), carbon nitride based precious and non-precious metal nanostructure materials used for various fuel cell reactions. Moreover, NPs based heterogeneous catalyst for various organic conversions has been briefly discussed in the last section of this chapter.

1.2 Introduction

In 20th century, transportation has been developed mainly by the combustion of engine because of its high energy and power density. During the early of 21st century, combustion of hydrocarbons behaves as a popular energy source for transportation.[1] However, research on developing renewable energy resources and storage techniques has gained an impetus attention due to the continuous increasing concerns over the rapid depletion of fossil fuels and its negative impacts on environment.[2] According to the United States Energy Information Administration (US-EIA), average global energy consumption is yearly 14 Terawatt hour (TWh) and the predicted amount will be more than double by the year of 2050 and triple by 2100.[3] Furthermore, fossil fuels such as crude oil, coal and natural gas have been accounted for ~ 80% of primary energy sources **(Figure 1.1.a)**. About 10,000 million tons of petroleum has been consumed by the year of 2000 which is presumably to be doubled by the year of 2030 (**Figure 1.1.b**). Renewable technologies[4] have been developed rapidly due to the upsurge of global warming and the limited resources of fossil fuels. The renewable energy storage and conversion devices are broadly classified into three categories[5] such as

1) Thermal storage: ice storage and molten salt.

2) Mechanical storage: hydraulic power, compressed-air energy storage etc.

3) Electrochemical storage: rechargeable batteries, super-capacitors, and regenerative fuel cells.

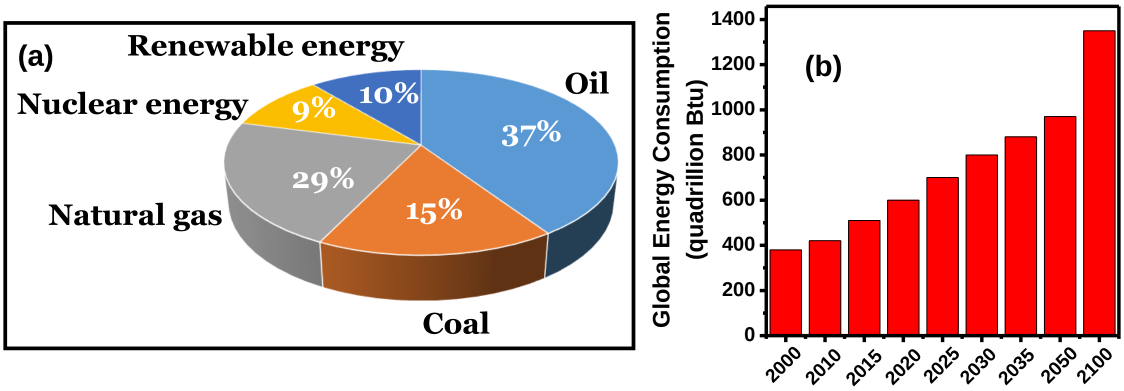

Figure 1.1. (a) Energy consumption from different energy sources. (b) Year wise projected energy consumption.

Among those different kinds of energy storages, thermal and mechanical storage are not used practically due to their potential hazardous behaviour. For example, the geothermal energy sources appear from the heat of the earth which is a green source but the potential dangers further prevent the use of geothermal power station anywhere. Wind and hydraulic power are also important renewable energy sources, but building of dam and wind farm is extremely expensive as well as it demands to have some special location and geological conditions. Biomasses and biofuels are potential renewable sources in developing high-quality energies (*i.e.* alcohol, biodiesel). However, it requires a large land and lots of labours to grow and burn the biomass. Moreover, the energy conversion efficiency of bio-fuels is low enough and in order to further use they have to mix with other gasoline to generate the machines properly. Electrochemical energy is one of the best ways to bridge between the fossil fuel and hydrogen fuel based devices.[6] The electrochemical energy conversion devices such fuel cells (FCs) and energy storage devices such as water splitting electrolyzer (WSE) have been demonstrated as the alternatives to the combustion engines. Regenerative fuel cells (RFCs) is an important electrochemical energy storage and conversion device where energy mainly carried by H_2-H_2O.[7] RFCs constitute of two compartments one is fuel cell stack and another is electrolyser stack. **Figure 1.2.** represents the utilization of RFCs in different potential applications. Generally, H_2 behaves as the energy carrier which reserves renewable electricity by splitting water into the corresponding H_2 and O_2 in a ‘electrolysis mode’. This H_2 is further stored on-site and for the time being it is consumed; providing electricity whenever it is needed.[8] Furthermore, RFCs are exclusively used in different vehicles, aircrafts and supply power for residential as well as commercial purposes. Being economically inexpensive, RFCs constitutes are used for centralized grid energy storages. However, RFCs based on H_2-O_2-H_2O cycle[9] have been attracted impetus attentions because of the eco-friendly and economically advantageous nature of all these three species. Thus for large-scale energy storage, RFCs are the most important and promising constituents.

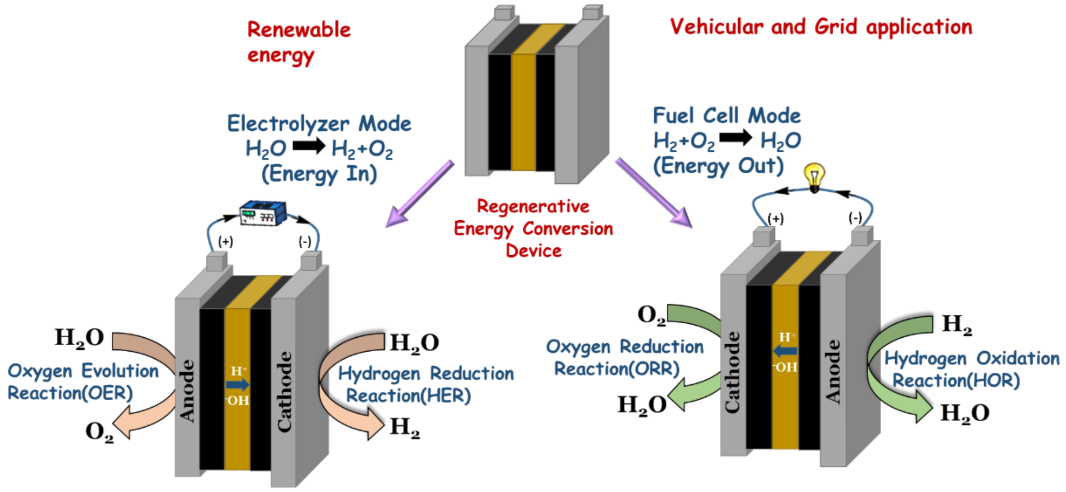

Figure 1.2. Utilization of RFCs for different potential applications.

Among the different fuel cells, H_2-O_2 fuel cell is a fascinating candidate for future renewable energy conversion technology; where electricity is generated from the chemical energy of H_2, used as flexible energy carrier. The electrolyser can generate fuels from renewable resources and store the electrical energy as of chemical bond. Depending upon the nature of the electrolytes, RFCs are generally classified into two types; (1) proton exchange membrane (PEM) and (2) anion exchange membrane (AEM). The PEM system is generally worked under acidic electrolytic (i.e. lower pH) environment wherein the protons (H) are generated from electrolytes or products of anodic reactions, exchanged between anodic and cathodic compartments.[10] Anion exchange membrane (AEM) system is mainly worked under alkaline electrolyte environments (*i.e.* higher pH) and exchanges hydroxyl anion between anodic and cathodic compartment.[11]

1.3 Various Reactions Involved in RFCs

The RFCs mainly consist of four different reactions namely hydrogen oxidation reaction (HOR), oxygen reduction reaction (ORR) in fuel cell stack and hydrogen evolution reaction (HER), oxygen evolution reaction (OER) in water electrolyzer stack. All the electrochemical processes occurred in the RFCs and corresponding over potentials are shown in **Figure 1.3**.

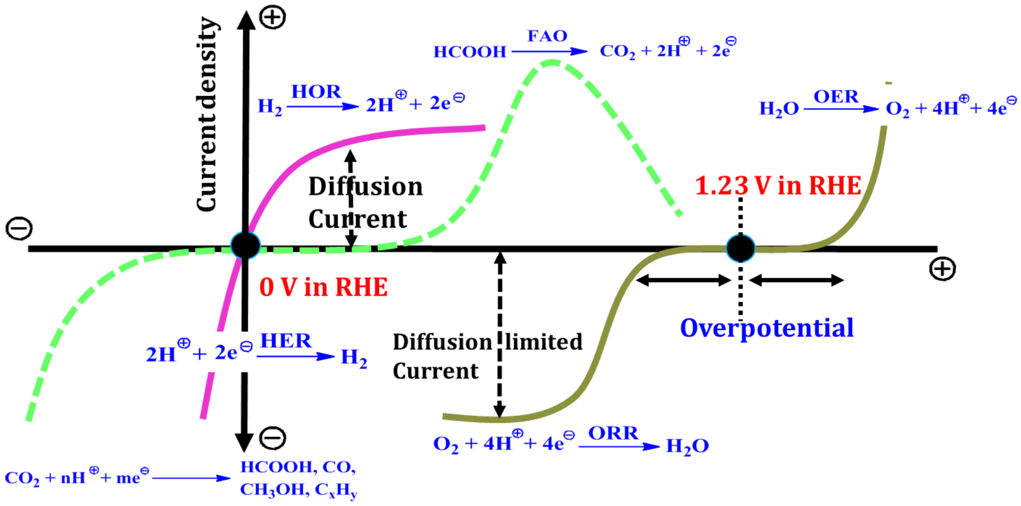

Figure 1.3. Different electrochemical processes and their corresponding polarization curves.

1.3.1 Fuel Cell Stack:

Fuel cell stack is an electrochemical device that converts chemical energy from fuels (such as hydrogen and formic acid) directly into electricity through a continuous chemical reaction. In 1839, the first fuel cell was developed as gas battery by renowned physicist Sir William Robert Grove. He mixed hydrogen and oxygen in the presence of an electrolyte and produced electricity and water. After that, in 1889, Ludwig Mond and Charles Langer first time introduced the term 'Fuel Cell'. After 50 years, in 1939, Francis Thomas Bacon successfully developed a 5 kW stationary alkaline fuel cell. In 1955, chemist W. Thomas Grubb modified and improved the efficiency of original fuel cell by using a sulphonated polystyrene ion-exchange membrane as the electrolyte. After several modifications, in 1991, Roger Billings first time developed a H_2 fuel cell for automobile. But the main problem arises due to its very large size and non-portability. In 2009, FCs are first time sold commercially and used for electric vehicles. PMEFC is the most efficient types of FCs as it has high power density as compared to the other types FCs.

The reaction sequences occurred in the PMEFCs are schematically represented in **Figure1.4**.

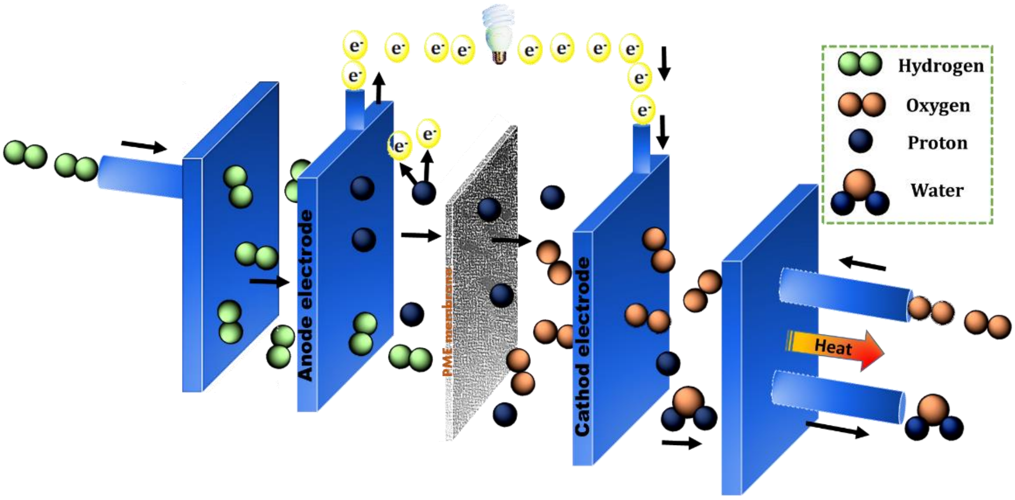

Figure 1.4. Schematic representation of working principle of PEMFCs.

The sequential steps are demonstrated as follows:

Step I: Hydrogen fuel and oxygen is channelled to anode and cathode compartment respectively.

Step II: In anode compartment, hydrogen is oxidised into hydronium ion which is further demonstrated as hydrogen oxidation reaction (HOR).

Step III: At the same time, in the cathode compartment oxygen is reduced into hydroxide ion represented as oxygen reduction reaction (ORR).

Step IV: The positive hydronium ions from anodic compartment cross the PEM membrane and combined with hydroxide ion (anodic compartment) to generate water.

Step V: The negatively charged electron is travelled through external circuit from anode to cathode and generated electricity.

The half- cell reactions have been discussed as follows:

Hydrogen Oxidation Reaction:

Hydrogen Oxidation reaction (HOR) is the most important anodic half-cell process of H_2 fuel cell technology. The systematic literature study reveals that Pt and Ir metal catalysts have highest electrocatalytic HOR activity in acidic electrolyte. Gasteiger and co-workers reported[12] a systematic analysis of HOR kinetics of carbon supported different Pt-group metals such as Pt, Ir, Rh, Pd electrocatalysts in acidic medium. The trend of activity is followed the order Pt>Ir>>Rh>Pd. Durst et al.[13] and Zheng et al.[14] have demonstrated the similar kind of activity trends for Pt-group metals in acidic electrolyte and ~10 folds lower HOR activity in alkaline medium. Several literature reports[14-16] further suggested that pH dependent hydrogen binding energy (HBE) plays crucial role for HOR activity in both higher and lower pH values. A. Satsuma and his co-workers reported[17] alloyed nanoparticles of Ru and Ir (Ru-Ir/C-20) has four times higher HOR activity than Pt/C catalyst in alkaline medium. They suggested that the lower HBE of Ru-Ir/C-20 is the main factor for higher HOR activity of the catalyst. Soon after that, Markovic and his co-workers reported[18] that Ir(111) catalyst has 25-flod higher HOR activity than Pt(111) in alkaline medium. The same groups synthesized[18] $Pt_{0.1}Ru_{0.9}$ electrocatalyst, showing 25-flod higher HOR activity than Pt/C catalyst in alkaline medium and the HOR activity of $Pt_{0.1}Ru_{0.9}$ in alkaline medium is equal with HOR activity of Pt/C in acidic medium. Based on those observations, Markovic et al. further proposed that besides the substrate-H_2 and substrate-H^* binding energy, substrate-OH_{ad}^* interactions plays important role for overall HOR kinetics. Wang et al. reported[19] that PtRu/C catalyst has more than two times faster rate of HOR than that of Pt/C catalyst in alkaline medium and it is mainly generated due to the lower oxophilicity of PtRu/c catalyst. However it is not very clear about the main descriptor for HOR activity of a catalyst in alkaline medium.

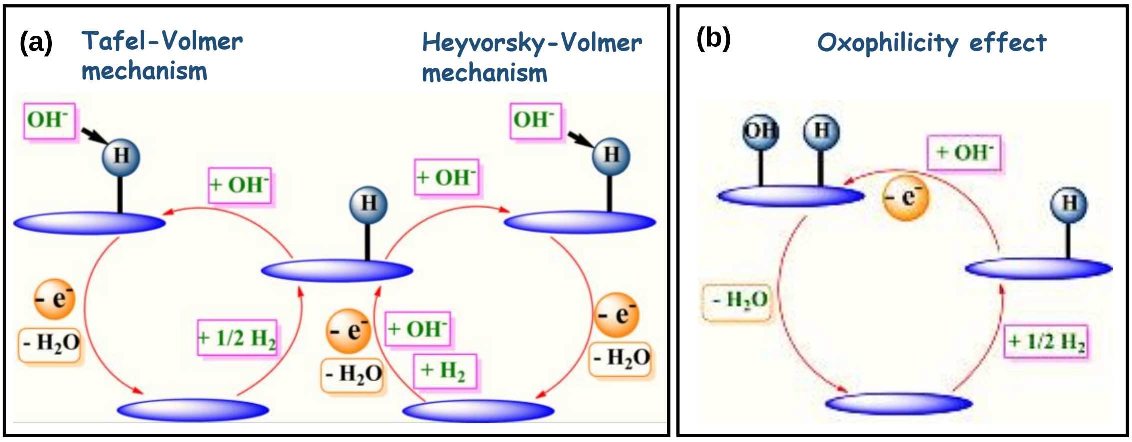

Figure 1.5. (a) HOR reaction mechanism in alkaline medium. (b) HOR mechanism with involvement of adsorbed hydroxyl ion. Partly reproduced from ref. 20 with permission. Copyright 2018, with permission from Elsevier.

HOR Reaction Mechanism:

The HOR reaction consists of three elementary steps i)Tafel, ii) Heyrovsky, and iii) Volmer. The reaction steps are shown in **Table 1.1.** and **Table 1.2**. HOR reaction consists with dissociative adsorption, formation of H* followed by a fast charge transfer and desorption of proton in acidic electrolyte or water in basic electrolyte. The HOR mechanism can follow either Tafel-Volmer or Heyrovsky-Volmer pathway in both the acidic and basic electrolyte solutions.[20] The reaction mechanism in basic medium is shown in **Figure 1.5.a**. In this mechanism, the involved hydroxyl (-OH) ion comes from electrolyte solution. In addition of this mechanism, several groups reported another possibility where hydroxyl (-OH) ion is also adsorbed on the catalyst's surface and involved in the reaction mechanism (**Figure 1.5.b**).

Table 1.1. HOR reaction steps in acidic electrolyte.

Overal reaction	Reaction pathway	Name
$2H^+ + 2e^- = H_2$	**Step I** $H_2 \rightarrow H^+ + e^- + A\text{-}H^*$ or	Heryovsky
	$H_2 \rightarrow 2A\text{-}H^*$	Tafel
	Step II $A\text{-}H^* \rightarrow H^+ + e^- + A$	Volmer

The reaction mechanism describes in **Figure 1.5.b**, clearly indicates that HOR reaction kinetics in both acidic and alkaline medium is mainly controlled by hydrogen binding energy (HBE). But in second mechanism, both HBE and oxophilicity of the catalyst are responsible for HOR kinetics.

Table 1.2. HOR reaction steps in alkaline electrolyte.

Overal reaction	Reaction pathway	Name
$2H_2O + 2e^- = H_2 + 2\,OH^-$	**Step I** $H_2 + H_2O \longrightarrow H_2O + e^- + A\text{-}H^*$ or	Heryovsky
	$H_2 \longrightarrow 2A\text{-}H^*$	Tafel
	Step II $A\text{-}H^* + OH^- \longrightarrow H_2O + e^- + A$	Volmer

Oxygen Reduction Reaction:

Electrochemical oxygen reduction reaction (ORR) is an important cathodic half cell reaction in fuel cells. ORR is the main reaction for PMEFCs including direct methanol or formic acid fuel cell (DMFCs/DFFCs), Zn-Air batteries and Li-Air batteries. Last few decays, carbon supported polyhedral Pt NPs (3–5 nm of Pt/C) is considered as the state-of-the-art electrocatalyst for ORR in PMEFCs. Despite of their better activities, Pt/C catalyst has some major drawbacks caused by mainly its stability issues such as Pt dissolution, migration, Ostwald ripening and anion adsorption during the time of electrocatalytic reactions. However, several strategies have been employed to overcome all these problems for further utilization of the Pt catalyst for ORR. Size and shape controlled Pt nanostructures is one of the important developments.[21-22] Recently, Dauan and his co-workers reported[23] a very high mass activity of 13.6 A $mgPt^{-1}$ for ultrafine jagged platinum nanowires, which is 52 times better than that of the comm. Pt/C electrocatalyst. Furthermore, several studies revealed the relatively strong adsorption of oxygen species (e.g. O and OH) onto the Pt surface. In order to reduce the O and OH adsorption strength, Pt metal is being alloyed with other metals.[24-25] Chen et al. have reported[25] Pt_3Ni nano-frame catalysts which can achieve 36 factors and 22 factors enhancement in mass activity and specific activity respectively, relative to the state-of- -art comm. Pt/C catalyst. Adzic and his co-workers reported[26] a systematic studies of ORR activity of Pd-supported Pt-M mixed monolayers (where M is the strong OH absorbing substrate). OH coverage on Pt surface reduces by the lateral repulsion of adsorbed OH on a neighbouring surface metal (M) and adsorbed Pt. This study further suggested 21 times higher ORR activity of $(Pt_{80}Ir_{20})_{ML}$/Pd/C catalyst as compared to the comm. Pt/C. In addition, the ligand and strain effects are the main two factors for determining the catalytic activity. The ligand effect is mainly caused by the different electronegative atoms adjacent to Pt metal which further reinforce the electronic charge transfer process between the atoms and affecting their electronic d-band structures. In order to maintain the d-band structures, an expansion of surface occurs; consequently the energy also increases, which will generate stronger interaction with the adsorbate as well as stronger bonding with the surface. On the other hand, compression of the surface reduces the energy, thus reduces the interaction between the surface and the adsorbate, and weakens the bonding. Toyoda et al. showed [27] the variation of ORR activities with the changing of the d-band centre of Pt catalyst. On the other hand, the strain effects are generally originated from different atomic arrangements on the surface/interface atoms and the defects in crystals. Recently, AEMFCs have gained attentions as a promising alternative technology due to easy designing and synthesis of non-platinum based electrocatalysts such as Pd[28], Ru[29], Ag[30] and Co[31]. In recent years, one of the most important achievements of AEMFCs is the development of metal free electrocatalyst for ORR.[32-33] Superior ORR activity of one dimensional graphitic carbon nitrides in alkaline medium was reported by Tahir and his co-workers. This result suggested 1D graphitic carbon nitride nanofiber (GCNNF) and tubular 1D graphitic carbon nitride (TGCN) has onset potential of − 0.15 and − 0.14 V in Ag/AgCl respectively, in comparison to comm. Pt/C catalyst (− 0.02 V).

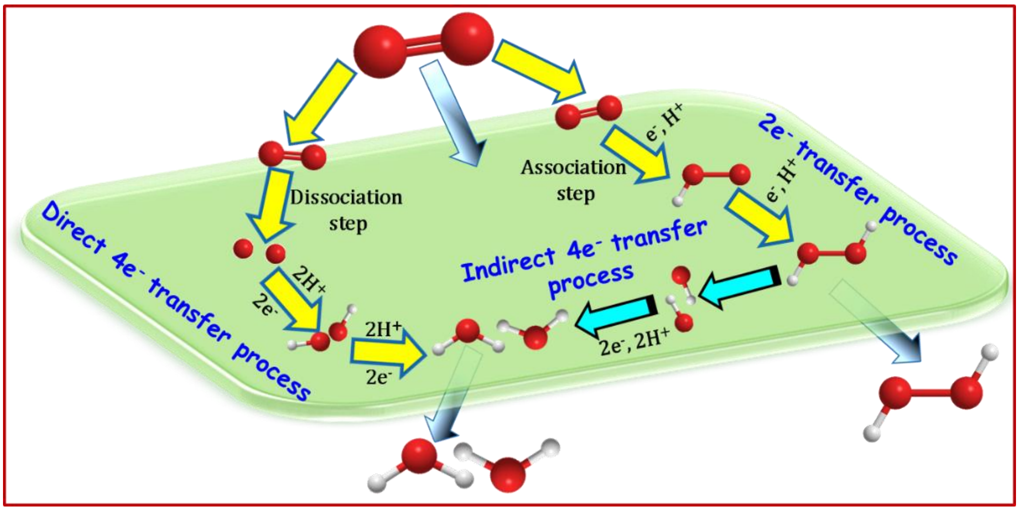

Figure 1.6. Possible different ORR reaction pathway.

ORR Reaction Mechanism:

In FCs, oxygen reduction at cathode can happen either by a direct four-electron pathway where an oxygen molecule adsorbs onto the catalyst surface and reduces to water, or two-electron transfer pathway with the formation of hydrogen peroxide. The reaction steps for ORR reaction are describes in **Table 1.3**. There are another possibility where ORR is occurred through indirect $4e^-$ transfer pathway, involving the formation of hydrogen peroxide intermediate which can further reduce to water or chemically decomposes to water.

Table 1.3. Possible ORR reaction pathway.

Direct $4e^-$ path	Direct $2e^-$ path	Indirect $4e^-$ path
$O_2 + M \longrightarrow M\text{-}O_2^*$ $M\text{-}O_2^* + M \longrightarrow 2M\text{-}O^*$ $M\text{-}O^* + e^- + H^+ \longrightarrow M\text{-}OH^*$ $M\text{-}OH^* + H^+ + e^- \longrightarrow H_2O$	$O_2 + M \longrightarrow M\text{-}O_2^*$ $M\text{-}O_2^* + H^+ + e^- \longrightarrow M\text{-}OOH^*$ $M\text{-}OOH^* + H^+ + e^- \longrightarrow H_2O_2$	$O_2 + M \longrightarrow M\text{-}O_2^*$ $M\text{-}O_2^* + H^+ + e^- \longrightarrow M\text{-}OOH^*$ $M\text{-}OOH^* \longrightarrow M\text{-}O^* + M\text{-}OH^*$ $M\text{-}O^* + H^+ + e^- \longrightarrow M\text{-}OH^*$ $M\text{-}OH^* + H^+ + e^- \longrightarrow H_2O$

Depending upon the reaction conditions and behaviour of the electrocatalyst, ORR on the different electrode may follow direct four-electron pathway or two-electron pathway or indirect four-electron transfer process. Nobel metal catalyst generally follows direct 4e- transfer process whereas the metal free electrocatalyst follows 2e pathway and generates peroxide which is somehow unwanted for FCs. Yang et al.[34] introduced boron-doped carbon nanotubes as electrocatalyst for superior ORR activity but the catalyst follows $2e^-$ process over all the potential ranges. Therefore, in order to design FCs catalyst, the process should follow 4e pathway to avoid the technical hazards of FCs**.** Moreover, it is very daunting task to develop the efficient electrocatalyst for ORR process.

Formic Acid Oxidation (FAO):

H_2-PEMFCs are considered as important candidates as a substitute of batteries.[35] But low gas phase energy density and potential danger of H_2 in the transport restrict its wide spread applications. Recently, direct methanol fuel cells (DMFCs) and direct formic acid fuel cells (DFAFCs) are gaining attentions due to their moderate energy density, easy handling etc.[36] However, DFAFCs technology generates more attentions over DMFCs because of the smaller crossover flux through Nafion membrane and higher oxidation rate of HCOOH.[36] Formic acid oxidation reaction (FAO) is the anodic process of DFAFCs. Pt-based catalysts are generally exclusively employed in the anodic layer for DFAFCs. Weber et al.[37] first reported that the formic acid was electrochemically more active fuel than that of methanol on both Pt-black and Pt/Ru catalysts. After that, Pt-based catalysts especially bimetallic systems have been exclusively studied for FAO reactions. In 1923, Müller et al.[38] first time reported that FAO on Pt proceeds through two different mechanisms.One is dehydrogenation process wherein the direct path involves oxidation of formic acid to carbon dioxide ($HCOOH = CO_2 + 2H^+ + 2e^-$) and second one follows indirect pathway (dehydration path) via intermediate formation that is the oxidation of adsorbed CO species ($HCOOH = CO_{ads} + H_2O = CO_2 + 2H^+ + 2e^-$).[39] The main problem regarding FAO reaction is adsorption of CO on Pt surfaces. The intermetallic phase of Pt[40-41] with Bi, As, Pb, In, Sn, improves the activities of catalyst and reduces the number of adsorption sites for CO. This type of effect is called "third body" effect. CO molecule are not desired for FCs as it adsorbs on the catalytic surface and reduces the number of active site available for HCOOH. Recently, Pd metal based catalysts[40, 42] are being widely used as catalyst for FAO reaction. But the catalytic activity of Pd based catalyst decreases with the cell operation time; consequently the efficiency of DFAFCs decreases. Therefore, till now the development of robust and highly active catalyst for DFAFCs is a challenging task.

1.3.2. Electrolyser Stack:

Electrolyser is a device where electrolysis of water into molecular H_2 and O_2 is occurred. Water splitting reaction is an endothermic, nonspontaneous process. Therefore, energy is required to precede the reaction in forward direction. However, in electrolyser device this amount of energy is provided as the electrical current through an electrochemical cell. Among all the different processes, the electrochemical water splitting is the best way to bridge between the global energy supply and future era of hydrogen economy. A simple schematic representation of an electrolyzer cell has been shown in **Figure 1.7.** Based on the electrolytes used in electrolyser, the electrolyser technology can be classified into two categories: 1) Proton electrolyte membrane water electrolyser (PEMWEs) and 2) Alkaline electrolyte membrane water electrolyser (AEMWEs). Traditionally, large scale H_2 is produced from chloro-alkali industry during the electrocatalytic formation of chlorine and caustic soda in AEMWEs. The first commercially available AEMWEs has 40-80% efficiency of current density in-between

250-500 mA cm^{-2} whereas PEMWEs has the same efficiency with the current density ranges from 1500 to 2000 mA cm^{-2}. Although both the processes have same efficiency, PEMWEs has several advantages over AEMWEs because of its higher current density, low operational temperature and it has produced high purity of H_2. In addition, cheap material is being used in AEMWEs unlike the case of PEMWEs. Therefore, both the processes are equally important for the development of WEs technology. In WEs, water is oxidised into oxygen and solvated protons at the anode which is further called as oxygen evolution reaction (OER).

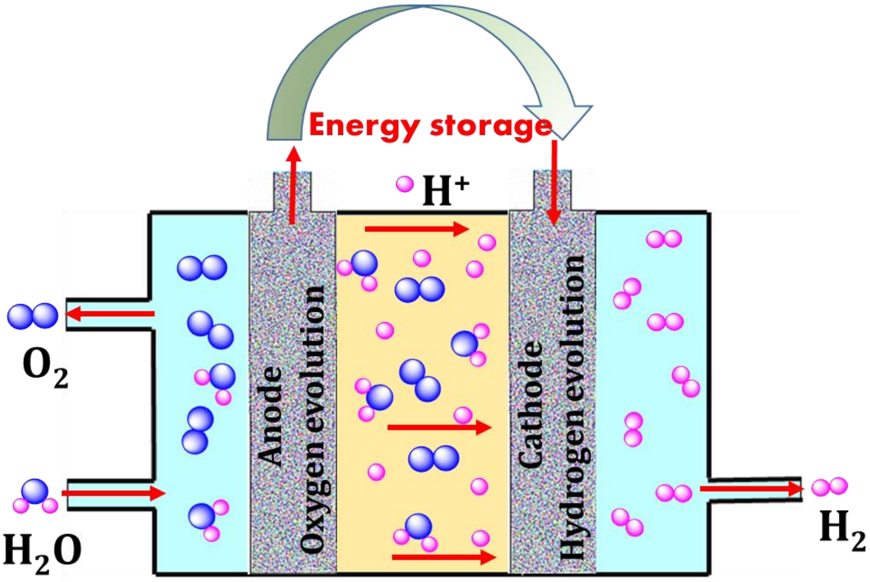

Figure 1.7. Schematic presentation of water electrolyser system.

The protons are then conducted through the electrolyte and reduced to generate hydrogen gas at cathode, known as hydrogen evolution reaction (HER). The cathodic and anodic processes in WEs are describes as follows:

Hydrogen Evolution Reaction:

Platinum group metals (PGMs) including Pt, Pd, Rh, Ru and Ir have been proven as excellent cathode materials for EWEs. Among all these materials, Pt is still considered as one of the best electrocatalysts for HER in both acidic and alkaline medium.[43]

Although several non-noble metal based electro catalysts have been showed promising HER activities, still Pt catalyst are considered as a state-of-art catalyst under acidic environment due to its extreme chemical inertness under working conditions and near-zero overpotential. However, high scarcity and low abundance are the main obstacles for its commercialization. To overcome such problems, several strategies have been adopted such as (i) increasing the active site by modifying the surface structures with different nanostructures, (ii) lowering Pt by depositing it on the low-cost materials, (iii) devolving other PGMs nanostructures with superior catalytic activities and (iv) developing non-noble metal catalysts which are effective under acidic environment. Y. Chen and his co-workers reported[44] polyethyleneimine functionalized Pt superstructure which has an onset reduction potential of +64.6 mV as compared to comm. Pt/C catalyst. Xioang et al. [45] have synthesised PtFeCo TriStar nanostructure, achieving a current density of 1325 $mAcm^{-2}$ at 0.4 V in RHE potentials. In addition, loading of Pt decreases by depositing it on low cost materials such as graphene,[46] WC,[47] singled walled carbon nanotubes[48] and nitrogen-doped graphene nanosheets.[49] Furthermore, other PGMs nanocatalysts have been developed to reduce the excessive uses of expensive Pt metal. Pd–Cu–S material[50] has a superior HER activity in 0.5 M H_2SO_4 with overpotentials of 58 mV at 10 mA cm^{-2} and a Tafel slope of only 35 mV dec^{-1}. Shao and his co-workers[51] developed a rhodium/silicon HER electrocatalyst which supresses the comm. Pt/C catalyst. NiRu@N–C nanohybrid catalyst[52] displayed HER active in both acidic and alkaline medium. It showed overpotentials of 50 and 32 mV in 0.5M H_2SO_4 and 1.0 M KOH respectively, corresponding to Tafel slopes values of 36 (in 0.5 M H_2SO_4) and 64mV dec^{-1} (in 1.0M KOH).[52] Various cost effective strategies have been explored in order to develop non-noble metal based catalysts such as amorphous tungsten phosphide,[53] nanostructured nickel phosphide.[54] Furthermore, MoS_2 supported on nanosized tungsten monocarbide (WC) decorated RGO (MoS_2/WC/RGO) composite and metallic Ni_3N nanosheets were synthesized.[55]

In alkaline environment Pt metal catalyst has 10 fold lower HER activity as compared to acidic environment and it requires very large amount of Pt loading (~0.5mg cm^{-2}). Therefore, effective HER catalyst is highly desirable for the development of alkaline electrolyzers. In this aspect, it is worth mentioned that, non-noble metal based catalyst are attracted more attentions as a cathode materials due to their cost effectiveness as well as enhanced HER activities under alkaline environment. First row transition metals, dichalcogenides as well as chalcogenides have been well demonstrated as cathode materials for AEWEs.[56-57] First row transition metal oxide or double hydroxide materials are also active for HER activity in AEWEs.[58-59] On the other hand, Markovic and his co-workers recently revealed a bi-function HER mechanism in alkaline medium and an improved HER kinetics on Pt metal catalyst by depositing Pt on OH^- ion promoter such as $Ni(OH)_2$ layer. After proposing the bi-functional mechanism, several reports of HER activity in alkaline electrolyte have been introduced. Ru–MoO_2 nanocomposites showed effective HER activity in 1 M KOH electrolyte.[60] Qiao and his co-workers introduced NiO as a promoter for bi-functional HER activity of RuO_2 in alkaline electrolyte.[61]

Table 1.4. HER reaction steps and their theoretical Tafel slopes in acidic electrolyte.

Overal reaction	**Reaction pathway**	**Name**	**Tafel slope mV/dec**
$2H^+ + 2e^- = H_2$	**Step I** $H^+ + e^- + A \longrightarrow A\text{-}H^*$	**Volmer**	**120**
	Step II $H^+ + e^- + A\text{-}H^* \longrightarrow H_2$ **or**	**Heryovsky**	**40**
	$2A\text{-}H^* \longrightarrow H_2$	**Tafel**	**30**

The same groups further reported Ru-graphitic carbon nitride complex, supported on carbon (Ru/C_3N_4/C) as HER catalyst in 0.1 M KOH electrolyte and revealed the effectiveness of the catalyst which was higher than the comm. Pt/C catalyst.[62] Therefore, till now designing of a HER catalyst with excellent activity as well as long term durability, is a very challenging task.

Table 1.5. HER reaction steps and their theoretical Tafel slope in alkaline electrolyte.

Overal reaction	Reaction pathway	Name	Tafel slope mV/dec
$2H_2O + 2e^- = H_2 + 2\,OH^-$	**Step I** $H_2O + e^- + A \longrightarrow A\text{-}H^* + OH^-$	Volmer	120
	Step II $H_2O + e^- + A\text{-}H^* \longrightarrow H_2 + H_2O$	Heryovsky	40
	or $2A\text{-}H^* \longrightarrow H_2$	Tafel	30

HER Reaction Mechanism:

HER reaction mainly consists of three elementary steps.[63] The reaction steps in acidic and alkaline medium are describes in **Table 1.4** and **1.5** respectively. The first step is the Volmer steps where H^+ electronically discharges and adsorbs on the catalyst surface as H_{ad}*. After that, the absorbed H_{ad}* can desorb as H_2 either by chemical desorption process or by electrochemical desorption process.

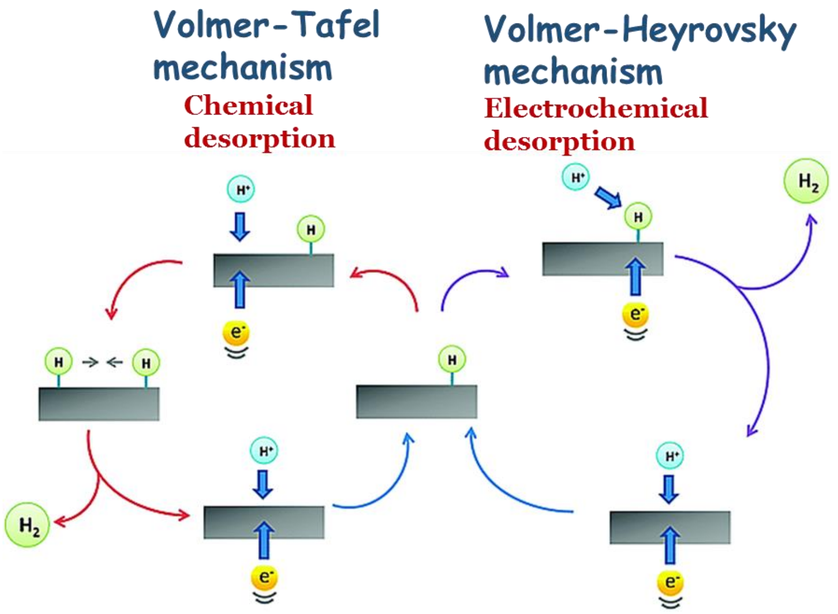

Figure 1.8. Possible HER reaction mechanism in acidic electrolyte. Partly reproduced from ref. 63 with permission. Copyright 2014, with permission from American Chemical Society.

In chemical desorption process another proton was adsorbed on the catalyst surface and both H_{ad}* are combined which is called Tafel step. On the other hand, in electrochemical desorption process, adsorbed H_{ad}* combines with electron and another H^+ from solution which is called Heyrovsky step. The possible HER reaction mechanism in acidic electrolyte is presented in **Figure 1.8**. In alkaline medium, first step is the dissociation of water and adsorpion on the catalyst surface as H_{ad}* and after that it follows the similar steps as describes above.

Oxygen Evolution Reaction:

Since 1960s, Ruthenium oxides (RuO_2) and iridium oxides (IrO_2), have been used widely in industrial electrolyzers as an anodes materials due to their unmatched OER activities in acidic environment. The IrO_2 anodes are known to be much more stable for O_2 evolution in acidic environment than RuO_2, showing only a slightly lower electrocatalytic activity. However, RuO_2 is known as the most active oxide for anodic oxygen evolution, but it suffers from lack of stability under strong acidic environment. Therefore, in acidic environment, the anodic OER suffers from several challenges such as high loading of precious metals and insufficient durability. In order to increase the efficiency of OER in acidic environment, Walton and his co-workers[64] synthesized a mixed ruthenium–iridium pyrochlore for OER under acidic condition. Although the mixing of Ru and Ir pyrochlore improves the overall OER stability of the materials but high loading of the precious metals are the main drawbacks incorporated with this process. In this aspects, a new strategy was involved by alloying the RuO_2 and IrO_2 with cheap transition metals such as SnO_2 [65-66], Ta_2O_5,[67-68]. But in all the cases, the alloyed materials show lower activity as compared to pure IrO_2 or RuO_2. Strasser and his co-workers[69] reduced the amount of precious metal loading towards OER activity in acidic environments by synthesizing oxide-supported $IrNiO_x$ core–shell particles which showed 2.5 times higher Ir-mass-based activity as compared to comm. IrO_x/C with a superior stability for a period of 20 h at constant current density. Krtil et al. recently reported[70] a cost effective stable electrocatalyst for OER activity by introducing Zn into RuO_2 moiety. In acidic environment, the usage of non-noble metal based catalyst is mainly restricted because of their increasing complex oxide phases at pH>7. Recently, very few reports put forward the usage of the cost effective non-noble metal based catalysts under strong acidic conditions.[71-72] In compare with the acidic electrolyser, alkaline electrolyser is much more cost effective due to the use of cheap earth abundant materials. Recently, many catalysts for OER based on abundant 3d metals, such as iron (Fe), cobalt (Co), nickel (Ni), and manganese (Mn), have been introduced. Among all these catalysts, Ni based catalyst are known to be the best one towards alkaline electrolysis. Different first row transition metal chalcogenide, nitride, carbide are reported for the OER in alkaline medium. But according to the solid state chemistry, the metal sulfide, phosphide, nitrides, as well as selenide show lower thermodynamical stability under oxidising condition (OER process) as compared to corresponding hydroxide or oxide.[73] During OER reaction conditions, the metal chalcogenides either form metal hydroxide or it form oxide layer around the metal chalcogenides. However, during this process sometimes it can also completely transform into amorphous metal oxide/hydroxide.[74,73] Recently, several groups reported[74-75] in-situ surface oxidation of metal phosphide into metal hydroxide or oxide after OER activity. In this context, it should be mentioned that, various perovskite materials are cheap as well as abundant. They also exhibit moderate OER overpotentials under alkaline conditions. Schmidt et al. reported[76] $La_{1-x}Sr_xCoO_3$ perovskites for OER in alkaline condition. First row transition metal based layered double hydroxides (LDH) materials also display superior OER activity. Huang and his co-workers reported[77] 3D hierarchical LDH structure of Ni_5Fe LDH@NF, exhibiting low overpotential of 210 mV at 10 mA cm^{-2} current density and showed an appealing potential of 1.59 V at 10 mA

cm^{-2} for overall water splitting. Hu and his groups reported 3D-transition metal based different LDH materials and demonstrated that NiFe NS has the best catalytic activity, having Tafel slope of 39 mV/dec as well as the TOF value of 0.05 s^{-1}. However, most of the cases, the hydroxide, double hydroxide materials are being suffered with lack of conductivity and stability. The electronic conductivity of the oxide, LDH materials can be improved through decorating on conducting materials (NF, graphene). Sasaki et al. reported[78] superlattice stacking between Ni-Fe Hydroxide and graphene nanosheets that provided an improved OER activity with over potential of 0.21 V and Tafel plot of 40 mV/decade as compared to free Ni-Fe Hydroxide (Over potential of 0.23 V and Tafel slope of 42 mV/dec).

OER Reaction Mechanism:

Compared to HER the oxygen evolution reaction, OER, is more complex one and it involves several intermediates. Due to the complexity of the oxygen evolution reaction, many mechanisms have been proposed by several groups. Sato and his co-workers[79] first time summarised the different reaction mechanisms for the OER in both acidic and alkaline medium. In alkaline electrolyte, all of the proposed reaction mechanisms have a common initial step - the adsorption of the hydroxide ions on the catalytically active site followed by different intermediate M-O, M-OH, M-OOH formation. The reaction steps and theoretical Tafel slope values are described in **Table 1.6.** The first step is the dissociation of water and adsorption of hydroxyl ion on the catalyst surface. After that the reaction proceeds with the formation of intermediate $S-O^-$ and S-OOH.

1.3.3. Theoretical Aspect of Electrochemical Reactions:

Over the past few years, considerable amount of research efforts have been employed to know the kinetics and mechanistic pathways for different electrochemical reactions.

Table 1.6. OER reaction steps in both acidic and alkaline electrolyte.

Overall Reaction (Condition)	Reaction pathway	Tafel Slope value (mV/dec)
$2H_2O \longrightarrow O_2 + 4H^+ + 4e^-$	$S + H_2O \longrightarrow S\text{-}OH + H^+ + e^-$	118
(Acidic condition)	$S\text{-}OH \longrightarrow S\text{-}O + H^+ + e^-$	39
	$S\text{-}O + H_2O \longrightarrow S\text{-}OOH + H^+ + e^-$	24
	$S\text{-}OOH \longrightarrow S\text{-}O_2 + H^+ + e^-$	17
	$S\text{-}O_2 \longrightarrow S + O_2$	
$4OH^- \longrightarrow O_2 + 2H_2O + 4e^-$	$S + OH^- \longrightarrow S\text{-}OH + e^-$	118
(Alkaline condition)	$S\text{-}OH + {}^-OH \longrightarrow S\text{-}O + H_2O + e^-$	39
	$S\text{-}O + {}^-OH \longrightarrow S\text{-}OOH + e^-$	24
	$S\text{-}OOH + {}^-OH \longrightarrow S\text{-}O_2 + e^-$	17
	$S\text{-}O_2 \longrightarrow S + O_2$	

In this regards, theoretical studies have put forward a significant understanding of these processes. The crucial factor of all these studies is the rationalization of the relative electrocatalytic activities of different electrode materials in terms of a descriptor. The descriptor may be defined as a single microscopic parameter which controls the catalytic process. In generally, a descriptor can be represented as the interaction between a key reaction intermediate and the catalytic surface. The plot of catalytic activity vs descriptor follows the Sabatier principle which mainly describes that the heterogeneous reaction shows a maximum rate at a particular reactivity of catalytic surface. This type of plot, known as a volcano plot is shown in **Figure 1.9.a**. The plot describes that the optimal interaction (neither too weak nor too strong between the key intermediate and catalyst surface) shows maximum activity. If the catalysts fail into the right side of the plot that means the interaction is too weak; the catalyst is not too much activate. On the other hand, the catalyst which is placed at the left side of the plot, have too strong interaction. Thus it is blocked by the intermediates or products.

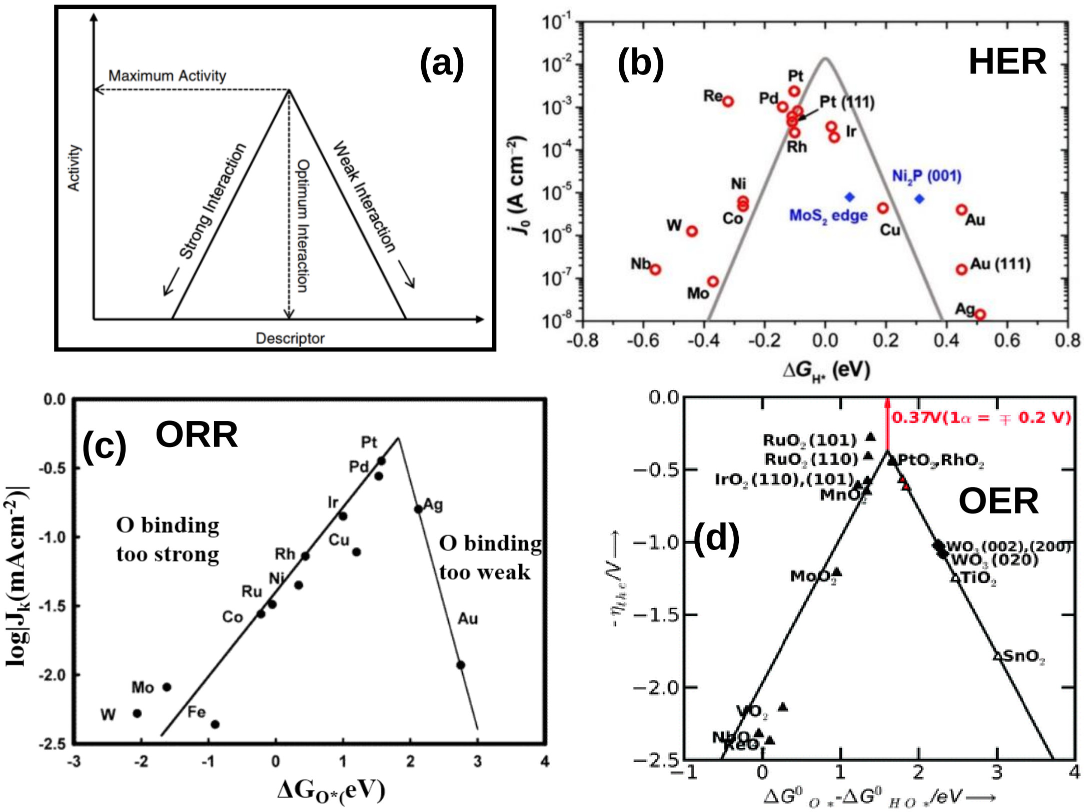

Figure 1.9. Volcano plot for (a) general all electrochemical processes, (b) HER, Reprinted with permission from ref. 63. Copyright 2014 American Chemical Society. (c) ORR Reprinted with permission from ref. 81. Copyright 2004 American Chemical Society and (d) OER, reproduced from ref. 83 with permission. Copyright 2012, Royal Society of Chemistry.

For HER, the chemical adsorption and desorption of H* atoms on an electrode surface are two competitive processes and control the rates of H_2 production. Therefore, G_H* value is considered as the main descriptor for HER. Parsons and his co-workers proposed a volcano-type plot associated of J_0 for HER with the thermodynamically derived ΔG_{H*}. This volcano plot shows a maximum peak at $\Delta G_{H*}=0$ with two symmetrical linear branches towards $\Delta G_{H*}>0$ and $\Delta G_{H*}<0$. However, obtaining the exact thermodynamic value of ΔG_{H*} is the main challenge regarding the construction of volcano plot. Nørskov et al.[80] first time demonstrated DFT study for the calculation of exact ΔG_{H*} for different systems for an constructed volcano plot for different metal catalysts as shown in **Figure**

1.9.b which clearly shows that the metals (Ag, Zn, Al), positioned at right side of the volcano plot, adsorb hydrogen weakly and those which positioned at left side (Mo, Ta, W) adsorb H strongly although both the cases exhibit low J_0 value. However, the elements, much closed to maximum peak point show moderate hydrogen adsorption (Pt, Pd, and Rh, have very high values of J_0). Moreover, the activity trends of different systems for different electrochemical processes such as OER and ORR[81] can be described by volcano plot (**Figure 1.9.c** and **1.9.d**). In volcano plot, the free energy for OH* oxidation on catalyst site ($\Delta G_{O*} - \Delta G_{HO*}$) is used as descriptor for the OER[82-83] whereas for ORR[81, 84] the free energy changes for intermediate (O*) binding (ΔG_{O*}) is used as descriptor.

1.4. Kinetics of Electrochemical Reaction

The electrochemical process is defined as the chemical reaction occurred via the transfer of the charge across the interface between electrode and electrolyte solution. The electrochemical process at solid electrocatalyst and liquid electrolyte interfaces occur via two processes:

(a) Faradic process where electron transfer involves at electrode/electrolyte interfaces.

(b) Non-faradic process where only adsorption/desorption process occurs at electrode/electrolyte interfaces.

Both the faradic and non-faradic process involves at electrode/electrolyte interfaces during any electrochemical process. But for most of the electrochemical reactions, faradic process is the primary interest of study.

An electrocatalyst can drive a reaction out of equilibrium by means of addition or subtraction of charges from or on the surface of the electrode. Faradic process on the electrode surface can be represents as:

$$\text{Ox (aq)} + \text{ne}^{-} \text{(electrode)} = \text{Red (aq)}$$

The basic electrochemical reaction follows a sequence of basic steps as follows:[85]

(a) Reactant transfer occurs from bulk of electrolyte to the electrode surface via a mass transfer process and vice versa.

(b) Surface phenomenon such as adsorption, crystallisation occur.

(c) Electron transfers to or from the electrode surface.

(d) Heterogeneous chemical reactions.

The simple electrochemical reaction can follow first three steps where no chemical reaction is occurred. The kinetics of a system is strongly influenced by the applied potential. In addition, the kinetics is furthermore influenced by the nature and structures of the reacting species, the solvent, the electrode materials and adsorbed layers on the electrode.

The current flow from the electrode for a simple faradic process can be represented as:

$$i_a = AFr_o c_{Ox}$$

Where i is current flow from electrode, A is the electrode surface area, F is the Faraday's constant (84548), r_o is the electron transfer rate and c_{Ox} is the concentration of the reactant.

Herein all terms are constant for a particular catalyst except the rate of the electron transfer from the electrode. In addition, the rate of the electron transfer is controlled by the potentials applied on the electrode. Furthermore, the electrochemical reactions are in equilibrium and provide an activation barrier. So the potential applied on electrode can be given by

$$\Delta E = -\frac{\Delta G}{nF}$$

Where ΔE is the electrode potential, n is the number of electrons transferred and ΔG is the free energy of the activation barrier. In electrochemistry two terms is very important

(a) **Overpotential (η):** It is defined as the difference in electrode potential at equilibrium (E_e) and the potential at a given current density (E_i).

$$\eta = E_e - E_i$$

(b) **Charge Transfer Coefficient (α):** It is defined as the amount of charge transfer at a particular overpotential.

In electrocatalysis it is possible to drive a reaction out of equilibrium and it is possible by applying some overpotentials to the electrode. So the free energy of activation barrier will be defined as:

$$\Delta G_c = \Delta G_{c,eq} + \alpha_c n_e F\eta$$
$$\Delta G_a = \Delta G_{a,eq} - \alpha_a n_e F\eta$$

Where $\Delta G_{c,eq}$ and $\Delta G_{a,eq}$ are the potentials independent activation energy, $\alpha_a$and α_c are the anodic and cathodic charge transfer coefficient, F is the faraday's constant, η is the overpotential applied on electrode. The rate of a reversible electrochemical reaction can be presented as:

$$r = k_a c_{ox} - k_c c_{red}$$

Where k_a and k_c are the rate constant of anodic and cathodic process.
According to Arrhenius equation, the rate constant of a reaction is given by

$$k = k_0 e^{-E_a/kT}$$

$$k_a = k_0 e^{-\Delta G_a/RT}$$

For cathode

$$k_c = k_0 e^{-\Delta G_c/RT}$$

Where k_0 defined as potentials independent rate constant and other terms are defined their usual meaning.

Now putting the value of ΔG_c and ΔG_a, we get

$$k_a = k_0 e^{(-\Delta G_{a,eq} + \alpha_a n_e F\eta)/RT}$$

$$k_c = k_0 e^{(-\Delta G_{c,eq} - \alpha_c n_e F\eta)/RT}$$

As the equilibrium activation free energy term is also an potential term, therefore the rate constant value generates as

$$k_a = {k_0}^a e^{\alpha_a n_e F\eta/RT}$$

$$k_c = {k_0}^c e^{-\alpha_c n_e F\eta/RT}$$

So now if we put the equation in

$$r = {k_0}^a c_{ox}\, e^{\alpha_a n_e F\eta/RT} - {k_0}^c c_{red}\, e^{-\alpha_c n_e F\eta/RT}$$

If we convert the rate of the reaction in terms of the current, we get

$$\text{Or } r = \frac{i}{nF} = {k_0}^a c_{ox}\, e^{\alpha_a n_e F\eta/RT} - {k_0}^c c_{red}\, e^{-\alpha_c n_e F\eta/RT}$$

$$\text{Or } \; i = nFk_0(c_{ox}\, e^{\alpha_a n_e F\eta/RT} - c_{red}\, e^{-\alpha_c n_e F\eta/RT}) \text{ as } {k_0}^c = {k_0}^a = k_0$$

$$\text{Or } \; i = i_0(c_{ox}\, e^{\alpha_a n_e F\eta/RT} - c_{red}\, e^{-\alpha_c n_e F\eta/RT}) \text{ where } nFk_0 = i_0$$

Here i_0 represented the exchange current density.

So finally we get the classical Butler-Volmer equation:

$$i = i_0(c_{ox}\, e^{\alpha_a n_e F\eta/RT} - c_{red}\, e^{-\alpha_c n_e F\eta/RT})$$

This classical Butler-Volmer equation is the fundamental equation for electrode kinetics and it represents the relationship between the total current density with exchange current density, overpotential and transfer coefficient **(Figure 1.10.a)**. At higher overpotentials the reaction is out of equilibrium. Either the anodic or the cathodic current is dominating in the total current density measurement.

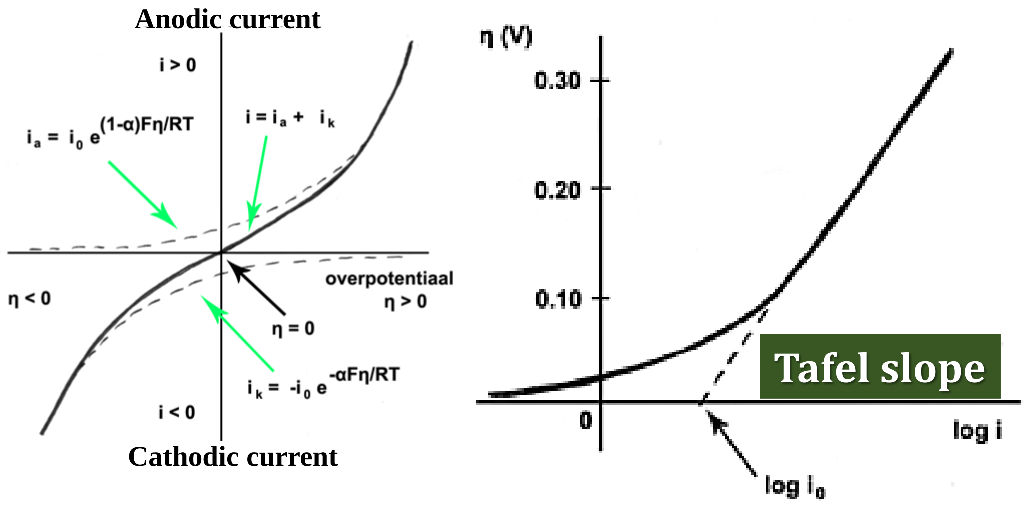

Figure 1.10. (a) Butler-Volmer plot, (b) Tafel plot for electrochemical reaction.

The Butler-Volmer equation becomes

$$\log(i) = \log(i_0) + \frac{\alpha_c \eta F}{2.303RT} \qquad \text{at higher cathodic potentials}$$

$$\log(i) = \log(i_0) - \frac{\alpha_a \eta F}{2.303RT} \qquad \text{at higher anodic potential}$$

This two equations are called as Tafel Equations. The logarithm of the current density log|i| can be plotted as a function of the overpotential and the slope of linear region of the plot is called Tafel slope **(Figure 1.10.b)**. From the Tafel analysis we get two parameter (a) exchange current density (i_0) and (b) Tafel slope $\frac{2.303\ RT}{\alpha_{a/c} n_e F}$.

The slope is expressed in units of mV decade^{-1}. The equation may be written in different way as:

$$\eta = a + b \log(i)$$

where a and b are the constant.

The Tafel slope determines the changes of electrocatalytic performance of the catalyst over a potential ranges. By determining the Tafel slopes, we can easily compare the catalytic performances of different catalysts. Smaller the Tafel slope, better will be the catalytic activity that is the catalyst requires smaller increment of overpotential for a given increase of current density. The theoretical Tafel slope value for a multistep reaction, comprising a series of elementary steps can be represented by:

$$b = \frac{2.303 \times RT}{\alpha \times F}$$

Where Temperature (T), charge transfer coefficient (a) and R is gas constant, F is the Faraday. The charge transfer coefficient (α) can be calculated by:

$$\alpha = \frac{n_f}{v} + n_r \beta$$

n_f= Number of electron transfer before the rate determining step.
v= Number of times rate determining step occurred.
n_r= Number of electron involved in the rate determine step.
β = The symmetrical factor generally considered as 0.5.

The rationalization of HER mechanism is quite easy to interpret by Tafel slope because there are only two possible pathways. But for OER it is difficult to rationalize as it, involves via transfer of 4 electrons and 4 protons thus provides many possible pathways. However, the OER reaction mechanism is confirmed by comparing the experimental data with theoretical complementary data (e.g. DFT calculations).

The exchange current density is equivalent to the rate constant of a heterogeneous catalyst. It provides both the thermodynamics as well as the kinetic informations. Higher i_0 value defines no activation barrier in electrolysis reaction whereas; low i_0 reflects the high activation barrier. That is why the rate of the reduction and oxidation process become sluggish.

1.5. Heterogeneous Catalysis

On growing demands of portable power systems for automobiles and different electronic equipments, PEM fuel cell creates attentions.[86] But the storage of large amount of hydrogen and its reliable supply restricts the widespread use of PEM fuel cell. There are several classes of solid hydrogen storage materials *i.e.* activated carbon, metal amide, nano carbon such as graphene, carbon nanotube (CNT) etc.[87] But low gravimetric efficiency prevents their practical applications. However, in recent times, scientific communities have been focused on the pyrolysis or hydrolysis of the metal hydrides ($NaBH_4$, H_3N-BH_3) because of their high theoretical hydrogen content, releasing capacity of pure hydrogen.[88-90] At the same time, using the in-situ released hydrogen in heterogeneous organic transformation specially any environmental remediation process is very challenging task.[91-92] Water pollution is considered as an acute problem of global environment. The maximum no of death and diseases causes mainly due to the water pollutants. Among different anthropogenic contaminants, 4-nitrophenol is one of the toxic pollutant and hazardous materials, declared by U.S. Environmental Protection Agency. Therefore, remediation of aromatic nitro compounds is an important task.[93] Several conventional technologies[93-94] are being widely used for waste water treatment such as biological, chemical reduction/oxidation, adsorption, degradation etc. The available conventional treatment technologies have inherent challenges and short comings with respect to applications, designing, effectiveness, and economics.[95] In this point it should be mentioned that the chemical oxidation/reduction process with heterogeneous catalyst is most advantageous.[96] Sun and his co-workers reported[92] graphene supported NiPd alloy nanoparticle for the dehydrogenation of ammonia borane and in-situ hydrogenation of nitro/nitrile compounds. Kim et al. reported[97] Pd−Pt−Fe_3O_4 nanoflake behaving as a robust heterogeneous catalyst for the chemoselective reduction of nitroarene. Heterogeneous catalyst are those where the catalyst is work in a separate phase than the reactants. Generally, heterogeneous catalysts are solid materials and reactions occurred on the catalyst surface. Recently, along with homogeneous and enzyme catalysis, heterogeneous catalysis create more attentions in field of organic catalysis.

Heterogeneous catalyst has several advantages over homogeneous catalyst such as i) their stability to severe reaction condition, ii) easily separated from reaction mixture and recycled for several times. Carbon-carbon bond formation reaction is one of the central interest for the construction of symmetrical and unsymmetrical biaryl moiety in complex molecule such as pharmaceutical reagent and alkaloid.[98] In 1901, F. Ullmann first reported[99] copper catalysed ullmann reaction for the formation of symmetrical biaryl components. Generally, ullmann reaction is homogeneously catalysed by copper (Cu) at 200 ^oC. But there are some problems associated with homogeneous catalyst such as it is very difficult to separate the product from the metal catalyst. Recently, different groups reported the synthesis of symmetrical and unsymmetrical biaryl moiety by heterogeneous catalysis. Y. Sasson and his co-workers reported[100] heterogeneous Pd catalyst Heak reaction in aqueous solution. Calo et al. reported[101] Pd nanoparticles catalysed ullmann coupling reaction in ionic liquid solvent. The Size and shape controlled activity is one of the important properties of heterogeneous catalysis. Recently, Kiwi-Minsker and his group reported[102] a shape and size controlled alkynol hydrogenation on Pd nanocrystal. Therefore, development of nano materials based heterogeneous catalyst is very advantageous.

1.6. Development of Electrocatalysts

Kinetics of all these electrochemical processes is very sluggish without any suitable catalyst. Therefore, it is a daunting task to design a superior electro-catalyst for ensuring high efficiency by minimizing overpotential losses for electrocatalytic energy conversions and storage reactions. In last few years, the interest on nanoscience and nanotechnology is growing worldwide due to their potential applications in different fields such as optoelectronics,[103] photocatalytic[104] and electrocatalytic renewable energy conversion devices.[105] Nanomaterials are foundation stone of nanoscience and nanotechnology.[106] Nanomaterials can be defined as a structural mater with an external dimension in nanoscale region (size range from approximately 1 – 100 nm) or having internal structure or surface structure in the nanoscale region (**Figure 1.11.a**).

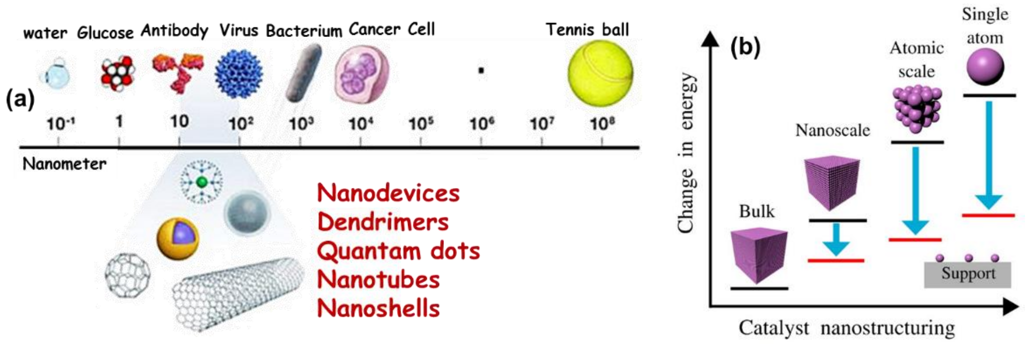

Figure 1.11. (a) Different materials and their respective size. (b) Change of band gap with particle size. Reprinted from ref. 107, an open access journal.

Nanomaterials have several advantages over the bulk materials such as it comprises of relatively high chemical activity, specificity of interaction and large surface-to-volume ratio.[106] Furtheremore, nanoparticles, providing highly active centres, has different physicochemical properties as compare to the bulk materials.[107] However, the insufficient thermodynamically stability of the nanomaterial's is the main drawback. Structure of very small size as well as high surface energy makes the NPs thermodynamically very unstable. In order to develop stable NPs, it is necessary to control the reactions and terminate the growth of the NPs. In this regard several strategies have been exploited (**Figure 1.12**) such as

(a) Addition of organic ligands or inorganic capping materials.

(b) Addition of other metal salts for making core-shell type particles..

(c) Utilization of colloids and soluble polymers.

(d) Dispersion of the nanoparticles on the solid support or composite formation.

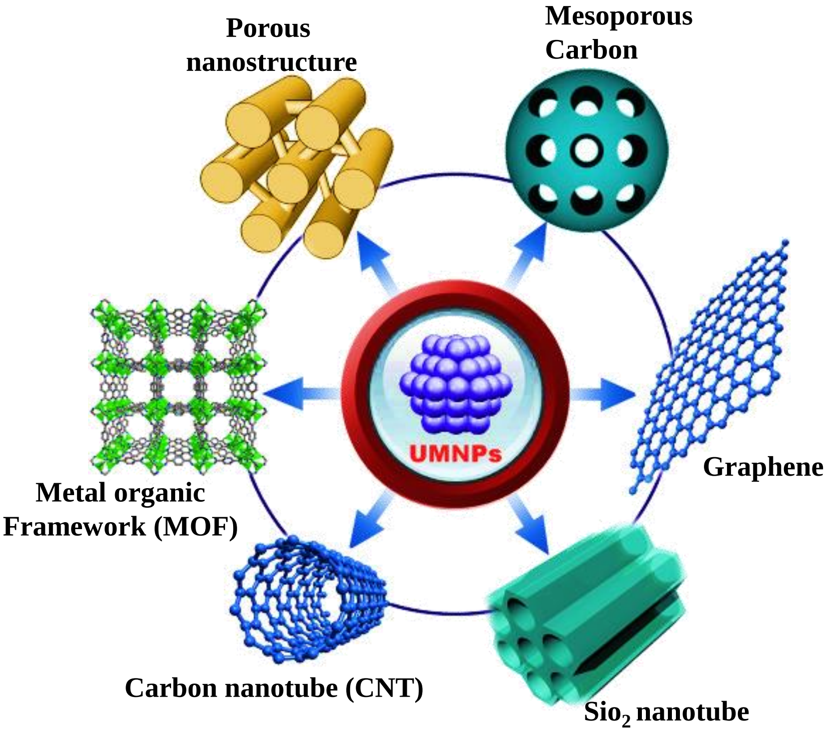

Figure 1.12. Different solid supported materials used for stabilization of NPs. Partly reproduced from ref. 109 with permission. Copyright 2016, Elsevier.

Among those process, in this thesis we have dealt with composite materials or dispersed nanoparticles on the solid supported due to its several advantages as a catalyst such as it maximizes the electrochemically active surface area (ECSA) of the NPs with the minimal use of the metal thus providing greater efficiency as well as lower cost of the catalyst.[108] In literature several solid materials[109] including metal organic framework (MOF),[110] metal oxide[111] and nanocarbon materials[112] are creating lots of attentions in last few years. In this thesis we mainly describe nanocarbon based composite materials because of its easy availability and low cost. Commercially available catalysts are generally dispersed on carbon balk (surface area-200–1000 m^2 g^{-1}).[113] For example, a spherical morphology of Pt nanoparticles, supported on conducting carbon materials (Pt/C) is considered as reference ECs for HER and ORR. All the electrocatalytic processes are occurred at interface of the catalyst. But one of the major limitations for carbon supported catalyst is its low electrocatalytic stability, arises due to the rapid depletion of carbon.

The carbon supported catalyst is easily oxidized under cathodic potentials in strong acidic condition. Recently, Finsterwalder and co-worker have reported[114] that comm. carbon support, Vulcan X-72 could easily oxidized under cathodic environment in polymer electrolyte fuel cell (PEFC). For the development of the ECs, the interaction between the NPs and supported materials plays crucial role because it controls the porosity and wettability of the electrode. An ideal supported[115] materials should have some characteristics such as (i) higher number of active site for NPs allowing uniform dispersions of NPs on surface for maximum ECSA, (ii) higher electrical conductivity which reduces the interfacial resistance, (iii) higher porosity that enhances reactant or products access (iv) it should be compatible for different fabrications processes (v) higher stability under both transient and operational conditions and (vi) it should be manufactured from low cost environmentally process. The catalytic activity of a carbon supported ECs not only losses by carbon corrosion but it can take place through several mechanisms, including particles aggregations (Ostwald ripening), crystal migrations, and dissolutions/precipitations. The support is also responsible for determining the agglomerate structures and microstructures of the catalyst layer. An effective supported nanostructure provides well-connection, high ECSA and efficient mass transport of reactants to the triple phase boundary (TPB) where the electrolyte, catalyst and fuel meets at a reactive site.

Layered double hydroxides (LDHs)[116] are a particular class of two dimensional (2D) anionic clay materials. LDHs materials mainly possess brucite-like host layers made up with uniform distribution of positively charge particles (cation) and exchangeable charge compensating inter layer anions or solvent molecules. The general formula of a LDH material can be represented as $[M^{2+}{}_{1-x}\ M^{3+}{}_{x}\ (OH)_2]^{+}{}_{x}\ [(A^{n-})_{(x/n)}.\ mH_2O]$. In LDH materials, divalent cation (M^{2+}) and trivalent cation (M^{3+}) are coordinated octahedrally with hydroxyl group in a brucite-like host layer. The value of x represents the fraction of M^{3+} which uniformly replaces the M^{2+} ion in a brucite-like host layer and it is varied from 0.2 to 0.4. A^{n-} are mainly inorganic anions such as CO^{3-}, X^- (X=F, Cl, Br, I), $SO_4{}^{2-}$, NO_3^- etc. or organic anion (acetate, lactate, dodecyl sulfate etc.). A Schematic representation of classical LDHs structure is shown in **Figure 1.13.**

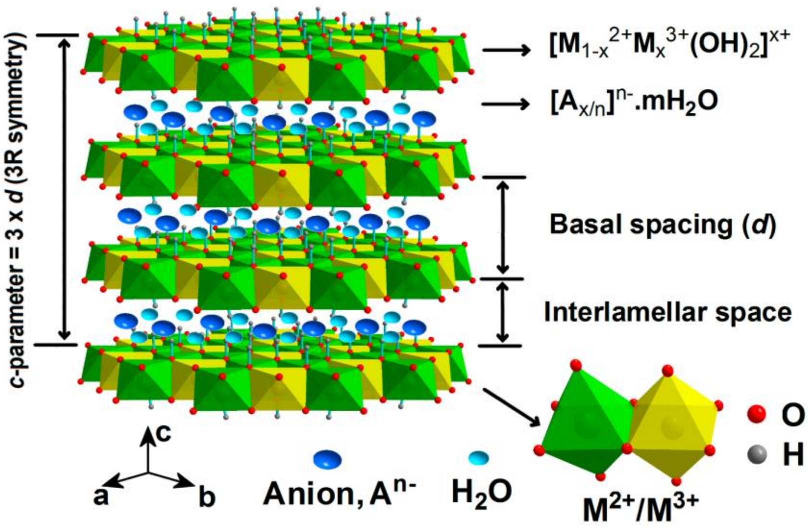

Figure 1.13. Structure of classical LDH. Adapted from open access journal, ref. 120.

LDH based materials are very attractive in the field of catalysis because of its robust structure, feasibility towards the incorporation of mixed metal ion in different composition, relative weak interlayer bonding allowing the easy exchangeable inter layer anion. In addition, the physical and chemical properties of the LDH materials can be easily tailored by changing the nature of metal cations, molar ratio M^{3+}/ M^{2+} and interlayer anion. Among different LDH materials, transition metal based LDHs (TM-LDHs) are gaining more attentions due to their intrinsic activity towards electrocatalysis, pharmaceuticals materials and various catalysis.[117] Furthermore, LDH materials can be converted into the corresponding mixed metal oxides (MMOs) with a uniform distribution of M^{2+} and M^{3+} with a high surface area after calcination treatment. Recently, F. Li and his co-workers reported[118] nickel-based mixed-metal oxides from LDH materials by calcination. LDH materials possess relatively weak interlayer interactions. Tatsumi et al. reported[119] intercalation of polyoxalate of tungsten (W) and molybodenam (Mo) into Mg-Al LDH with out compromising their structural features and employed it for epoxidation of cyclohexene. The main drawback of the TM-LDH based materials is their lower electrical conductivity. Several groups demonstrated[117, 120-121] the co-assembly of LHD materials with other functional semiconductor materials which further improves the conductivity as well catalytic activity of the composite materials. F.Li and his co-workers reported[121] the multiwall-CNT as functional support materials for NiAl–LDH to improve the electrocatalytic activity of the LDH materials. Moreover, the hybridization with semiconducting materials improves significantly visible light absorption power. Recently, M.Wi and co-workers reported[122] NiTi–LDH/reduced graphene oxide (RGO) nanosheets, showing excellent photocatalytic activity for water oxidation under visible light irradiation with high quantum efficiency of 61.2%.

Carbon is a tetravalent nonmetallic element which exists in different allotropes from zero-dimensional (0D) to three-dimensional (3D) such as diamond, graphite, fullerenes, carbon nanofibers (CNFs) carbon nanotubes (CNTs) and graphene (G).[123] Among different nanocarbon materials, graphene,[124] carbon nanotube (CNTs)[125] are extremely used as support materials for nanomaterial's. Graphene[126] is single two-dimensional (2D) layer of sp^2 hybridized carbon. Herein, the monolayer of sp^2 carbon atoms are packed by covalent bonded to form honeycomb network crystal which is the basic building block for the other allotropes such as 3D graphite, 1D carbon nanotube and 0D fullerene. High electrical and thermal conductivity, mechanical elasticity and theoretical high surface area make the graphene highly desirable for its use as a two dimension (2D) catalyst support.[127] However, two major hurdles remain in developing large-scale graphene-supported catalyst systems. Firstly low wettability of grapheme in solution and the second one is the low attachment between nanoparticles and graphene sheet. These result increases the dissolutions of metal NPs and lowers the stability under different electrochemical or heterogeneous catalytic applications. Several literature reports[128-130] suggested that heteroatoms (N, S) doped on the graphene improves the metal NPs anchoring ability as well as the catalytic activity of the graphene. On the other hand, graphitic carbon nitride[131] (g-C_3N_4) is a 2D materials, having graphene like structure. It has a layered structure with C-N covalent bonding in-plane layer structures and it experiences a week Van der Waal force between the layer structures. The g-C_3N_4 has two structural models[132] (a) condensed s-triazine units with a periodic array of single-carbon vacancies and (b) another one is constructed by the condensation of tri-s-triazine subunits, connected through the tertiary amine groups (**Figure 1.13.(a,b)**).

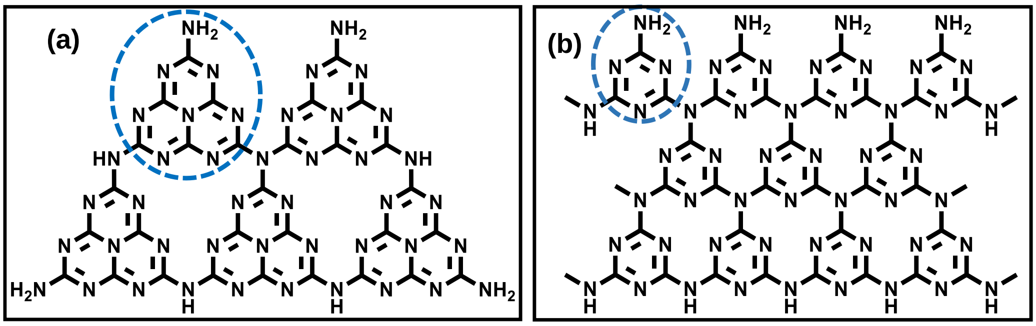

Figure 1.14. Proposed structures of g-C_3N_4 with (a) heptazine building block, (b) s-triazine building block.

The theoretical calculation predicts that the g- C_3N_4 can exist in seven different allotropes[133] such as α-C_3N_4 (band gap of 5.5 eV), β- C_3N_4 (band gap of 4.85 eV), cubic C_3N_4 (band gap of 4.3 eV), pseudo cubic C_3N_4 (band gap of 4.13 eV), g-h-triazine (band gap of 2.97 eV), g-o-triazine (band gap of 0.93 eV), and g-h-heptazine (band gap of 2.88 eV). Although the first principle calculation suggests α- C_3N_4 (band gap of 5.5 eV), β-C_3N_4 (band gap of 4.85 eV) and g-C_3N_4 are the stable allotropes of the carbon nitride. But experimentally it has been observed that g-C_3N_4 is the energetically stable phase at ambient conditions. Comparing with the other different types of interfaces, composite materials with 0D-2D, 1D-2D and unique 2D-2D layered structures possess much larger surface contact as well as interfacial charge separations. Nanoparticles doped in g-C_3N_4 composites are considered as 0D-2D structures. The nanoparticles are doped into g-C_3N_4 moiety by two ways[134] (a) cave doping wherein the NPs are incorporated through the coordination interaction and (b) interlayer doping wherein the NPs are doped through the interlayer bridging. Antonietti and his co-workers[135] reported PdNPs@mpg-C_3N_4 nanocomposite exhibited efficient and selective catalytic activities towards the hydrogenation of phenol to cyclohexanol. Vinu and his groups[136] fabricated AuNPs on the mesoporous C_3N_4 for the efficient three component reactions.

1.7. Aims of the Present Thesis

(i) Design and synthesis of different composite’s nanostructures by mechanical and/or chemical processes.

(ii) Graphitic carbon nitride has been developed as a supported material for different metal, metal oxide and layered double hydroxide nanostructure.

(iii) The g-carbon nitride based composite materials have been characterised by p-XRD, FT-IR, XPS and UV-vis spectroscopy.

(iv) Morphological studies of the composite nano-materials were performed by using FE-SEM and TEM instrument.

(v) After successfully synthesis of the composite nanostructures, the materials was explored as a heterogeneous catalyst for 4-nitrophenol reduction and ullmann coupling reaction in aqueous medium.

(iv) Different electrocatalytic applications for energy storage and conversion such as HOR, HER, OER, ORR and FAO were exploited with different g-CN_x based composite materials.

(v) Mechanistic study of electrocatalytic activity of the different catalysts were also studied.

(vi) Electrochemical impedance spectroscopy (EIS), double layer capacitance, and electrochemical surface area (ECSA) were calculated to understand the factors responsible for superior activity.

1.8. Scopes and Challenges of the Present Thesis

The forgoing discussions clearly demonstrate that there is an upsurge in the research activities of nanocomposite owing to their potential applications such as electrochemical energy conversion as well as Organic Reactions. The present thesis is mainly concerned with the rational design, syntheses and characterizations of various graphitic nanocomposites and their various potential applications as electrocatalysts for energy conversions as well as organic catalyst. The main benefit of the present thesis is the easy synthetic procedure for the development of nanocomposites showing efficient catalytic behaviour for both organic reactions and electrochemical reactions occurred in fuel cells. Additionally, our efforts were extended to understand the mechanistic aspects and reaction kinetics of various catalytic reactions.

1.9. Outline of the Present Thesis

The present thesis contains nine chapters. **Chapter 1** records an account of current literature pertaining to current and future energy demands and explored the importance of renewable energy sources and storage techniques. Different fuel cells reactions *i.e.*

hydrogen oxidation reaction (HOR), oxygen reduction reaction (ORR), hydrogen evolution reaction (HER), oxygen evolution reaction (OER) has been briefly discussed. **Chapter 2** describes various instrumental methods and techniques. **Chapter 3** describes synthesis of porous palladium nanoparticles-carbon nitride composite (Pd-CN_x) for superior HER activity in both acidic and alkaline media. Furthermore, this catalyst displays superior HOR activity with a broad range of pH (0-14) in different buffer solution. **Chapter 4** deals with the superior electrocatalytic ORR activity of porous palladium nanoparticles-carbon nitride (Pd-CN_x) composite in both alkaline and acidic medium. Additionally, this nanocomposite shows excellent methanol tolerance and long term durability better than that of commercial Pt/C in both acidic and alkaline media. **Chapter 5** reports the growth of one dimensional crystalline RuO_2 nanowires for efficient hydrogen and oxygen evolution reactions over all pH values. Moreover, the 1D-RuO_2-CN_x catalyst displays superior stability in compare to comm. RuO_2 and IrO_2. **Chapter 6** reports describes the efficient electrocatalytic activity of palladium nanoparticles-carbon nitride composite (PdNPs/CN_x) towards the formic acid oxidation (FAO) with high mass activity (1640 $mAmg_{Pd}^{-1}$) in acid electrolyte. **Chapter 7** demonstrates the synthesis of highly active and durable bi-functional electrocatalyst *i.e.* cobalt iron layered double hydroxide ($Co_{1-\delta}Fe_{\delta}$ LDH) and g-carbon nitride composite ($Co_{1-\delta}Fe_{\delta}$ LDH/g-CN_x) for efficient OER and HER in alkaline electrolyte. **Chapter 8** describes the synthesis of composite cobalt aluminium layered double hydroxide-carbon nitride ($Co_1Al_{\delta}(OH)_m$-CN_x) by simple microwave heating method and their potential applications towards water oxidation reaction in alkaline medium. Moreover, the catalyst displays high stability and long term durability under OER conditions. **Chapter 9** describes a facile synthesis of highly dispersed palladium nanoparticles embedded on graphitic carbon nitride (Pd@CN_x) by ultrasound assisted method without aid of any external reducing agent. This nano composite further displays highly selective nitro groups reduction in presence of other reducible groups with good stability. Furthermore, the catalyst shows superior catalytic activity towards ullmann coupling reaction of different aryl halides with broad range of substrates scope.

1.10. References

1. Johnston, B.; Mayo, M. C.; Khare, A., *Technovation* **2005,** *25*, 569-585.

2. Dresselhaus, M. S.; Thomas, I. L., *Nature* **2001,** *414*, 332-337.

3. Whitesides, G. M.; Crabtree, G. W., *Science* **2007,** *315*, 796-798.

4. Jacobson, M. Z., *Energy Environ. Sci.* **2009,** *2*, 148-173.

5. Rostrup-Nielsen, J. R., *Catal. Rev.* **2004,** *46*, 247-270.

6. Goodenough, J. B.; Manthiram, A., *MRS Commun.* **2014,** *4*, 135-142.

7. Pettersson, J.; Ramsey, B.; Harrison, D., *J. Power Sources* **2006,** *157*, 28-34.

8. Schlapbach, L.; Zuttel, A., *Nature* **2001,** *414*, 353-358.

9. Shao, Y.; Markovic, N. M., *Nano Energy* **2016,** *29*, 1-3.

10. Kraytsberg, A.; Ein-Eli, Y., *Energy Fuels* **2014,** *28*, 7303-7330.

11. Gottesfeld, S.; Dekel, D. R.; Page, M.; Bae, C.; Yan, Y.; Zelenay, P.; Kim, Y. S., *J. Power Sources* **2018,** *375*, 170-184.

12. Durst, J.; Simon, C.; Hasché, F.; Gasteiger, H. A., *J. Electrochem. Soc.* **2015,** *162*, F190-F203.

13. Durst, J.; Siebel, A.; Simon, C.; Hasche, F.; Herranz, J.; Gasteiger, H. A., *Energy Environ. Sci.* **2014,** *7*, 2255-2260.

14. Zheng, J.; Sheng, W.; Zhuang, Z.; Xu, B.; Yan, Y., *Sci. Adv.* **2016,** *2*.

15. Sheng, W.; Zhuang, Z.; Gao, M.; Zheng, J.; Chen, J. G.; Yan, Y., *Nat. commun.* **2015,** *6*, 5848.

16. Zheng, J.; Zhuang, Z.; Xu, B.; Yan, Y., *ACS Catal.* **2015,** *5*, 4449-4455.

17. Ohyama, J.; Kumada, D.; Satsuma, A., *J. Mater. Chem. A* **2016,** *4*, 15980-15985.

18. Strmcnik, D.; Uchimura, M.; Wang, C.; Subbaraman, R.; Danilovic, N.; van der, V.; Paulikas, A. P.; Stamenkovic, V. R.; Markovic, N. M., *Nat. Chem.* **2013,** *5*, 300-306.

19. Wang, Y.; Wang, G.; Li, G.; Huang, B.; Pan, J.; Liu, Q.; Han, J.; Xiao, L.; Lu, J.; Zhuang, L., *Energy Environ. Sci.* **2015,** *8*, 177-181.

20. Cong, Y.; Yi, B.; Song, Y., *Nano Energy* **2018,** *44*, 288-303.

21. Koenigsmann, C.; Scofield, M. E.; Liu, H.; Wong, S. S., *J. Phys. Chem. Lett.* **2012,** *3*, 3385-3398.

22. Zhongwei, C.; Mahesh, W.; Wenzhen, L.; Yushan, Y., *Angew. Chem. Inter. Ed.* **2007,** *46,* 4060-4063.

23. Li, M.; Zhao, Z.; Cheng, T.; Fortunelli, A.; Chen, C.-Y.; Yu, R.; Zhang, Q.; Gu, L.; Merinov, B.; Lin, Z.; Zhu, E.; Yu, T.; Jia, Q.; Guo, J.; Zhang, L.; Goddard, W. A.; Huang, Y.; Duan, X., *Science* **2016**.

24. Chen, C.; Kang, Y.; Huo, Z.; Zhu, Z.; Huang, W.; Xin, H. L.; Snyder, J. D.; Li, D.; Herron, J. A.; Mavrikakis, M.; Chi, M.; More, K. L.; Li, Y.; Markovic, N. M.; Somorjai, G. A.; Yang, P.; Stamenkovic, V. R., *Science* **2014,** *343,* 1339-1343.

25. Lim, B.; Jiang, M.; Camargo, P. H. C.; Cho, E. C.; Tao, J.; Lu, X.; Zhu, Y.; Xia, Y., *Science* **2009,** *324,* 1302-1305.

26. Zhang, J.; Vukmirovic, M. B.; Sasaki, K.; Nilekar, A. U.; Mavrikakis, M.; Adzic, R. R., *J. Am. Chem. Soc.* **2005,** *127,* 12480-12481.

27. Toyoda, E.; Jinnouchi, R.; Hatanaka, T.; Morimoto, Y.; Mitsuhara, K.; Visikovskiy, A.; Kido, Y., *J. Phys. Chem. C* **2011,** *115,* 21236-21240.

28. Kabir, S.; Serov, A.; Atanassov, P., *J. Power Sources* **2018,** *375,* 255-264.

29. Prakash, J.; Joachin, H., *Electrochim. Acta* **2000,** *45,* 2289-2296.

30. Guo, J.; Hsu, A.; Chu, D.; Chen, R., *J. Phys. Chem. C* **2010,** *114,* 4324-4330.

31. Liang, Y.; Wang, H.; Diao, P.; Chang, W.; Hong, G.; Li, Y.; Gong, M.; Xie, L.; Zhou, J.; Wang, J.; Regier, T. Z.; Wei, F.; Dai, H., *J. Am. Chem. Soc.* **2012,** *134,* 15849-15857.

32. Yao, Z.; Yan, J.; Mietek, J.; Yonggang, J.; Zhang, Q. S., *Small* **2012,** *8,* 3550-3566.

33. Zhang, J.; Xia, Z.; Dai, L., *Sci. Adv.* **2015,** *1*.

34. Lijun, Y.; Shujuan, J.; Yu, Z.; Lei, Z.; Sheng, C.; Xizhang, W.; Qiang, W.; Jing, M.; Yanwen, M.; Zheng, H., *Angew. Chem. Inter. Ed.* **2011,** *50,* 7132-7135.

35. Rees, N. V.; Compton, R. G., *J. Solid State Electrochem.* **2011,** *15,* 2095-2100.

36. Yu, X.; Pickup, P. G., *J. Power Sources* **2008,** *182,* 124-132.

37. Weber, M.; Wang, J. T.; Wasmus, S.; Savinell, R. F., *J. Electrochem. Soc.* **1996,** *143,* L158-L160.

38. Müller, Z. E., *Elektrochem.* **1923,** *29,* 264-274.

39. Cuesta, A.; Cabello, G.; Osawa, M.; Gutiérrez, C., *ACS Catal.* **2012,** *2,* 728-738.

40. Rice, C.; Ha, S.; Masel, R. I.; Wieckowski, A., *J. Power Sources* **2003,** *115,* 229-235.

41. Choi, J.-H.; Jeong, K.-J.; Dong, Y.; Han, J.; Lim, T.-H.; Lee, J.-S.; Sung, Y.-E., *J. Power Sources* **2006,** *163,* 71-75.

42. Waszczuk, P.; Barnard, T. M.; Rice, C.; Masel, R. I.; Wieckowski, A., *Electrochem. Commun.* **2002,** *4,* 599-603.

43. Sheng, W.; Gasteiger, H. A.; Shao-Horn, Y., *J. Electrochem. Soc.* **2010,** *157,* B1529-B1536.

44. Xu, G.-R.; Bai, J.; Jiang, J.-X.; Lee, J.-M.; Chen, Y., *Chem. Sci.* **2017,** *8,* 8411-8418.

45. Nana, D.; Chengming, W.; Xijun, W.; Yue, L.; Jun, J.; Yujie, X., *Adv. Mater.* **2016,** *28,* 2077-2084.

46. Song, B.; Chengming, W.; Mingsen, D.; Ming, G.; Yu, B.; Jun, J.; Yujie, X., *Angew. Chem. Inter. Ed.* **2014,** *53,* 12120-12124.

47. Regmi, Y. N.; Waetzig, G. R.; Duffee, K. D.; Schmuecker, S. M.; Thode, J. M.; Leonard, B. M., *J. Mater. Chem. A* **2015,** *3,* 10085-10091.

48. Tavakkoli, M.; Holmberg, N.; Kronberg, R.; Jiang, H.; Sainio, J.; Kauppinen, E. I.; Kallio, T.; Laasonen, K., *ACS Catal.* **2017,** *7,* 3121-3130.

49. Cheng, N.; Stambula, S.; Wang, D.; Banis, M. N.; Liu, J.; Riese, A.; Xiao, B.; Li, R.; Sham, T.-K.; Liu, L.-M.; Botton, G. A.; Sun, X., *Nat. commun.* **2016,** *7,* 13638.

50. Xu, W.; Zhu, S.; Liang, Y.; Cui, Z.; Yang, X.; Inoue, A.; Wang, H., *J. Mater. Chem. A* **2017,** *5,* 18793-18800.

51. Zhu, L.; Lin, H.; Li, Y.; Liao, F.; Lifshitz, Y.; Sheng, M.; Lee, S.-T.; Shao, M., *Nat. commun.* **2016,** *7,* 12272.

52. Xu, Y.; Yin, S.; Li, C.; Deng, K.; Xue, H.; Li, X.; Wang, H.; Wang, L., *J. Mater. Chem. A* **2018,** *6,* 1376-1381.

53. McEnaney, J. M.; Chance Crompton, J.; Callejas, J. F.; Popczun, E. J.; Read, C. G.; Lewis, N. S.; Schaak, R. E., *Chem. Commun.* **2014,** *50,* 11026-11028.

54. Popczun, E. J.; McKone, J. R.; Read, C. G.; Biacchi, A. J.; Wiltrout, A. M.; Lewis, N. S.; Schaak, R. E., *J. Am. Chem. Soc.* **2013,** *135,* 9267-9270.

55. Gao, D.; Zhang, J.; Wang, T.; Xiao, W.; Tao, K.; Xue, D.; Ding, J., *J. Mater. Chem. A* **2016,** *4,* 17363-17369.

56. Huang, Z.-F.; Song, J.; Li, K.; Tahir, M.; Wang, Y.-T.; Pan, L.; Wang, L.; Zhang, X.; Zou, J.-J., *J. Am. Chem. Soc.* **2016,** *138,* 1359-1365.

57. Kong, D.; Cha, J. J.; Wang, H.; Lee, H. R.; Cui, Y., *Energy Environ. Sci.* **2013,** *6,* 3553-3558.

58. Gong, M.; Zhou, W.; Tsai, M.-C.; Zhou, J.; Guan, M.; Lin, M.-C.; Zhang, B.; Hu, Y.; Wang, D.-Y.; Yang, J.; Pennycook, S. J.; Hwang, B.-J.; Dai, H., *Nat. commun.* **2014,** *5,* 4695.

59. Jin, H.; Wang, J.; Su, D.; Wei, Z.; Pang, Z.; Wang, Y., *J. Am. Chem. Soc.* **2015,** *137,* 2688-2694.

60. Jiang, P.; Yang, Y.; Shi, R.; Xia, G.; Chen, J.; Su, J.; Chen, Q., *J. Mater. Chem. A* **2017,** *5,* 5475-5485.

61. Jinlong, L.; Yao, Z.; Yan, J.; Zhenyu, W.; Zhouguang, L.; Anthony, V.; Shi-Zhang, Q., *Small* **2018,** *14,* 1704073.

62. Zheng, Y.; Jiao, Y.; Zhu, Y.; Li, L. H.; Han, Y.; Chen, Y.; Jaroniec, M.; Qiao, S.-Z., *J. Am. Chem. Soc.* **2016,** *138,* 16174-16181.

63. Morales-Guio, C. G.; Stern, L.-A.; Hu, X., *Chem. Soc. Rev.* **2014,** *43,* 6555-6569.

64. Kripasindhu, S.; Enrico, P.; I., H. C.; B., S. J. D.; P., W. P.; E., R. A.; J., K. R.; Jeremy, S.; I., W. R., *Angew. Chem. Inter. Ed.* **2014,** *126*, 11140-11144.

65. Marshall, A.; Børresen, B.; Hagen, G.; Tsypkin, M.; Tunold, R., *Electrochim. Acta* **2006,** *51,* 3161-3167.

66. Murakami, Y.; Ohkawauchi, H.; Ito, M.; Yahikozawa, K.; Takasu, Y., *Electrochim. Acta* **1994,** *39,* 2551-2554.

67. Chen, A.; Miller, B., *J. Phys. Chem. B* **2004,** *108,* 2245-2251.

68. Murakami, Y.; Tsuchiya, S.; Yahikozawa, K.; Takasu, Y., *Electrochim. Acta* **1994,** *39,* 651-654.

69. Nong Hong, N.; Oh, H. S.; Reier, T.; Willinger, E.; Willinger, M. G.; Petkov, V.; Teschner, D.; Strasser, P., *Angew. Chem. Inter. Ed.* **2015,** *54,* 2975-2979.

70. Petrykin, V.; Macounova, K.; Shlyakhtin, O. A.; Krtil, P., *Angew. Chem. Inter. Ed.* **2010,** *49,* 4813-4815.

71. Mondschein, J. S.; Callejas, J. F.; Read, C. G.; Chen, J. Y. C.; Holder, C. F.; Badding, C. K.; Schaak, R. E., *Chem. Mater.* **2017,** *29,* 950-957.

72. Huynh, M.; Bediako, D. K.; Nocera, D. G., *J. Am. Chem. Soc.* **2014,** *136,* 6002-6010.

73. Jin, S., *ACS Energy Lett.* **2017,** *2,* 1937-1938.

74. Stern, L.-A.; Feng, L.; Song, F.; Hu, X., *Energy Environ. Sci.* **2015,** *8,* 2347-2351.

75. Dutta, A.; Samantara, A. K.; Dutta, S. K.; Jena, B. K.; Pradhan, N., *ACS Energy Lett.* **2016,** *1,* 169-174.

76. Cheng, X.; Fabbri, E.; Nachtegaal, M.; Castelli, I. E.; El Kazzi, M.; Haumont, R.; Marzari, N.; Schmidt, T. J., *Chem. Mater.* **2015,** *27,* 7662-7672.

77. Ying, Z.; Qi, S.; Yecan, P.; Jun, G.; Xiaoqing, H., *Small* **2017,** *13,* 1700355.

78. Ma, W.; Ma, R.; Wang, C.; Liang, J.; Liu, X.; Zhou, K.; Sasaki, T., *ACS Nano* **2015,** *9,* 1977-1984.

79. Matsumoto, Y.; Sato, E., *Mater. Chem. Phy.* **1986,** *14,* 397-426.

80. Seh, Z. W.; Kibsgaard, J.; Dickens, C. F.; Chorkendorff, I.; Nørskov, J. K.; Jaramillo, T. F., *Science* **2017,** *355.*

81. Nørskov, J. K.; Rossmeisl, J.; Logadottir, A.; Lindqvist, L.; Kitchin, J. R.; Bligaard, T.; Jónsson, H., *J. Phys. Chem. B* **2004,** *108,* 17886-17892.

82. C., M. I.; Hai-Yan, S.; Federico, C. V.; A., H. H.; I., M. J.; G., I. N.; John, K.; F., J. T.; K., N. J.; Jan, R., *ChemCatChem* **2011,** *3,* 1159-1165.

83. Valdes, A.; Brillet, J.; Gratzel, M.; Gudmundsdottir, H.; Hansen, H. A.; Jonsson, H.; Klupfel, P.; Kroes, G.-J.; Le Formal, F.; Man, I. C.; Martins, R. S.; Norskov, J. K.; Rossmeisl, J.; Sivula, K.; Vojvodic, A.; Zach, M., *Phys. Chem. Chem. Phys.* **2012,** *14,* 49-70.

84. Rossmeisl, J.; Nørskov, J. K., *Surf. Sci.* **2008,** *602,* 2337-2338.

85. I. Chorkendorff, J. W. N., *Wiley-VCH* **2003**.

86. Marder, T. B., *Angew. Chem. Inter. Ed.* **2007,** *46,* 8116-8118.

87. Züttel, A., *Mater. Today* **2003,** *6,* 24-33.

88. Peng, B.; Chen, J., *Energy.Environ.Sci.* **2008,** *1,* 479-483.

89. Demirci, U. B.; Miele, P., *Eneregy Environ. Sci.* **2009,** *2,* 627-637.

90. Zhan, W.-W.; Zhu, Q.-L.; Xu, Q., *ACS Catal.* **2016,** *6,* 6892-6905.

91. Aditya, T.; Pal, A.; Pal, T., *Chem. Commun.* **2015,** *51,* 9410-9431.

92. Göksu, H.; Ho, S. F.; Metin, Ö.; Korkmaz, K.; Mendoza Garcia, A.; Gültekin, M. S.; Sun, S., *ACS Catal.* **2014,** *4,* 1777-1782.

93. Robinson, T.; McMullan, G.; Marchant, R.; Nigam, P., *Bio. Technol.* **2001,** *77,* 247-255.

94. C., V. P.; Roberto, B.; Willy, V., *J. Chem. Technol. Biotechnol.* **1998,** *72,* 289-302.

95. P., S. J.; F., O. D., *Environ. Prog.* **1995,** *14,* 88-103.

96. Astruc, D.; Lu, F.; Aranzaes, J. R., *Angew. Chem. Int. Ed.* **2005,** *44,* 7852-7872.

97. Byun, S.; Song, Y.; Kim, B. M., *ACS Appl. Mater. Interfaces* **2016,** *8,* 14637-14647.

98. Polshettiwar, V.; Varma, R. S., *Green Chem.* **2010,** *12,* 743-754.

99. Fanta, P. E., *Chem. rev.* **1964,** *64,* 613.

100. Mukhopadhyay, S.; Rothenberg, G.; Joshi, A.; Baidossi, M.; Sasson, Y., *Adv. Synth. Catal.* **2002,** *344,* 348-354.

101. Calò, V.; Nacci, A.; Monopoli, A.; Cotugno, P., *Chem. Eur. J.* **2009,** *15,* 1272-1279.

102. Crespo-Quesada, M.; Yarulin, A.; Jin, M.; Xia, Y.; Kiwi-Minsker, L., *J. Am. Chem. Soc.* **2011,** *133,* 12787-12794.

103. Jariwala, D.; Sangwan, V. K.; Lauhon, L. J.; Marks, T. J.; Hersam, M. C., *Chem. Soc. Rev.* **2013,** *42,* 2824-2860.

104. Ibhadon, A.; Fitzpatrick, P., *Catalysts* **2013,** *3,* 189.

105. Yao, Z.; Yan, J.; Mietek, J.; Zhang, Q. S., *Angew. Chem. Inter. Ed.* **2015,** *54,* 52-65.

106. Lee, J.; Mahendra, S.; Alvarez, P. J. J., *ACS Nano* **2010,** *4,* 3580-3590.

107. Pomerantseva, E.; Resini, C.; Kovnir, K.; Kolen'ko, Y. V., *Adv. Phys.* **2017,** *2,* 211-253.

108. Zhu, Y.; Zhou, W.; Shao, Z., *Small* **2017,** 1603793-n/a.

109. Zhu, Q.-L.; Xu, Q., *Chem 1,* 220-245.

110. Liu, H.; Liu, Y.; Li, Y.; Tang, Z.; Jiang, H., *J. Phys. Chem. C* **2010,** *114,* 13362-13369.

111. Seth, J.; Dubey, P.; Chaudhari, V. R.; Prasad, B. L. V., *New J. Chem.* **2018,** *42,* 402-410.

112. Xu, X.; Li, Y.; Gong, Y.; Zhang, P.; Li, H.; Wang, Y., *J. Am. Chem. Soc.* **2012,** *134,* 16987-16990.

113. Borup, R.; Meyers, J.; Pivovar, B.; Kim, Y. S.; Mukundan, R.; Garland, N.; Myers, D.; Wilson, M.; Garzon, F.; Wood, D.; Zelenay, P.; More, K.; Stroh, K.; Zawodzinski, T.; Boncella, J.; McGrath, J. E.; Inaba, M.; Miyatake, K.; Hori, M.; Ota, K.; Ogumi, Z.; Miyata, S.; Nishikata, A.; Siroma, Z.; Uchimoto, Y.; Yasuda, K.; Kimijima, K.-i.; Iwashita, N., *Chem. Rev.* **2007,** *107,* 3904-3951.

114. Maass, S.; Finsterwalder, F.; Frank, G.; Hartmann, R.; Merten, C., *J. Power Sources* **2008,** *176*, 444-451.

115. Di Noto, V.; Negro, E.; Vezzù, K.; Bertasi, F.; Nawn, G., *Electrochem. Soc. Interface* **2015,** *24,* 59-64.

116. Long, X.; Wang, Z.; Xiao, S.; An, Y.; Yang, S., *Mater. Today* **2016,** *19,* 213-226.

117. Fan, G.; Li, F.; Evans, D. G.; Duan, X., *Chem. Soc. Rev.* **2014,** *43,* 7040-7066.

118. Xiang, X.; Hima, H. I.; Wang, H.; Li, F., *Chem. Mater.* **2008,** *20,* 1173-1182.

119. Takashi, T.; Katsutoshi, Y.; Hiroshi, T.; Hiro-o, T., *Chem. Lett.* **1992,** *21,* 815-818.

120. Li, T.; Miras, H.; Song, Y.-F., *Catalysts* **2017,** *7,* 260.

121. Wang, H.; Xiang, X.; Li, F., *J. Mater. Chem.* **2010,** *20,* 3944-3952.

122. Li, B.; Zhao, Y.; Zhang, S.; Gao, W.; Wei, M., *ACS Appl. Mater. Interfaces* **2013,** *5,* 10233-10239.

123. Sheng, S. D.; Robert, S., *ChemSusChem* **2010,** *3,* 136-168.

124. Haixin, C.; Hongkai, W., *Adv. Funct. Mater.* **2013,** *23,* 1984-1997.

125. Qian, H.; Greenhalgh, E. S.; Shaffer, M. S. P.; Bismarck, A., *J. Mater. Chem.* **2010,** *20,* 4751-4762.

126. Novoselov, K. S.; Fal'ko, V. I.; Colombo, L.; Gellert, P. R.; Schwab, M. G.; Kim, K., *Nature* **2012,** *490*, 192-200.

127. Stankovich, S.; Dikin, D. A.; Dommett, G. H. B.; Kohlhaas, K. M.; Zimney, E. J.; Stach, E. A.; Piner, R. D.; Nguyen, S. T.; Ruoff, R. S., *Nature* **2006,** *442*, 282.

128. Duan, J.; Chen, S.; Jaroniec, M.; Qiao, S. Z., *ACS Catal.* **2015,** *5,* 5207-5234.

129. Wang, H.; Maiyalagan, T.; Wang, X., *ACS Catal.* **2012,** *2*, 781-794.

130. Ci, L.; Song, L.; Jin, C.; Jariwala, D.; Wu, D.; Li, Y.; Srivastava, A.; Wang, Z. F.; Storr, K.; Balicas, L.; Liu, F.; Ajayan, P. M., *Nat. Mater.* **2010,** *9,* 430.

131. Wang, X.; Blechert, S.; Antonietti, M., *ACS Catal.* **2012,** *2,* 1596-1606.

132. Yong, W.; Xinchen, W.; Markus, A., *Angew. Chem. Inter. Ed.* **2012,** *51,* 68-89.

133. Teter, D. M.; Hemley, R. J., *Science* **1996,** *271,* 53-55.

134. Zhao, Z.; Sun, Y.; Dong, F., *Nanoscale* **2015,** *7,* 15-37.

135. Wang, Y.; Yao, J.; Li, H.; Su, D.; Antonietti, M., *J. Am. Chem. Soc.* **2011,** *133,* 2362-5.

136. Datta, K. K.; Reddy, B. V.; Ariga, K.; Vinu, A., *Angew. Chem. Int. Ed.* **2010,** *49,* 5961-5.

Chapter 2

General Experimental Methods and Techniques

2.1. Introduction

This chapter mainly deals with the basic principle of various instruments which have been used in this present thesis. The experimental details, involved in this thesis work for various experiments have been briefly discussed.

2.2. Materials

The materials and chemicals involved in this thesis are directly taken from commercially available samples without further purification. A list of the names of materials and chemicals involved in the thesis, along with their formulas, and supplier name is shown below in **Table 2.1**.

Table 2.1. List of the chemicals along with their formulas and company names.

Name of Chemicals	**Chemical formula**	**Company name**
Formamide	$HCONH_2$	Sigma Aldrich
Palladium (II) chloride	$PdCl_2$	Sigma Aldrich
Ruthenium(III)chloride hydrate	$RuCl_3 . xH_2O$	Sigma Aldrich
Cobalt(II) nitrate hexahydrate	$Co(NO_3)_2 . 6H_2O$	Merck
Iron(III)nitrate, nonahydrate	$Fe(NO_3)_3 . 9H_2O$	Merck
Aluminium (III) nitrate, nonahydrate	$Al(NO_3)_3 . 9H_2O$	Merck
Ammonium fluoride	NH_4F	Merck
Hexamethylene tetra amine	$(CH_2)_6N_4$	Merck
Sodium borohydride	$NaBH_4$	Merck
Potassium hydroxide	KOH	Merck
Sulphuric acid	H_2SO_4	Merck
Perchloric acid	$HClO_4$	Alfa Asear

Acetic acid	CH_3COOH	Sigma Aldrich
Boric acid	H_3BO_4	Sigma Aldrich
Sodium bicarbonate	$NaHCO_3$	Merck
Phosphatebuffer solution	PBS	Merck
Platinum on graphitic carbon	Pt/C (40 wt.%)	Sigma Aldrich
Palladium carbon	Pd/C (40 wt.%)	Sigma Aldrich
Ruthenium oxide	RuO_2	Sigma Aldrich
Iridium oxide	IrO_2	Sigma Aldrich
Ethanol	CH_3CH_2OH	Merck
Water	H_2O	

2.3. Different Methods for Synthesis:

Ion-Exchange Reduction Method:

The Ion-Exchange reduction methods are extremely used for NPs synthesis. This method requires the precipitation of the metals from aqueous or non-aqueous solutions by chemical reduction of a metal cation. For green synthesis procedure, aqueous solvent is preferable used. The most commonly used reducing agents are gaseous H_2, solvated alkali metal borohydride ($NaBH_4$, $LiAlBH_4$, $H_3N\text{-}BH_3$), polyol process (ethyleneglycol), hydrazine hydrate (N_2H_4,H_2O) and hydrazine dihydrochloride (N_2H_4, HCl). Sometimes during the reduction of metal, some precursors need some energy sources such as ultrasound, heat.

Sonochemical Methods:

Sonochemistry mainly deals with the effect of sonic waves and wave properties on chemical systems. Most of the ultrasonic instruments operate at 20 or 40 kHz frequency (**Figure 2.1.**). Ultrasound energy enhances the mass transportation, reduces the layer thickness as well as deposits metal salts. In ultrasound methods both reduction of metal salts and deposition of the NPs occur almost consecutively which make the process of supported metal NPs more efficient and environmental friendly. Generally, sonochemical mediated metal nanoparticles are formed by acoustic cavitation process. The proposed mechanistic pathway[1] for sonochemical formation of metal nanoparticles is described below:

First sonolysis of water into ·H and ·OH

$$H_2O = \dot{H} + \dot{O}H$$

This ·H actually acts as a reductant of metal salts.

Second step is the generation of an secondary radical which promotes the reduction rate

$$RH + \dot{H} = \dot{R} + H_2$$

Third step is the reduction of metal salt by ·H formed form sonolysis of H_2O

$$M(II) + \dot{R} \text{ or } \dot{H} = M(0)$$

The ·H radical, formed during ultrasounds may reduce Pd(II) ions into Pd(0)NPs.

Figure 2.1. Photograph of ultrasonicator.

In this thesis, ultrasound was performed in SINEO UWave-1000 (Shanghai, China) instrument.

Microwave Irradiation:

Microwave irradiation methods are very commonly used for synthesizing supported NPs (**Figure 2.2.**). It is occurred through an interaction between light waves and polar solvents. Several groups have reported the synthesis of supported metal NPs from the solution of the metal salts by irradiating microwave light. The microwave irradiation on a high dielectric solvent generates very fast and uniform heating which further allows a quick reduction of the metal precursor and deposits on the support materials. Advantages of microwave irradiation methods over the conventional heating's are (a) very fast heating during microwave irradiation decreases the reaction time. (b) Formation of very small as well as very narrow size distribution.

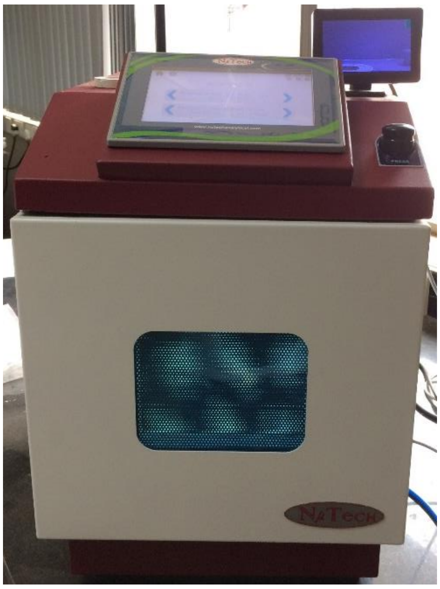

Figure 2.2. Photograph of microwave synthesizer.

In this thesis synthesis was performed using MAS-II microwave synthesizer from Sineo Microwave Chemistry Technology Company (Shanghai, China) and from NμTech (India) private limited company.

Co-Precipitation and Deposition:

In precipitation-deposition method, dissolved metal precursors have been precipitated by adjusting the pH of the solution or by hydrolysing the metal with weak hydrolysing agents. The precipitate metal precursor may be deposited on the surface of any supported materials that is already present in the solution or it can be impregnated separately on the support surface by any mechanical process. Although this method is most frequently applied for transition metal hydroxide or oxide nanostructures but sometimes it is further extended to synthesize noble metal nanoparticles. Haruta et al. reported[2] complete precipitation of the $Au(OH)_3$ by adjusting pH ~ 8 from the aqueous solution of $HAuCl_4$ and its deposition on the support surface. Among different metal oxides or hydroxides, layered doubled hydroxide based materials are open layered structure of mono or bi metal. LDH based composite materials are prepared by slow hydrolysis of metal salts following the same precipitation-deposition principle.

2.4. Instruments and Instrumental Techniques

X-ray diffraction (XRD):[3,4]

It is a widely used to measure the phase and bulk crystallinity *i.e.* inter planar spacing of the examined materials. In this method, a monochromatic electromagnetic radiation with a fixed wavelength (a few angstroms) passes through the sample. The X-ray is mainly generated from X-ray tube which is comprised of a heated tungsten filament enclosed in an evacuated ceramic vessel as cathod and water cooled Cu foil as anode. The electrons, emitted from tungsten are accelerated towards a water cooled metal and can knock out the electrons in the inner shells of Cu atoms – resulting in a relaxation of valence electron to inner position followed by the generation of X-ray. Cu-source, used as an X-ray source can generate X-ray of two characteristic wave lengths such as Cu Kα ($\lambda = 0.154$ nm) and Cu Kβ ($\lambda = 0.139$ nm). As the X-ray source should be monochromatic, therefore the Kβ line in the X-ray spectrum is removed by using Nickel filter. When X-ray is irradiated on the sample, it penetrates into the samples followed by the interaction with the solid's internal structure. The incident X-ray beam interacts with different crystalline planes of the solids at angle θ and reflected towards the detector- a positive interference is occurred which can be correlated by Bragg's diffraction equation:

$$n\lambda = 2d\ sin\theta$$

Where d is the spacing between the layers of the atom, λ is the wavelength of the incident beam, θ is the angle between incident rays and lattice plane, n is the order of interference (**Figure 2.3.(a,b)**).

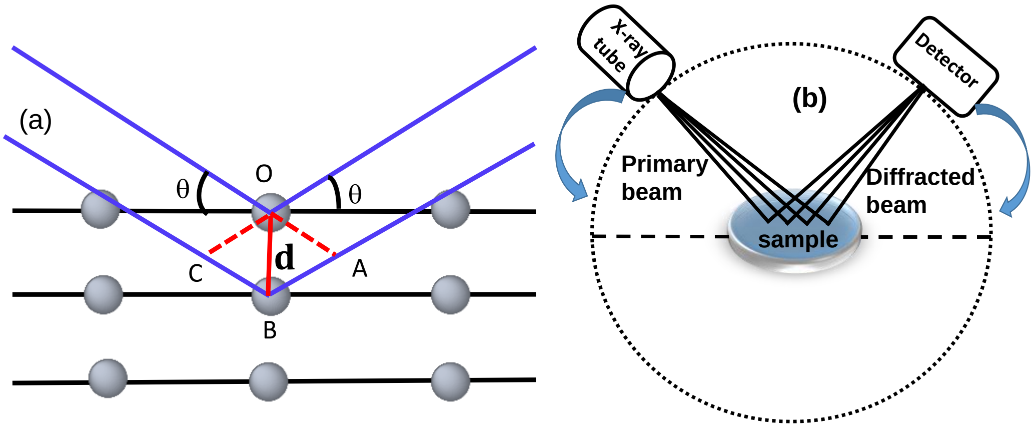

Figure 2.3. Schematic illustration of (a) X-ray scattering. (b) Alignment of X-ray source and detector.

In this thesis, X-ray spectra were collected on Bruker DAVINCI D8 ADVANCE diffractometer equipped with Cu Kα radiation (λ 0.15406 nm).

Transmission Electron Microscope (TEM):[5]

Transmission Electron Microscope (TEM) provides the morphological features of sample in atomic scale region. In this technique, the images are recorded by collecting electrons that are transmitted through the examined sample. Herein, the sample should be thick (few nm) as the fact that the images have been captured from transmission electron beams from sample. The transmitted electrons are focused by an objective lens followed by the projective lens. This projective lens then magnifies the ‘image’ which can be finally detected by a fluorescent screen. There are two types of imaging in the TEM instrument *i.e.* bright field (BF) mode or dark field mode. Transmitted beam is used for bright field imaging mode whereas diffracted beam is generally used for dark field imaging mode. High Resolution TEM (HRTEM) is another mode of this technique that is mainly used for high resolution imaging of crystalline materials. HRTEM can provide images up to 0.8 A°. Herein, several diffracted beams are being used to generate the images. For a crystalline sample, the electron can diffract through the crystal planes and thus generates interfere followed by diffraction patterns. Dark selected area electron diffraction (SAED) pattern provides the information about the crystallinity pattern of the sample as well as the basic information about the phase of the sample.The crystal planes of the sample, parallel to the direction of propagation of the electron beam will be diffracted according to the Bragg’s law. This diffraction pattern is a Fourier transformation of the periodic potential of the electron. These diffracted electrons along with the electrons in the primary interfere causing a back transformation (or inverse Fourier transform) resulting in an image.

In this thesis work, the morphology and chemical composition of the prepared samples were captured by transmission electron microscopy in JEM –2100, JEOL and JEM –2100F, JEOL operated at 200 kV.

Field Emission Scanning Electron Microscope (FESEM):[6]

Field Emission Scanning Electron Microscope (FESEM) is generally used to know the morphological details of small objects (few micrometres to nanometres). In this method, a negatively particle (electron) plays crucial roles. FESEM instrument generally consists of two parts (a) electron column and (b) Electronic console. In electron column, electrons are emitted from a field emission source under a high vacuum and then accelerated in a high electrical field gradient. The generated electrons, namely primary electrons are then deflected by electronic lenses producing a narrow scan beam which further bombarding the object. Thereafter, the secondary electrons are ejected from each spot of the object. In this context, it should be mentioned that the velocity as well as angle of the secondary beam is directly related to the surface structures of the object.

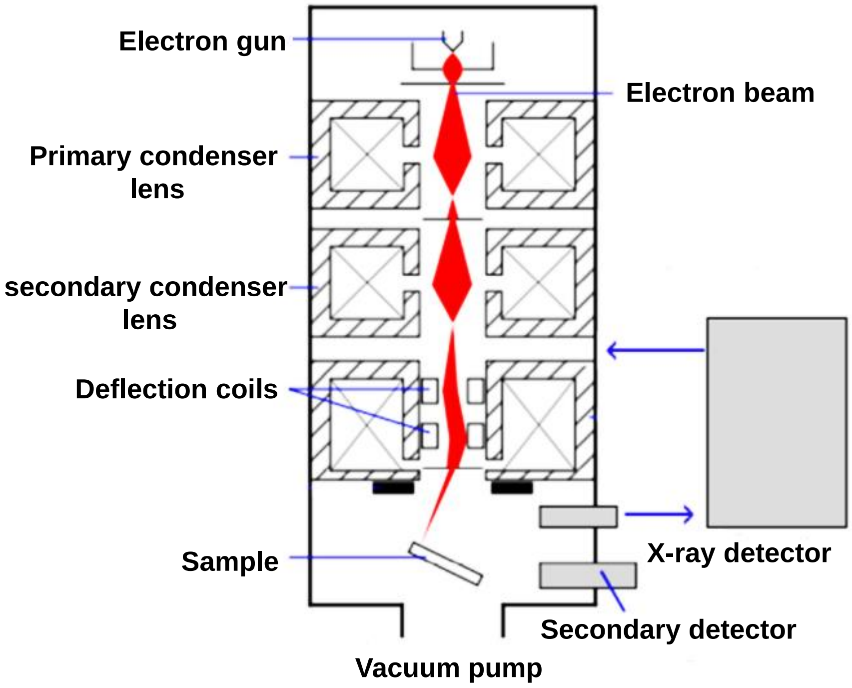

Figure 2.4. Schematic diagram of FESEM.

A detector located above the sample holder collects the secondary electron followed by the production of an electronic signal which is further amplified and transformed as a scanned image. On the other hand, the electronic console is mainly consisted of control knobs and switches. Electronic console further allows the adjustment of filament current, accelerates voltage. Thus increases magnification, brightness and contrast of the instrument. Along with the production of secondary electrons, several processes such as generation of back scattered, electrons and X-ray also occurs. FESEM measurement mainly provides the surface morphology of the sample. The schematic presentation of FE-SEM was show in **Figure 2.4**.

In this thesis, Field-emission scanning electron microscope (FESEM) datas were collected on Carl Zeiss, Germany (Model: ∑igma).

Energy-Dispersive X-ray spectroscopy (EDX):

FE-SEM and TEM is often complemented with energy-dispersive X-ray spectroscopy (EDX), enabling the user to determine the composition of the features from FE-SEM or TEM figure. As describes earlier that the supra X-ray is emitted from the FE-SEM and

TEM sample. The composition of the materials can be achieved by positioning the X-ray detector which interrupts the X-ray and generates a small current which is then converted to a voltage pulse. This voltage plus is proportional to the frequency detected in X-ray. Energy dispersive spectroscopy was obtained from a spectrometer attached to Carl Zeiss (Germany made, Model: ∑igma)

X-ray photoelectron spectroscopy (XPS):[7]

X-ray photoelectron spectroscopy (XPS) is a surface characterization technique that can measure the surface composition of various materials and the oxidation state of the corresponding element. It is a quantitative spectroscopic technique where the chemical as well as electronic state of the elements, elemental compositions, and empirical formulas of the examined materials can be measured. Herein, the sample is irradiated with X-rays. The electron will escape from the surface of the atom if the incident X-ray contains sufficiently higher energy to overcome the binding energy of electron. In this process, the irradiated X-ray is first absorbed by the core shell electrons followed by the escape of core shell electrons (**Figure 2.5**) by a kinetics energy given by:

$$h\gamma = \text{binding energy (BE)} + \text{kinetic energy (KE)}$$

The XPS measurement is performed under ultra-high vacuum condition that provides the shorter mean free path of the electrons. The X-ray source for XPS is obtained either from monochromatic Aluminum K with the main radiation peak centred at $h\nu = 1486.6$ eV or non-monochromatic Magnesium K with main radiation peak centred at $h\nu = 1253.6$ eV. As each element has specific major and minor peaks in the XPS spectra, XPS can be used to identify the elements by the comparison with a reference database. In addition, the intensity of the XPS peak can also be used to measure the concentration of each elements composed by the sample. When U.V photon is used instead of X-ray photon it is called UV-ray photoelectron spectroscopy (UPS).

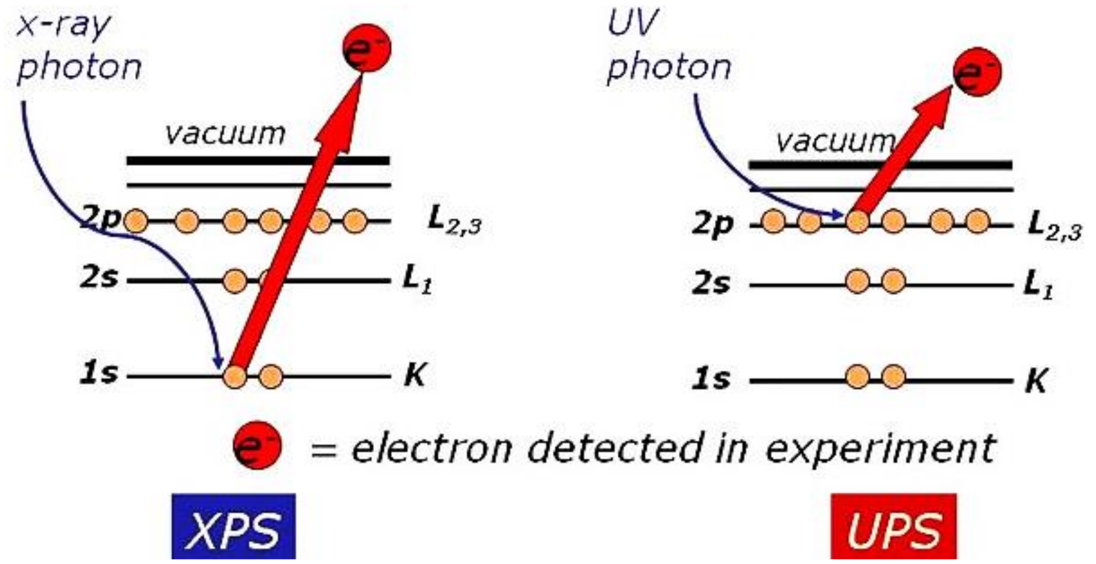

Figure 2.5. Schematic representation of working principle of XPS and UPS.[5]

XPS measurements were performed using Kratos Axis Ultra and VG Microtech under ultra-high vacuum condition, using a monochromatic Al Kα X-ray was used as the source.

Thermo-gravimetric analysis (TGA):

Thermo-gravimetric analysis (TGA) is widely used to examine the chemical composition and thermal stability of the sample. In TGA technique, the change of weight percentage of materials during the heating process in a N_2 atmosphere is being monitored.

Thermo gravimetric analysis (TGA) of the synthesized sample was carried out by TA Instrument (Model: Discovery TGA).

Fourier Transform Infra-red Spectroscopy (FTIR):[8]

Fourier Transform Infra-red Spectroscopy (FTIR) is a sensitive technique mainly used for the identification the functional groups present in the molecule. FT-IR spectra are recorded by using infrared region electromagnetic radiation. The absorption mainly relates with the vibrations of the bonds present in the molecule. First the background emission spectrum of the IR source should be measured then one can record the emission spectrum of the IR source with the sample. The ratio of the sample spectrum to the background spectrum is directly related to the sample's absorption spectrum.

All FT-IR spectra in this thesis were collected from Perkin Elmer RXI FT-IR spectrophotometer.

UV-Vis Spectroscopy:[9]

UV-visible spectroscopy is an absorption spectroscopy in which visible (400-1200 nm) and Ultra-Violet (200-400 nm) light is absorbed by the examined molecule when the electron excites from ground state to higher energy state.

It follows Lambert Beer’s law which is

$$A= \log\left(\frac{I_0}{I}\right) = \varepsilon\ c\ l$$

Where A is the optical density or absorbance, I_0 is the incident light intensity and I is the transmitted light, ε is the molar absorption coefficient, c is the concentration of the solution of the sample and l is the path length of light beam passing through the solution.

The optical absorbance of the synthesized compounds was performed using Varian Cary 100 Bio UV-visible Spectrophotometer.

Inductive Coupled Plasma-Optical Emission Spectroscopy (ICP-OES):[10]

The ICP-OES instrument combines with inductive couple plasma as atomizer and optical emission spectroscopy as an analyser. In Inductive couple plasma chamber, the sample is first nebulized and then atomized with the energy of plasma. Then the carrier gas (Ar), pushes this plasma through a differential vacuum interphase, where it cools down and thus emission rays releases. The released emission rays are being focused into the optical emission chamber, corresponding to the photon wavelength followed by the measurement. The element type is determined based on the position of the photon rays, whereas, the content of each element is determined based on the intensity of the photon. ICP-OES measurements have several advantages over other experiments such as:

(a) It simultaneously measures multiple elements.

(b) It has very low chemical and ionization interference.

(c) It provides very high sensibility; lower limit of 10 ppb.

In this thesis, ICP-OES was performed on iCAP 7000 Series (Thermo Scientific).

Elemental Analysis:[10]

Elemental analysis is an experiment that can determine the amount (typically a weight percent) of elements present in a compound. The CHNS analysis mainly measures the amount of carbon, hydrogen, nitrogen and sulphur in any sample materials. It is generally followed the combustion process at high temperature in presence of ultra-high pure oxygen followed by a GC separation and quantification using a thermal conductivity detector (TCD). In combustion process, (at 1000° C), carbon is converted to carbon dioxide; hydrogen to water; nitrogen to nitrogen gas/ oxides of nitrogen and sulphur to sulphur dioxide. These gases are then isolated and equilibrated in ballast known as ballast collation. Then sampling of the combustion gas is performed and the measurement of carbon and hydrogen was done by infrared spectroscopy. After that, the gases enter into a mixing volume chamber to make a homogeneous mixture at constant temperature and pressure. The homogeneous mixture then passes through a series of thermal conductivity detectors and provides the N amounts.

In this thesis, EuroEA Elemental Analyser was used for CHN measurement of as synthesized sample.

Nuclear Magnetic Resonance (NMR) Spectroscopy:[10]

NMR is a property of a nucleus in an atom. Nucleus in an atom behaves as a tiny bar magnet having nuclear spin (I). When this nucleus is placed in an external magnetic field generates a torque which further generates the different alignments of the nucleus followed by the energy transition. Some atoms *i.e.* for ^{12}C nuclear spins are paired against each other, having no overall spin *i.e.* I = 0. So, ^{12}C is not NMR active whereas, for both ^{13}C and ^{1}H nuclear spin I = 1/2. In presence of external magnetic field two spin states generate *i.e.* I = +1/2 and I = -1/2. These two spin states contain two different energy levels; one spin is aligning with the external magnetic field and another is opposite to the external magnetic field. Transition of nucleus occurs either by the absorption of energy or by the release of energy.

Electrochemical Measurement:[11]

All electrochemical performances in this thesis work were carried out in a conventionally three electrode glass cell as shown in **Figure 2.6** and the data were recorded from an electrochemical workstation (Autolab, Metrohm, PGSTAT 320N). Glassy carbon electrode (GC, diameter 3 mm and 5 mm) was used as a working electrode whereas platinum wire and Ag/AgCl in 3 M KCl was used as counter and reference electrode. Before performing any electrochemical study, GC was polished with alpha alumina powder (0.3 micron), suspended in deionized water on a Nylon polishing pad (Metrohm). After each polishing, the GC electrode was rinsed with deionized water and sonicated in ethanol for 2 minutes. The current density reported herein was normalized by the geometrical area of the working electrode and all potentials were reported in reversible hydrogen electrode (RHE) scale. The potential measured in Ag/AgCl was converted into RHE by Nernst equation, $E_{RHE} = E_{Ag/AgCl} + E^0_{Ag/AgCl} + 0.059$ pH where $E_{Ag/AgCl}$ is the working potential, $E^0_{Ag/AgCl} = 0.1976$ at 25^0C.

Voltammetry:

Voltammetry is a technique where potential is ramped with certain rate and the corresponding current is recorded. It is surface sensitive technique. It provides the measurement of the current (charge) transfer between electrode-electrolyte interfaces.

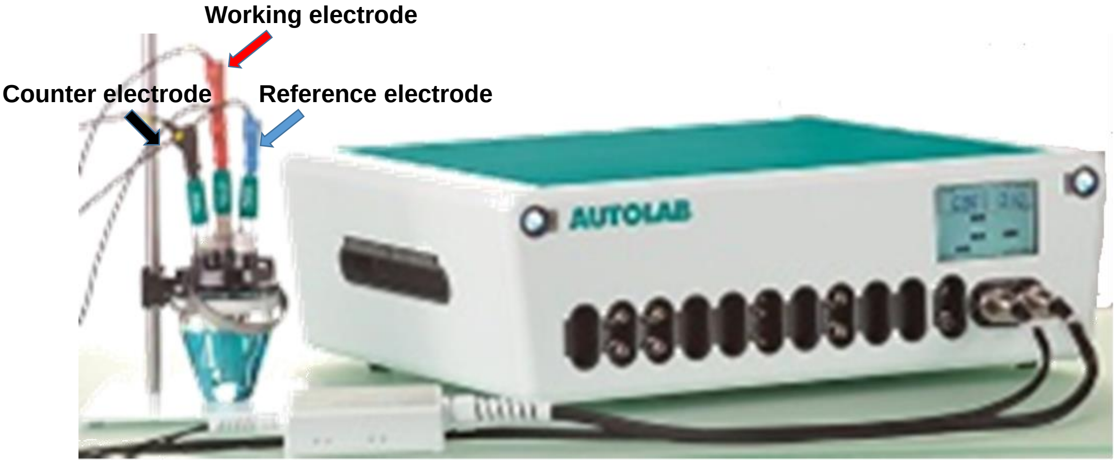

Figure 2.6. Photograph of conventional three electrode set up of Autolab instrument.[13]

Two types of Voltammetry are exclusively used to examine the surface process- (a) cyclic voltammetry (CV) wherein the changes of potential occur linearly from one potential (V1) to another potential (V2) and thereafter it is changed from V2 to V1. (**Figure 2.7.a**) (b) linear sweep voltammetry (LSV) where the potential linearly changes from one potential (V1) to another potential (V2) (**Figure 2.7.b**). Voltammetry process can provide the current vs potential plot of different interface process but the identification of process is very difficult task. CV current depends on four factors (a) current two different reactions and (b) corrosion of the electrode and charges of the electrode. Therefore, the steady state current at the interfaces consist of four components: $i = i_{reaction1} + i_{corrosion} + i_{reaction\ 2} + i_{charge}$. LSV is a voltammetric method to measure the current density at a working electrode based on the overpotential. Both CV and LSV process are mainly used to study HOR, HER, OER and ORR. CV technique can be used for the electro deposition of metal oxides/oxo hydroxides onto the conductive substrates from metal-salt solutions. The amount of the metal deposited depends on the cycle number and the potential region between which the CV run.

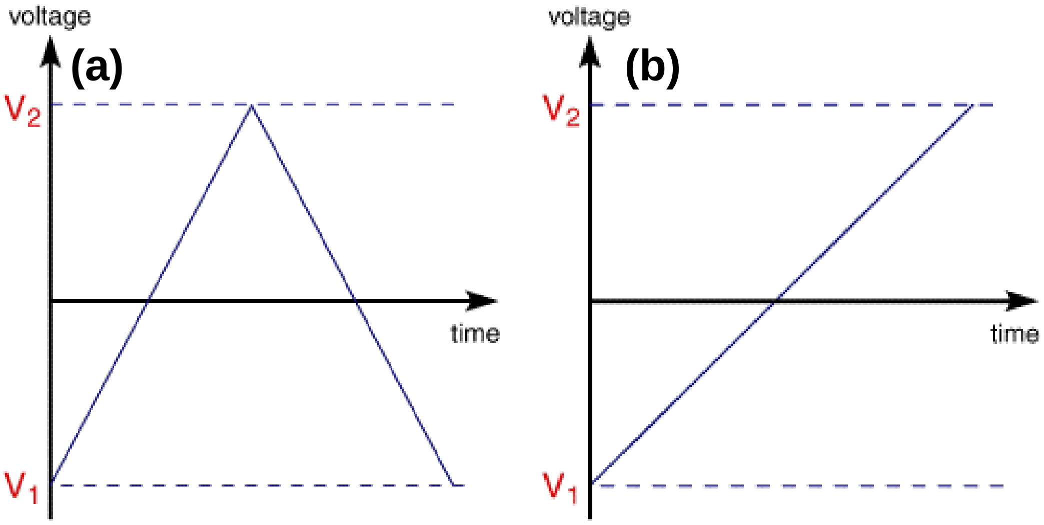

Figure 2.7. Voltage vs time profile of (a) cyclic voltammetry and (b) linear sweep voltammetry.[11]

Chronoamperometry (CA):

Chronoamperometry technique is mainly used to measure the current of a system at a particular potential with time. Chronoamperometry technique provides information about the durability of an electrocatalyst. Occasionally this technique used to determine the Tafel slope accurately. Quantitative information can also be obtained from CA measurements. The amount of charged passed through the electrode is obtained by the integrating the current over a certain time. It is used to know the stability of the catalyst.

Chronopotentiometry:

Chronopotentiometry is a galvanostatic technique where it is preferably used to fix a current and measure requirement of the potential over time. Stability of the electrocatalyst can be measured by this technique.

Impedance Spectroscopy:[14]

An electrical circuit has an ability to resist the current pass through the circuit and the resistant can be defined by the ohm's law

$$R = \frac{E}{I}$$

Where E is the potential (V) and I is the current (A). This can be employed only for the ideal circuit but for real circuit the alternative current (AC) responses and applied voltage signal are not in same phase. So for real circuit, impedance can be defined by the frequency dependent resistance.

$$Z_{\omega} = \frac{E_{\omega}}{I_{\omega}}$$

Where Z_{ω} is the impedance, E_{ω} is the frequency dependent potential and I_{ω} is frequency dependent AC current.

The potentials response signal is

$$E(t) = E_0 \sin(\omega t)$$

Where the radial frequency $\omega = 2\pi f$.

The corresponding AC current signal follows as:

$$I(t) = I_0 \sin(\omega t + \varphi)$$

Where φ is phase difference and I_0 is the response signal amplitude. Now in according to the impedance (Z_{ω})-

$$Z_{\omega} = \frac{E_0\, sin\,(\omega t)}{I_0 sin(\omega t+\varphi)} = Z_0 \frac{sin\,(\omega t)}{sin(\omega t+\varphi)} = Z_0\{\cos(\varphi) + i\sin(\varphi)\} = Z_{real} + Z_{imag}$$

Table 2.2. The detailed descriptions of Bode and Nyquist plot.

Parameter	Bode plot	Nyquist plot
Process	The individual electron transfer process was describes	The individual electron transfer process was describes
Frequency	Frequency was well defined.	Frequency was not well defined.
Nature	Both small and large impedance was defined simultaneously.	In presence of large impedance, small impedance was not well defind.

So total impedance is a complex quantity and has two counterparts one is real part another is imaginary part. The EIS of a compound can be represented by two ways (a) by plotting the real part on x-axis and the negative of the imaginary part on the y-axis, producing a Nyquist plot and (b) Logarithm of both x-axis and y-axis produced Bode Plot.

Table 2.3. The components and their indications for equivalent circuit.

Equivalent	**Impedance**	**Indication**
Resistance	R	
Capacitance	C	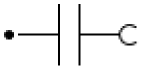
Inductance	L	
Constant phase element	Q	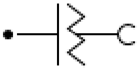
Warburg Impedence	W	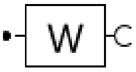

A details description of the Bode and Nyquist plot is described in **Table 2.2**. For a particular circuit if capacitive and resistance elements are parallel to each other, then the Nyquist plot would look like the one where low frequency is plotted on the right side and high frequency data is placed on the left side. The electrochemical cell can be represented by a network frame of passive electrical elements and it is termed as equivalent circuit. The elements of equivalent circuit are presented in **Table 2.3**.

Gas Chromatography:

Gas chromatography is a quantification and separation technique for the mixture of components. In GC the components are separated as a function of their retention coefficients in liquid or solid stationary phase in a column. The column, connected between injector and detector, is placed in an oven which is heated at different temperature depending upon the types of gasses. A carrier gas (inert in nature) *i.e.* argon is flowed continuously through the column. A calibrated gas tight syringe is used to take sample from the headspace of the electrochemical cell and it injects in the injection port. Thereafter, the analyte gas is being flowed through the column with carrier inert gas and thus different analytes arrive to the detector separately at different time intervals depending upon their retention coefficients. Thermal conductivity detector (TCD) with argon (Ar) as a carrier is used for the gas phase analysis. After getting the signal, detector sends it to computer and then it is plotted as a function of the retention time. For each analyte, a peak is appeared in the chromatogram at a specific time. The area of the peaks is correlated with the % of that gas present in the headspace of the electrochemical cell. It has several advantages as follows:

(a) High thermal stability, fast response as well as exceptional sensitivity over a wide range of applications.
(b) Dedicated filaments are available for corrosive samples.

Faradaic Efficiency:

The amount of the evolved gas from cathode and anode is quantified by gas chromatography. A 250 ml five neck sealed glass cell is used for the measurement of of O_2 and H_2. Before starting the experiment, the glass cell has to be purged with Ar (99.9%) for 45 min. The electrolysis is performed with Glassy carbon electrode (GC, diameter 5 mm), used a working electrode whereas platinum wire and Ag/AgCl in 3 M KCl is used as counter and reference electrode. The working electrode has modified by drop casting the catalyst suspension on GC electrode of diameter 5 mm with constant catalyst loading of 0.14 mg cm^{-2}. The chronoamperometry experiment was performed with modified working electrode at a particular current density and at different time interval gas was analyzed with GC instrument (Thermo scientific, Model: Trace 1110) with thermal conductive detector (TCD) and argon as carrier gas. The theoretical amount of gas (O_2

and H_2) was calculated from accumulated charge during galvanostatic electrolysis by assuming 100% faradic efficiency.

Theoretical amount (n in mole) of gas (H_2, O_2) $= \frac{Q}{e \times F} = \frac{I \times t}{e \times F}$

Where I is the current in Amp, t is time in sec, e is the number of electrons which is 2 for HER and 4 for OER and F is the Faraday constant (96485.3 C mol^{-1}).

Exchange Current:

The exchange current represents the amount of current passes through the electrode at thermodynamic equilibrium potential. It reflects the intrinsic rate of electron that transfers at electrode-electrolyte interface between reactant and catalyst. Generally, exchange current density is measured from the intercept of the extrapolated to the linear region of Tafel plot. The value should measure the effectiveness of the catalyst. Greater the magnitude of the exchange current, greater will be the activity of the catalyst.

Turn Over Frequency (TOF) Calculation:

Here are some assumptions as follows**:**

(a) Every metal atom present on the glassy carbon electrode should be involved in OER/HER reaction.

(b) It is the lower limit of the TOF value.

The TOF per active site for OER/HER reaction can be calculated by following equation:

$$\mathrm{TOF}(H_2/\mathrm{O_2/s}) = \frac{\text{Total oxygen/Hydrogen turnover per geometrical area of working electrode}}{\text{Total no active site per geometrical area of working electrode}}$$

$$\mathrm{TOF}(\mathrm{s^{-1}}) = \frac{J \times A}{4 \times F \times n}$$

Where J is the current density (mA cm^{-2}) at particular overpotential (η= 0.35 V), A is the geometrical area (cm^{-2}), F is the Faraday constant (96485.3 C mol^{-1}) and n is the mole of the active site on the electrode.

Double Layer Capacitance:

The double layer capacitance (C_{dl}) of the catalyst can be measured form the CV plot of the catalyst taken in a non-faradic region with small potential windows. Before taken the charging-discharging CV plots in different scan rate, working electrode has to be scanned 20 CV cycling in a particular potentials region to stabilize the electrode. The slop of the linear pot of current density (mA cm^{-2}) at a particular potential (RHE) vs scan rate, gives the C_{dl} (mF cm^{-2}). In addition we have calculated the roughness factor (R_f) of the materials was calculated from C_{dl} by

$$R_f = C_{dl}/C_s$$

Where C_s is the double layer capacitance of an atomically smooth planar surface of per unit area under identical conditions. Herein, we have considered bear GC electrodes as the planer surface. For bear GC electrode Cs is considered as 0.082 mF cm^{-2}.

2.5. References:

1. Bang, J. H.; Suslick, K. S., *Adv. Mater.* **2010,** *22,* 1039-1059.

2. Haruta, M.; Tsubota, S.; Kobayashi, T.; Kageyama, H.; Genet, M. J.; Delmon, B., *J. Catal.* **1993,** *144,* 175-192.

3. W. H. Bragg, W.L. Bragg, “The reflexion of X-rays by crystals”. Proc R. Soc. Lond. A; **1913**, 88, 428–38.

4. A. R. West, “Solid state chemistry and its applications”, John Wiley & Sons, New York, 1984.

5. S. Amelinckx, D. V. Dyck, J. V. Landuyt, G.V. Tendeloo, “Electron microscopy: Principles and fundamentals” VCH, University of Michigan, 1997.

6. J. W. S. Hearle, J. T. Sparrow and P. M. Cross, J. Appl. Cryst. **1974, 7**, 513-514.

7. C. D. Wagner. Handbook of x-ray photoelectron spectroscopy: a reference book of standard data for use in x-ray photoelectron spectroscopy, 2010.

8. P. Griffths; J. A. de. Hasseth; “Fourier Transform Spectroscopy” (2nd ed.), Wiley-Blackwell, 2000.

9. Y. R. Sharma, “Elementary organic spectroscopy; Principles and chemical applications” S. Chand, New Delhi, 1980.

10. J.M. Hollas, Modern Spectroscopy, **2003**, Wiley, Fourth Edition.

11. Allen J. Bard, Larry R. Faulkner “Electrochemical Methods: Fundamentals and Applications” Wiley, 2000.

12. http://www.metrohm-autolab.com/download/Autolab_Brochure_2013_EN_LR.pdf.

13. www.ceb.cam.ac.uk/research/groups/rg-eme/teaching-notes/linear-sweep-and-cyclic-voltametry-the-principles

14. www.gamry.com/application-notes/EIS/basics-of-electrochemical-impedance-spectroscopy.

Chapter 3

Palladium Nanoparticle-Graphitic Carbon Nitride Porous Composite: Synthesis and Its Application in HER/HOR at all pH Values

3.1 Abstract

The hydrogen evolution reaction (HER) and hydrogen oxidation reaction (HOR) are two fundamental reactions for the development of non-fossil energy storage and conversion devices. The carbon supported platinum (Pt/C) based catalysts are universally used in cathodes and anodes for fuel cell; however, the poor durability of Pt/C due to degradation of the catalyst in the strongly oxidizing environment prevents its widespread applications. Here, we report the synthesis of a porous palladium nanoparticle-carbon nitride composite (Pd-CN_x) for its superior activity and high durability toward the HER/HOR in acidic and alkaline media. The Pd-CN_x composites exhibited superior HER activity in acidic media with a small overpotential of −55 mV for 10 mA cm^{-2} current, low Tafel slope of 35 mV dec^{-1}. Furthermore, this catalyst has also displayed superior HOR activity, measured by a rotating-disk experiment (RDE) with a broad range of pH (0−14) in different buffer solutions. The HOR activity of Pd-CN_x gradually decreases with an increasing solution pH. The pH dependency HOR activities of porous Pd-CN_x composite were correlated with the hydrogen binding energy (HBE) of the catalyst surface.

3.2 Introduction

Hydrogen evolution (HER) and hydrogen oxidation reaction (HOR) are two important catodic and anodic process in FCs and electrolyzer respectively. In the polymer electrolyte membrane fuel cell (PEMFC) carbon supported platinum (Pt/C) based catalysts are universally used in cathode and anode. In practice, large-scale electrochemical hydrogen production is generally restricted by two main problems: (1) the precious metal platinum dependency and (2) lack of stability of the electrode materials under strong acidic condition of PEM cells. One of the most effective and cheaper catalyst for anode materials of PEMFC is Pd based catalysts, since Pd based materials is about five times cheaper than Pt based materials13 and also has stronger CO tolerance14. Different groups develops noble metal Ir,[1] Ru,[2] Pd[3] nanoparticles dispersing on highly conducting with high surface area commercial activated carbon (XC-72R) as a HER/HOR catalyst. But the major drawback of carbon supported catalyst was low durability. The carbon supported catalyst is easily oxidized under cathodic potentials in strong acidic condition. Most of HOR studies on the Pd based catalysts were on bimetallic systems, for example Pd deposited on other foreign metal such as Ru,[4] Pt,[4] Au,[5] Ir,[4] Re,[4] Ag.[6] Furthermore, there were some report of HOR studies on monometallic Pd supported on carbon,[3] WC,[7] WC-CNT[8] etc.

In order to understand apparent reaction mechanism of HOR/HER, kinetic parameters of electrochemistry such as Tafel slope with anodic and cathodic transfer coefficient (α), exchange current density (J_0) at particular temperature and pressure are very important. The rate of reaction on the electrode surfaces is generally governed by the different consequent steps[9] such as water dissociation step, interaction between metal surfaces and dissociated products, recombination of H_{abs} and H_2 production, and lastly OH_{abs} desorption. The kinetic parameters mainly transfer coefficient (α) and tafel slope are allowed to determine which combination of steps occurred and which one is the rate determine step. Conventionally and most frequently the RDE method is used for measuring the electrochemical kinetic parameters of different single-crystalline and polycrystalline electrode. In the RDE method, a Pt metal[10-11] shows highest HER/HOR activity among different monometallic system in acidic medium. Several groups reported[10, 12] the HER exchange current density in acidic medium of Pt metal in RDE method is the order of 1 mAcm^{-2} which are two fold lower than the value obtained in H_2 pump methods. Palladium or palladium based[13-14] catalysts is reported to have much poorer HER/HOR performances in comparisons to pt-based catalysts. N. M. Markovic and his coworkers reported[15] 220 mV/dec anodic tafel slope of Pd_{ML}/Au catalyst. S. N. Pronkin and his co-workers reported[3] the HOR exchange current density of Pd/C with particle size 2.6 nm in 0.1 M $HClO_4$ medium was found to be 0.22 mAcm^{-2} which was two order magnitude lower than the measured exchange current of Pt/C by gas diffusion method. Furthermore, HOR properties of Pt metals gradually decrease with increasing the pH values. The reason behind of decreased activity and also rate controlled process for HOR in alkaline medium is not very clear. Recently, Durst et al. suggested[10] that noble metals form a stronger M-H bond in basic medium compare to acidic medium and HOR activity decreases in basic media is due to formation of strong M-H bond. Meanwhile, Markovic et al.[16] and Kopper et al.[17] separately reported a bi-functional mechanism for HOR in acidic and basic medium. The M-H bond strength in acid and M-OH bond strength (oxophilic effect) determine the HOR activity.

The size, structure, morphology, and nature of support materials of supported metal nanostructures generally determine the performances of these catalysts. The supported palladium nanoparticles exhibit superior catalytic activity for various reactions such as alcohol fuel cells[18] and organic reactions.[19] Zhang and co-workers[20] demonstrated the presence of $Pt^{\delta+}$ charged particles in Pt/FeO_x and the superior catalytic behavior of Pt/FeO_x toward CO oxidation. In the recent years, carbon materials, especially two dimensional graphene and commercial volcano carbon, have been used as support materials due to their high surface area and conductivity.

However, one of the major limitations of carbon-supported catalysts has been that low electrocatalytic stability arises due to the rapid depletion of carbon. Recently, Kangasniemi et al.[21] reported that the common carbon catalyst for electrocatalysis Vulcan X-72 was easily oxidized in a cathodic environment in a polymer electrolyte fuel cell (PEFC). Several sustainable attempts were devoted to improving tolerance and preventing oxidation of the supported materials under cathodic potentials. One of the constructive strategies was incorporation of a heteroatom, for example nitrogen, that coordinates different NPs easily and overcomes the durability problem. Various groups reported[22-23] that heteroatoms such as nitrogen-based ligands can easily coordinate metal nanoparticles and the metal–support interaction improves the tolerance as well as activity of the electrocatalysts under oxidation conditions. Graphitic carbon nitride, g-C_3N_4 (graphene-like structure), consisting of repetitive s-triazine units, has become a versatile support material of metal NPs due to the presence of a large number of active binding sites for their dispersion. g-C_3N_4 and its composite have attracted attention due to their intriguing potential applications for various fields such as photocatalysis,[24-25] energy conversion,[26-28] sensing,[29-30] organic transformations,[31] etc. Recently, Di Noto and co-workers reported[23, 32] a relationship among nitrogen concentration, structure, and electrochemical ORR performance of PdCoNi "core-shell" g-C_3N_4 electrocatalysts. When the concentration of N in the carbon nitride shell was low and the cell constant ofthe PdCoNi alloy NPs was the shortest, the best ORR activities were observed. Even today, finding a good support material and then developing a good electrocatalyst with superior catalytic activities and high durability remains a great challenge.

Herein we report a facile synthesis of porous Pd-CN_x composites and their applications in hydrogen evolution and hydrogen oxidation reactions (HER/HOR). The porous network structure of Pd-CN_x composite is formed due to reduction of $PdCl_2$ in the presence of CN_x nanosheets with $NaBH_4$ and ultrasound treatment. The porous Pd-CN_x composite shows superior catalytic activity toward the hydrogen evolution reaction in acidic media. It exhibited an onset overpotential at -12 mV and a current density of 10 mA cm^{-2} at a small HER overpotential of -55 mV and a Tafel slope of 35 mV dec^{-1} with excellent durability. The HER activity of porous Pd-CN_x composite in acid medium is comparable with that of commercial Pt/C; however, in basic media the HER activity of this catalyst is lower than that of Pt/C and is much better than that of commercial Pd/C. Most importantly, this Pd-CN_x composite displayed very high durability in strongly acidic media, much higher than that of commercial Pt/C. In addition, this catalyst also exhibits good HOR activity over a wide pH range, 0−14. The catalytic activity of the HOR in different buffer solutions is also discussed, and a correlation of the catalytic HER/HOR behavior of Pd-CN_x catalyst in solutions of different pH with the hydrogen binding energy (HBE) was done. Our results support the hypothesis that HBE is the sole reaction descriptor for HER/HOR activity on monometallic palladium. The superior HER/HOR activities and high durability of porous Pd-CN_x catalyst was explained on the basis of the porous structure of the catalysts, strong metal carbon (Pd−C) bonds, improved charge transport, and synergetic effects between CN_x support and Pd-NPs.

3.3 Experimental Section

Preparation of g-C_3N_4:

The synthesis of carbon nitride quantum dots (g-CNQDs) from formamide was done by a microwave-mediated method[51,52] reported by our group previously. In brief, 30 mL of formamide was heated using a microwave synthesizer for 2 h at 180 °C. The resulting brown solution was evaporated at 180 °C in a rotary evaporator to obtain a bulk amount of black product. This product was washed with water, filtered and vacuum-dried to give a dry solid of g-CNQDs.

Preparation of Porous Pd-CN$_x$ Composite:

Initially, 5 mg of g-CNQDs was dispersed in 2 mL of deionized water with sonication using a bath sonicator for 10 min, forming a black solution. In another beaker 0.14 mol of $PdCl_2$ was dissolved in 6 mL of deionized water by adding 50 μL of 10% HCl solution to form a brownish $PdCl_4^{2-}$ solution. Then, the $PdCl_4^{2-}$ solution was poured into the g-CNQDs dispersion and sonicated for 10 min. A 700 μL portion of 0.1 M $NaBH_4$ solution was directly added to the mixed solution with constant sonication. Finally, the resultant black reaction mixture was sonicated with a probe sonicator operating at 28 kHz frequency (power 420 W) for 180 min. The formation of a black solution indicated the formation of metallic Pd-NPs. After ultrasound treatment a black mass precipitated out from the solution. The black precipitate was separated by centrifugation at 10000 rpm for 30 min and washed with deionized water twice. Finally, this solid black product was kept under vacuum overnight for drying.

Preparation of Working Electrode:

A glassy-carbon (GC) electrode was polished with 1.0, 0.1, and 0.05 mm alumina slurry on a Buehler micro polishing cloth. An aqueous solution of the Pd-CN$_x$ composite was prepared by dispersing 0.5 mg of Pd-CN$_x$ in 1 mL of deionized Millipure water by sonication in a bath sonicator for 30 min. Pd-CN$_x$ modified GC was prepared by drop-casting 10 μL of the solution on a GC electrode of diameter 3 mm and drying at ambient temperature in air. No polymer binder was used for the preparation of the Pd-CN$_x$ electrode. However, Pt/C and Pd/C electrodes were prepared by immobilizing the catalyst on a GC electrode surface using Nafion as polymer binder. Details of Pt/C and Pd/C modified GC electrode preparations are given.

3.4 Results and Discussion

Characterization of Porous Pd-CN_x Composite:

The Pd-CN_x composite was synthesized by ultrasound-mediated reduction of $PdCl_4^{2-}$ with sodium borohydride ($NaBH_4$) in the presence of graphitic carbon nitride nanosheets. **Figure 3.1** shows the powder X-ray diffraction patterns (p-XRD) of porous Pd- CN_x composite and g-C_3N_4. The p-XRD pattern of g-C_3N_4 and Pd-CN_x composite has a diffraction peak at a 2θ value of 27.2° with interlayer spacing of 3.3 Å, corresponding to the graphitic reflection plane (002) of carbon nitride.[33] In addition, five well resolved, highly intense diffraction peaks positioned at 40.10, 46.70, 68.70, 80.90, and 86.70° in Pd-CN_x composite correspond to the (111), (200), (220), (311), and (222) reflection planes of face-centered cubic palladium (JCPDS No 89-4897).

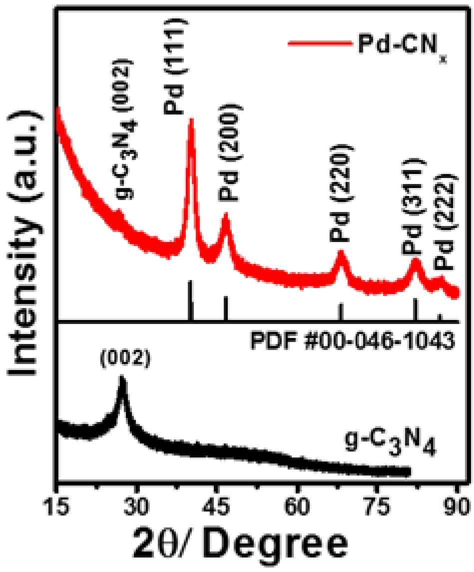

Figure 3.1. p-XRD pattern of Pd-CN_x composite and g-C_3N_4.

This suggests the formation of Pd-NPs on CN_x sheets by ultrasound-mediated borohydride reduction methods. In addition, the Bragg diffraction peak positioned at 2θ = 40.1° for the Pd (111) plane was used to calculate the particle size of Pd-NPs using the Debye−Scherer equation:

$$\mathbf{B(2\theta)} = \frac{K\lambda}{L\cos\theta}$$

Where L is the mean size of the ordered (crystalline) domains, K is a dimensionless shape factor, with a value close to unity. The shape factor has a typical value of about 0.9, but varies with the actual shape of the crystallite, λ is the X-ray wavelength (0.154 nm), B is the line broadening at half the maximum intensity (FWHM) in radians. So by determining the width of the (111) Bragg reflection of PdNPs at half maxima.

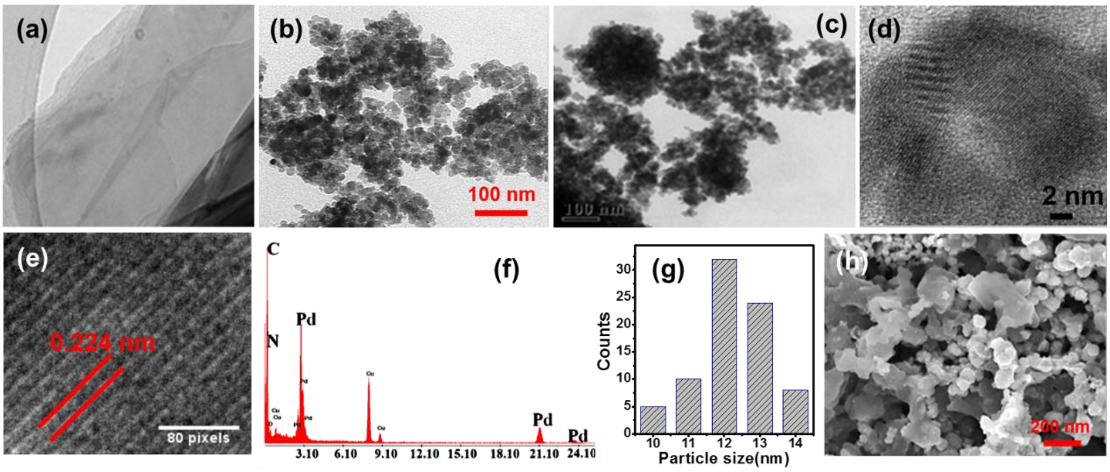

Figure 3.2. (a) TEM image of two dimensional g-C_3N_4 sheets. (b,c) TEM images and (d,e) HR-TEM images of Pd-CN_x composite. (f) EDS spectra, (g) particle size distribution plot and (h) FESEM image of porous Pd-CN_x composite.

From the Debye−Scherer analysis, the average size of Pd-NPs on the porous Pd-CN_x composite was found to be ~14 nm. TEM and FESEM measurements were done to investigate the morphology of Pd-CN_x catalyst and size distribution of Pd-NPs on carbon nitride. TEM and FESEM samples were prepared by evaporation of an aqueous solution of Pd-CN_x composite on a TEM grid and a Si wafer, respectively. It was reported[51] by our group recently that the two-dimensional thin sheets (**Figure 3.2.a**) of the g-CN_x are formed on evaporation-induced self-assembly and condensation of g-CNQDs. **Figure 3.2.**(**b,c**) gives representative TEM images of Pd-CN_x composite, showing the porous morphology of the composite. It clearly shows that the porous structure is formed through interconnection of small CN_x sheets containing Pd-NPs. The HR-TEM images of Pd-CN_x composite are shown in **Figure 3.2.(d,e)**. The lattice fringes with d spacing of 2.24 Å corresponding to the (111) lattice plane of Pd-NPs are clearly seen. The EDX spectrum of porous Pd-CN_x composite (**Figure 3.2.f**), taken from **Figure 3.2.b**, shows the presence of carbon (C), nitrogen (N), and Pd, confirming the deposition of Pd-NPs on carbon nitride sheets. The particle size of the Pd-CN_x catalyst was determined from **Figure 3.2.c** and Pd-NP size distribution in Pd-CN_x is shown in **Figure 3.2.g**. The particle size of Pd-NPs in porous Pd-CN_x composite are between 10 and 14 nm with an average size of 12 nm, which is good agreement with the particle size measured using the Debye−Scherer equation. The FE-SEM images of Pd-CN_x composite are shown in **Figure 3.2.h**. In the FESEM images of Pd-CN_x composite, the porous structures of the composite are also clearly visible. It also shows that nanoparticles are self-assembled on CN_x matrix and interconnected to form a porous morphology of this composite. The electronic state of the Pd-NPs and nature of interaction between CN_x support and Pd-NPs were investigated by using X-ray photoelectron spectroscopy (XPS) and Fourier transform infrared (FT-IR) spectroscopy. The XPS survey scan of porous Pd-CN_x composite, as shown in **Figure 3.3.a**, clearly indicates the presence of carbon (C), nitrogen (N), palladium (Pd), and oxygen (O) atoms. The 3d XPS of metallic palladium (Pd) always appeared as a doublet ($3d_{5/2}$ and $3d_{3/2}$) due to spin−orbital coupling that was separated by 5.26 eV. The $3d_{3/2}$ peaks for metallic palladium are known to appear at 335.6 eV[56], and electron-withdrawing groups are known to increase the binding energy of Pd-NPs. The 3d XPS of porous PdNPs supported on carbon nitride is shown in **Figure 3.3.b**. It shows that the Pd $3d_{5/2}$ and $3d_{3/2}$ peaks of Pd-CN_x composite appear at 338.92 and 344.3 eV, respectively, which can be attributed to metallic palladium with higher binding energy.

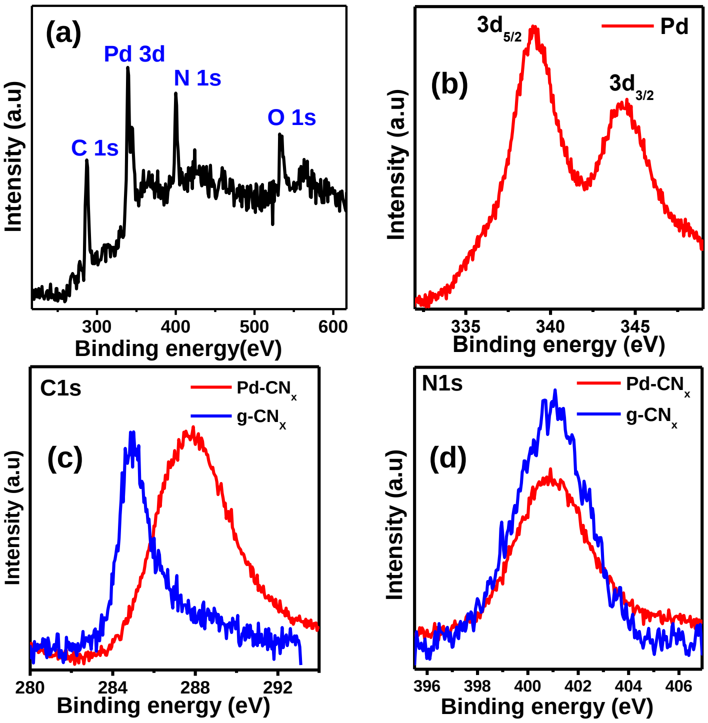

Figure 3.3. (a) XPS survey scan and (b) high resolution Pd 3d XPS spectra of porous Pd-CN_x composite. (c, d) Comparison of high resolution spectra of C 1s and N 1s XPS spectra of g-C_3N_4 and porous Pd-CN_x.

A comparison of the C1s XPS of the CN_x support and of Pd-CN_x composite is shown in **Figure 3.3.c**, whereas a comparison of their N 1s XPS is given in **Figure 3.3.d**. It shows that the C 1s peak of Pd-CN_x composite becomes broad and is shifted towards 2.9 eV higher binding energy in comparison to that of free CN_x; however, the position of the N 1s peak remains unaltered. This binding energy shift suggests a strong interaction between Pd-NPs and the CN_x support. As shown in **Figure 3.4.(a,b)**, the carbon (C 1s) and nitrogen (N 1s) XPS spectra of g-CN_x were deconvoluted to three and two main Gaussian peaks, respectively. The binding energies of 285.3 and 286.45 eV are due to the presence of $N(sp^2)–C=N(sp^2)$ (carbon bonded to two nitrogen atoms) and $C(–N)_3$ (planartrigonal carbon geometry), respectively,[34] whereas the peak at 288.8 eV is attributed to CO_x.[35] The peak at 400.1 eV refers to the presence of $C(sp^2)–N1=C(sp^2)$ nitrogen bonds to two carbon atoms, whereas the second peak in this region at 401.6eV corresponds to graphitic nitrogen.[36] In addition, large shifts of binding energy of carbon and no change in binding energy of nitrogen are also observed when Pd-NPs are supported on a CN_x framework.

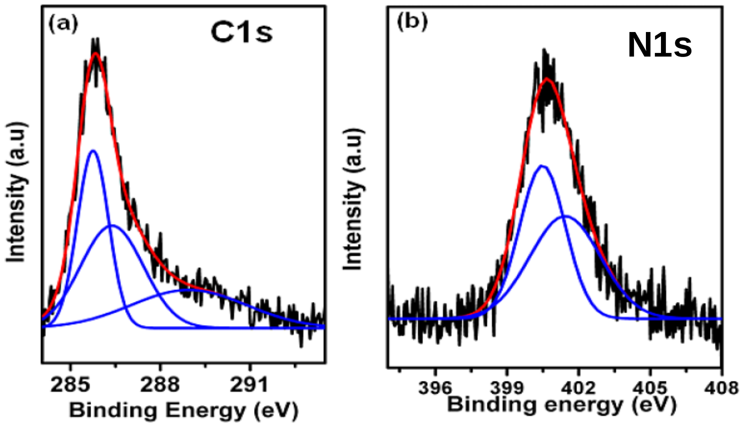

Figure 3.4. Deconvulated (a) C1s and (b) N1s XPS spectra of g-C_3N_4.

It has also been reported[37-38] that the binding energy of palladium is shifted to higher values on formation of a Pd−C bond. Thus, this higher binding energy of Pd in porous Pd-CN_x can be attributed to the formation of a Pd−C_x bond. The large binding energy changes of carbon and palladium confirm that there is a very strong interaction between carbon and Pd in the porous Pd-CN_x composite. The Fourier transform infrared (FT-IR) spectra of carbon nitride and Pd-CN_x composite are given in **Figure 3.5**.

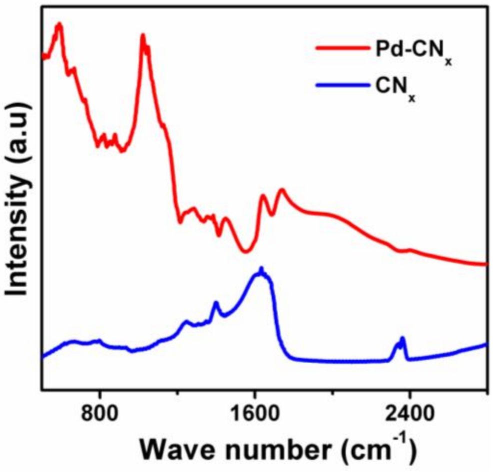

Figure 3.5. FT-IR spectra of porous Pd-CN_x composite and g-C_3N_4.

In the IR spectrum of CN_x, three bands appeared at 1213, 1317, and 1408 cm^{-1} that can be assigned to aromatic C=N stretches and a peak at 1600 cm^{-1} that corresponds to a C-N stretch. The intensity of these peaks decreases and two new intense peaks appear at 1128 and 1025 cm^{-1} when Pd-NPs are dispersed on a CN_x matrix. These two new peaks are assigned to C−N single-bond stretching. This appearance of a new C−N single-bond IR band and decrease in intensity of the C=N double-bond peak also suggests a strong interaction between the CN_x framework and Pd-NPs. The metal–carbon stretching bands for the complexes of Rh, Ir, Ga, and In are reported[39] to be appear between 500 and 580 cm^{-1}. The peak at 590 cm^{-1} can be assigned as a Pd−C stretch. It is known[40-41] that Pd has a strong affinity toward C atoms and Pd-NPs are generally attached to a graphene support due to their donation−back-donation interaction. The small electron donation from the 4d orbital of Pd to the 2s orbital of carbon occurs, and then back-donation from the 2p (C) orbital to the 5s (Pd) orbital takes place. In this work, nucleation/ growth of Pd occurs at carbon atoms due to the strong affinity of Pd-NPs for carbon. We recently reported[42] the bottom-up synthesis of g-carbon nitride sheets from g-carbon nitride quantum dots (g-CQDs) due to condensation of the g-CQDs and uniform growths in two dimensions. However, reduction of $PdCl_2$ in the aqueous g-CQD solution leads to the nucleation of Pd-NPs on carbon due to the strong chemical affinity of Pd toward carbon atoms.

Table 3.1. Different microanalyses for measured Pd metal loading in porous Pd-CN_x composite.

catalysed	Experiment	Pd loading on CN_x sheet of Pd-CN_x (wt.%)
Porous Pd-CN_x composite	EDX in FE-SEM	62.4
	TGA	60.0
	ICP-OES	59.8

The presence of Pd-NPs on CN_x prevents the uniform growth of carbon nitride nanosheets. Self-assembly and nonuniform growth of carbon nitride nanosheets containing Pd-NPs lead to formation of this porous structure of the Pd-CN_x composite. From p-XRD, TEM, FESEM, EDX, XPS, and FT-IR spectral studies it can be concluded that the porous morphology of the Pd-CN_x composite formed due to ultrasonication and $NaBH_4$ reduction of $PdCl_2$ in the presence of CN_x. The amount of loading of Pd-NPs was measured with the help of ICP-OES and thermogravimetric analysis (TGA). The ICP-OES analysis of Pd-CN_x determined a 59.4 wt % Pd loading in Pd-CN_x composite (**Table 3.1.).** The TGA plot of CN_x and Pd-CN_x composite is shown in **Figure 3.6**. The TGA curve of Pd-CN_x composite showed that the catalyst contained ~60 wt % of Pd, which is in good agreement with ICP-OES results. The Pd wt.% values in the Pd-CN_x catalyst calculated from different microanalyses are summarized in **Table 3.1**.

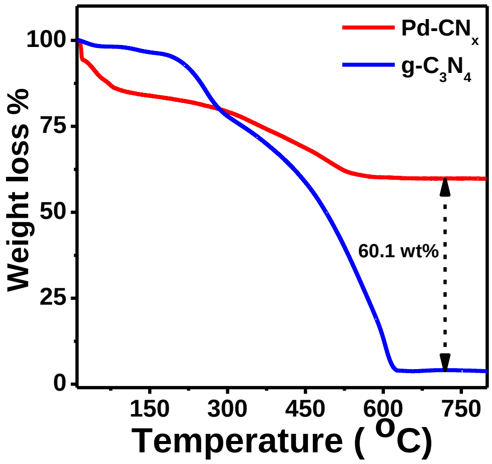

Figure 3.6. Comparative TGA curve of g-C_3N_4 and porous Pd-CN_x composite.

Thus, different microanalyses confirm the ~60 wt % Pd loading in porous Pd-CN_x composite. In addition, also CHN analysis and EDX was performed to determine the composition of supported g-CN_x. According to the CHN analysis the N/C ratio in free g-C_3N_4 was ~1.1,[42] whereas after Pd loading it decreased slightly to ~0.87 (**Table 3.2.**).

Table 3.2. Details of CHN analysis of g-C_3N_4 and porous Pd-CN_x composite.

Catalyst	Carbon(C) (wt.%)	Nitrogen (N) (wt.%)	Oxygen (O) (wt.%)	Hydrogen(H) (wt.%)	N/C ratio
g-C_3N_4	43.13	47.3	5.78	3.79	~1.09
Porous Pd-CN_x	9.75	8.69	-	3.18	~0.87

Proton Adsorption−Desorption Behavior of Pd-CN_x Composite:

Palladium metal is highly active for various electrochemical reactions occurring in galvanic cells, such as cathodic hydrogen evolution reactions, small organic molecule oxidation reactions, anodic hydrogen oxidation reactions, etc. The electrochemical process involving hydrogen has aroused interest among the scientific community, since the chemisorbed atomic H species acts as an intermediate for several HOR/HER reactions occurring at electrode surfaces. Unlike platinum, palladium metal has attracted much more interest toward adsorption of H under the same electrochemical conditions. The noble metal is reported to have two types of electrodeposited H intermediates during electrochemical reactions: (i) under potential deposition of hydrogen (UPD-H), which commenced at positive to reversible H^+/H_2 potentials, and (ii) overpotential deposition of hydrogen (OPD-H) which commences at potentials very close to reversible H^+/H_2 potentials or negative potentials to reversible H^+/H_2 potentials. Chemically there is no distinct difference between OPD-H and UPD-H, but in surface science UPD-H has received major attention due to its surface structure dependent properties. The UPD-H process can be represented as

$$M(hkl) + H_3O^+ e^- \leftrightarrow M(hkl)/H_\theta + H_2O$$

To understand the electrochemical behavior of the prepared porous Pd-CN_x composite, the CV studies were performed in both acidic and alkaline medium as shown in **Figure 3.7**. The CVs of porous Pd-CN_x, g-CN_x modified GC electrode and GC electrode in

0.5 M H_2SO_4 solution are shown in **Figure 3.7.a**. Pd-CN_x shows strong proton adsorption–desorption peaks, whereas GC and CN_x/GC do not have any proton adsorption–desorption peaks. A broad anodic peak at E ≈1.0 V corresponds to the formation of Pd–O and its corresponding cathodic peak at 0.68 V for the reduction of Pd–O. The symmetrical anodic and cathodic peaks at 0.16 and 0.23 V are assigned to UPD hydrogen adsorption (UPD-H_{ads}) and desorption (UPD-H_{des}) from Pd-CN_x surfaces, respectively. The calculated ΔE_p value for UPD-H of Pd-CN_x composite was ∼70 mV, which is close to the reversible value of 60 mV. Recently, Gasteiger and co-workers reported[13] that the ΔE_p value for reversible UPD-H on Pd/C surfaces was ∼100 mV, whereas that of Pt/C was 50 mV. Thus, porous Pd-CN_x composite was more reversible and the rate of H-UPD was much higher than those of Pd/C surfaces. The anodic peak at 0.09 V was assigned to oxidation of the Hads on the surface of Pd-CN_x composite. **Figure 3.7.b** shows a cathodic peak at ∼0.012 V assigned to the OPD-H absorption peak and its corresponding asymmetric desorption peak at ∼0.2 V. From **Figure 3.7.b**, it is evident that, when potentials reach a potential negative to reversible H^+/H_2 potentials, the anodic desorption peak appears as a broad and large peak overlaying other desorption properties such as UPD-H or anion desorption. The major issue is to separate UPD-H from the desorption peak of H_{ads}. The palladium bulk metal or polycrystalline Pd(poly)[43] are unable to separate UPD-H from other electrochemical behaviors. In the literature, very few reports[44] are available for Pd-based catalysts where UPD-H peaks are well separated from other behaviors. For example, for ultrafine NPs[45] or Pd layers on an Au surface[46] UPD-H can be separated from other behavior. The Pd-CN_x composite can also easily separate the UPD-H from other behavior that makes it a potential electrocatalyst. In addition, CV of Pd-CN_x in 0.5 M KOH was also performed and is shown in **Figure 3.7.c**. In alkaline medium also the catalyst can easily have a UPD-H peak separated from other processes. In the case of Pd-CN_x during the HER, it can form an equilibrium between adsorbed and dissolved H with the Pd lattice which leads to the formation of Pd-H_x.

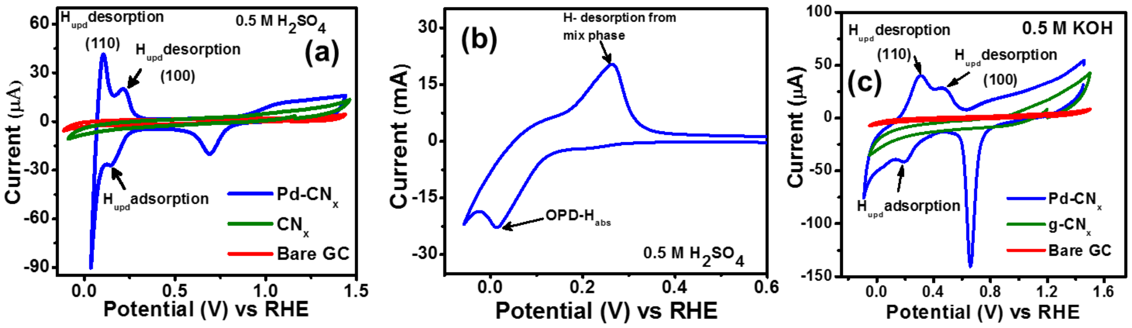

Figure 3.7. Cyclic Voltagrams of porous Pd-CN_x in comparison with GC and g-CN_x in (a) 0.5 M H_2SO_4, (c) 0.5 M KOH electrolyte. (b) CV of porous Pd-CN_x composite in 0.5 M H_2SO_4 electrolyte run from -0.08 V to +0.6 V. All the CV experiment was performed with 30 mV/sce scan rate with constant Pd loading 0.043 mg/cm^2.

Electrochemical behavior has been used to investigate the relation between the phase structure and applied potentials. Russell and co-workers[47] distinguished the potential regions for different Pd–H phase formations, where potentials at $E \geqslant 0.05$ V were due to β-hydride formation and potentials more negative than $E = 0.028$ V were identified as a hyperstoichiometric phase. The H absorption on Pd-CN_x composite commenced at the potential $E = 0.015$ V, which corresponds to formation of the hyperstoichiometric phase. The H/Pd ratio increases with increasingly negative potentials, indicating that the PdH_x stoichiometry was very high and may greater than 1. The H_{abs} absorption peak of Pd-CN_x, close to reversible potentials and lower than 0.028 V, can be considered as a hyperstoichiometric phase. Several groups reported[48] a hyper stoichiometric phase of PdH_x for Pd nanoparticles supported on zeolite or Na Y zeolite due to spillover of hydrogen on supported materials. The high stoichiometry of hydrogen for Pd-CN_x composite may be attributed to spillover of H on supported materials and also to the porous nature of the electrode easily trapping the H_2 molecule in its pores and re-oxidizing it repetitively.

HER Study on Porous Pd-CN_x Composite:

The electrocatalytic activities of Pd-CN_x/GC toward the HER were investigated in N_2-saturated 0.5 M H_2SO_4 by the linear sweep voltammetry (LSV) method, performed in a standard three electrode electrochemical cell with a scan rate of 10 mV/s. Representative LSV curves of geometric current density (mA cm^{-2}) vs applied potential for Pd-CN_x catalyst are shown in **Figure 3.8.a**. For comparison the catalytic activities of Pt/C, Pd/C, and g-CN_x modified GC electrode toward the HER were also investigated, as shown in **Figure 3.8.a**. The g-CN_x electrode was found to be very inactive toward HER, as it shows a very high onset potential (−170 mV) with a very low cathodic current density. The Pt/C catalyst exhibits a very good HER performance with an onset potential near 0 V. The porous Pd-CN_x modified GC electrode also exhibits excellent HER activity with a small onset potential of −12 mV, which is much smaller than that for Pd/C (−41 mV) and close to that of the commercial Pt/C. For practical purposes, it is more appropriate to compare the overpotentials (η) required to achieve a current density of 10 mA cm^{-2}, which is an important parameter for construction of a fuel cell. To acquire a current density of 10 mA cm^{-2}, commercial Pt/C and Pd/C take over potentials need −58 and−170 mV, respectively. The porous Pd-CN_x needs only −55 mV, which is much lower than that for Pd/C and comparable with that of Pt/C. In order to reach a current density of 50 mA cm^{-2} the porous Pd-CN_x needed only −77 mV, which is lower than those of both Pd/C (−315 mV) and Pt/C (−112 mV). This clearly demonstrates that the HER kinetics on Pt-CN_x is very fast, like that of Pt/C. The onset potential of Pd-CN_x was much lower than that of Pd/C and was close to that of Pt/C in acidic medium. The Tafel slope is an inherent property of the catalysts, and it is used as a significant standard for the HER to determine the exact mechanism as well as the rate-determining step.

The Tafel slope can be calculated from the Tafel equation

$$\eta = a + b \log J$$

where η = overpotential, b = Tafel slope, and J = current density.

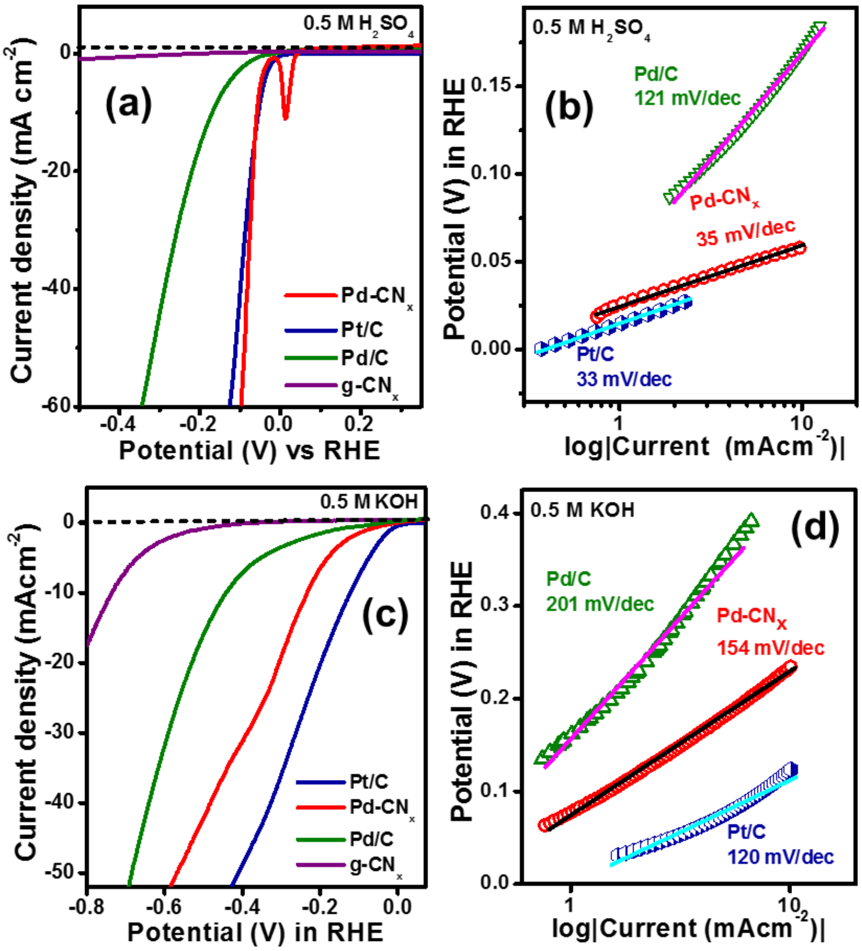

Figure 3.8. (a) HER LSV curves of Pd-CN$_x$, Pt/C, Pd/C, and g-CN$_x$ in 0.5 M H_2SO_4 with scan rate 10 mV/sec. (b) The corresponding HER Tafel plot of porous Pd-CN$_x$, Pt/C and Pd/C. (c) LSV curves of Pd-CN$_x$, Pt/C and Pd/C in 0.5 M KOH solution. (d) Tafel plot of porous Pd-CN$_x$, Pt/C and Pd/C in 0.5 M KOH. All the experiment was performed with constant metal loading of 0.043 mg/cm^2. All the LSV curves are iR corrected.

Tafel plots of Pd-CN$_x$, Pt/C, and Pd/C are represented in **Figure 3.8.b**. Commercial Pt/C catalyst shows high HER catalytic activity near 0 mV overpotential with a Tafel slope of 33 mV/dec, which is consistent with the previous literature value. In addition, the Pd-CN$_x$ catalyst also exhibits Tafel slope of 35mV/dec, which is lower than that of commercial Pd/C (121 mV/dec) and close to that of Pt/C. It is well-known that due to very high H_{ads} coverage on Pt surfaces, HER activity proceeds through the Volmer−Tafel mechanism. The low Tafel slope indicated that porous Pd-CN_x composite also follows the Volmer-Tafel mechanism. Another important kinetics parameter for electrocatalytic HER measurement is exchange current density (J_0), which correlates the rate of electron transfer under reversible conditions. Conventional ideal catalysts have low Tafel slopes and higher exchange current densities (J_0). The Pd-CN_x catalyst has an exchange current density of 0.4 mA cm^{-2}, which is better than that of the commercial Pd/C (0.12 mA cm^{-2}). The specific exchange currents of Pd-CN_x and Pd/C were 138 and 35 mA cm^{-2} mg^{-1}, respectively. The comparison of HER performances of Pd-CN_x with those of Pd/C are summarized in **Table 3.3**. From **Table 3.3**, it is obvious that Pd-CN_x exhibits catalytic activity higher than that of Pd/C and activity comparable with that of Pt/C toward the HER. A good HER catalyst should be capable of operating efficiently over a broad range of pH. To evaluate the versatility of Pd-CN_x catalyst, we also studied the HER activity of porous Pd-CN_x in basic 0.5 M KOH medium. **Figure 3.8.c** shows the LSV curve of porous Pd-CN_x and commercial Pt/C and Pd/C in N_2-saturated 0.5 M KOH with a scan rate of 10 mV/s. The Pt/C catalyst, as usual, exhibits the best catalytic activity with a very small onset potential, ∼0 V (RHE). Porous Pd-CN_x catalyst exhibits an onset potentials (η) of −75 mV (RHE), which is smaller than that of commercial Pd/C catalyst (−170 mV). To find the exact kinetics on the electrode surfaces, we also carried out a Tafel analysis of Pt/C, Pd/C, and porous Pd-CN_x composite, as shown in **Figure 3.8.d**. The Tafel slope values of commercial Pd/C and Pt/C are found to be 201 and 120 mV/dec, respectively, in KOH solution. In comparison, porous Pd-CN_x composite has a Tafel slope value of 154 mV/dec.

Table 3.3. Different HER parameters of porous Pd-CN_x composite, Pt/C and Pd/C catalyst in 0.5 M H_2SO_4.

Catalyst	**Onset potential (mV)**	**Overpotential at 10 mAcm^{-2} (η_{10})**	**Overpotential at50mA/cm^2 (η_{50})**	**Tafel slope (mV/dec) (b)**	**Exchange current mAcm^{-2} (i_o)**	**Specific exchange current (mAcm^{-2}mg^{-1})**
Porous Pd-CN_x	-12	- 55	-87	35	0.40	138
Pt/C	- 0	-57	-112	33	0.41	NA
Pd/C	-40	-170	-315	60	0.12	35

The exchange current density is calculated in a way similar to that described in the case of acidic medium. The exchange current densities of Pd/C and porous Pd-CN_x composite are found to be 0.190 and 0.245 mA cm^{-2}, respectively. Thus, porous Pd-CN_x electrocatalyst easily outperforms the Pd/C catalyst in basic medium on the basis of onset potentials, Tafel slope, and exchange current density. The degradation of the carbon support for commercial Pt/C catalyst occurs due to oxidation under strongly oxidizing acidic conditions, which has prevented the successful commercialization of PEM fuel cells. The durability of the catalyst is thus one of the most serious issues for a HER catalyst. The durability of porous Pd-CN_x catalyst was investigated by using continuous LSV scans in N_2 (**Figure 3.9.a**) saturated 0.5 M H_2SO_4 solutions with a potential window of 0.5 to −0.1 V at a scan speed of 10 mVs^{-1}. The HER performance such as onset potential and current density at any overpotential was improved after 10,000 cycles of LSV scans, suggesting the superior long-term stability of Pd-CN_x catalyst. A comparison of time-dependent current density curves under a static overpotential at −60 mV of Pd/CN_x with commercial Pt/C and Pd/C was also made, as shown in **Figure 3.9.b**. The commercial Pt/C and Pd/C show a significant loss of current density within 10 h of chronoamperometric measurements. In contrast, the current density of Pd-CN$_x$ catalyst shows a dramatic increase from 14 mA cm^{-2} (at 0 h) to 28 mA cm^{-2} (at 24 h), and it remains almost constant for at least 100 h (**Figure 3.9.c**). The enhanced electrocatalytic performance of Pd-CN$_x$ in chronoamperometric scans is probably due to cleaning of the pores of porous Pd-CN$_x$ composite, facilitating mass transport, and thus the current density of Pd-CN$_x$ composite is increased. It is important to mention that no polymer binder was used for the preparation of a Pd-CN$_x$ electrode. For the durability test, the Pt/C and Pd/C-modified GC electrodes were prepared by immobilization of these catalysts on electrode surfaces using a polymer binder, Nafion. Similar behavior was also observed when all three electrodes (Pd/C, Pt/C, Pd-CN$_x$) were prepared without any external polymer binder.

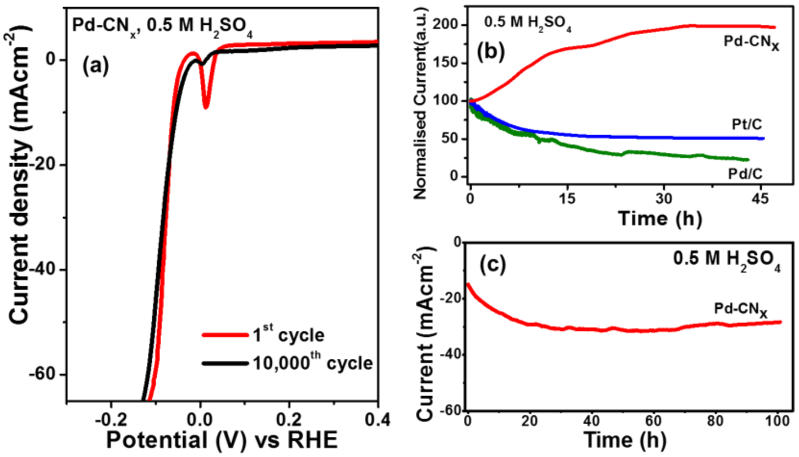

Figure 3.9. (a) First and 10,000th LSV curve of Pd-CN$_x$ at 50 mV/sec scan rate. (b) Chronoamperometry responses of Pd-CN$_x$, Pd/C and Pt/C at η = -60 mV in RHE for 48hrs. (c) Chronoampermetric response of Pd-CN$_x$ at at η = -60 mV in RHE for 100 hrs.

The superior HER activity and excellent durability of Pd-CN$_x$ composite in acidic medium suggest the promise of replacement of Pt/C catalyst with new polymer binder free Pd-CN$_x$ electrocatalyst in PME fuel cells. A comparison of catalyst mass loading, onset potential, exchange current density, and Tafel slope of Pd-CN$_x$ with those of other catalysts is given in **Table 3.4**. The mass loading of porous Pd-CN$_x$ catalyst is much lower than that of other previously reported catalysts.

Table 3.4. Comparisons of HER activities of different Pt and non Pt group metal catalysts in acidic medium.

Catalyst	**Catalyst loading**	**Onset potential (mV vs RHE)**	**Over potential (mV vs RHE)(current density (mA cm^{-2}))**	**Tafel slope (mV/dec)**	**Exchange current (mAcm^{-2})**	**Ref**
Ni-Mo-N nanosheet	0.25	-78	-200 (3.5 mA cm^{-2})	35.9	0.24	49
$CoSe_2$	0.37	-30	-90 (4.0 mA cm^{-2})	40	0.037	50
MoP	1.0	-50	-180 (10 mA cm^{-2})	54	0.034	51
MoC_x	0.8	-25	-142 (10 mA cm^{-2})	53	0.023	52
Pt-SiO_2	0.168	-0.225(SHE)	-500 (200 mA cm^{-2})	32	-	53
Pt-TiO_2	0.04	-	-300 (97 mA cm^{-2})	32	0.19	54
Ni_2P	-	-25	-130 (20 mA cm^{-2})	46	0.033	55
Pt-W_2C	2	-	-10 (16 mA cm^{-2})	103	2.08	56
Pt-SnO_2	0.13		-300 (40 mA cm^{-2})	111	0.46	57
Pt-TiO_2-N-rGO	0.04	-	-300 (126 mA cm^{-2})	32	0.22	54
Pt/C	0.042	-0	-112(50 mA cm^{-2})	33	0.41	This work
Pd/C	0.043	-45	-315 (50 mAcm^{-2})	60	0.12	This work
Porous Pd-CN_x	0.043	-12	-87 (50 mA cm^{-2})	35	0.4	This work

The onset potential of Pd-CN_x catalyst is −12 mV, which is much lower than that for catalysts based on other non-Pt-group metals such as Mo, Ni, W, and Co and is comparable with that of other Pt-based catalysts. In addition, in terms of exchange current density and Tafel slope the Pd-CN_x catalyst is better than any other non-noble-metal catalyst and is also comparable with other noble-metal catalyst systems. From **Table 3.4**, it is obvious that Pd-CN_x catalyst has better electrochemical hydrogen evolution activity (onset potential, durability, exchange current, catalyst loading) in comparison to that of Pt- and non-Pt-based catalysts in acid media.

HOR Study on Pd-CN_x Surfaces over a Broad pH Range. In PME fuel cells, the HOR is the one of the important reactions in the cathode compartment. In a completely reversible PME fuel cell, the HOR and HER occur simultaneously. The Pd-CN_x catalyst showed very good proton adsorption and superior HER activity in both acidic and basic medium; we also examined the HOR activity of this Pd-CN_x catalyst in solutions of different pH. **Figure 3.10.a** shows HOR polarization (positive direction) curves of Pd-CN_x catalyst in H_2-saturated 0.1 M H_2SO_4 solution at different rotation speeds.

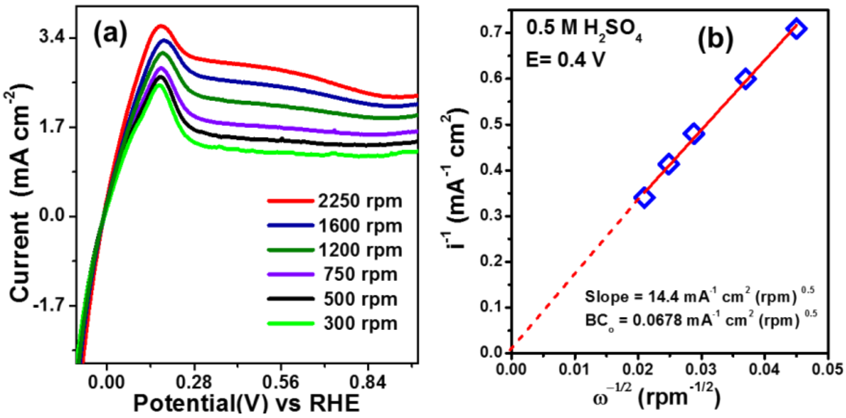

Figure 3.10. (a) HER/HOR polarization curve (positive going) on porous Pd-CN_x in 0.1 M H_2SO_4 solution saturated with H_2 (~1 atm) with different rotation speed ranging from 300 to 2250 rpm. (b) Koutech-levich plot at 0.4V in RHE.

All polarization curves represented here are iR corrected. The limiting current density (J_L) gradually increases with an increase in the rotation speed from 300 to 2250 rpm. The limiting current density (J_L) obtained in RDE measurements included two factors: (a) the kinetic current density (J_k) and (b) the diffusion current density (J_d). The diffusion limiting current was calculated using the equation

$$\frac{1}{J_L} = \frac{1}{J_k} + \frac{1}{J_d} = \frac{1}{J_k} + \frac{1}{BC_0\ \omega^{1/2}}$$

Where diffusion controlled current follow the Levich equation:

$$J_d = 0.62nFD^2/3v^{-1/6}C_0\ \omega^{1/2} = BC_0\ \omega^{1/2}$$

Where n is the number of electrons involved in the oxidation reaction, F is Faraday constant (96,498 C mol^{-1}), D is the diffusion coefficient of the reactant (cm^2 s^{-1}), ν is the viscosity of the electrolyte (cm^2 s^{-1}), C_0 is the H_2 concentration in the solution and ω is the rotation speed (rpm). BC_0 is a constant related to the concentration and diffusivity of the gas, number of the electron transfer in the reaction, kinetic velocity of the electrolyte.

The kinetics parameter of the HOR reaction was obtained by plotting J_L^{-1} vs $\omega^{-1/2}$ at particular potentials (Koutecky-Levich plot). The K-L plot of Pd-CN_x constructed at 0.4 V gives a straight line passing through the origin as shown in **Figure 3.10.b.** This result confirms that the limiting current at 0.4 V potentials was fully controlled by diffusion of H_2 mass. The BC_0 value of Pd-CN_x catalyst in 0.1 M H_2SO_4 was 0.066 mA/ (cm^2 (disk rpm)$^{0.5}$) which good agreement with the calculated value 0.0678 mA/ (cm^2 (disk rpm)$^{0.5}$).

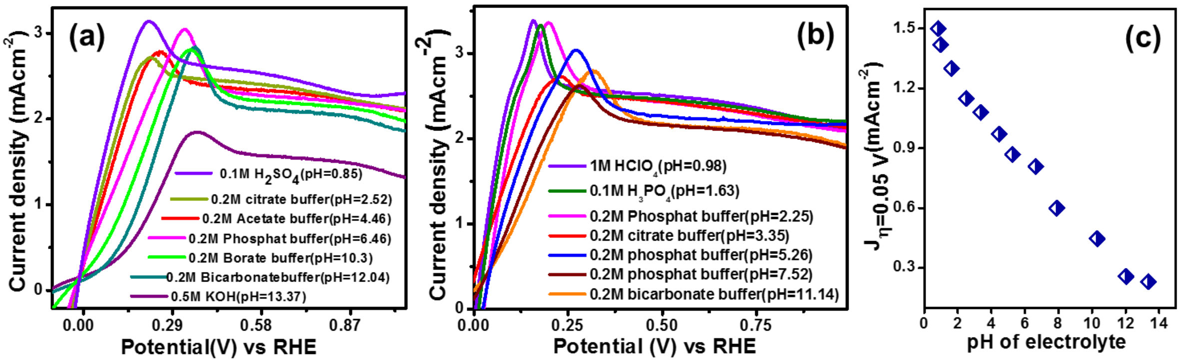

Figure 3.11. (a,b) HER/HOR polarization curve (positive going) on Pd-CN_x composite in H_2 saturated (1 atm) different selected pH electrolyte at scan rate 20 mV/sec with rotating speed 1600 rpm.(c) Comparison of current density at 0.05 V in RHE.

Therefore, the diffusion limiting current at 1600 rpm in 0.1 M H_2SO_4 was 2.54 mA/cm^2, which matches the experimentally measured limiting current density. **Figure 3.11.(a,b)** represents the polarization curve of HOR in H_2 saturated different selected pH medium with rotation speed 1600 rpm. The polarization curves in different pH solution have anodic peaks in the potential range 0.09V to 0.3V due to H desorption. The HOR/HER potentials were corrected by diffusion potentials limitation as describes by

$$\eta_{diff} = -\frac{RT}{2F}\ln(1-\frac{J}{J_L})$$

where J and J_L are measured and diffusion limited current densities respectively.

The diffusion-corrected and iR-corrected polarization curves are shown in **Figure 3.12. (a,b)**.

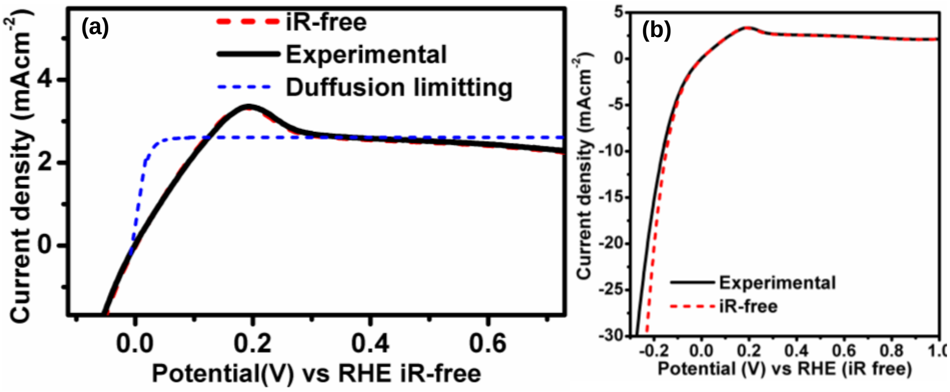

Figure 3.12. (a) Diffusion corrected potentials plot and (b) iR corrected potentials plots of Pd-CN_x composite in 0.5 M H_2SO_4 solution.

In 0.1 M H_2SO_4 solution the polarization curve of porous Pd-CN_x composite has a plateau region with limiting current density of 2.54 mA cm^{-2}, which was due to limiting H_2 mass transportation. The limiting plateau current density decreases gradually with increasing pH of the solution, and the limiting current density in strongly basic medium, 0.5 M KOH (pH 13.7), reaches 1.52 mA cm^{-2}, as shown in **Figure 3.13.(a,b)**. The H_2 mass transport gradually decreases with an increase in the pH of the solutions. Recently,Yan and co-workers demonstrated[70] the decrease of limiting current with the increase in pH of the solution for polycrystalline Pt metal.

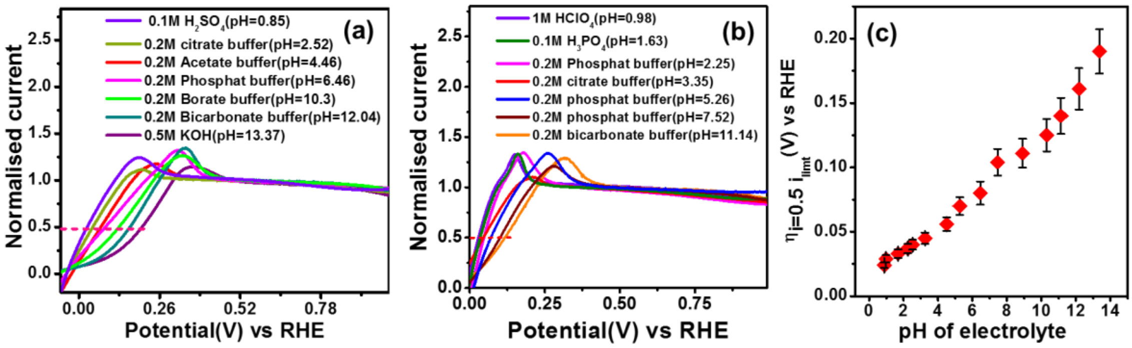

Figure 3.13. (a,b) HOR/HER polarization curve normalized to the corresponding maximum limiting current (i_{lim}) in different selected pH electrolyte. (c) Variation of half wave potentials in whole range of pH. Pd loading: 0.043 mg/cm^2.

Furthermore, we have measured the current density at 0.05 V in different pH solution and it is shown in **Figure 3.13.c.** The current density at 0.05 V gradually decreases with increasing the pH of the electrolyte. This results reveals that HOR activity decreases with increasing pH of the electrolyte. The polarization curves normalized by their corresponding maximum limiting current (J_L) in solutions at different pHs are shown in **Figure 3.13.(a,b)**. The overpotential where the current density is half of the normalized limiting current density ($\eta_i = 0.5i_{lim}$) is described as the half-wave potential. With increasing pH, the half-wave potentials gradually shifted toward positive potentials, from 0.02 V at pH 0.8 to 0.19 V at 13.7 pH. The half-wave potentials of the HOR were shifted by 0.18 V toward the positive side as the solution pH was changed from 0.8 (0.1 M H_2SO_4) to 13.7 (0.1 M KOH). A plot of the half-wave potential vs the pH of the solution is shown in **Figure 3.13.c**. It is observed that the half-wave potential increases slowly when the pH <6. This suggests the fast HOR kinetics on Pd-CN_x composite is controlled by H_2 mass transport. When pH >6, half-wave potentials increase more rapidly, suggesting a continuous decrease of the HOR activity. The kinetic parameters such as transfer coefficient (α), Tafel slope and exchange current density of the HOR/HER was obtained from a plot of kinetic current vs overpotential by fitting the Butler−Volmer equation.

$$J_k = i_0 \left[e^{[\frac{\alpha F}{RT}]\eta} - e^{-[\frac{(\alpha-1)F}{RT}]\eta} \right]$$

where J_k is the kinetics current density (mA cm^{-2}), i_0 is the exchange current density (mA cm^{-2}), α represents the transfer coefficient, F is the Faraday constant (96,485 C/mol), R is the universal gas constant (8.314 J/(mol K)), and T is the temperature in Kelvin.

The kinetics current density was extracted from the positive direction polarization curve by using the first-order Koutecky−Levich correction

$$j_k = j(j_{lim}/(j_{lim} - j))$$

where j_k is the kinetics current density (mA cm^{-2}), j is the measured current density (mA cm^{-2}) at 1600 rpm, and jlim is the diffusion limiting current. **Figure 3.14(a,b)** show the kinetic current vs potential plots of porous Pd-CN$_x$ (square symbols) and corresponding Butler−Volmer fits (dotted line) in 0.1 M H_2SO_4 solution and 0.1 M KOH medium, respectively.

The HER/HOR kinetic current data were fitted by considering first α_a, α_c, and i_0 as variable parameters. In acidic medium the fitting was performed over a short-range (−40 to +40 mV region) by considering the sum of the transfer coefficients equals 1. The fitted (red dashed line) curve matched the experimental curve well with asymmetric values of $\alpha_c = 0.62$ and $\alpha_a = 0.38$. The exchange current density calculated from the Butler−Volmer equation in acid medium is 0.84 mV. The reported exchange currents of Pd-based catalyst measured in acidic medium by RDE methods ranged from 0.2 mA to 0.8 mA.

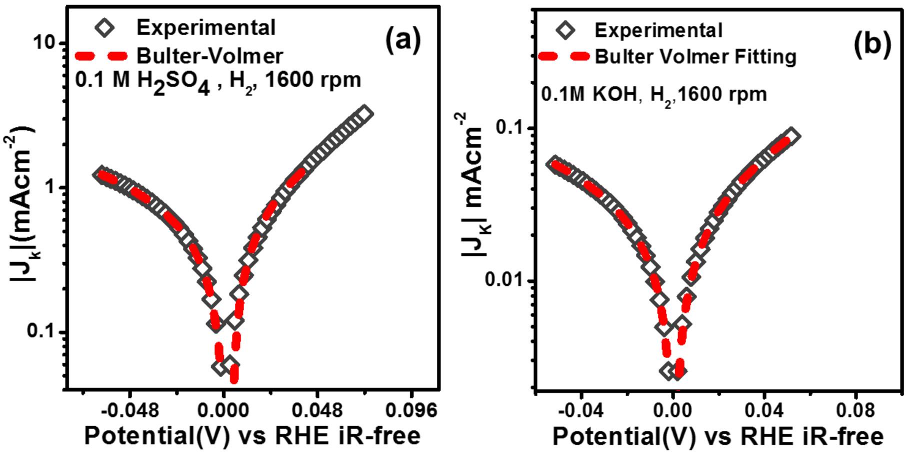

Figure 3.14. Kinetics current vs potential plots of Porous Pd-CN$_x$ (square symbol) and corresponding Butler-Volmer fitting (dotted line) in (a) 0.1 M H_2SO_4 solution and (b) 0.1M KOH medium.

Recently, Pronkin et al. recently reported[20] the exchange current of Pd/C in acidic medium with RDE method was 0.22 mA/cm^2, which was 4 times less than our result.Thus, the HOR activity of Pd-CN$_x$ composite in acidic medium was better than that of the reported Pd-based catalyst. In addition, a Butler−Volmer fit of the kinetic current vs potential plot in basic medium (0.5 M KOH) is shown in **Figure 3.14.b**. The best fit was obtained with the transfer coefficients α_a = 0.50 and α_c = 0.53. The exchange current density (i0) in basic medium was 0.037 mA cm^{-2}. The kinetic parameter Tafel slope value was calculated by

$$2.303RT/\alpha F$$

The specific exchange current density of Pd-CN$_x$ was 280 and 14 mA cm^{-2} mg^{-1} in acidic and basic medium, respectively. The Tafel slope values of the cathodic and anodic branches of the HOR/HER are summarized in **Table 3.5**. Norskov and coworkers reported,[71] on the basis of their DFT calculations, α values for Tafel and Heyrovsky steps should be 0.64 and 0.45, respectively.

Table 3.5. Butler-Volmer fitting parameters of Pd-CN_x both acidic and basic medium.

Catalyst	Electrolyte solution	Exchange current density (i_0) (mAcm^{-2})	Specific exchange current (mAcm^{-2}mg^{-1})	Anodic transfer coefficient (α)	Anodic Tafel slope(b_a) (mV/dec)	Cathodic transfer coefficient (α)
Porous Pd-CN_x	0.1M H_2SO_4	0.84	280	0.62	96	0.38
	0.1M KOH	0.037	14	0.53	112	0.5

Pd-CN_x catalyst in acidic medium shows the best fit of the cathodic branch with α = 0.61, which is close to the calculated α value for the Tafel step.[71] This confirms that the HER on Pd-CN_x catalyst in acidic medium follows the Volmer−Tafel mechanism which is good agreement with the proposed mechanism based on Tafel slope described in the previous section.

Correlating HBE of Pd-CN_x Composite with UPD-H_{des} Peak in Different Buffer Solutions:

Recently Auinger and co-workers suggested[58] that the HOR/HER response in unbuffered solution remains unchanged on changing the pH of the solution due to the local pH gradient. On the other hand, T.M. Koper and co-workers reported[59] a change in the HOR/HER on polycrystalline Pt surfaces in phosphate buffer solutions over wide range of pH. Unlike unbuffered solutions, where the kinetics are not affected by pH, the HER/HOR kinetics in buffer solution is fully controlled by the pH gradient of the solution. To understand the reason behind the pH-dependent HER/HOR properties of porous Pd-CN_x composite, we have examined the surface properties of Pd-CN_x composite, especially the hydrogen binding energy (HBE) value. Several groups suggested[1] that the UPD-H desorption peak is not influenced by the pre adsorbed species and its position in CV is easily correlated with the HBE of the corresponding active site.

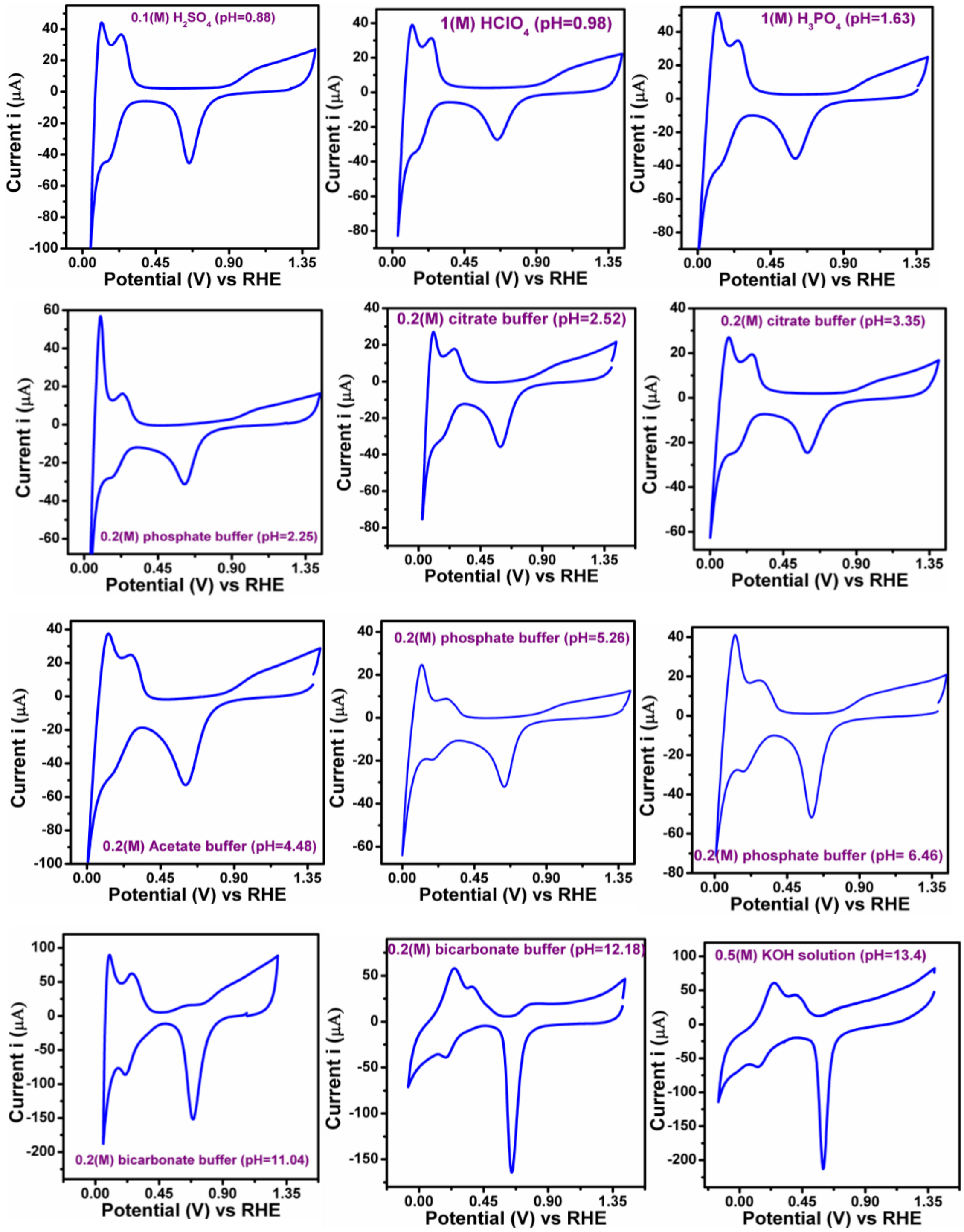

Figure 3.15. CVs of Pd-CN_x composite in N_2 saturated different electrolyte solution at 30 mV/sec scan rate.

By considering the Langmuir adsorption assumption, one can easily derive the relation between the peak potential of UPDH$_{\mathrm{des}}$ in CV with the HBE of the corresponding active site from the equation

$$\Delta G(\mathrm{M{-}H}) = -FE_{\mathrm{peak}}$$

where ΔG = hydrogen binding energy, F = Faraday constant (96,485 C/mol), and E_{peak} is directly taken from the CVs.

In order to calculate the HBE of Pd-CN$_x$ composite, we have examined the CV profile on Pd-CN$_x$ composite in different buffer media under the same electrochemical conditions as shown in **Figure 3.15**. The CV profiles of Pd-CN$_x$ composite in selected buffer solutions are shown in **Figure 3.16.a**. In the CV profile a cathodic peak below the potential 0.6 V in RHE is considered the UPD-H region of the Pd-CN$_x$ composite.

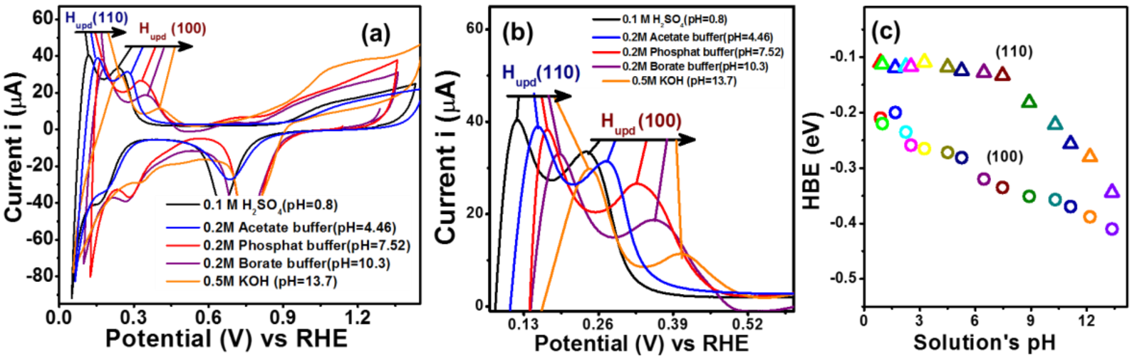

Figure 3.16. (a) CVs of Pd-CN$_x$ composite in N_2 saturated selected pH solution with scan rate 30mV/sec. (b) Proton desorption and UPD-H$_{\mathrm{des}}$ region in cathodic portion of CVs which indicating shifting of desorption peak potential towards higher value with pH of electrolyte. (c) Plot of HBE vs pH of the electrolyte. All the experiment was performed with constant Pd loading on electrode surface of 0.043 mg/cm^2.

The UPD region of Pd-CN$_x$ composite has two desorption peaks. The desorption peak at lower potential (weakly bonded H) corresponds to H desorption and the desorption peak at relatively higher potentials (strongly bonded H) corresponds to the UPD-H$_{\mathrm{des}}$. Both the UPD-H and H desorption peaks shift on changing the pH of the buffer solution. **Figure 3.16.b** represents the anodic plot of CV in the UPD-H region. From **Figure 3.16.b** it is clear that the peak position gradually shifts to positive potentials with an increase in the pH of the electrolyte. **Figure 3.16.c** shows the HBE calculated from the UPD-H peak potential vs pH. It clearly shows that gradually HBE increases with an increase in the solution pH. The binding energy linearly changes with the pH with a slope of −16 meV. In addition, we also studied the anion effect on the HBE in 0.1 M KOH solution. **Figure 3.17.(a,b)** shows that there is no significant change in position of the UPD-H peak on addition of 0.1 M $KClO_4$ and 0.1 M Na_2SO_4 separately in 0.1 M KOH solution. This behavior suggests that the HBE of Pd-CN_x surface was not affected by anion adsorption. Recently, Markovic and co-workers suggested[16] that the HER/HOR kinetics changes on replacing an acidic electrolyte with a basic electrolyte and also OH_{ads} acts as an intermediate in the HOR reaction. The M−OH_{ads} bond energy is responsible for the change in HOR activity.

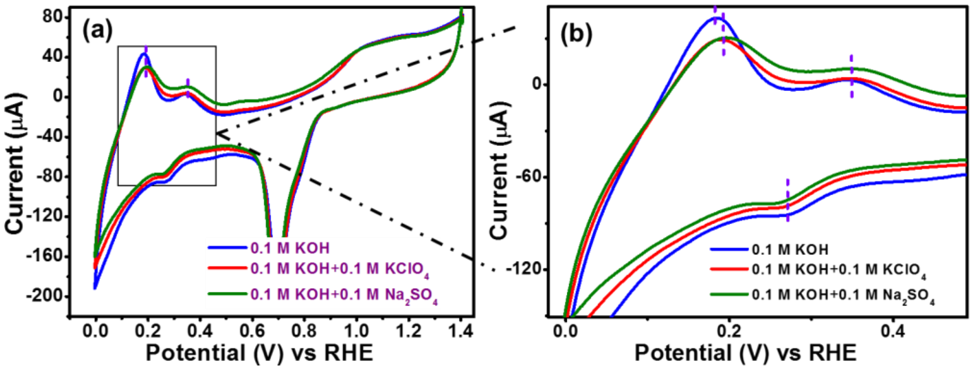

Figure 3.17. Anion effect of HOR on Pd-CN_x surface in 0.1 M KOH solution. (a) CVs of Pd-CN_x composite in 0.1 M KOH solution and with 0.1 M $KClO_4$ or 0.1 M Na_2SO_4 at sweep rate 30 mV/sec. (b) UPD-H region of CVs.

In contrast, Stimming and co-workers reported[60] that the intermediate, H_{ads}, and metal (M−H) bond length controlled the reaction kinetics for the Pt electrode. Durst et al.[10] and Yan et al.[61] hypothesized that the HOR/HER properties on noble metals (Pt, Ir) in solutions of different pHs were controlled by the HBE of the surface. On the basis of the steady-state CV profile of Pd-CN_x catalyst and recent literature reports, it can be concluded that the HER/HOR kinetics in different electrolyte solutions is totally controlled by the pH of the electrolyte and that the HBE is sole descriptor for the HOR/HER on monometallic palladium metal.

Effect of Support and Morphology of Pd-CN$_x$ in HER/ HOR:

The electrochemical performance of porous Pd-CN$_x$ composite toward the HOR/HER in acidic media is better than that of commercial Pt/C catalysts; in basic media its HOR/HER activity is slightly poorer than that of Pt/C but better than that of commercial Pd/C. These superior activities of porous Pd-CN$_x$ are probably due to the combined effects of several factors.

(i) The strong chemical interaction between Pd-NPs and g-CN$_x$ may lead to selective growth of Pd-NPs and CN$_x$ sheets. The large exposed accessible edges of the composite may act as active sites for HER/HOR. The intimate contact between Pd-NPs and g-CN$_x$ support provides good mechanical adhesion and electrical connections that may facilitate a good electron transport between CN$_x$ and Pd-NPs during cathodic polarization. The strong support−catalyst interactions in Pd-CN$_x$ composite were confirmed by XPS and FT-IR studies. In the XPS measurements, a very large carbon 1s binding energy shift of ~2.9 eV and a large BE shift of ~3.3 eV for Pd metal were observed. These large BE shifts for C and Pd confirm that there is strong interaction between Pd-NPs and CN$_x$ leading to formation of strong organometallic (metal−carbon) bond formation. The presence of a Pd−C bond was also confirmed by FT-IR studies. Thus, good electron transfers between Pd-NPs and CN$_x$ sheets occur during the HER/HOR process due to the strong organometallic Pd−C$_x$ bonds in Pd-CN$_x$ composite. In a PEM fuel cell, Pt/C catalysts are normally used in both the anode and cathode compartments. The main drawback for the Pt/C catalyst is the degradation of the catalysts due to oxidation of the support in the strongly oxidizing environment of the cathode. However, this Pd-CN_x composite displayed superior durability in strong acidic media. This is probably due to strong metal–carbon bonds, which may prevent oxidation of the support and force NPs to remain bonded with the CN_x support. Thus, g-CN_x can be an alternative support for metal nanoparticles for electrochemical applications.

(ii) The porous structure of Pd-CN_x composite allows efficient mass transport through the catalyst. The reactant can easily reach active sites such as defects, edges, etc. and the product can easily come out from the active sites through the pores. This may also be helpful in enhancing HER/HOR catalytic activities. Recently morphology-dependent electrocatalytic activities toward hydrogen evolution were reported by several groups.[62-63] The adhesion of evolved gas on a flat electrode surface is a great problem because adhesion of gas bubbles blocks electrolyte diffusion, leading to ohmic drop and a decrease in performance of the catalyst. A nanostructured MoS_2 film was reported to have much higher HER activities (overpotential, stability) in comparison to those of flat MoS_2 film due to the low gas adhesion force of the nanostructured MoS_2 electrode.[62] The superior hydrogen evolution at microand nanostructured CoS_2 in comparison to that of flat CoS_2 film was also reported[63] due to enhanced release of evolved gas from the electrode surface. On the basis of previous results and this work we may conclude that the highly porous morphology of Pd-CN_x catalyst may enhance mass transport to catalytic sites and could significantly contribute to HER activity.

(iii) The change in Fermi energy level of palladium nanoparticles may take place due to electron transfer between the support and NPs resulting from the difference in chemical potential of the support and metal nanoparticles. It is reported[64] that the enhanced activity of gold nanoparticles on metal oxide surfaces is due to the extra negative charge on the periphery of gold due to strong interaction between gold and the support.

The extra positive charge in Pt-FeO_x, resulting from electron transfer, and strong metal−support interactions are responsible for superior catalytic activity toward CO reduction.[20]

(iv) The presence of pyridinic and graphitic N atom concentrations in Pd-CN_x composite improves the charge transfer kinetics due to the interaction of protons with N atoms. Kim and co-workers suggested[65] that presence of the N species improved the electrocatalytic activity of cobalt-doped g-C_3N_4 and also showed that among the different types of N functional groups graphitic and pyridinic N is known to play a more significant role in the improvement of electrocatalytic affects due to superior charge transfer. Juan and co-workers reported[40] that Pd atoms have strong affinity toward C−C bonds and prefer to absorb C−C bond sites in comparison to any other sites of graphene. Their DFT studies showed that the C−C bonds near Pd absorption sites became weak due to the formation of Pd−C bonds. When hydrogen adsorption occurred, new Pd−H bonds were formed at the expense of weakening of Pd−C and C−C bonds. It was also shown that the Pd−C bonds remain intact even after hydrogen adsorption and Pd-NPs act as a bypass for hydrogen transfer to carbon supports. This spillover effect could be one of the reasons for the superior HER performance on Pd-CN_x composite. The spillover effect of hydrogen is the chemisorption and dissociation of hydrogen molecules into atomic hydrogen and their subsequent migration onto the support through surface diffusion. The hydrogen molecules or adsorbed H atoms during cathodic polarization spill over from the Pd particles and diffuse into the CN_x surface. The spillover effect is increased due to the presence of large of pyrrolic/pyridinic N atoms in these composites owing to the formation of N−H bonds. Thereby, large amounts of hydrogen can be stored on the CNx surface, from which it is subsequently released.

(v) For electrochemical measurements, in general polymer binders such as Nafion and PTFE are used to immobilize the catalysts on electrode surfaces. The effective activity of the catalysts is reduced due to use of polymer binder, since this polymer binder may block active sites of the catalysts as well as reduce diffusion[66-67] and also increase the series resistance.[67] For the electrochemical performance of the Pd-CN_x catalyst, no external binder is used for immobilization of the catalyst on electrode surfaces. Thus, better catalytic activities and durability of this catalyst in comparison to commercial Pt/C or Pd/C is expected. Thus, on the basis of various reports and our results it may be concluded that the superior and stable electrocatalytic activity of Pd-CN_x composite toward the HER/HOR can be explained on the basis of synergistic effects between Pd-NPs and g-CN_x support resulting from the strong organometallic metal–carbon bond.

Electrochemical Impedance Spectroscopic (EIS) Study:

Electrochemical impedance spectroscopy (EIS) is a widely used technique to characterize the HER kinetics and to find the actual interfacial process occurring at solid–solution interfaces in the HER/HOR process.

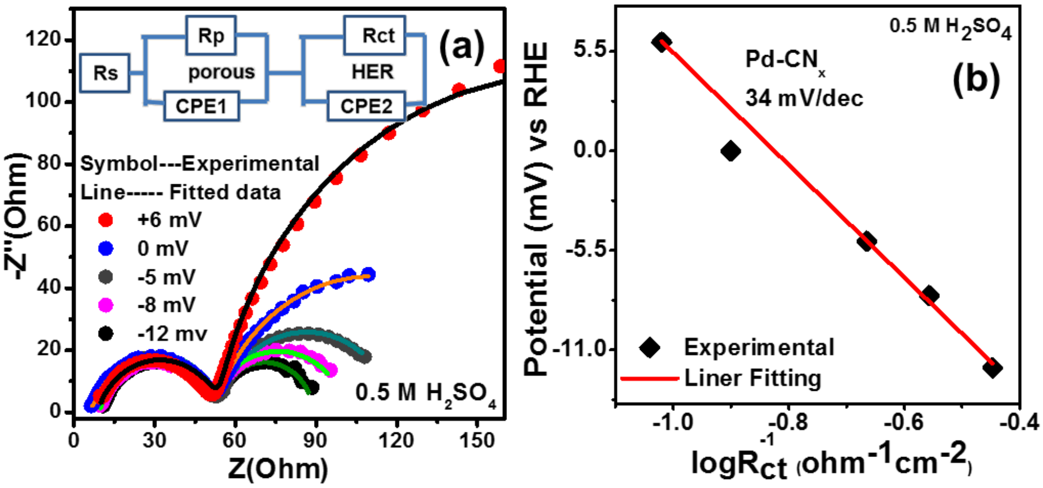

Figure 3.18. (a) EIS spectra of Pd-CN_x composite at different overpotential (from +6 mV to -12 mV). (b) Tafel plot from EIS spectra of Pd-CN_x composite in 0.5 M H_2SO_4. All the experiments were performed in 0.5 M H_2SO_4 solution with constant Pd loading to 0.043 mg/cm^2.

Figure 3.18.a shows the Nyquist plot of the EIS response of porous Pd-CN$_x$ composite at different overpotentials in 0.5 M H_2SO_4 solution. However, the Nyquist plot of Pd-CN$_x$ consists of two quasi-semicircles, indicating the porous nature of the electrode.[80] This confirms that, when Pd-NPs are incorporated on CN$_x$ sheets, a porous network structure of the Pd-CN$_x$ composite is formed. The FE-SEM and TEM images also suggested the porous morphology of this composite. The experimental data of impedance spectra have been fitted with an electrical equivalent circuit as shown in the insets of **Figure 3.18.a**. In the equivalent circuit diagram, R_s is the series resistance, R_p is the polarization resistance related to the porosity of the surface, CPE_1 and CPE_2 are the two constant phase element (CPEs), and R_{ct} denotes the overpotential dependence charge transfer coefficient. The fitting parameters of Pd-CN$_x$ at different overpotentials are summarized in **Table 3.6**.

Table 3.6. Fitting parameters of impedance spectra of Pd-CN$_x$ composite at different over potential.

Potential(η) / **Parameters**	**η=+6 mV**	**η=0 mV**	**η= −5 mV**	**η= −8 mV**	**η= −12 mV**
R_s (Ω)	11.4	15.34	13.7	15.4	11.4
R_{ct} (Ω)	40.1	41.9	44.0	41.3	43.1
CPE1(μmho)	47.2	52.3	60.3	69.0	90.6
R_p (Ω)	175.0	116.0	66.1	51.0	34.1
CPE2 (mmho)	12.3	10.0	13.12	16.30	20.5
N	0.83857	0.8229	0.84104	0.83024	0.86576

Table 3.7 Shows that R_{ct} of Pd-CN$_x$ composite gradually decreases from 175 Ω at +6 mV to 34.4 Ω at −12 mV with increasing overpotential. **Figure 3.19** shows the EIS of g-CN$_x$ and inset shows the circuit for fitting.

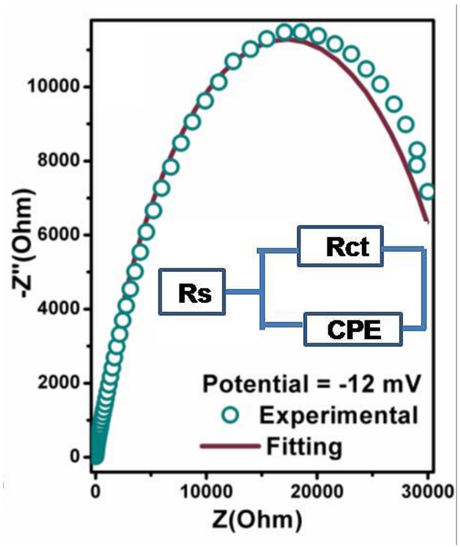

Figure 3.19. EIS spectra of g-CN_x at -12 mV overpotential.

Table 3.7 further gives a comparison of impedance parameters of Pd-CN_x and g-CN_x at −12 mV overpotentials. The R_{ct} value of g-CN_x at −12 mV was found to be 34400 Ω, and it significantly decreases to 34.1 Ω got Pd-NPs dispersed in a CN_x matrix.

Table 3.7. Fitting parameters of EIS for g-C_3N_4 and Pd-CN_x at over potential (η)= -0.12V.

Catalyst / Parameter	Pd-CN_x	g-C_3N_4
R_s (Ω)	11.4	10.07
R_{ct} (Ω)	43.1	34400
CPE1(μmho)	90.6	10.4
R_p (Ω)	34.1	-
CPE2 (mmho)	20.5	-
N	0.86576	0.73863

This implies that the HER kinetics at the Pd-CN_x composite increases due to superior electron conduction through a porous network resulting from strong chemical interaction between Pd-NPs and CNx matrix in Pd-CN_x composite. In addition, the plot of log R_{ct-1} vs the overpotential of Pd-CN_x composite (**Figure 3.18.b**) gives rise to a Tafel slope of 34 mV/dec, confirming the Tafel−Volmer mechanism of the HER. Thus, the reaction mechanism of the HER was further verified by EIS spectroscopy.

3.5 Conclusions

In summary, we have demonstrated an ultrasound-mediated facile method for the synthesis of porous Pd-CN_x composite. The superior HER catalytic behavior of Pd-CN_x in both acid and alkaline medium was demonstrated. The HER activity of porous Pd-CN_x catalyst is superior to that of commercial Pt/C catalyst in acid media, whereas its activity is lower than that of Pt/C in basic media but better than that of reported Pd metal based electrocatalysts. Most importantly, the durability of the Pd-CN_x catalyst is much higher than that of commercial Pt/C or Pd/C in acid media and the current density at any overpotential remains unchanged for at least 100 h. In addition, hydrogen oxidation reactions at different pHs (0−14) were studied using rotating disk electrode (RDE) methods. The HER/HOR activity for solutions at different pHs was also successfully correlated with the hydrogen binding energy (HBE) of Pd-CNx composite, and HBE was found to be the sole descriptor for the HER/HOR. The porous morphology of the catalyst, strong chemical bonding between palladium and CN_x (Pd−C bond), improved charge transfer, and synergetic effects between the CN_x support and Pd-NPs are responsible for the outstanding HER/HOR catalytic activities and excellent durability at the porous Pd-CN_x composite. The excellent HER/HOR activity of porous Pd-CN_x catalyst with excellent durability and low catalyst loading makes them promising polymer binder free electrocatalysts for fuel cell (PEMFC) and water splitting or other electrochemical devices.

3.6 References

1. Zheng, J.; Zhuang, Z.; Xu, B.; Yan, Y., *ACS Catal.* **2015,** *5,* 4449-4455.

2. Ohyama, J.; Sato, T.; Yamamoto, Y.; Arai, S.; Satsuma, A., *J. Am. Chem. Soc.* **2013,** *135,* 8016-8021.

3. Pronkin, S. N.; Bonnefont, A.; Ruvinskiy, P. S.; Savinova, E. R., *Electrochim. Acta* **2010,** *55,* 3312-3323.

4. Greeley, J.; Nørskov, J. K.; Kibler, L. A.; El-Aziz, A. M.; Kolb, D. M., *ChemPhysChem* **2006,** *7,* 1032-1035.

5. Simonov, A.; Pyrjaev, P.; Moroz, B.; Bukhtiyarov, V.; Parmon, V., *Electrocatalysis* **2012,** *3,* 119-131.

6. Pluntke, Y.; Kibler, L., *Electrocatalysis* **2011,** *2,* 192-199.

7. Park, H.-Y.; Park, I.-S.; Choi, B.; Lee, K.-S.; Jeon, T.-Y.; Sung, Y.-E.; Yoo, S. J., *Phys. Chem. Chem. Phys.* **2013,** *15,* 2125-2130.

8. Han, S.; Youn, D. H.; Lee, M. H.; Lee, J. S., *ChemCatChem* **2015,** *7,* 1483-1489.

9. Markovic, N. M., *Nat. Mater.* **2013,** *12,* 101-102.

10. Durst, J.; Siebel, A.; Simon, C.; Hasche, F.; Herranz, J.; Gasteiger, H. A., *Energy Environ. Sci.* **2014,** *7,* 2255-2260.

11. Paddison, S.; Gasteiger, H., PEM Fuel Cells, Materials and Design Development Challenges. In *Fuel Cells*, Kreuer, K.-D., Ed. Springer New York: **2013**; Chapter 11, 341-367.

12. Zheng, J.; Yan, Y.; Xu, B., *J. Electrochem. Soc.* **2015,** *162,* F1470-F1481.

13. Durst, J.; Simon, C.; Hasché, F.; Gasteiger, H. A., *J. Electrochem. Soc.* **2015,** *162,* F190-F203.

14. Shao, M., *J. Power Sources* **2011,** *196,* 2433-2444.

15. Schmidt, T. J.; Stamenkovic, V.; Markovic, N. M.; Ross Jr, P. N., *Electrochim. Acta.* **2003,** *48,* 3823-3828.

16. Strmcnik, D.; Uchimura, M.; Wang, C.; Subbaraman, R.; Danilovic, N.; van der, V.; Paulikas, A. P.; Stamenkovic, V. R.; Markovic, N. M., *Nat. Chem.* **2013,** *5,* 300-306.

17. Koper, M. T. M., *Nat. Chem.* **2013,** *5,* 255-256.

18. Moghaddam, R.; Pickup, P., *Electrocatalysis* **2011,** *2,* 159-162.

19. Fihri, A.; Bouhrara, M.; Nekoueishahraki, B.; Basset, J.-M.; Polshettiwar, V., *Chem.Soc.Rev.* **2011,** *40,* 5181-5203.

20. Qiao, B.; Wang, A.; Yang, X.; Allard, L. F.; Jiang, Z.; Cui, Y.; Liu, J.; Li, J.; Zhang, T., *Nat. Chem.* **2011,** *3,* 634-641.

21. Kangasniemi, K. H.; Condit, D. A.; Jarvi, T. D., *J. Electrochem. Soc.* **2004,** *151,* E125-E132.

22. Perini, L.; Durante, C.; Favaro, M.; Perazzolo, V.; Agnoli, S.; Schneider, O.; Granozzi, G.; Gennaro, A., *ACS Appl. Mater. Interfaces.* **2015,** *7,* 1170-1179.

23. Di Noto, V.; Negro, E.; Polizzi, S.; Agresti, F.; Giffin, G. A., *ChemSusChem* **2012,** *5,* 2451-2459.

24. Zheng, Y.; Liu, J.; Liang, J.; Jaroniec, M.; Qiao, S. Z., *Energy Environ. Sci.* **2012,** *5,* 6717-6731.

25. Wang, X.; Maeda, K.; Thomas, A.; Takanabe, K.; Xin, G.; Carlsson, J. M.; Domen, K.; Antonietti, M., *Nat. Mater.* **2009,** *8,* 76-80.

26. Di Noto, V.; Negro, E.; Polizzi, S.; Riello, P.; Atanassov, P., *Applied Catalysis B: Environmental* **2012,** *111–112,* 185-199.

27. Kundu, M. K.; Bhowmik, T.; Barman, S., *J. Mater. Chem. A* **2015,** *3,* 23120-23135.

28. Wang, H.; Thia§, L.; Li, N.; Ge, X.; Liu, Z.; Wang, X., *ACS Catal.* **2015,** *5,* 3174-3180.

29. Huang, H.; Chen, R.; Ma, J.; Yan, L.; Zhao, Y.; Wang, Y.; Zhang, W.; Fan, J.; Chen, X., *Chem. Commun.* **2014,** *50,* 15415-15418.

30. Kundu, M. K.; Sadhukhan, M.; Barman, S., *J. Mater. Chem. B* **2015,** *3,* 1289-1300.

31. Wang, Y.; Wang, X.; Antonietti, M., *Angew. Chem. Int. Ed.* **2012,** *51,* 68-89.

32. Mahoney, E. G.; Sheng, W.; Yan, Y.; Chen, J. G., *ChemElectroChem* **2014,** *1,* 2058-2063.

33. Barman, S.; Sadhukhan, M., *J. Mater. Chem.* **2012,** *22,* 21832-21837.

34. Xingbin, Y.; Tao, X.; Gang, C.; Shengrong, Y.; Huiwen, L.; Qunji, X., *J. Phys D: Appl. Phys.* **2004,** *37,* 907.

35. Thomé, T.; Colaux, J. L.; Louette, P.; Terwagne, G., *J. Electron.Spectrosc. Relat. Phenom.* **2006,** *151,* 19-23.

36. Arrigo, R.; Havecker, M.; Schlogl, R.; Su, D. S., *Chem. Commun.* **2008,** 4891-4893.

37. Sridhar, V.; Kim, H.-J.; Jung, J.-H.; Lee, C.; Park, S.; Oh, I.-K., *ACS Nano* **2012,** *6,* 10562-10570.

38. Teschner, D.; Borsodi, J.; Wootsch, A.; Révay, Z.; Hävecker, M.; Knop-Gericke, A.; Jackson, S. D.; Schlögl, R., *Science* **2008,** *320,* 86-89.

39. Lai, W.; Lau, M.-K.; Chong, V.; Wong, W.-T.; Leung, W.-H.; Yu, N.-T., *J. Organomet. Chem.* **2001,** *634,* 61-68.

40. López-Corral, I.; Germán, E.; Juan, A.; Volpe, M. A.; Brizuela, G. P., *J. Phys. Chem. C* **2011,** *115,* 4315-4323.

41. Parambhath, V. B.; Nagar, R.; Ramaprabhu, S., *Langmuir* **2012,** *28,* 7826-7833.

42. Sadhukhan, M.; Barman, S., *J. Mater. Chem. A* **2013,** *1,* 2752-2756.

43. Jerkiewicz, G., *Electrocatalysis* **2010,** *1,* 179-199.

44. Zalineeva, A.; Baranton, S.; Coutanceau, C.; Jerkiewicz, G., *Langmuir* **2015,** *31,* 1605-1609.

45. Tateishi, N.; Yahikozawa, K.; Nishimura, K.; Suzuki, M.; Iwanaga, Y.; Watanabe, M.; Enami, E.; Matsuda, Y.; Takasu, Y., *Electrochim. Acta.* **1991,** *36,* 1235-1240.

46. Baldauf, M.; Kolb, D. M., *Electrochim. Acta.* **1993,** *38,* 2145-2153.

47. Rose, A.; Maniguet, S.; Mathew, R. J.; Slater, C.; Yao, J.; Russell, A. E., *Phys. Chem. Chem. Phys.* **2003,** *5,* 3220.

48. Vannice, M. A.; Neikam, W. C., *J. Catal.* **1971,** *20,* 260-263.

49. Chen, W.-F.; Sasaki, K.; Ma, C.; Frenkel, A. I.; Marinkovic, N.; Muckerman, J. T.; Zhu, Y.; Adzic, R. R., *Angew. Chem. Int. Ed.* **2012,** *51,* 6131-6135.

50. Kong, D.; Cha, J. J.; Wang, H.; Lee, H. R.; Cui, Y., *Energy Environ. Sci.* **2013,** *6,* 3553-3558.

51. Xiao, P.; Sk, M. A.; Thia, L.; Ge, X.; Lim, R. J.; Wang, J.-Y.; Lim, K. H.; Wang, X., *Energy Environ. Sci.* **2014,** *7,* 2624-2629.

52. Zhang, K.; Zhao, Y.; Fu, D.; Chen, Y., *J. Mater. Chem. A* **2015,** *3,* 5783-5788.

53. Khdary, N. H.; Ghanem, M. A., *RSC Adv.* **2014,** *4,* 50114-50122.

54. Roy, N.; Leung, K. T.; Pradhan, D., *J. Phys. Chem. C* **2015,** *119,* 19117-19125.

55. Popczun, E. J.; McKone, J. R.; Read, C. G.; Biacchi, A. J.; Wiltrout, A. M.; Lewis, N. S.; Schaak, R. E., *J. Am. Chem. Soc.* **2013,** *135,* 9267-9270.

56. Ham, D. J.; Ganesan, R.; Lee, J. S., *Int. J. Hydrogen Energy.* **2008,** *33,* 6865-6872.

57. Zhang, H.; Hu, C.; Chen, S.; Zhang, K.; Wang, X., *Catal. Lett.* **2012,** *142,* 809-815.

58. Auinger, M.; Katsounaros, I.; Meier, J. C.; Klemm, S. O.; Biedermann, P. U.; Topalov, A. A.; Rohwerder, M.; Mayrhofer, K. J. J., *Phys. Chem. Chem. Phys.* **2011,** *13,* 16384-16394.

59. Gisbert, R.; García, G.; Koper, M. T. M., *Electrochim. Acta.* **2010,** *55,* 7961-7968.

60. Nørskov, J. K.; Bligaard, T.; Logadottir, A.; Kitchin, J. R.; Chen, J. G.; Pandelov, S.; Stimming, U., *J. Electrochem. Soc.* **2005,** *152,* J23-J26.

61. Zheng, J.; Sheng, W.; Zhuang, Z.; Xu, B.; Yan, Y., *Sci. Adv.* **2016,** *2.*

62. Lu, Z.; Zhu, W.; Yu, X.; Zhang, H.; Li, Y.; Sun, X.; Wang, X.; Wang, H.; Wang, J.; Luo, J.; Lei, X.; Jiang, L., *Adv. Mater.* **2014,** *26,* 2683-2687.

63. Faber, M. S.; Dziedzic, R.; Lukowski, M. A.; Kaiser, N. S.; Ding, Q.; Jin, S., *J. Am. Chem. Soc.* **2014,** *136,* 10053-10061.

64. Herzing, A. A.; Kiely, C. J.; Carley, A. F.; Landon, P.; Hutchings, G. J., *Science* **2008,** *321,* 1331-1335.

65. Lee, J. H.; Park, M. J.; Yoo, S. J.; Jang, J. H.; Kim, H.-J.; Nam, S. W.; Yoon, C. W.; Kim, J. Y., *Nanoscale* **2015,** *7,* 10334-10339.

66. Roy-Mayhew, J. D.; Boschloo, G.; Hagfeldt, A.; Aksay, I. A., *ACS Appl. Mater. Interfaces.* **2012,** *4,* 2794-2800.

67. Luo, Y.; Jiang, J.; Zhou, W.; Yang, H.; Luo, J.; Qi, X.; Zhang, H.; Yu, D. Y. W.; Li, C. M.; Yu, T., *J. Mater. Chem.* **2012,** *22,* 8634-8640.

Chapter 4

Electrocatalytic Oxygen Reduction Reaction on Pd Nanoparticles-Porous Graphitic Carbon Nitride Composite

4.1 Abstract

The electrochemical oxygen reduction reaction (ORR) is a cathodic process of fuel cells. The carbon supported Platinum, Pt/C catalyst is universally used as cathode materials; but poor durability of Pt/C due to degradation of catalyst prevent its wide spread applications. It is thus important to develop new cathode material(s) with high activity and stability. We report here, superior electrocatalytic activity of palladium nanoparticles-carbon nitride (Pd-CN_x) composite towards ORR in both alkaline and acidic media. The ORR activity on Pd-CNx catalyst is better (half wave potential $E_{1/2}$ of 60mV more positive) than that of Pt/C in 0.5 M KOH solution and is almost comparable in acid media. Moreover, this porous composite display excellent methanol tolerance and has much better long term durability than that of commercial Pt/C in both acidic and alkaline media. Only 4 and 6 mV positive shift of $E_{1/2}$ after 1,500 potential cycles in basic medium and acid media respectively prove the excellent durability of this catalyst. The superior electrocatalytic activity and excellent stability of porous Pd-CN_x composite can be attributed to unique synergistic interaction between CN_x support and Pd nanoparticles (Pd-NPs), lower the d-band center of Pd, easy mass transport, and surface structure of Pd-NPs.

4.2 Introduction

The oxygen reduction reaction (ORR) is one of the important redox reaction[1] for development of proton exchange membrane fuel cell (PEMFCs), direct liquid fuel cells (DLFCs) and alkaline fuel cells (AFCs). Without any assistance of suitable catalyst, ORR kinetics becomes very sluggish. Platinum is known to be the universal catalyst for the ORR process. In practice, commercialization is restricted mainly by two major problems: (1) the precious platinum metal dependency and (2) lack of stability of the electrode materials under strong acidic condition of PEM cells. It is thus important to develop non platinum based highly active and durable ORR catalyst for commercialization of fuel cell. The palladium, another noble metal which has similar crystal structure, surface structure, has created enormous attention as fuel cell catalyst because Pd is more abundance than Pt and has similar activity with Pt.[2] The ORR reaction is highly depended on the size, shape and crystallinity of the electrode materials and also the electrolyte solution.[3-5] Generally, ORR proceeds on the noble metal through two steps process - (a) adsorption or electron transfer to O-O molecule and breaking the O-O bond (b) electro-reduction or hydrogenation of adsorbed oxygenated intermediated. The Pt and Pd metal has higher d band center as results O_2 molecule adsorbed on the surface site very strongly and dissociate the O-O bond quickly but electroreduction of oxygenated intermediated was very slow leading to sluggish the ORR kinetics.[6] In addition, Pd/C has generally 5 times lower ORR activity than Pt/C due to the stronger bonding of Pd metal surface with oxygenated species[6]. Several strategies were adopted to improve the ORR catalytic activity of Pd catalysts such as size, shape and facet controlled[7-12] synthesis of Pd nanoparticle, making bimetallic composite by alloying with other metals,[13-19] and Pd-NPs supported on different support materials[1, 20-23] for catalysis. Recently, J-J. Feng and his co-workers reported synthesis of PdPt@Pt nanocatalyst for enhanced ORR reaction.[24] X. Cui and his co-workers reported the synthesis of controlled surface structure of Pd@Pt core shell nanocatalyst for enhanced ORR reaction.[25] The electrocatalytic ORR reaction on metal nanoparticle is highly sensitive to the surface structure of the metal NPs.

N.Hoshi and his co-worker studied[5] the structure sensitivity ORR in $HClO_4$ solution on Pd-NPs and concluded that the reactivity order of Pd-NPs as Pd(100)> Pd(111)>>Pd(110). Shape dependency ORR activity Pd also studied by the several groups. Recently, M.Shao and his co-worker reported[10] cubic Pd nanoparticle has one magnitude higher ORR activity than octahedral Pd. Last few years, several factors such as down shift of d-centered band, reduced OH absorption, increased Pd d-band vacancy etc. have given importance to enhance the catalytic activity of the Pd catalyst while developing a new Pd catalyst.In addition, carbon supported Pd–NPs catalyst are gaining attentions as an anode and cathode electrode in fuel cell applications. Among various carbon supported materials Vulcan XC-72, carbon black, and ketjen black are used widely as supporting materials. The normally used carbon support can easily electrochemically oxidized to carbon dioxide under fuel cell operating condition and leads to structural degradation of support as well as electrically detachment of NPs from the support. The long term durability of a catalyst in fuel cell is reduced drastically due to migration, aggregation, Oswald ripening[26] of NPs. Recently, systematic attentions have been paid in order to develop new support materials for the dispersion of metal nanoparticles, since they play an intriguing role for the improvement of the catalytic activity and its durability. The support material can modify the electronic property as well as structure of metal nanoparticles dispersed on the surface of support. Good support materials can prevent metal leaching, agglomeration and dissolution of the nanoparticles during fuel cell operation. Good support materials provide “coordination nests”[27] for various metal nano-particles and can prevent metal leaching, agglomeration and dissolution of the nanoparticles during fuel cell operation due to the strong catalyst-support interactions. Recently K.Tammeveski and his co-worker reported[28] an enhanced ORR activity by fabricate Pd-NPs with multi walled carbon nanotube. Several groups reported [29-30] different supported materials for metal NPs with improved electrocatalytic activity. Graphene, a two dimensional support, has demonstrated as a very good supporting material[31] for dispersion of nanoparticles for their high electro-catalytic activity due to its unique physical and chemical properties.[32] Another two dimensional material, g-C_3N_4 which has similar graphene like structure, is also a promising support material[33] due to the presence of abundant Lewis acid/ base sites for anchoring nanoparticles. The g-C_3N_4 supported metal/semiconductor nanoparticles composite have gaining attentions as an effective composites for their versatile applications in photo-catalysis,[34] biosensors,[35] electrochemical applications[33, 36-37] etc. The conductivity of the carbon nitride support increases with decreasing concentration of nitrogen in support, and hence enhanced electrochemical ORR performances were reported by several groups.[36, 38-40]

Herein, we have reported a superior catalytic activity of porous Pd-CN_x composite, synthesized by ultrasound borohydride reduction method, towards electrochemical oxygen reduction (ORR). The Pd-CN_x composite shows ORR activity better than Pt/C catalyst in basic medium and comparable in acid medium. Tafel slope and K-L plot confirm that the oxygen reduction in acidic and basic media occurs via 4 electron pathways on Pd-CN_x catalysts. Most importantly, this catalyst shows a remarkable durability and long-term cyclic stability towards ORR as compare to Pd/C and Pt/C. The superior catalytic activity of Pd-CN_x can be mainly attributed to down shifting of d-centered band of Pd resulting from strong synergetic interaction between Pd nanoparticles and CN_x support. The superior catalytic activity of Pd-CN_x demonstrates that CN_x is a promising catalyst support for electrochemical applications.

4.3 Experimental Section

Preparation of g-C_3N_4:

The synthesis of graphitic carbon nitride form formamide (HCOOH) was done using by microwave mediate heating method [41]. In brief, 30 ml formamide was heated at 180^0 C for 2 hrs by irradiating microwave in a microwave synthesizer. The solution becomes brownish colour on microwave heating and then evaporating this solution in rotary evaporator at 180^0 C forms black product. The black products were washed with water and dry in vacuum to get g-$CN_{x.}$

Preparation of Pd-CN_x Composite:

The Pd-CN_x composite was prepared by using ultrasound mediated reduction method, reported recently by our group.[37] In brief, 5 mg of g-CN_x was dispersed in 2 ml water and then 8 ml aqueous solution of 0.14 mole $PdCl_4^{-2}$ was poured into the 2 ml g-CN_x water dispersion. Then, 700 μL of 0.1 M $NaBH_4$ solution was directly added into this mixed solution and finally the solution was sonicated by a probe sonicator operating at 28 kHz frequency (power 420 watt) for 180 minutes. A black product was separated by centrifugation at 10,000 rpm for 30 minutes and washed twice with de-ionised water.

Preparation of Working Electrode:

The stock suspension of the Pd-CN_x composite was prepared by dispersing 0.5 mg Pd-CN_x composite in 1 ml of de-ionized millipore water by a bath sonication. The 3 days aged stock suspension was used for electrode and microscopic sample preparation since slightly better ORR activity was observed when electrode was prepared from old stock suspension. The Pd-CN_x modified electrode was prepared by drop casting 10 □L of the suspension on GC of diameter 3 mm and drying in the ambient temperature on air. All the electrochemical performance of Pd-CN_x catalyst was carried out with a constant Pd loading of 0.043 mg cm^{-2} on GC electrode. No polymer binder was used for the preparation of Pd-CN$_x$ electrode. The glassy carbon (GC) electrode was polished with 1.0, 0.1, and 0.05 mm alumina slurry on Buehler micro polishing cloth.

4.4 Results and Discussion

Characterization of Porous Pd-CN$_x$ Composite:

As shown in **Figure 4.1**, p-XRD diffraction pattern of Pd-CN$_x$ composite demonstrate the diffraction peak at 39.20^0, 46.70^0, 68.70^0, 80.90^0, 86.70^0 corresponding to the (111), (200), (220), (311), and (222) reflection planes of face centered cubic palladium (JCPDS No 89-4897) and reveals the formation of Pd-NPs. The size of porous Pd-NPs in the composite could be determined from the following Debye–Scherer Equation describe bellow

$$\mathbf{B(2\theta)} = \frac{K\lambda}{L\cos\theta}$$

Where L is the mean size of the ordered (crystalline) domains, K is a dimensionless shape factor, with a value close to unity. The shape factor has a typical value of about 0.9, but varies with the actual shape of the crystallite, λ is the X-ray wavelength (0.154 nm), B is the line broadening at half the maximum intensity (FWHM) in radians.

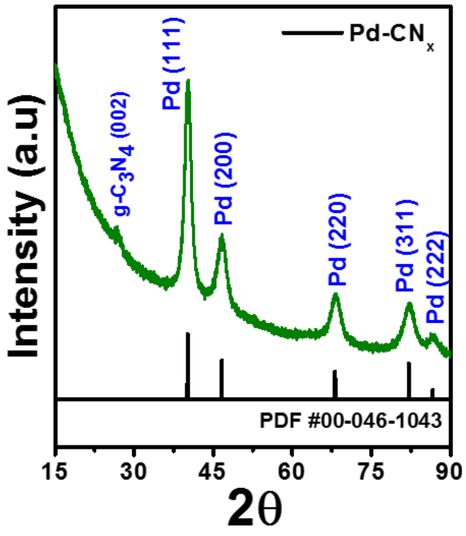

Figure 4.2. p-XRD pattern of Pd-CN$_x$ composite.

Table 4.1. Different parameter and average particle size of Pd-NPs in Pd-CN_x composite by Scherrer Equation.[37]

Catalyst	**Parameter**	**Parameter Value**	**Average Particle Size (nm)**
Pd-CN_x composite	K	0.9	10.6
	λ	0.154	
	cos(θ)	0.9423	
	B	0.01301	

By using Debye-Scherrer equation on Pd(111) reflection plane and calculate the avg. size of Pd-NPs found to be 10.6 nm (**Table 4.1**). In order to observe morphology of Pd-CN_x composite TEM and FE-SEM measurements were further carried out. For microscopic experiments, the samples were prepared by evaporation of 10 μl stock suspension of Pd-CN_x composite on TEM grid and Si-wafer respectively. **Figure 4.2.(a,b**) and **Figure 4.3.(a,b**) displayed the TEM images of the Pd-CN_x composite.

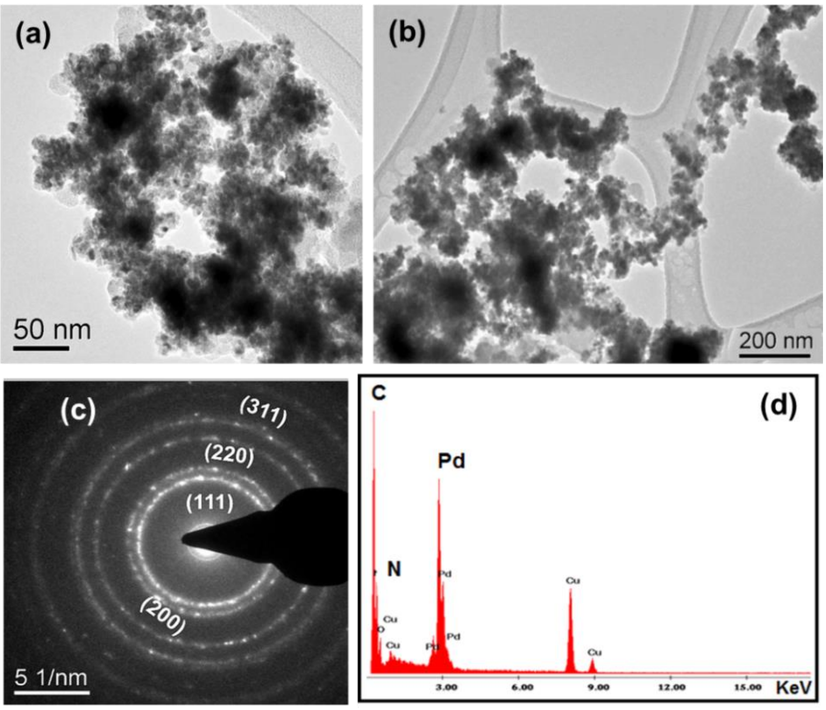

Figure 4.2. (a,b) TEM images of Pd-CN_x composite. (c) SEAD image of Pd-CN_x composite taken from **Figure 4.2.b**. (d) EDX spectra of Pd-CN_x composite.

From these images, it has been revealed that small CN_x sheets comprising of small Pd-NPs were interconnected together in order to form porous architecture of the composite. The particle size measurement of Pd-NPs on g-CN_x was carried out from **Figure 4.3.a** and found to be broad size distribution from 5 nm to 12 nm (**Figure 4.3.c**). The SAED image of Pd-CN_x composite is shown in **Figure 4.2.c**.

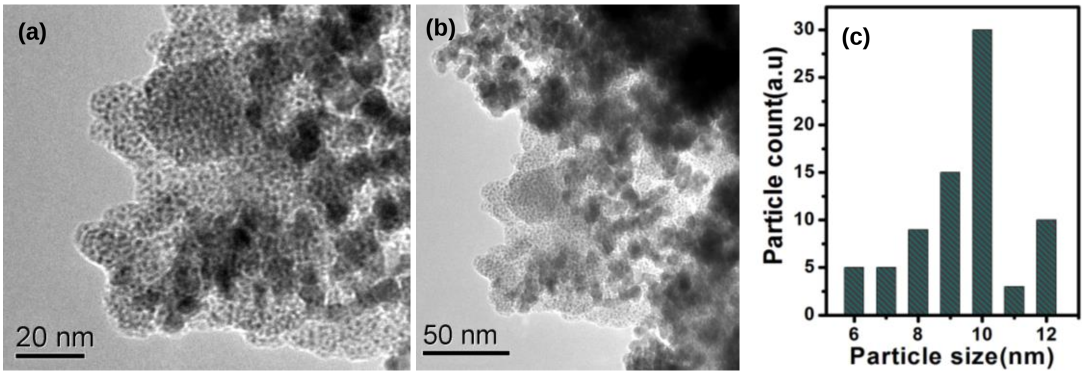

Figure 4.3. (a,b) TEM images of Pd-CN_x composite. (c) Size distribution profile taken from Figure **4.3.a**.

The interlayer spacing calculated from SAED image are 2.24, 1.95, 1.37, 1.17 Å corresponding to (111), (200), (220), and (311) planes of face centered cubic lattice of Pd. The EDS profile shows the presence of carbon (C) nitrogen (N), oxygen (O) and Pd metal (**Figure 4.2.d**). The FE-SEM image of PD-CN_x composite was shown in **Figure 4.4.a**. It shows the porous morphology of the composite.

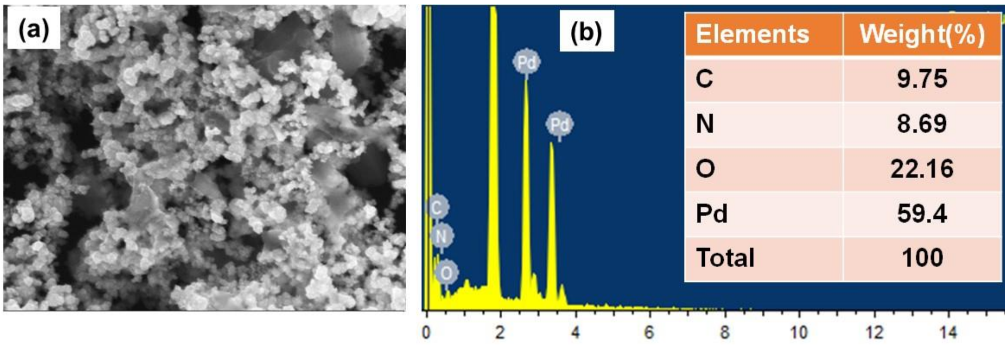

Elements	Weight(%)
C	9.75
N	8.69
O	22.16
Pd	59.4
Total	100

Figure 4.4. (a) FESEM image and (b) corresponding EDS profile of Pd-CN_x composite.

In addition, we have performed the FE-SEM EDS measurement and shown in **Figure 4.4.b.** In-set of **Figure 4.4.b** shows the atomic weight percentage of different elements presence in the composite materials. The Fourier transform infrared (FT-IR) spectra of g-CN_x and Pd-CN_x composite are shown in **Figure 4.5.** The IR spectra of free g-CN_x showed three peaks at 1213, 1317, 1408 cm^{-1} for aromatic C=N stretching and a peak at 1630 cm^{-1} can be assigned to C=N stretch[37]. In comparison, IR spectra of Pd-CN_x composite shows an appearance of two new intense peaks at 1130 cm^{-1} and 1086 cm^{-1} which can be attributed to the C-N single bond stretching.In addition another new peak at 590 cm^{-1} is due to Pd-C stretching.

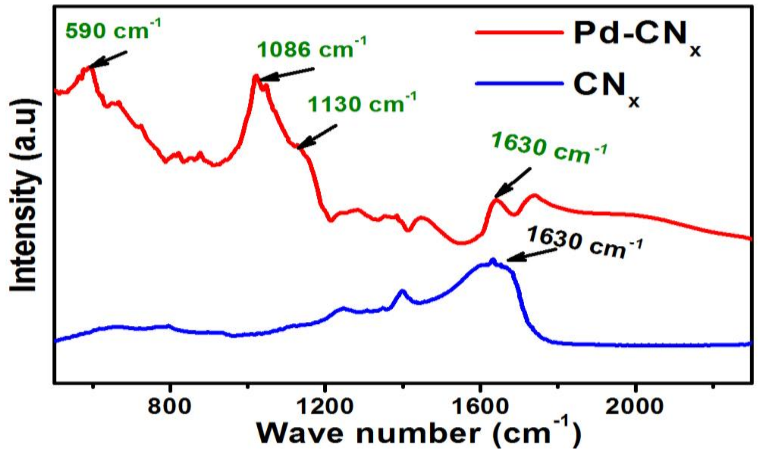

Figure 4.5. FT-IR spectra of Pd-CN_x composite and g-C_3N_4.

The appearance of new C-N stretching, Pd-C stretching IR peaks and decrease of intensity of C=N stretching peaks suggests a strong interaction between Pd-NPs and CN_x support.[37] The strong interaction between Pd and C was further confirmed by X-ray photoelectron spectroscopy (XPS). As shown in **Figure 4.6.(a-c)** (Appendix), the positive binding energy shift [37] of carbon and palladium proved that there is an strong interaction between Pd and carbon in the Pd-CN_x composite.

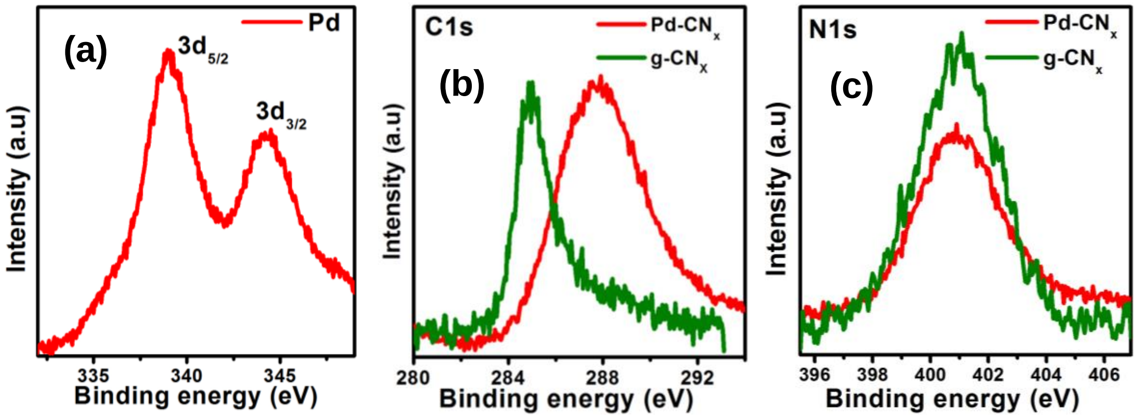

Figure 4.6. XPS spectra of (a) Pd 3d, (b) Carbon 1s, (c) Nitrogen 1s in Pd-CN$_x$ composite.

The metal loading in Pd-CN$_x$ composite was measured by ICP-OES (Inductive couple plasma emission spectroscopy). The exact loading of Pd in this composite was found to be 59.4 wt.%. The CHN analysis was further carried out to know the composition of CNx support. The wt.% of carbon, nitrogen in Pd-CN$_x$ composite was 9.75 and 8.69 wt.% whereas in free CN$_x$ moiety it was 43.13 and 47.3 wt.% respectively. The results of CHN analysis is given in **Table 4.1** and N/C ratio in free g-CNx and Pd-CN$_x$ were found to be ~1.1 and 0.89 respectively.

Table 4.2. Details of CHN analysis of g-C_3N_4 and porous Pd-CN$_x$ composite.

Catalyst	Carbon(C) (wt.%)	Nitrogen(N) (wt.%)	Oxygen (O) (wt.%)	Hydrogen (H) (wt.%)	N/C ratio
Porous Pd-CN$_x$	9.75	8.69	-	3.18	~ 0.89
g-C_3N_4	43.13	47.3	5.78	3.79	1.01

Electrochemical Behaviour of Pd-CN$_x$ Electrode:

The electrochemical behavior of Pd-CN$_x$ composite was first examined in both acidic and basic medium by using cyclic voltammetry (CV) method. The CV curve of porous Pd-CN$_x$, comm. Pt/C, comm. Pd/C electrode in 0.5 M $HClO_4$ solution are shown in **Figure 4.7.(a-c)**. The Pd-CN$_x$ shows two strong anodic peak between potential ranges from 0 V to 0.3 V. The peak at 0.105 V assigned for H-desorption from Pd (111) plane whereas peak at 0.22 V assigned for H-desorption from Pd (100) plane. A broad anodic peak at E⩾1.0 V corresponds to the formation of Pd-O and its corresponding cathodic peak at 0.67 V for the reduction of the Pd-O. An anodic peaks at 0.22 is assigned to UPD hydrogen adsorption (UPD-H_{ads}) from Pd (100) and a cathodic peak at 0.18 V are assigned to UPDH-desorption (UPD-H_{des}) from Pd (100) plane of Pd-CN_x surfaces respectively. This suggests the presence of electrochemically active Pd (100) plane along with Pd (111) plane. The electro chemical active surface area (ECSA) is one of the important parameter behind its catalytic activity.[37] The ECSA of the Pd-CN_x composite and commercial Pd/C and Pt/C catalyst was calculated from the reduction peak of PdO ~0.67 V (RHE).

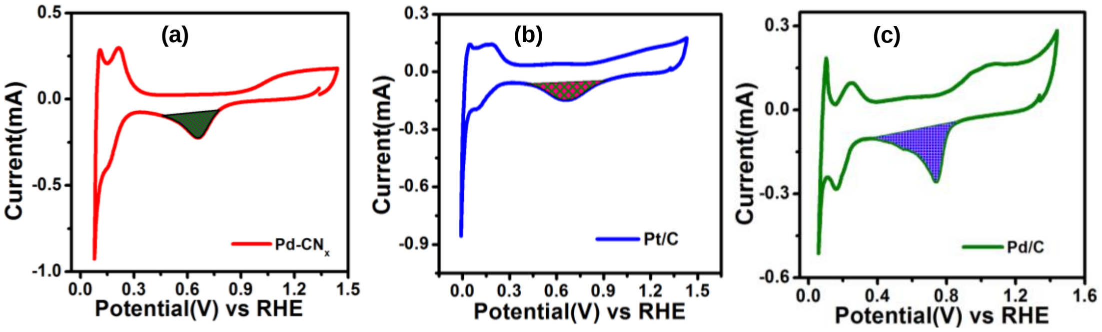

Figure 4.7. CV of (a) Pd-CN_x composite, (b) commercial Pt/C (10 wt%), (c) Pd/C (30 wt%) in 0.5 M $HClO_4$ solution with scan speed 100 mV/sec and ECSA calculate after 30 times CV run.

The detailed calculation procedure and value in both acidic and basic medium were describes as

$$\text{ECSA(from Pd-O peak)} = \frac{Q_S}{0.41 * M_{Pd}}$$

where Q_s is the average charge calculated from area under the voltragram of the H-desorption CV curve in mC /cm^2 unit

$$Q_s = \int \frac{I * dE}{v}$$

Where v is the scan rate. The constant 0.410 mC/cm^{-2} was calculated charge value for reduction of Pd-O peak, M_{Pd} loading of the Pd on the electrode. The ECSA of porous Pd-CN_x composite in basic medium was 63.34 m^2 g^{-1} whereas for Pt/C and Pd/C was 59.15 and 61.3 m^2 g^{-1} respectively. The Pd-CN_x composite has higher active surface area than Pd/C and Pt/C which could be originated from the high dispersion of small Pd nanoparticles and porous structure of the Pd-CN_x composite.

ORR Activity on Porous Pd-CN_x Composite in Basic Medium:

The electrochemical activity of porous Pd-CN_x sample towards oxygen reduction reaction (ORR) was measured in basic medium. The electrochemical reduction of oxygen on electrode surface generally takes place in two different ways - either via directly water formation (4e reduction) or via the intermediate H_2O_2 formation (2e reduction) followed by the reduction to water (another 2e pathway) or simply by chemically decomposing on electrode. The H_2O_2 produced in fuel cell can corrode the membrane electrode assembly. Therefore, Pt, Pd, Au based catalysts are gaining an attentions in order to reduce the overpotential and the H_2O_2 production. **Figure 4.8.a** shows the typical CV curves for ORR on porous Pd-CN_x modified rotating GC electrodes in O_2 and N_2 saturated 0.5 M KOH medium with each catalyst loading of 0.043 mg cm^{-2}. In comparison with the N_2 saturated solution, in O_2 saturated alkaline medium a distinct O_2 reduction peak was observed at ~ 0.83 V which reveals that Pd-CN_x catalyst was active towards ORR in basic medium. In addition, in presence of oxygen, a very large increase in the capacitive currents at the Pd-CN_x electrode was observed (**Figure 4.8.a**). It is reported[42] that the good capacitance behavior of mesoporous sulfur doped carbon monoliths in alkaline medium was due to the presence of sulphoxide and sulfones groups which significantly contribute to pseudocapacitance. T. J. Bandosz and coworker reported[42] that enhancement in capacitance of sulfer-doped carbon in presence of oxygen was linked to changes in the carbon texture and chemistry of sulfur. The nitrogen atom in pyrrolic and pyridinic groups is also known for the enhancement of capacitance of carbon electrodes due to the Faradic reactions.[43-44] In alkaline medium and in presence of oxygen molecule, N atoms of CN_x support of Pd-CN_x catalyst under potential are oxidized to form positively charged nitrogen (quaternary and pyridinic –N-oxide) and the faradic reaction on this charged nitrogen is probably the reason for large increase in the capacitance current in Pd-CN_x. The LSV comparison curves of Pt/C, Pd/C and Pd-CN_x composite in O_2 saturated 0.5 M KOH medium with 1600 rpm rotation was presented in **Figure 4.8.b**.

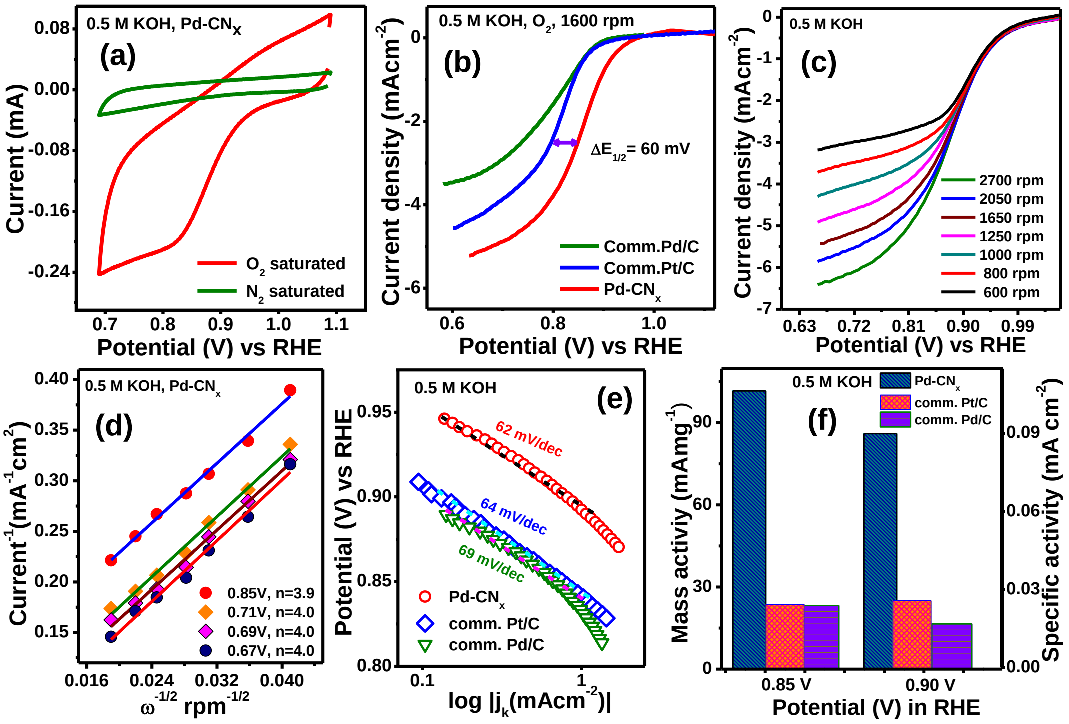

Figure 4.8. (a) Cyclic voltammograms of Pd-CN_x composite in O_2 and N_2 saturated 0.5 M KOH solution with scan rate 100 mV/sec. (b) Comparison of LSV curves of porous Pd-CN_x, Pt/C and Pd/C modified GC electrode in O_2 saturated 0.5 M KOH with 1600 rpm rotation at 100 mV/sec scan rate. (c) LSV curves of Pd-CN_x modified electrode in O_2 saturated 0.5 M KOH solution with rotating speed varying from 600 rpm to 2700 rpm. (d) The corresponding K-L plots at different potentials. (e) Mass transfer corrected Tafel slope of Pd-CN_x composite in comparison with Pt/C and Pd/C catalyst in basic medium. (f) The mass activity and specific activity of Pd-CNx, Pt/C and Pd/C modified electrode at different potentials.

The ORR onset potentials of Pt/C and Pd/C was at ~0.91 V and ~ 0.87 V and half wave potentials was ~ 0.81 and ~0.75 V respectively. But after the modification of GC electrode with porous Pd-CN_x composite, a stronger cathodic peak and more positive onset potential at ~ 0.96 V was observed. The $E_{1/2}$ of Porous Pd-CN_x composite at ~ 0.87 V which is ~ 60 mV more positive than start-of- art Pt/C catalyst and ~ 120 mV better than Pd/C catalyst. The rotating disk electrode (RDE) method was carried out in order to measure the kinetics of ORR at the modified porous Pd-CN_x electrode in oxygen saturated 0.5 M KOH solution. **Figure 4.8.c** presents the linear sweep voltammetry (LSV) polarization curves for ORR on porous Pd-CN_x modified GC electrode at variable rotation speed from 600 rpm to 2700 rpm. The polarization current density gradually increases with increasing the rotation speeds. However, the current density at positive potential of 0.96 V is independent on the rotation speed because the current density was fully kinetic controlled. Whereas the current density at potentials negative to 0.85 V, remains unaltered with changing the potential, but this current (limiting current) increases with rotation rate *i.e.* electron transfer in this region are fully controlled by the diffusion process[28, 45]. The current density in the potential region from 0.85 to 0.96 V was controlled by the mixed kinetics.[28, 45] However in ORR, number of involved electron per O_2 can be obtained by Koutecky-Levich (K-L) equation:

$$1/j = 1/j_k + 1/j_d = -1/nFkC_{O_2} - 1/B\omega^{1/2}$$

where j is the measured current density, j_k, j_d is the kinetic and diffusion limited current density, ω is the electrode rotating rate. B can be determined from the slope of K-L plot and theoretically can be obtained from the following equation:

$$B = 0.62\, nF(D_{O_2})^{2/3}\nu^{-1/6}C_{O_2}$$

where Faraday constant (F= 96485 C mol^{-1}), diffusion coefficient (D_{O_2}) of O_2 in 0.5 M KOH (1.8×10^{-5} cm^2 s^{-1}), kinetic viscosity ($\nu = 0.01$ cm^2 s^{-1}) and C_{O_2} is the bulk concentration of O_2 (1.13×10^{-6} mol cm^{-3}). **Figure 4.8.d** shows that K-L plot of ORR on porous Pd-CN_x composite electrode at different voltage, ranging from 0.67 to 0.82 V constructed from **Figure 4.8.c**. For all the potentials, inverse of the total current density linearly was varied with inverse of square root of angular rotation rate. Near parallelism of the K-L plots reveals that the reaction kinetics was first order with respect to dissolved oxygen concentration. The average value of n at different potentials obtained from the K-L plot was 4. According to K-L plot, Pd-CN_x composite can be able to reduce the O_2 molecule directly to H_2O by transferring 4e. In order to obtain Tafel plots, diffusion correction of measured current was done to get true kinetic currents in the mixed activation-diffusion region. The kinetic current was measured from the equation:

$$j_k = j\, j_d/(\, j_d - j\,)$$

Where $j/(\, j_d - j\,)$ is the mass correction term.

The limiting diffusion current was calculated from the equation:

$$j_d = B\omega^{1/2}$$

Where ω is the rotation rate (rpm) of the electrode.

Figure 4.8.e shows the mass corrected Tafel plot of Pd-CN_x composite, commercial Pt/C and Pd/C catalyst. Generally, Pt/C catalyst exhibits two step Tafel slope *i.e.* 60 mV/dec (lower current density region) to sifted 120 mV/dec (higher current density region). Similar behavior for Pd-based electrocatalysts was also reported [46-48] by various groups. K. Tammeveski and his co-workers reported[28] that at low over potentials region Pd-O formation was predominant and ORR kinetics was influenced by the surface oxide of Pd-NPs and given Tafel slope 60 mV/dec whereas at higher onset potentials only metallic Pd was exists and given the Tafel slope 120 mV/dec. But in both the case the mechanism of the ORR reduction reaction was same. From the **Figure 4.8.e**, it is clear that Pd-CN_x and Pd/C has a two-step Tafel slope, one is for low over potentials region and another for high over potentials region. The tafel slope for Pd-CN_x sample is ~62 mV dec^{-1} in

low current density region whereas for Pt/C and Pd/C is 64 mV/dec and 69 mV/dec respectively.This suggests that Pd-CN_x also follows the similar mechanism as Pt/C, and Pd/C catalyst and electron transfer to O_2 molecule is the rate determining step for O_2 reduction on Pd surface in alkaline medium. The specific activity (J_{SA}) and mass activity (J_{MA}) of Pt/C, Pd/C and Pd-CN_x composite were evaluated by normalized J_k with corresponding active area and metal loading on GC electrode respectively by using these equations

$$J_{SA} = J_k / A_r$$

Here J_k is the kinetic current and A_r is the electrochemical active area of Pd-CN_x on the electrode.

Mass activity of the electrode were evaluated from equation below

$$J_{MA} = J_k / m_{Pd}$$

Here m_{Pd} is the mass of Pd on the electrode.

The mass activity (J_{MA}) and specific activity (J_{SA}) of Pd-CN_x, Pt/C and Pd/C catalysts were determined at different potentials as shown in **Figure 4.8.f**. At an applied potential of 0.90 V the J_{MA} values of Pd-CN_x composite (86.68 $mAmg^{-1}$) were at least 3.45 and 5.29 times higher than that of Pt/C and Pd/C catalysts respectively whereas, at 0.85 V, J_{MA} of Pd-CN_x was ~4.5 times higher than Pt/C or Pd/C. The J_{MA} and J_{SA} of Pd-CN_x composite were not only higher than commercial Pt/C or Pd/C catalyst but also comparable or sometimes slight lower than the different reported catalysts[49-50]. Although Pd-CN_x catalyst has slightly higher ECSA, the specific activity of Pd-CN_x composite at all potentials is also much higher than that of Pd/C or Pt/C catalyst. For example, J_{SA} of Pd-CN_x at 0.9 V was 3.5 and 4.9 times higher than that of commercial Pt/C and Pd/C respectively.

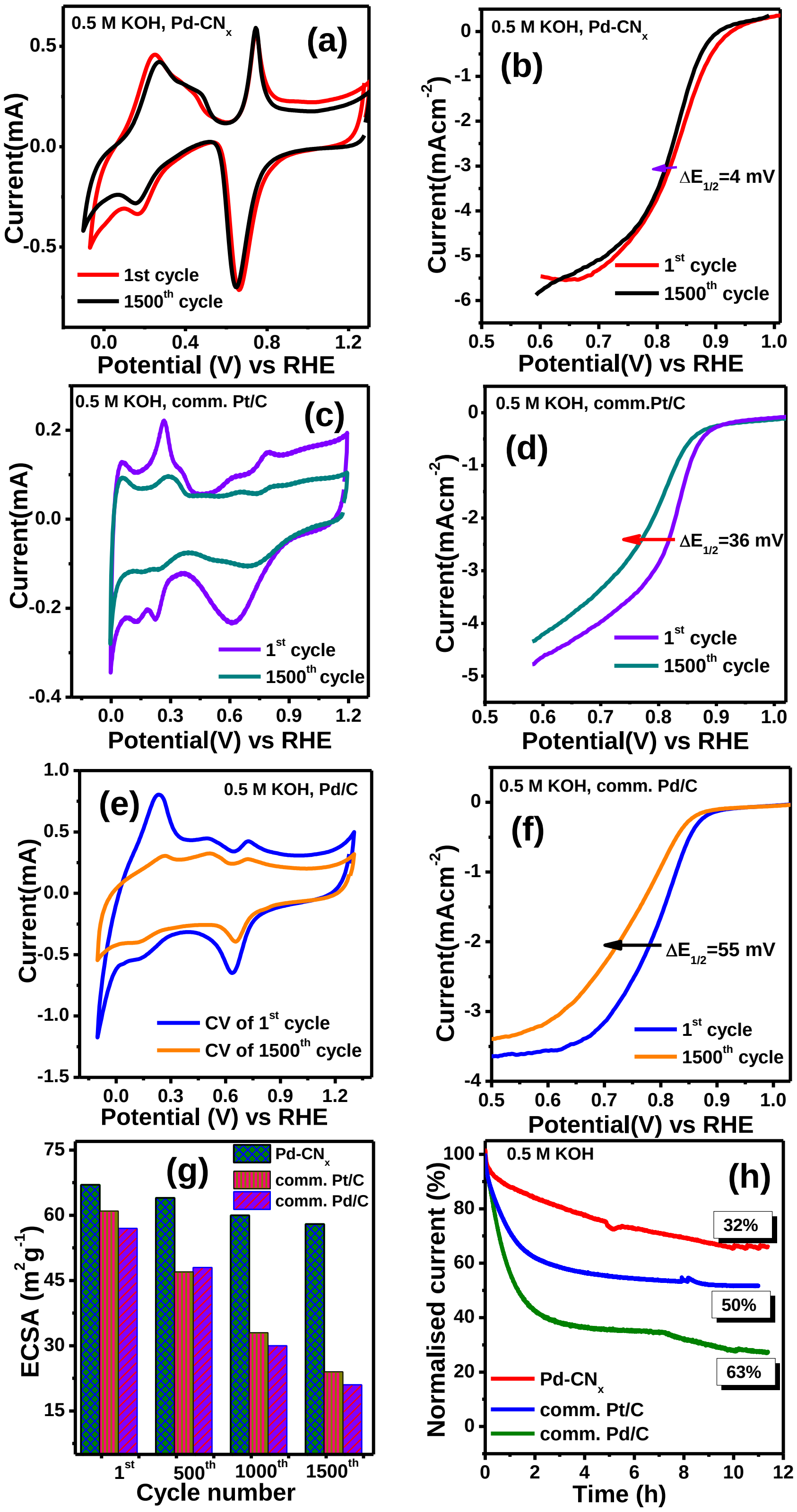

Figure 4.9. (a,c,e) CVs of Pd-CN$_x$, Pt/C and Pd/C in N$_2$ saturated 0.5 M KOH after and before 1500 CV cycles respectively. (b,d,f) LSV curves of Pd-CN$_x$, Pt/C, Pd/C in O$_2$ saturated 0.5 M KOH solution after and before 1500 LSV cycles with rotating speed 1600 rpm respectively. (g) Changes of ECSA values with CV cycle number of Pd-CN$_x$, Pt/C and Pd/C catalysts. (h) Steady state chronoamperometric response of Pd-CN$_x$ composite, Pt/C and Pd/C at a constant potential of 0.7 V.

The much higher J_{SA} and J_{MA} values of Pd-CN_x catalyst demonstrate the superior catalytic (ORR) performance of Pd-CN_x compared to commercial Pt/C or Pd/C in alkaline medium. Besides its high catalytic activity towards ORR, Pd-CN_x also exhibits exceptional stability in basic medium. **Figure 4.9.(a,c,e**) show the CVs (1st and 1500th cycle) of Pd-CN_x, Pt/C and Pd/C in N_2 saturated 0.5 M KOH solution respectively. The CV profile of Pd-CN_x composite remained almost unchanged after 1500 cycles while large changes were observed for the commercial Pt/C and Pd/C catalysts. In addition, LSV cycling stability of Pd-CN_x, Pt/C and Pd/C catalysts in ORR condition was also examined. The comparison of 1st cycle and 1500th cycle LSV polarization curves for Pd-CN_x, Pt/C and Pd/C in O_2 saturated 0.5 M KOH solution was shown in **Figure 4.9.(b,d,f**) respectively. After 1500 continuous LSV cycles, the half wave potential, $E_{1/2}$ of Pd-CN_x composite showed a small negative shift of only 4 mV. This is much lower than that of commercial Pt/C (negative shift of 36 mV; **Figure 4.9.d**) and Pd/C (55 mV negative shift, **Figure 4.9.f**). **Figure 4.9.g** shows the bar plot of change in ECSA of Pd-CN_x composite in comparison with Pd/C catalyst with cycle number. After 1500 cycle, ECSA of Pd-CN_x composite decreases only 4% whereas the decrease for Pt/C and Pd/C catalysts was 70% and 80% respectively. These stability tests undoubtedly prove the stability of porous Pd-CN_x catalyst is much higher than commercial Pd/C or Pt/C catalyst. The durability of Pd-CN_x catalyst was evaluated by chronoamperometric study in O_2 saturated 0.5 M KOH solution. In practical fuel cell application it is important to develop the polymer binder free highly stable catalyst. No polymer binder was used for the preparation of Pd-CN_x electrode whereas the Pt/C and Pd/C modified GC electrodes were prepared by immobilizing of these catalysts on electrode surfaces using a polymer nafion binder. **Figure 4.9.h** shows the comparison of chronoamperometric response in O_2 saturated 0.5 M KOH electrolyte at 0.7 V potential. After 10 hours, Pd-CN_x catalyst retained 70% of initial current whereas Pd/C and Pt/C catalyst retained only 54% and 32% respectively. This chronoamperometric study suggests binder free Pd-CN$_x$ catalyst has much better stability than that of commercial Pd/C or Pt/C catalyst. The superior durability of Pd-CN$_x$ catalyst is probably due to the strong catalyst-support interactions which prevents agglomeration and detachment of Pd nano-particles from CN$_x$ support.

ORR Activity on Porous Pd-CN$_x$ Electrode in Acidic Medium:

The electrocatalytic ORR activity of Pd-CN$_x$ was further evaluated in acidic medium by using CV and LSV techniques. The CVs of Pd-CN$_{x,}$ modified electrode in N$_2$ and O$_2$ saturated 0.5 M HClO$_4$ medium are shown in **Figure 4.10.a**. There was no significant peak in N$_2$ medium in between 0.6 to 1.0 V potentials region but in O$_2$ saturated solution catalyst contained a distinct reduction peak at 0.75 V (RHE) suggesting the high O$_2$ reduction catalytic activity of Pd-CN$_x$ composite in acid media. **Figure 4.10.b** show the LSV curves of Pd-CN$_x$, Pt/C and Pd/C modified GC electrode in O$_2$ saturated 0.5 M HClO$_4$ with each catalyst loading of 0.043 mg cm^{-2}.This shows Pt/C and Pd-CN$_x$ catalysts has almost similar activity. The Pt/C catalyst has a half wave potential of 0.83 V (RHE) in 0.5 M HClO$_4$ medium. The half wave potential ($E_{1/2}$) of Pd-CN$_x$ is only ~3 mV negatively shifted compared to Pt/C, but it was 80 mV better than that of Pd/C. To understand insight in the catalytic activity of Pd-CN$_x$ catalyst towards ORR, rotating disk experiment in different rotation was performed in O$_2$ saturated HClO$_4$ solution. The LSV curves at different rotating speeds ranging from 350 rpm to 2500 rpm were shown in **Figure 4.10.c**. The current density gradually increase with the increasing the rotation. The number of electron transfer in the ORR process was calculated by similar way as discussed in equation. The K-L plot at 0.54, 0.59, 0.70 and 0.76 V potential in 0.5 M HClO$_4$ medium was shown in **Figure 4.10.d**. At all potentials K-L plot maintained good linearity and all plots are parallel with n value of ~ 4.0.

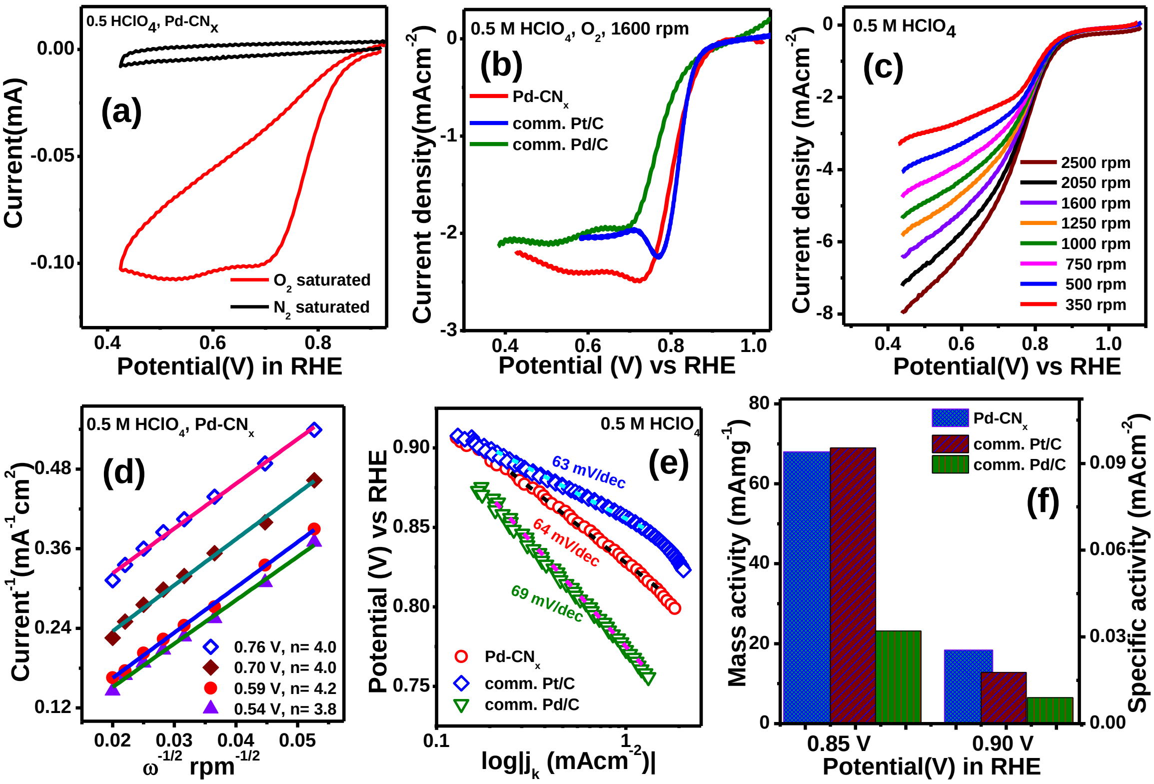

Figure 4.10. ORR of Pd-CN$_x$ composite in 0.5 M HClO$_4$ medium: (a) CV of Pd-CN$_x$ composite in O$_2$ saturated 0.5 M HClO$_4$ scan speed 100 mV/sec (b) LSV curves of porous Pd-CN$_x$, Pt/C, and Pd/C modified GC electrode in O$_2$ saturated 0.5 M HClO$_4$ at scan rate of 100 mV/sec. (c) LSV curves of Pd-CN$_x$ modified GC electrode in O$_2$ saturated 0.5 M HClO$_4$ solution with rotating speed varying from 350 rpm to 2500 rpm. (d) The corresponding K-L plot of Pd-CN$_x$ composite at different potentials. (e) Mass transfer corrected Tafel slope of Pd-CN$_x$ composite in comparison with Pt/C and Pd/C in acidic medium. (f) The mass activity and specific activity on Pd-CNx composite, Pt/C, and Pd/C at different potentials.

Thus, ORR on Pd-CN$_x$ catalyst in acidic medium at all potentials mainly abides by first order 4e transfer process. Mass transfer corrected Tafel slopes of Pd-CN$_x$, Pt/C and Pd/C composite was shown in **Figure 4.10.e**. It is known that the tafel slope value of Pt based catalyst was ~60 mV/dec in lower current density region and increase up to 120 mV/dec in higher current density region.[51] The Tafel slope of Pd-CN$_x$ was found to be 64 mV/dec whereas for Pt/C and Pd/C these values were 63 mV/dec and 69 mV/dec respectively. In addition, chronoamperometric measurements and long term cycling stability were performed to examine the stability of this composite in acid media. The comparison of J$_{MA}$ and J$_{SA}$ of Pd-CN$_x$ with Pd/C and Pt/C catalyst in 0.5 M HClO$_4$ electrolyte at 0.9V and 0.85 V was shown in **Figure 4.10.f**. It shows that the J$_{MA}$ of Pd-CN$_x$ at 0.9 V is 1.5

and 3.1 times higher than Pt/C and Pd/C respectively whereas Pd-CN$_x$ and Pt/C has comparable J$_{MA}$ value at 0.85 V (RHE). The J$_{SA}$ of Pd-CN$_x$ composite at 0.9 V was 1.4 times and 2.3 times higher as compared to the commercial Pt/C and Pd/C catalyst. This suggests the comparable catalytic activity of Pd-CNx and Pt/C towards ORR in acid medium. The J$_{SA}$ and J$_{MA}$ of Pd-CN$_x$ composite was also higher or comparable as compared to reported different Pd based catalyst[10, 36, 40] such as Pd/C octahedral,[10] Pd/C-HT.[10] The chronoamperometric measurement of different catalysts Pd-CN$_x$, Pt/C and Pd/C in 0.5 M HClO$_4$ was carried out at a constant potential of 0.68 V (RHE) as shown in **Figure 4.11.a** which shows that Pd-CN$_x$ composite loses only 32% of its initial current after 10h whereas Pt/C and Pd/C has lost 65% and 75% respectively of its initial current.

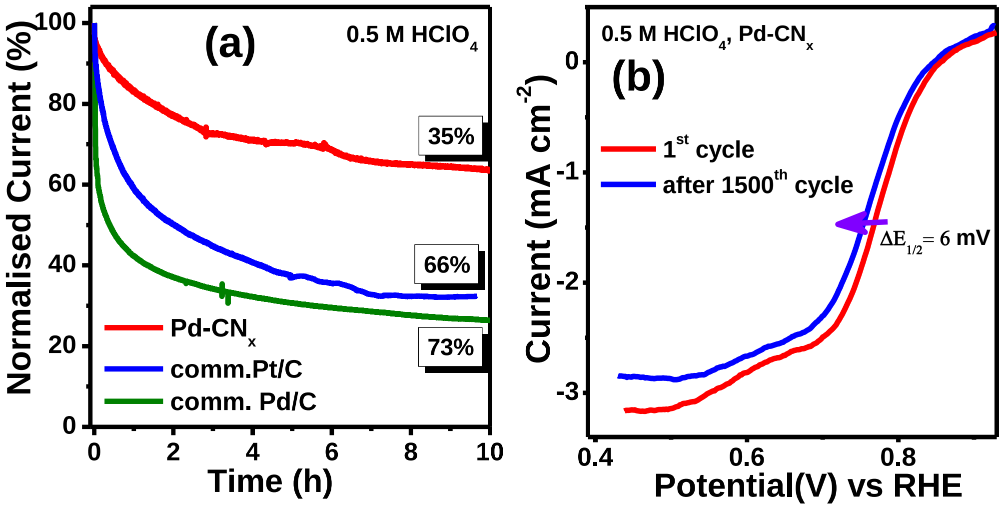

Figure 4.11. (a) Steady state chronoamperometric response of Pd-CN$_x$ composite in 0.5 M HClO$_4$. (b) LSV curve of Pd-CN$_x$ composite in O$_2$ saturated 0.5 M HClO$_4$ solution after and before 1500 LSV cycles with rotating speed 1600 rpm.

The LSV comparison of Pd-CN$_x$ catalyst before and after 1,500 cycles was shown in **Figure 4.11.b** which show only 6 mV negative shift of E$_{1/2}$ after 1,500 continuous cycles suggesting excellent long term stability of the Pd-CN$_x$ composite in acid media. The ORR activity of Pd-CN$_x$ composite was slight higher as compared to the activity in alkaline medium. Pan et al. reported[52] that the two different catalytic centers of Fe–N-doped graphene electrocatalysts are responsible for the ORR activities in acid and basic medium. The enhanced ORR activity in basic media was mainly because of presence quaternary N and Fe/Fe_3C sites, whereas Fe–N_x complexes were responsible for the ORR performance in acidic media. FT-IR (**Figure 4.5**) and XPS (**Figure 4.6**) studies confirmed that there is a strong interaction between Pd and C in Pd-CN_x composite. The CN_x support contains large number quandary nitrogen and PdC_x type complex are present in Pd-CN_x composite. Therefore, ORR activity of Pd-CN_x catalyst in alkaline media is thus higher than that of acid media. In addition, methanol crossover effect is one of the major drawbacks associated with methanol fuel cell for Pt/C catalyst. In an alcohol fuel cell the cathodic Pt/C catalyst is involved in the methanol oxidation reaction due to the presence of the methanol molecules. As a result of methanol oxidation reaction, the catalytic activity of the Pt/C catalyst decreases significantly and gradually obtained a mixed kinetics[15]. One of the important parameter of a superior electrocatalyst for ORR is methanol tolerance. **Figure 4.12.a** shows the CVs of Pt/C electrode in O_2 saturated 0.5 M KOH in presence and absence of methanol. The Pt/C catalyst shows a strong ORR peak at 0.81 V (when no methanol is present), whereas very strong methanol oxidation peak (0.83V) and very weak oxygen reduction peak (0.81 V) were observed in solution containing methanol molecules. But, the CVs of Pd-CN_x electrode in O_2 saturated 0.5 M KOH are almost identical in presence and absence of methanol (**Figure 4.12.b**). This result clearly proves that the porous Pd-CN_x catalyst exhibits superior ORR activity with a very good tolerance of cross-over effect of methanol. It is well known that Pt metals have higher dissociative adsorption power of methanol and different intermediate as compared to Pd metal.[2, 53] The methanol and its different dissociated intermediate generally block the active catalytic site of Pt surface. Therefore, the ORR activity in presence of methanol on Pt–surface is reduced drastically.

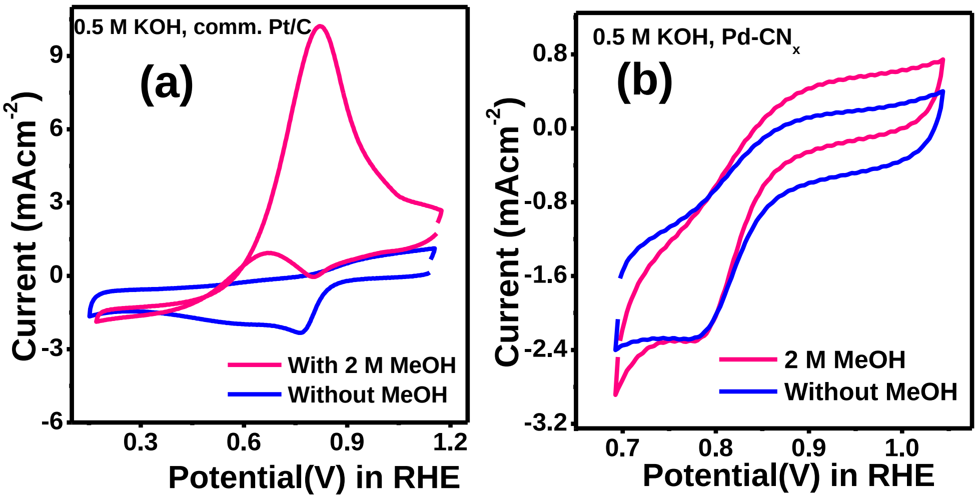

Figure 4.12. CVs of (a) Pt/C and (b) Pd-CN$_x$ in O_2 saturated 0.5 M KOH with and without methanol.

V.D.Noto and co-workers recently demonstrated[40] that the N-based ligand in CN$_x$ matrix easily prevent the adsorption of the poising molecules such as methanol during the ORR performance. The Pd-CN$_x$ composite exhibited very good tolerance towards methanol oxidation is probably due to presence of large number of nitrogen in CN$_x$ support. Thus Pd-CN$_x$ catalyst is better than the commercial available Pt/C catalyst in terms of ORR half wave potential, stability and methanol tolerances.

Factors Responsible for Superior ORR Activity of Pd-CN$_x$ Composite:

The electrochemical performances of porous Pd-CN$_x$ composite towards ORR are better than that of commercial Pt/C and Pd/C catalysts. The superior catalytic activity and long term durability of Pd-CN$_x$ towards ORR in both acidic as well as basic medium can be attributed to the several factors:

The superior catalytic activity of Pd-CN$_x$ composite towards ORR reaction can mainly be attributed to the shifting of d-band center of Pd. Generally, ORR occurred on metal by adsorption/desorption mechanism. First step is the formation of adsorbed oxygenated species (O_{ads}) on metal surface through the activation of O_2 by transferring both electron and proton, followed by breaking of O-O bond. Second step is desorption of oxygenated intermediated Products. Good ORR catalytic active catalyst should have high adsorption properties of the intermediate O_{ads} species and then easy desorption of the O_{ads} species. According to the d-band theory,[54] high energy laying d-band center has strong binding affinity with oxygen generated high surface coverage of oxygenated species On the other hand low laying d-band center has ability to easy desorption of the surface adsorbed oxygenated products. So catalyst should have optimum d-band center for efficient electrocatalytic activity. Several groups reported that Pd metal makes stronger bond with O_2 molecule due to higher laying d-band center and it formed 10 times stronger bond with O_{ads} intermediate than Pt metal. Thus high coverage of O_{ads} and slow the ORR kinetics as well as high overpotentials was observed. Valence d band center can be influenced by the two factors - (a) geometrical effect of structure and (b) ligand effect. Recently, R.R.Adzic and his co-worker reported[55] up-shifting of Pt d-band by making monolayer on Au(111) due to tensile strain, whereas down shifting of d-center was done by alloying with Ir(111). Several groups also reported[52-54] that the shifting of d-band center of Pd metal occurred by making bimetallic alloy with different foreign metals. The strong synergistic interactions between Pd and carbon in Pd-CN_x composite was reported recently by our group[37]. FT-IR and XPS studies of Pd-CN_x confirmed that there is strong interaction between carbon and Pd in Pd-CN_x composite. The BE of carbon and Pd was shifted in Pd-CN_x composite due to the synergistic interaction between Pd and CN_x support. The positive BE shifts of Pd suggests broadening of Pd d-band and down shifting of d-band center. Due to this down shifting of the d-band center, the Pd-O_{ads} bond strength was decreased and superior ORR activity was observed. In addition, Noto et al. demonstrated[27, 40, 51, 56] that the presence of nitrogen atoms in CN-based electrocatalyst helped to enhance the ORR activity due to bi-functional mechanism. The presence of nitrogen atoms in Pd-CN_x composite is also helped to enhance ORR performances. Several group reported[16-17, 45] the structure depend ORR reactions under acidic and basic condition. It was generally accepted that the activity of Pd decreases as Pd(100)> Pd(111)> Pd(110). The CV curve of Pd-CN_x composite has two strong anodic peak in H-desorption region where peak at lower potential assigned for Pd (111) facet and peak at higher potentials for Pd (100) facet as discussed earlier. So Pd-CN_x composite has electrochemically active Pd (100) facets along with Pd (111) facets.

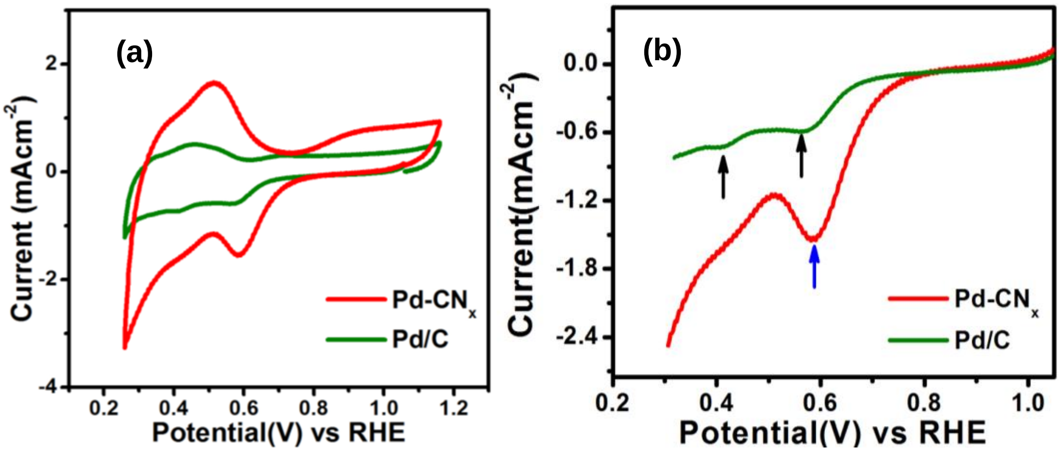

Figure 4.13. Cu stripping UPD spectra of Pd-CN_x composite and Pd/C in 0.05 M $HClO_4$ + 0.05 M $CuSO_4$ with scan speed 50 mV/sec: (a) full CV,(b) Cathodic part of CV.

The Cu stripping experiment was also performed to confirm the predominant active facets of Pd-NPs under electrochemical condition. The full CV comparison curve of Pd/C and Pd-CN_x composite for Cu stripping experiment was shown in **Figure 4.13.a**, which showed an anodic peak at 0.3 V, assigned for dissolution of under deposited Cu from Pd (111) or Pd (100) facet[57]. In addition, different groups reported to distinguish the Pd (111) and Pd (100) facets from cathodic peak position in Cu stripping experiment. It was stated that cathodic peak ~ 0.5 V (RHE) assigned for Pd (111) facet whereas peak position ~ 0.56 V (RHE) corresponding for Pd (100) facet. The cathodic CV portion of Cu stripping experiment was shown in **Figure 4.13.b**. Commercials Pd/C catalyst contained two cathodic peak due to polycrystalline nature of the catalyst whereas Pd-

CN_x composite has a single peak at ~ 0.59 V suggesting the presence of active Pd (100) facets. The active Pd (100) facets of Pd-CN_x catalyst under electrochemical condition enhance the catalytic activity towards ORR. In addition, low nitrogen content in the catalyst support g-CN_x and the porous morphology of this composite which helps easy mass transport of reactants and products are also helped to enhance the catalytic activity of Pd-CN_x.

4.5 Conclusions

In summary, we have demonstrated that the porous Pd-CN_x composite is a superior electrocatalysts than commercial Pt/C or Pd/C for electrocatalytic oxygen reduction in both basic and acid media. The ORR half wave potentials of Pd-CN_x is 60 mV more positive than that of Pt/C in basic medium. Although ORR activity of Pd-CN_x in acid media is comparable to Pt/C, but, its stability in both acid and basic media is much higher than Pt/C or Pd/C. The stability test showed a negligible decay of its catalytic activity on continuous cycling. The excellent catalytic activity and durability of Pd-CN_x composite is mainly due to the change of electronic structure of Pd metal (down shifting of d-centered band) resulting from synergistic interaction between Pd and C of CN_x support. The excellent ORR activity of Pd-CN_x composite with good durability and methanol tolerance are making them a promising electrocatalyst for fuel cells or other electrochemical devices.

4.6 References

1. Guo, L.; Jiang, W.-J.; Zhang, Y.; Hu, J.-S.; Wei, Z.-D.; Wan, L.-J., *ACS Catal.* **2015,** *5,* 2903-2909.
2. Shao, M., *J. Power Sources* **2011,** *196,* 2433-2444.
3. Yin, A.-X.; Min, X.-Q.; Zhang, Y.-W.; Yan, C.-H., *J. Am. Chem. Soc.* **2011,** *133,* 3816-3819.
4. Brocato, S.; Serov, A.; Atanassov, P., *Electrochim. Acta* **2013,** *87,* 361-365.

5. Kondo, S.; Nakamura, M.; Maki, N.; Hoshi, N., *J. Phys. Chem. C* **2009,** *113,* 12625-12628.

6. Lima, F. H. B.; Zhang, J.; Shao, M. H.; Sasaki, K.; Vukmirovic, M. B.; Ticianelli, E. A.; Adzic, R. R., *J. Phys. Chem. C* **2007,** *111,* 404-410.

7. Ding, W.; Li, L.; Xiong, K.; Wang, Y.; Li, W.; Nie, Y.; Chen, S.; Qi, X.; Wei, Z., *J. Am. Chem. Soc.* **2015,** *137,* 5414-5420.

8. Lee, C.-L.; Chiou, H.-P.; Liu, C.-R., *Int. J. Hydrogen Energy* **2012,** *37,* 3993-3997.

9. St. John, S.; Atkinson, R. W.; Dyck, O.; Sun, C.-J.; Zawodzinski, T. A.; Papandrew, A. B., *Chem. Commun.* **2015,** *51,* 16633-16636.

10. Shao, M.; Yu, T.; Odell, J. H.; Jin, M.; Xia, Y., *Chem. Commun.* **2011,** *47,* 6566-6568.

11. Jiang, L.; Hsu, A.; Chu, D.; Chen, R., *J. Electrochem. Soc.* **2009,** *156,* B643-B649.

12. Lee, C.-L.; Chiou, H.-P., *Appl. Catal. B: Environ.* **2012,** *117–118,* 204-211.

13. Chen, D.; Li, C.; Liu, H.; Ye, F.; Yang, J., *Sci. Rep.* **2015,** *5,* 11949.

14. Yang, T.; Ma, Y.; Huang, Q.; Cao, G., *Nano Energy* **2016,** *19,* 257-268.

15. Lv, J.-J.; Li, S.-S.; Wang, A.-J.; Mei, L.-P.; Feng, J.-J.; Chen, J.-R.; Chen, Z., *J. Power Sources* **2014,** *269,* 104-110.

16. Shao, M.-H.; Sasaki, K.; Adzic, R. R., *J. Am. Chem. Soc.* **2006,** *128,* 3526-3527.

17. Wang, X.; Vara, M.; Luo, M.; Huang, H.; Ruditskiy, A.; Park, J.; Bao, S.; Liu, J.; Howe, J.; Chi, M.; Xie, Z.; Xia, Y., *J. Am. Chem. Soc.* **2015,** *137,* 15036-15042.

18. Pan, Y.; Zhang, F.; Wu, K.; Lu, Z.; Chen, Y.; Zhou, Y.; Tang, Y.; Lu, T., *Inter. J. Hydrogen Energy* **2012,** *37,* 2993-3000.

19. Bhowmik, T.; Kundu, M. K.; Barman, S., *Inter. J. Hydrogen Energy* **2016,** 10.1016/j.ijydene.2016.05.295.

20. Pu, Z.; Liu, Q.; Tang, C.; Asiri, A. M.; Qusti, A. H.; Al-Youbi, A. O.; Sun, X., *J. Power Sources* **2014,** *257,* 170-173.

21. Deming, C. P.; Mercado, R.; Gadiraju, V.; Sweeney, S. W.; Khan, M.; Chen, S., *ACS Sustainable Chem. Eng.* **2015,** *3,* 3315-3323.

22. Xie, X.; Nie, Y.; Chen, S.; Ding, W.; Qi, X.; Li, L.; Wei, Z., *J. Mater. Chem. A* **2015,** *3,* 13962-13969.

23. Di Noto, V.; Negro, E.; Polizzi, S.; Riello, P.; Atanassov, P., *Appl. Catal. B: Environ.* **2012,** *111–112,* 185-199.

24. Li, S.-S.; Lv, J.-J.; Teng, L.-N.; Wang, A.-J.; Chen, J.-R.; Feng, J.-J., *ACS Appl. Mater. Interfaces* **2014,** *6,* 10549-10555.

25. Qi, K.; Zheng, W.; Cui, X., *Nanoscale* **2016,** *8,* 1698-1703.

26. Shao-Horn, Y.; Sheng, W. C.; Chen, S.; Ferreira, P. J.; Holby, E. F.; Morgan, D., *Top. Catal.* **2007,** *46,* 285-305.

27. Di Noto, V.; Negro, E.; Vezzù, K.; Bertasi, F.; Nawn, G., *Electrochem. Soc. Interface* **2015,** *24,* 59-64.

28. Jukk, K.; Alexeyeva, N.; Johans, C.; Kontturi, K.; Tammeveski, K., *J. Electroanal. Chem.* **2012,** *666,* 67-75.

29. Ge, X.; Goh, F. W. T.; Li, B.; Hor, T. S. A.; Zhang, J.; Xiao, P.; Wang, X.; Zong, Y.; Liu, Z., *Nanoscale* **2015,** *7,* 9046-9054.

30. Lin, Y.; Cui, X.; Ye, X., *Electrochem. Commun.* **2005,** *7,* 267-274.

31. Choe, J. E.; Ahmed, M. S.; Jeon, S., *J. Power Sources* **2015,** *281,* 211-218.

32. Geim, A. K., *Science* **2009,** *324,* 1530-1534.

33. Zhang, W.; Huang, H.; Li, F.; Deng, K.; Wang, X., *J. Mater. Chem. A* **2014,** *2,* 19084-19094.

34. Bhowmik, T.; Kundu, M. K.; Barman, S., *RSC Adv.* **2015,** *5,* 38760-38773.

35. Kundu, M. K.; Sadhukhan, M.; Barman, S., *J. Mater. Chem. B* **2015,** *3,* 1289-1300.

36. Feng, J.-J.; Chen, L.-X.; Song, P.; Wu, X.-l.; Wang, A.-J.; Yuan, J., *Inter. J. Hydrogen Energy* http://dx.doi.org/10.1016/j.ijhydene.2016.03.108.

37. Bhowmik, T.; Kundu, M. K.; Barman, S., *ACS Catal.* **2016,** *6,* 1929-1941.

38. Kundu, M. K.; Bhowmik, T.; Barman, S., *J. Mater. Chem. A* **2015,** *3,* 23120-23135.

39. Negro, E.; Polizzi, S.; Vezzù, K.; Toniolo, L.; Cavinato, G.; Di Noto, V., *Int. J. Hydrogen Energy* **2014,** *39,* 2828-2841.

40. Negro, E.; Vezzù, K.; Bertasi, F.; Schiavuta, P.; Toniolo, L.; Polizzi, S.; Di Noto, V., *ChemElectroChem* **2014,** *1,* 1359-1369.

41. Barman, S.; Sadhukhan, M., *J. Mater. Chem.* **2012,** *22,* 21832-21837.

42. Singh, K.; Seredych, M.; Rodriguez Castellon, E.; Bandosz, T. J., *ChemElectroChem* **2014,** *1,* 565-572.

43. Hulicova-Jurcakova, D.; Seredych, M.; Lu, G. Q.; Bandosz, T. J., *Adv. Funct. Mater.* **2009,** *19,* 438-447.

44. Wang, D.-W.; Li, F.; Yin, L.-C.; Lu, X.; Chen, Z.-G.; Gentle, I. R.; Lu, G. Q.; Cheng, H.-M., *Chem. Eur. J.* **2012,** *18,* 5345-5351.

45. Hitotsuyanagi, A.; Kondo, S.; Nakamura, M.; Hoshi, N., *J. Electroanal. Chem.* **2011,** *657,* 123-127.

46. Erikson, H.; Kasikov, A.; Johans, C.; Kontturi, K.; Tammeveski, K.; Sarapuu, A., *J. Electroanal. Chem.* **2011,** *652,* 1-7.

47. Lüsi, M.; Erikson, H.; Sarapuu, A.; Tammeveski, K.; Solla-Gullón, J.; Feliu, J. M., *Electrochem. Commun.* **2016,** *64,* 9-13.

48. Jukk, K.; Alexeyeva, N.; Sarapuu, A.; Ritslaid, P.; Kozlova, J.; Sammelselg, V.; Tammeveski, K., *Int. J. Hydrogen Energy* **2013,** *38,* 3614-3620.

49. Fu, G.; Liu, Z.; Chen, Y.; Lin, J.; Tang, Y.; Lu, T., *Nano Res.* **2014,** *7,* 1205-1214.

50. Erikson, H.; Sarapuu, A.; Alexeyeva, N.; Tammeveski, K.; Solla-Gullón, J.; Feliu, J. M., *Electrochim. Acta* **2012,** *59,* 329-335.

51. Di Noto, V.; Negro, E., *Electrochim. Acta* **2010,** *55,* 1407-1418.

52. Pan, F.; Zhao, Q.; Wang, J.; Zhang, J., *ChemElectroChem* **2015,** *2,* 2032-2040.

53. Antolini, E., *Energy Environ. Sci.* **2009,** *2,* 915-931.

54. Kitchin, J. R.; Nørskov, J. K.; Barteau, M. A.; Chen, J. G., *J. Chem. Phys.* **2004,** *120,* 10240-10246.

55. Zhang, J.; Vukmirovic, M. B.; Xu, Y.; Mavrikakis, M.; Adzic, R. R., *Angew. Chem. Int. Ed.* **2005,** *44,* 2132-2135.

56. Di Noto, V.; Negro, E.; Lavina, S.; Gross, S.; Pace, G., *Electrochim. Acta* **2007,** *53,* 1604-1617.

57. Kumar, A.; Buttry, D. A., *J. Phys. Chem. C* **2015,** *119,* 16927-16933.

Chapter 5

One Dimensional RuO_2 Nanowires on g-Carbon Nitride for Hydrogen and Oxygen Evolution Reactions at All pH Values

5.1 Abstract

Development of highly efficient and durable bifunctional electrocatalyst for hydrogen and oxygen evolution reactions (HER and OER) is essential for the efficient solar fuel generation. The commercial RuO_2 or IrO_2 based catalysts are highly active towards OER; but their poor stability under different operating conditions is the main obstacle for their commercialization. Herein, we report growth of one dimensional highly crystalline RuO_2 nanowires on carbon nitride (1D-RuO_2-CN_x) for their applications in HER and OER at all pH values. The 1D-RuO_2-CN_x, as an OER catalyst, exhibits low onset overpotential of ~ 200 mV in both acidic and basic media whereas Tafel slopes are 52 mV/dec and 56 mV/dec in acidic and basic media respectively. This catalyst requires low overpotential of 250 mV and 260 mV to drive the current density of 10 mA/cm^{-2} in acidic and basic media respectively. The mass activity of 1D-RuO_2-CN_x catalyst is 352 mA mg^{-1} which is ~14 time higher than that of commercial RuO_2. Most importantly, the 1D-RuO_2-CN_x catalyst has remarkably higher stability in compare to commercial RuO_2. This catalyst also exhibits superior HER activity with current density of 10 mA cm^{-2} at ~93 and 95 mV in acidic and basic media. The HER Tafel slopes of this catalyst are 40 mV/dec in acidic condition and 70 mV/dec in basic condition. The HER activity of this catalyst is slightly lower than Pt/C in acid media whereas in basic media is comparable or even well than that of Pt/C at higher over-potentials. This superior catalytic activity of 1D-RuO_2-CN_x composite can be attributed

to catalyst-support interaction, enhanced mass and electron transport, one dimensional morphology and highly crystalline rutile RuO_2 structure.

5.2 Introduction

To solve energy crisis and environmental problem, world-wide efforts are going on to find renewable energy sources alternative to fossil fuels.[1-2] Hydrogen is considered as one of most clean renewable energy source, alternative to fossil fuel.[3-4] Overall water splitting to produce molecular hydrogen is a promising method to store solar/ electric energy into chemical fuels[5] as H_2. The water splitting consists of two half cell reactions[6] such as hydrogen evolution reaction (HER) and oxygen evolution reaction (OER). Without any suitable catalyst both the processes are very slow. Apart from H_2 storage application, HER/OER catalysts are also directly coupled with various renewable energy conversion and storage systems[7-8] such as metal-air batteries, fuel cells, solar cells etc. OER is a bottleneck process for water splitting because of its sluggish kinetics due to multi step proton couple electron transfer process.[9] Although RuO_2 and IrO_2 are highly active electro-catalysts for OER reaction, IrO_2 is preferred as state of art catalyst for OER.[10] The both the state-of-art catalysts[11] show quite larger OER over-potentials as compared to the theoretical value of 1.23 V. The reduction of large overpotential to reach appreciable current density for OER is the major challenge of electrochemical water splitting which is obstacle for development of renewable energy conversion devices. The carbon supported platinum (Pt/C) is a state art catalyst for HER. Although Pt/C is highly active acid media, but, its activity in basic media is two order less as compared to acid media.[12] The slow kinetics of Pt/C towards HER in basic media restricted fuel efficiency and large amount Pt-catalyst is needed in basic media.[13-14] In addition, long term durability of Pt/C catalyst in strong oxidizing condition is another obstacle for its commercialization. The catalysis of HER as well as

OER processes in the same medium is attractive, since only one catalyst can be used for their integration. It is known that almost all good OER[15-19] catalysts are active mainly in basic media whereas good HER catalysts[20-24] perform well in acid media. Some HER catalysts[25-28] are active in acid, basic and neutral medium; but OER catalysts[29] which are active in all pH, are relatively very rare. It is thus highly desirable to find superior bi-functional catalysts for OER and HER to make an efficient overall water splitting, which can work effectively at all pH values. In addition, synthesis of highly crystalline one dimensional RuO_2 is important since ruthenium oxide is an attractive electrode material for various applications[30-33] due to its high conductivity, high catalytic activity, chemical stability etc. Although several methods are known for synthesis of RuO_2 nanowires are such as using template,[34] CVD,[35] reactive sputtering;[30] it is still remains a challenge to synthesize highly crystalline 1D RuO_2 nanowires, specially 1D-RuO_2 on carbon support. The metal oxide based HER catalyst is always advantageous over metallic HER catalyst such as Pt since metal oxides are less sensitive towards poisoning by under potential deposition (UPD) phenomena which affects stability of a electrocatalyst.[36] The RuO_2 or its composites are moderately active towards HER reported by several groups.[36-39] For example, Trasatti and co-workers first time investigated[40] the HER properties of RuO_2. Mayrhofer and co-workers reported[41] a comparative HER and OER study between Ru, RuO_2, Ir and IrO_2 nanoparticle. Although OER activity of RuO_2 is better than the IrO_2 but much higher stability of IrO_2 is making it a preferred state-of-art catalyst. The Poor stability of RuO_2 is due to the formation less stable RuO_4. In addition the cost of RuO_2 is also another problem of their commercialization.[42] To reduce the cost, nanostructures of RuO_2 for OER have been widely studied in recent years.[43-46] It is thus essential to enhance long term stability of the RuO_2 based catalyst without affecting its catalytic activity.

Herein, we report a facile thermal method for the growth of single crystalline one dimensional RuO_2 nanowire on carbon nitride support (1D-RuO_2-CN_x). This 1D-RuO_2-CN_x compo-site is also highly active towards both HER and OER in all pH range. The HER activity of 1D-RuO_2-CN_x slightly lower than Pt/C in acid and is comparable to commercial Pt/C in basic media. This catalyst needs low overpotential of ~ 93 mV and 95 mV to achieve current density of 10 mA cm^{-2} for HER in both acid and base media. The OER activity of 1D-RuO_2-CN_x composite in both acid and basic media is better than that of state of art catalyst RuO_2 or IrO_2. This catalyst show low OER overpotential of 250 mV at 10 mA cm^{-2} and small Tafel slopes (52 mV/dec in acid and 56 mV/dec in base), which are better than the state of art catalysts. The mass activity of this catalyst (352 mA mg_{ox}^{-1}) is ~14 times higher than commercial RuO_2. This catalyst also exhibited excellent stability for both HER and OER in all pH solutions. The superior OER and HER performances of this catalyst make CN_x supported 1D-RuO_2 catalyst one of the best catalysts for water splitting.

5.3 Experimental Section

Synthesis of Graphitic Carbon Nitride (g-C_3N_4):

Formamide was used as precursor for synthesis of graphitic carbon nitride (g-C_3N_4) as previously reported by our group.[47-48] In a typical procedure, 30 ml formamide was taken in 100 ml three-neck round bottom flask (RB) fitted with temperature controlled probe and heated at 180 °C for 180 min by constant irradiation of microwave (300 watt). A brown color solution was obtained from colorless formamide and the resulting brownish solution, thus obtained was evaporated at 180 °C in a rotary evaporator to get bulk amount black solid product. Then this black solid product was washed 3 to 4 times with de-ionised (DI) water to remove un-reacted formamide and dried in a vacuum to obtain desired solid g-C_3N_4.

Synthesis of RuNPs-CN_x Composite:

RuNPs-CN_x composite was synthesized by sodium borohydride mediated hydrothermal reduction of ruthenium chloride ($RuCl_3$, xH_2O) in presence of g-C_3N_4. In briefly, 5 mg solid g-C_3N_4 was dispersed in 2 ml of DI water in a 30 ml sample glass vial and then 4 ml of 0.12 mmol aqueous solution of $RuCl_3$, xH_2O was poured into aqueous suspension of the g-CN_x. The mixed suspension was sonicated in a bath sonicator operating at 60 Hz for proper mixing. After that the suspension was transferred into a 100 ml seal tube and heated in an oil bath. When the temperature of the oil bath was reached at 65 °C, 2 ml of 1.58 mmol $NaBH_4$ was added to this suspension and kept for heating at 120 °C for 8 hrs with continuous stirring. After the completion of the reaction, the sealed tube was cooled down to room temperature. The suspension was then centrifuged at 16000 rpm for 20 min and dried in a vacuum. A solid black product was obtained after drying and named as RuNPs-CN_x composite.

Synthesis of 1D-RuO_2-CN_x Composite:

1D-RuO_2-CN_x was synthesized from prepared RuNPs-CN_x composite by thermal heating treatment. In details, the prepared RuNPs-CN_x composite was taken in an alumina crucible and subjected to heat at 350 °C in hot air oven with temperature accuracy ± 10 °C for 12 hrs. After 12 hours, it was cooled down to room temperature normally and resulting a black solid product. This product was washed with DI water twice and dried in vacuum and finally obtained the 1D-RuO_2-CN_x composite.

Electrode Preparation:

In details to prepare the catalyst modified GC electrode, 1.5 mg of 1D-RuO_2-CN_x (81 wt% RuO_2)was dispersed in 1 ml water by ultrasonication for 30 min and then 10 µl of the catalyst suspension was drop casted onto the GC electrode and drying at 60^0C. So loading on the electrode surface was obtained as 0.012 mg RuO_2 in 1D-RuO_2-CN_x.

Commercial RuO_2 modified GC electrode was prepared by directly making an aqueous suspension of RuO_2 and drop casting on GC electrode. In a typical procedure 1.2 mg commercial RuO_2 directly dispersed in 1 ml aqueous suspension and drop casting 10 µl aqueous suspension on GC electrode in ambient temperature. The comm. RuO_2-CN_x was prepared by homogeneously mixing 1.6 mg commercial RuO_2 and 0.4 mg g-C_3N_4 in solid state at room temperature. Comm. RuO_2-CN_x modified GC electrode was prepared by drop casting 10 µl aqueous suspension from a 1ml of 1.5 mg/ml aqueous suspension of comm.RuO_2-CN_x. In all the electrochemical experiment was performed with 0.012 mg RuO_2 loading on the GC electrode.

5.4 Results and Discussion

Characterization of 1D-RuO_2-CN_x Composite:

The one dimensional ruthenium oxide nanowires supported on carbon nitride (1D-RuO_2-CN_x) was prepared by a facile two steps method. In the 1st step, highly dispersed RuNPs on g-CN_x sheets was formed by hydrothermal sodium borohydride reduction of $RuCl_3$ in aqueous suspension of g-CN_x on a sealed tube at 120 °C. Then, thermal oxidation of this RuNPs-CN_x composite at 350 °C in air for 12 hrs leads to the growth highly crystalline RuO_2 nanowires on CN_x sheets. The p-XRD patterns of RuNPs-CN_x and 1D-RuO_2-CN_x composite were shown in **Figure 5.1**. The calculated diffraction pattern of RuO_2 (PDF #00-043-1027) and Ru (PDF #00-006-0663) were also given in for comparison. The diffraction peaks at 44.00^0, 58.32^0, 69.40^0, 78.39^0 and 84.70^0 corresponding to (101), (102), (110),(200) and (112) plane of metallic ruthenium(PDF #00-006-0663).

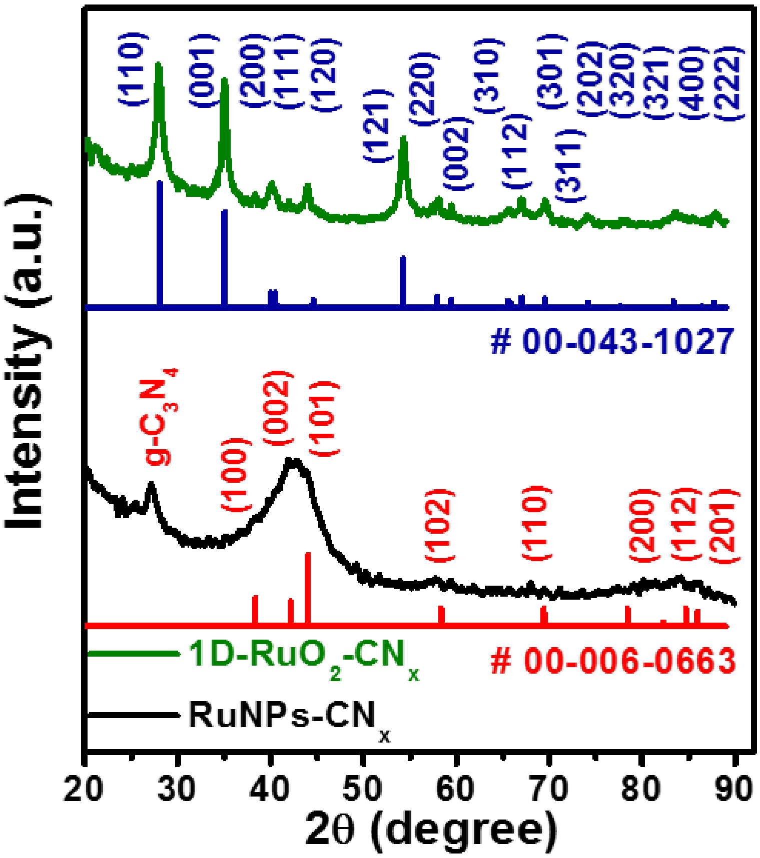

Figure 5.1. p-XRD patterns of RuNPs-CN_x and 1D-RuO_2-CN_x composite.

In addition, a diffraction peak at 27.3^0 of graphitic (002) plane of g-C_3N_4 was also present.[47, 49] The XRD pattern of 1D-RuO_2-CN_x nanowire showed diffraction peaks at 2θ values of 28.02^0, 35.06^0, 40.032^0, 40.54^0, 45.09^0, 54.24^0, 58.10^0, 59.38^0, 65.55^0, 66.98^0, 69.64^0, 72.24^0, 74.10^0, 76.14^0, 77.92^0, 83.52^0, 85.54^0 and 87.83^0 corresponding to (110), (101), (200), (111), (210), (211), (220), (002),(310), (112), (301), (311), (202), (320), (212), (321), (400) and (222) lattice plane respectively of RuO_2 (PDF #00-043-1027). The XRD pattern of 1D-RuO_2-CN_x confirmed the formation of crystalline tetragonal rutile ruthenium oxide (r-RuO_2) (space group $P4_2/mnm$) after annealing at 350 °C. This confirmed that growth of crystalline RuO_2 occurs due to the calcinations of RuNPs-CN_x at 350 °C in air. We have also prepared 1D-RuO_2-CN_x slightly lower temperature at 330 °C. The morphology of these two composites was studied using electron microscopic techniques.

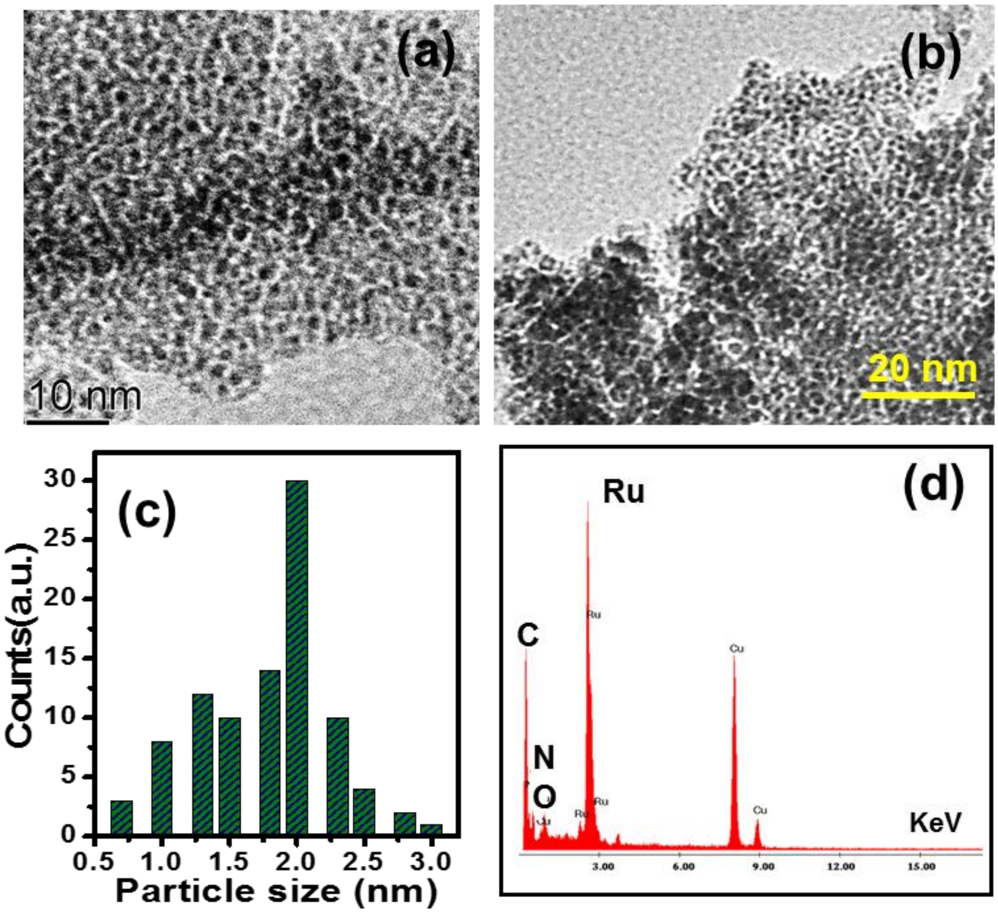

Figure 5.2. (a-b) TEM images, (c) Size distribution plot of RuNPs and (d) TEM EDS plot of RuNPs-CN_x composite.

The transmission electron microscopy (TEM) images of RuNPs-CN_x have shown in **Figure 5.2.a** and **Figure 5.2.b**. These TEM images show that ultra-small Ru nanoparticles are uniformly dispersed on the g-CN_x sheets. The size of these RuNPs varies from 0.5 nm to 2.5 nm with the average diameter of 1.5 nm (**Figure 5.2.c**). The Electron Dispersive Spectroscopy (EDS) profiles which were taken on TEM grid and Si wafer (**Figure 5.2.d**) showing the presence of carbon (C), nitrogen (N), ruthenium (Ru) and small amount of oxygen (O) confirming presence of RuNPs on CN_x sheets.

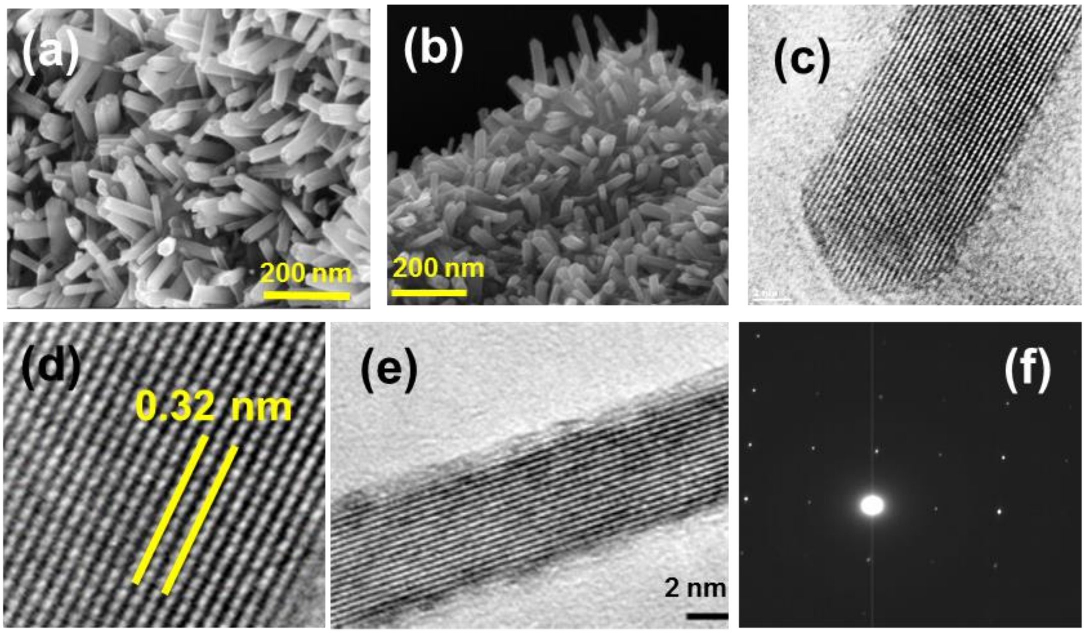

Figure 5.3. (a-b) FESEM images of 1D-RuO_2-CN_x. (c-e) HRTEM images of a single RuO_2 nanowire. (f) SEAD profile of the corresponding RuO_2 nanowire.

Figure 5.3.(a,b) represents the FESEM images of the 1D-RuO_2-CN_x composite. The 1D nanowire of RuO_2 are clearly seen and these RuO_2 nanowire are randomly grown with high density on the CN_x surface. The RuO_2 nanowire is straight and arranged randomly due to high density; one end of nanowire is facing outside as shown in **Figure 5.3.b**. The lateral diameters of the nanowire are found to be between 10 to 40 nm and their length varies ranging from 100 nm to 200 nm. The high resolution TEM images of two different RuO_2 nanowire were shown in **Figure 5.3.d** and **5.3.e**. These HRTEM images show highly order lattice fringes with the interlayer distance 0.32 nm corresponding to (110) plane of RuO_2. The SEAD profile RuO_2 is also shown in **Figure 5.3.f**. The HRTEM image and SAED image confirmed that RuO_2 nanowire have single crystalline structure. When RuNPs-CN_x composite was heated at 330 $^{\circ}$C, thin nanowires were formed; the diameter and length of the nanowires decreased as shown in **Figure 5.4.(a-d)**. The diameter of the thin wires from 5 to 15 nm and their length were in between 60 to 150 nm.

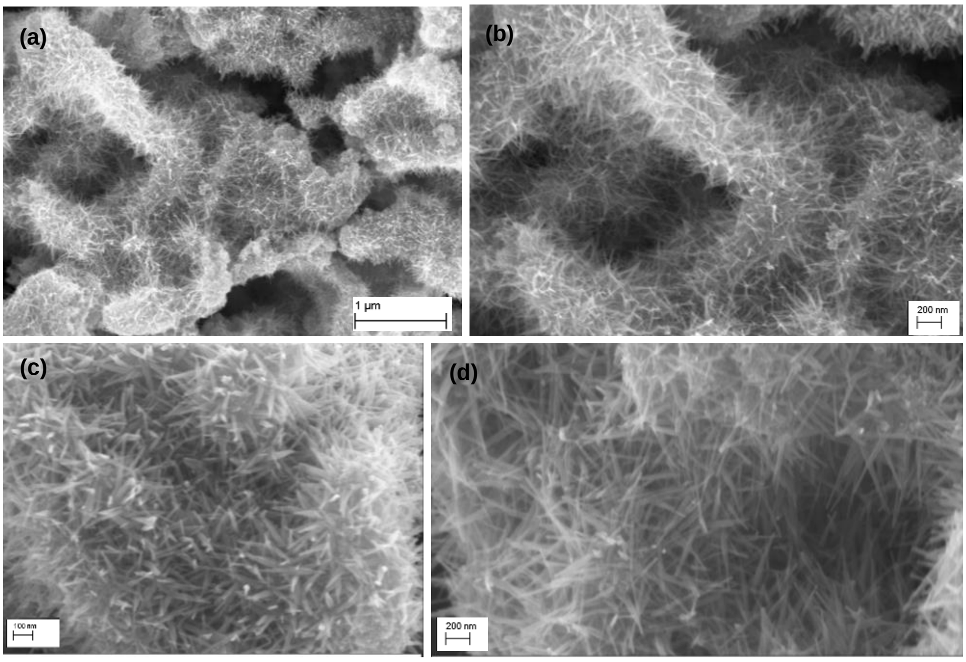

Figure 5.4. (a-d): FESEM images of 1D-RuO_2-CN_x composite synthesised at 330 °C.

This suggests that length and diameter of RuO_2 nanowire depends on calcination temperature. The EDS mapping of 1D-RuO_2-CN_x was shown in **Figure 5.5.(a-e)**. It is clearly shows Ru,C,N and O are uniformly distributed in the composite materials.

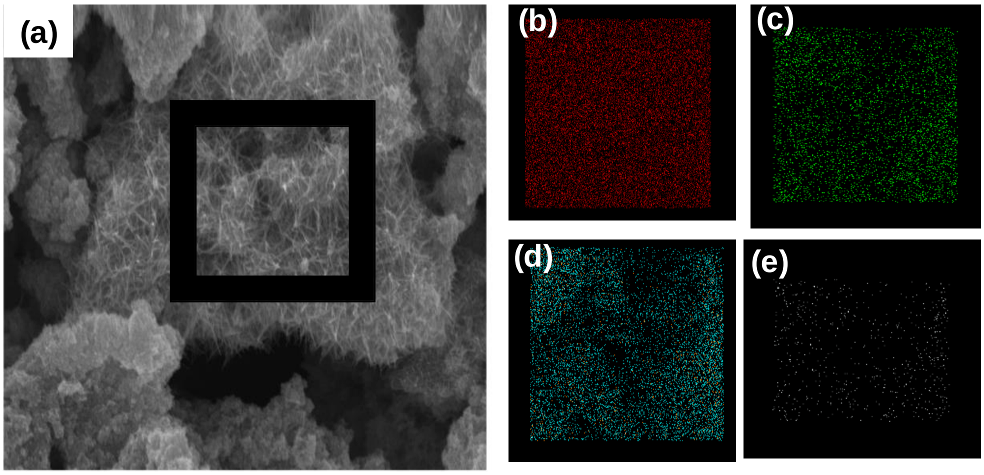

Figure 5.5. (a) FESEM image and corresponding mapping for element (b) Ruthenium, (c) Oxygen, (d) Carbon, (e) Nitrogen.

The elemental atomic percentage of 1D-RuO_2-CN_x was displayed in **Table 5.1** showing Ru:O atomic ratio was 1: 2.4.

Table 5.1. Summary of EDS results of 1D-RuO_2-CN_x in terms of atomic weight percentage.

Catalyst	Carbon (%)	Nitrogen (%)	Ruthenium (%)	Oxygen (%)
1D-RuO_2-CN_x	10.12	5.67	24.41	59.81

The 1D-RuO_2-CN_x nanowire was further characterized by using X-ray photo electron spectroscopy (XPS) and Raman spectroscopy. The XPS survey scan spectrum of 1D-RuO_2-CN_x composite was shown in **Figure 5.6.a.**

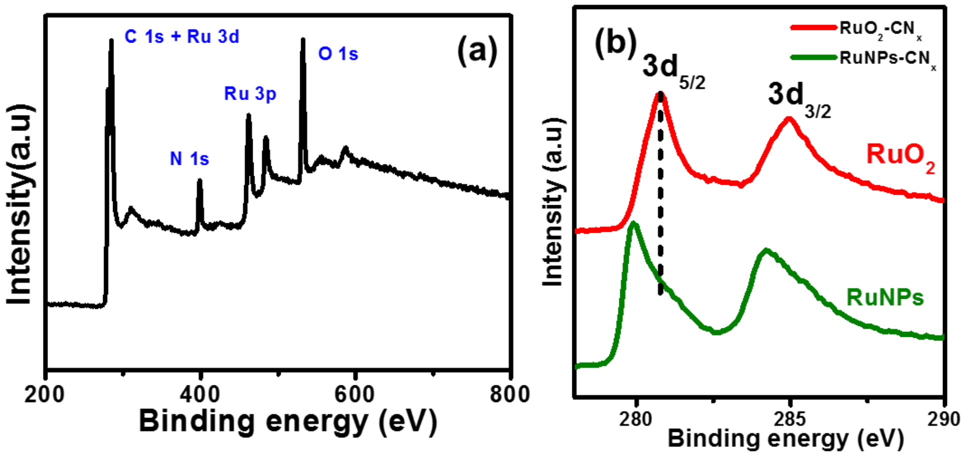

Figure 5.6. (a) Survey scan XPS spectra of 1D-RuO_2-CNx composite. (b) Comparison of high resolution 3d XPS spectra of Ru for RuNPs-CN_x composite and 1D-RuO_2-CN_x composite.

It is known that $3d_{5/2}$ and $3d_{3/2}$ peaks of metallic ruthenium generally appeared[50] at 280.0 and 284.7 eV respectively and for pure ruthenium oxide $3d_{5/2}$ and $3d_{3/2}$ peaks generally appeared[31, 51] at 280.8 and 285.2 eV respectively. The 3d Ru XPS spectrum of RuNPs-CNx and 1D-RuO_2-CN_x composites are presented in **Figure 5.6.b**. For RuNPs-CN_x the two peaks at 279.9 and 284.4 eV can be attributed to metallic ruthenium whereas two peaks at 280.7 eV and 284.9 eV for 1D-RuO_2-CN_x composites can attributed to $3d_{5/2}$ and $3d_{3/2}$ peaks of rutile RuO_2.

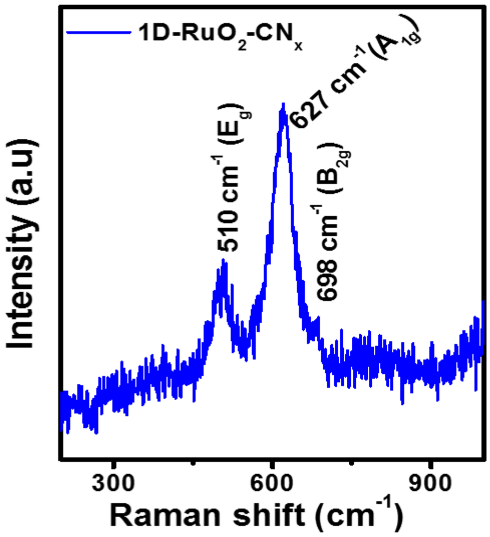

Figure 5.7. Raman spectrum of 1D-RuO$_2$-CN$_x$ composite.

As shown in **Figure 5.7**, Raman spectrum of composite exhibited three characteristic peaks at 507, 627 and 701 cm^{-1},which can be attributed to E$_g$, A$_{1g}$ and B$_{2g}$ phonon bands of rutile RuO$_2$.[30] Above measurements (XRD, TEM, SEM, XPS, Raman spectroscopy) confirmed the growth of single crystalline rutile RuO$_2$ nanowire on CN$_x$ support.

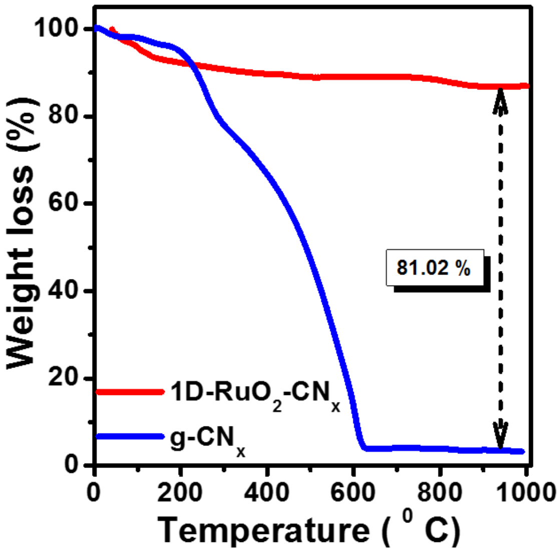

Figure 5.8. TGA plot of 1D-RuO$_2$-CN$_x$ and g-CN$_x$ in 20 ml/min Ar atmosphere with temperature ramping 10 °C/min.

Table 5.2. Details and summarized CHN results.

Catalyst	Carbon (C) wt.%	Nitrogen (N) wt.%	Hydrogen (H) wt.%	N:C ratio
Free g-CN_x	43.13	47.3	3.79	1.09
1D-RuO_2-CN_x	10.17	5.51	2.32	0.49

Here, g-CN_x layers are use as template for growth one directional RuO_2 nanostructures. At 350 °C, small Ru-NPs are oxidized in air to form RuO_2 and then preferential unidirectional growth of RuO_2 leads to formation of one dimensional tetragonal RuO_2 nanostructures. The amount of RuO_2 loading in the composite was measured by TGA measurement (**Figure 5.8**) and found that it was 81%. The CHN analysis suggest the N:C ratio in 1D-RuO_2-CN_x was found to be 0.49 whereas in the free g-CN_x ratio was 1.09 (**Table 5.2**).

OER Activity on 1D-RuO_2-CN_x Electrode:

OER activity of 1D-RuO_2-CN_x composite was performed in acidic, basic and neutral medium. Frist we examined OER activity in acidic medium, since polymer electrolyte membrane (PEM) water splitting which works under strong acidic condition, has some advantages over alkaline electrolyte membrane water splitting such as easy operation, high power density and high energy efficiency.[52-53] In addition, poor stability of most of the noble metal catalyst under PEM environment is another problem in PEM cell. The catalytic activity of 1D-RuO_2-CN_x composite towards oxygen evolution reaction (OER) was carried out in oxygen saturated 0.5 M H_2SO_4 electrolyte solution. As shown in **Figure 5.9.a**, the OER LSV polarization curves of 1D-RuO_2-CN_x, RuNPs-CN_x were performed at scan speed of 10 mv/sec with 1600 rpm rotation speed in O_2 saturated 0.5 M H_2SO_4 solution.

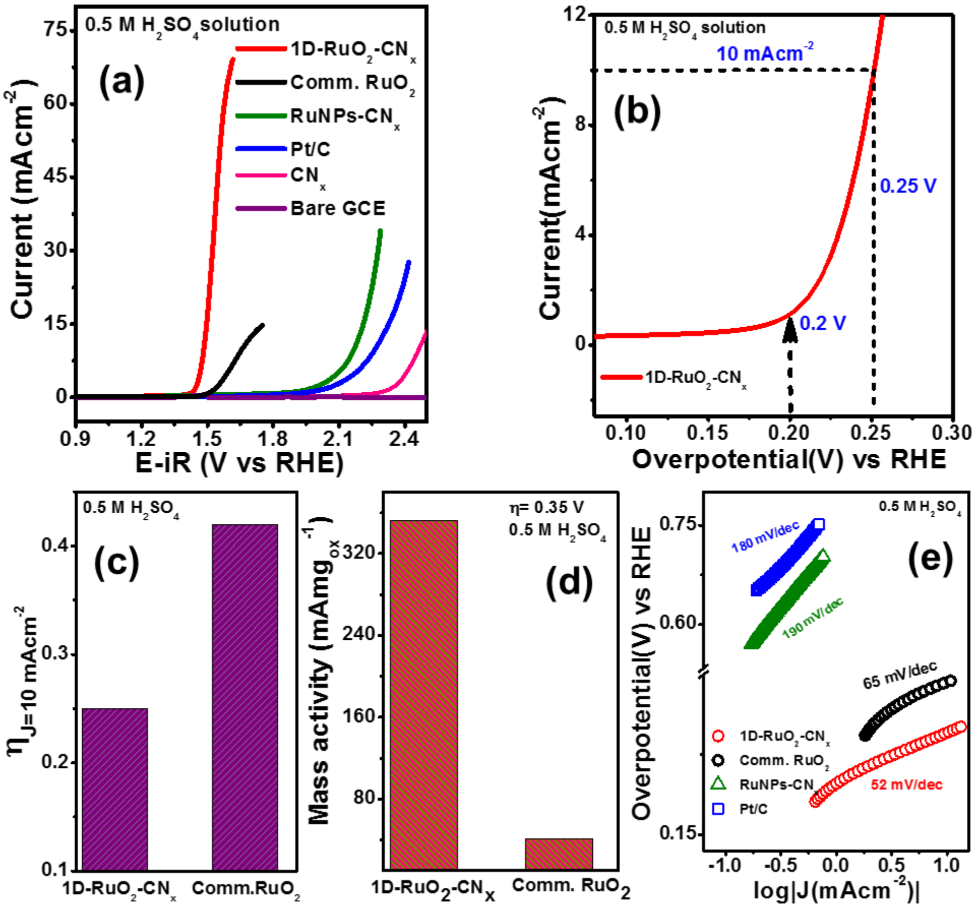

Figure 5.9. (a) LSV curves of 1D-RuO_2-CN_x comm. RuO_2, RuNPs-CN_x, Pt/C, g-CN_x and bare GC electrode in O_2 saturated 0.5 M H_2SO_4 electrolyte (Scan rate: 10 mV/sec). (b) LSV curve of 1D-RuO_2-CN_x showing onset potentials. Comparision of (c) $\eta_{10\ \mathrm{mAcm}^{-2}}$ (d) mass activity at η=0.35 overpotentials for comm. RuO_2 and 1D-RuO_2-CN_x in 0.5 M H_2SO_4 medium.(e) Tafel plot of different catalysts in 0.5 M H_2SO_4.

The OER activities of commercial RuO_2, Pt/C, CN_x, and bare GC were also measured for comparison under similar condition. **Figure 5.9.a** shows poor OER activates of GC and CN_x electrode. The Pt/C and RuNPs-CN_x catalysts showed moderate OER activity, but commercial RuO_2 and 1D-RuO_2-CN_x exhibited much higher OER activity. The 1D-RuO_2-CN_x catalyst exhibits low onset potentials of 200 mV which is 60 mV lower than that of commercial RuO_2 (**Figure 5.9.b**). The OER activity of these catalysts was further evaluated by comparing the overpotential required to obtain the current density of 10 mA cm^{-2} and shown in **Figure 5.9.c**. To reach the current density 10 mA cm^{-2}

overpotential required for 1D-RuO_2-CN_x and comm. RuO_2 are 250 mV and 344 mV respectively. The 1D-RuO_2-CN_x catalyst requires 94 mV lower overpotential than commercial RuO_2 to achieve 10 mA cm^{-2} current density. The comparison of mass activity of this catalyst with comm. RuO_2 is shown in **Figure 5.9.d**. The mass activity of this RuO_2-CN_x catalyst is 352 mA mg_{ox}^{-2} which is ~14 times higher than that of commercial RuO_2 (25.4 mA mg_{ox}^{-2}) at 0.35 V overpotential. The Tafel slope (log (J) vs V plot), an intrinsic property of electro-catalyst is important to get an insight of OER mechanism on the catalyst. Several groups reported[54-55] reported that the Tafel slope of polycrystalline RuO_2 nanoparticle should be 30 - 60 mV/dec at lower potential region of <1.52 V. Recently Lui et al.[56] theoretically calculated value of the Tafel slope for single crystalline RuO_2 (110) was 55 mV/dec in lower over potentials region. The experimentally found value[55] of Tafel slope for single crystalline RuO_2 (110) face was 59 mV/dec . The Tafel plot of different catalysts was shown in **Figure 5.9.e**. Tafel slope of this 1D-RuO_2-CN_x catalyst was 52 mV/dec (linear fitting between overpotentials between 0.18 V to 0.23 V) which is lower than that of commercial RuO_2 (65 mV/dec). The Tafel slope value of 1D-RuO_2-CN_x composite is close to theoretically calculated of Tafel slope of RuO_2(110) facet. J.Rossmeisl and his co-worker proposed[57] a four step reaction mechanism for OER in transition metal oxide. Very recently Z.P.Lui and his co-workers studied[56] the OER mechanism on RuO_2 (110) above and below 1.58 V by using DFT studies.

Table 5.3. Comparison of OER activity of different catalyst in 0.5 M H_2SO_4 solution.

Catalyst	Onset potential (V in RHE)	$\eta_{10\ mAcm^{-2}}$ (mV)	$J_{\eta=0.35V}$ ($mAcm^{-2}$)	Tafel slope (mV/dec)	TOF at η= 0.35 V (s^{-1})
1D-RuO_2-CN_x	1.43	1.48	47.82	52	0.0961
Comm. RuO_2	1.48	1.66	3.16	65	0.0063
Pt/C	1.75	2.21	0.32	180	0.00064

According to Lui et al.[56], OER on RuO_2 (110) at overpotential below 1.58 V takes place on mixed OH/O terminal phase. The oxygen evolution reaction on ruthenium oxide electrode occurs in acid media via several steps. The OER reaction occurs below 1.58 V on a mixed OH/O phase. Frist the OH/O mixed phase converts to O-terminated phase locally. Second step which is rate determining step, is the water dissociation on two surfaces O_s , O_{br} and O_t (Eley-Riedeal like mechanism) where O_{br} and O_t are the bridging and terminate oxygen atom on RuO_2 structure respectively. Water provides its H to O_{br} and OH of water bonds with O_t-Ru_{5c} to form H-O_{br} and HOO_t-Ru_{5c} where Ru_{5c} is co-ordinately unsaturated penta-coordinated Ru atom in RuO_2 structure. The third step is the release of H as a proton in to solution from HOO_t-Ru_{5c} to form adsorbed OO_t-Ru_{5c} species.

Table 5.4. Comparison of OER activity of different catalysts with 1D-RuO_2-CN_x on GC electrode in acidic and PBS medium.

Catalyst	Electrolyte	Current density ($mAcm^{-2}$)	Over potentials (mV)	Reference
IrO_2 (350ºC)	0.1M $HClO_4$	0.5	260	*J. Phys. Chem. Lett.* **2012**, *3*, 399-404[44].
IrO_2-mesopours templet	0.5 M H_2SO_4	0.5	228	*ChemSusChem* **2015**, *8*, 1908-1915[58].
RuO_2	0.1 M $HClO_4$	13	470	*J. Phys. Chem. Lett.* **2012**, *3*, 399-404[44]
$Ru_{0.2}Ir_{0.8}O_2$	0.5 M H_2SO_4	10	1.62	*Appl. Catal. B: Environ.* **2012**, *111–112*, 376-380[33].
IrO2@RuO_2	0.5 M H_2SO_4	11	270	*J. Phys. Chem. C* **2016**, *120*, 2562-2573[10].
$Ru_{0.7}Ir_{0.3}O_2$	0.5 M H_2SO_4	9	270	*Int. J. Hydrogen Energy.* **2014**, *39*, 16785-16796[43].
1D-RuO_2-CN_x	**0.5 M H_2SO_4**	**10**	**250**	**This work**
1D-RuO_2-CN_x	**0.1 M PBS**	**10**	**356**	**This work**

The final step is the release of O_2 molecule to form free vacant Ru_{5c} site where a water molecule can again adsorb and continued the reaction. Turnover frequency (TOF) of a catalyst is the catalytic activity per active site basis, an intrinsic property of a catalyst.[59] The TOF value of 1D-RuO_2-CN_x composite, comm. RuO_2 and Pt/C was calculated at $\eta = 0.35$ V in acid medium and shown in **Table 5.3.** In 0.5 M H_2SO_4 electrolyte solution TOF value of 1D-RuO_2-CN_x catalyst (0.0961 O_2 s^{-1}) is 15 times higher that of commercial RuO_2. The OER activity of the catalyst was compared with the different reported catalyst in acidic medium as shown in **Table 5.4**. These results suggest an outstanding OER activity of this 1D-RuO_2-CN_x catalyst in acidic medium. **Figure 5.10.a** shows the iR-corrected OER LSV curves of different catalysts in 0.5 M KOH electrolyte. The onset potential of 1D-RuO_2-CN_x composite was 190 mV which is 40 mV lower (more negative potential) than that of commercial RuO_2 (250 mV) (**Figure 5.10.b**). This catalyst exhibits current density of 10 mA cm^{-2} at 260 mV which is 70 mV lower than that of commercial RuO_2 (330 mV). The corresponding Tafel slope is shown in **Figure 5.10.c**. The Tafel slope value of 1D-RuO_2-CN_x composite in basic media was 56 mV/dec which was lower than the value for commercial RuO_2, RuNPs-CN_x and Pt/C.

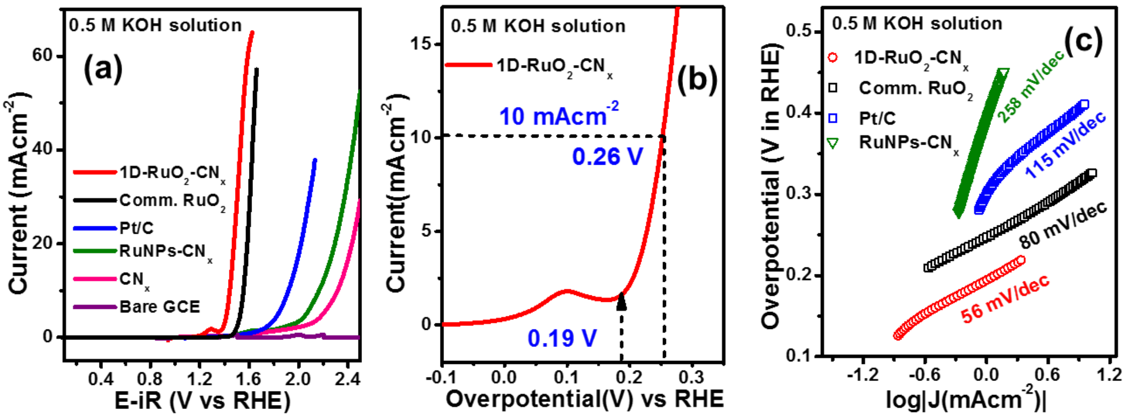

Figure 5.10. (a) LSV curves of 1D-RuO_2-CN_x comm. RuO_2, RuNPs-CN_x, Pt/C, g-CN_x and bare GC electrode in O_2 saturated 0.5 M KOH electrolyte (Scan rate: 10 mV/sec). (b) LSV curve of 1D-RuO_2-CN_x showing onset potentials and overpotential for 10 $mAcm^{-2}$ current density.(c)Tafel plot of different catalyst in 0.5 M KOH electrolyte.

In addition the Tafel slope value of 1D-RuO_2-CN_x composite was good agreement with the theoretical calculated[56] Tafel value of RuO_2(110). Recently Doyle et al. proposed[60] a reaction mechanism for OER reaction on RuO_2 in alkaline medium.[61] The reaction steps are discussed details in Electrochemical Characterizations. The low Tafel slope value of 56 mV/dec for 1D-RuO_2-CN_x composite suggested that 3rd setp is the rate determine step for OER of 1D-RuO_2-CN_x catalyst in alkaline medium. We have calculated the TOF of different catalyst at η= 0.35 V and tabulated in **Table 5.5**.

Table 5.5. Comparison of OER activity of different catalyst in 0.5 M KOH solution.

Catalyst	**Onset potential V (RHE)**	$\eta_{10\ mAcm^{-2}}$ **(mV)**	$J_{\eta=0.35V}$ **($mAcm^{-2}$)**	**Tafel slope (mV/dec)**	**TOF at η = 0.35 V (s^{-1})**
1D-RuO_2-CN_x	1.42	1.49	49.47	56	0.0995
Comm. RuO_2	1.46	1.56	10.24	80	0.0205
Pt/C	1.60	1.91	0.81	115	0.0016

At η= 0.35 V the TOF value of 1D-RuO_2-CN_x composite in basic media was 0.0995 O_2 s^{-1} which is ~5 times higher than comm. RuO_2 (0.0205 O_2 s^{-1}). The TOF value of this is also much higher than other reported[16, 62] catalysts. The OER catalytic activity of 1D-RuO_2-CN_x is not only better than commercial RuO_2 but also it has better or comparable than any other highly active OER catalyst such as IrO_2/C,[63] $Ba_{0.5}Sr_{0.5}Co_{0.8}Fe_{0}Z_{.2}O_{3-\delta}$,[64] NiFe-LDH/CNT,[18] $CoSe_2$/NrGO,[62] Ni-Co_3O_4-C_3N_4[65] as shown in **Table 5.6**.

The catalysis in neutral medium is also important since microbial electrolysis[26]. Thus, we have also checked OER activity of 1D-RuO_2-ctrolysis cell (MEC) which works under neutral condition, has low cost and better safety of the catalyst CN_x in 0.1 M PBS buffer (pH=7.4) solution.

Table 5.6. Comparison of OER activity of different catalysts with 1D-RuO_2-CN_x on GC electrode in basic medium.

Catalyst	Electrolyte	Current ($mAcm^{-2}$)	Potential (mV)	Reference
N-doped graphene-CoO	1 M KOH	10	340	*Energy Environ. Sci.* **2014**, *7*, 609-616.[66]
Mn_3O_4/$CoSe_2$	0.1 M KOH	10	450	*J. Am. Chem. Soc.* **2012**, *134*, 2930-2933[67] .
C-(Co0.54Fe0.46)2Fe	0.1 M KOH	10	370	*Nanoscale* **2016**, *8*, 3244-3247[68].
$CuCo_2O_4$/NrGO	0.1 M KOH	10	410	*J. Power Sources* **2015**, *281*, 243-251[69].
$CoSe_2$/NrGO	0.1 M KOH	10	370	*ACS Nano* **2014**, *8*, 3970-3978[62] .
CoC_2O_4, $2H_2O$ MRs	0.1 M KOH	10	436	*J. Mater. Chem. A* **2015**, *3*, 9707-9713[70].
Co-Bi NS/G	1 M KOH	10	290	*Angew. Chem. Int. Ed.* **2016**, *55*, 2488-2492[71].
3D-OMNiSA	0.1 M KOH	10	250	*ACS Catal.* **2016**, *6*, 1446-1450[16].
NiFe-LDH/CNT	1 M KOH	10	420	*J. Am. Chem. Soc.* **2013**, *135*, 8452-8455[18].
NiOOH	0.1 M KOH	10	590	*J. Am. Chem. Soc.* **2014**, *136*, 7077-7084[15].
$Ba_{0.5}Sr_{0.5}Co_{.8}Fe_{.2}O_{3-\delta}$	0.1 M KOH	10	350	*Science* **2011**, *334*, 1383-1385[64].
Ni-Co_3O_4-C_3N_4	0.1 M KOH	10	750 (SCS)	*Chem. Commun.* **2013**, *49*, 7522-7524[65].
Rutile RuO_2	0.1 M KOH	10	>470	*J. Phys. Chem. Lett.* **2012**, *3*, 399-404[44]
IrO_2/C	0.1 M KOH	10	370	*Nat. Commun.* **2013**, *4*.[63]
1D-RuO_2-CN_x	**0.5 M KOH**	**10**	**260**	**This work**

The LSV polarization curves of different catalyst in 0.1 M PBS buffer solution was shown in **Figure 5.11.a**. Tafel plot of LSV curves of 1D-RuO_2-CN_x commercial RuO_2 and RuNPs-CN_x composite was constructed in **Figure 5.11.b**. Thus OER activity in neutral media is also better than commercial RuO_2 and comparable or better than other OER neutral medium catalysts.

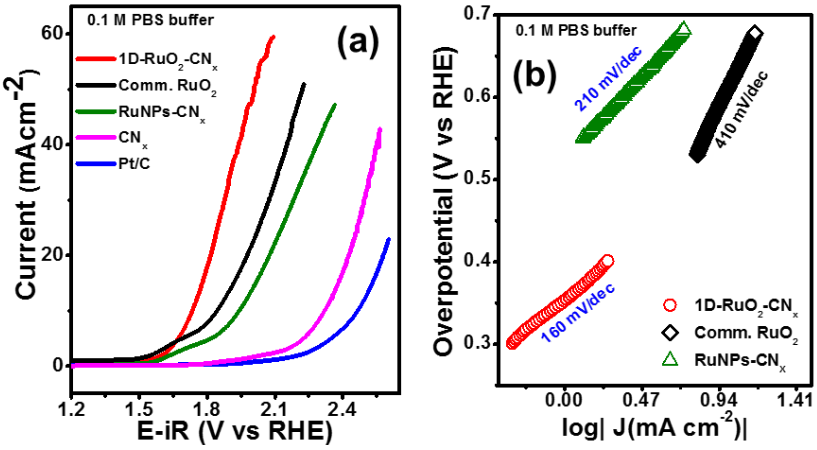

Figure 5.11. (a) LSV curves and (b) Tafel plot of 1D-RuO_2-CN_x comm. RuO_2, RuNPs-CN_x, Pt/C, g-CN_x and bare GC electrode in O_2 saturated 1 M PBS electrolyte.

The long term stability is one of the most important criteria for a good electrocatalyst. To test long term stability of 1D-RuO_2-CN_x catalyst we have performed continuous LSV cycling and chronoamperometry studies in both acidic and basic medium. The repeated LSV cycling of 1D-RuO_2-CN_x, commercial RuO_2 and IrO_2 catalysts between the potential ranges of 1.0 V to 2.0 V with an accelerating scan speed of 100 mV/sec at 1600 rpm rotation were first performed in acidic condition. In case of 1D-RuO_2-CN_x, the LSV polarization curves of 1st and 2000th cycles were very closely placed (**Figure 5.12.a**), suggesting very small degradation of the catalyst under acidic condition. In contrast, large shift of the LSV curve after 2000 cycles for state-of -art catalyst commercial RuO_2 and IrO_2 were observed (**Figure 5.12.b** and **5.12.c**). After 2000 continuous LSV cycle, the required overpotentials ($\eta_{10mA\ cm-2}$) to obtain current density,

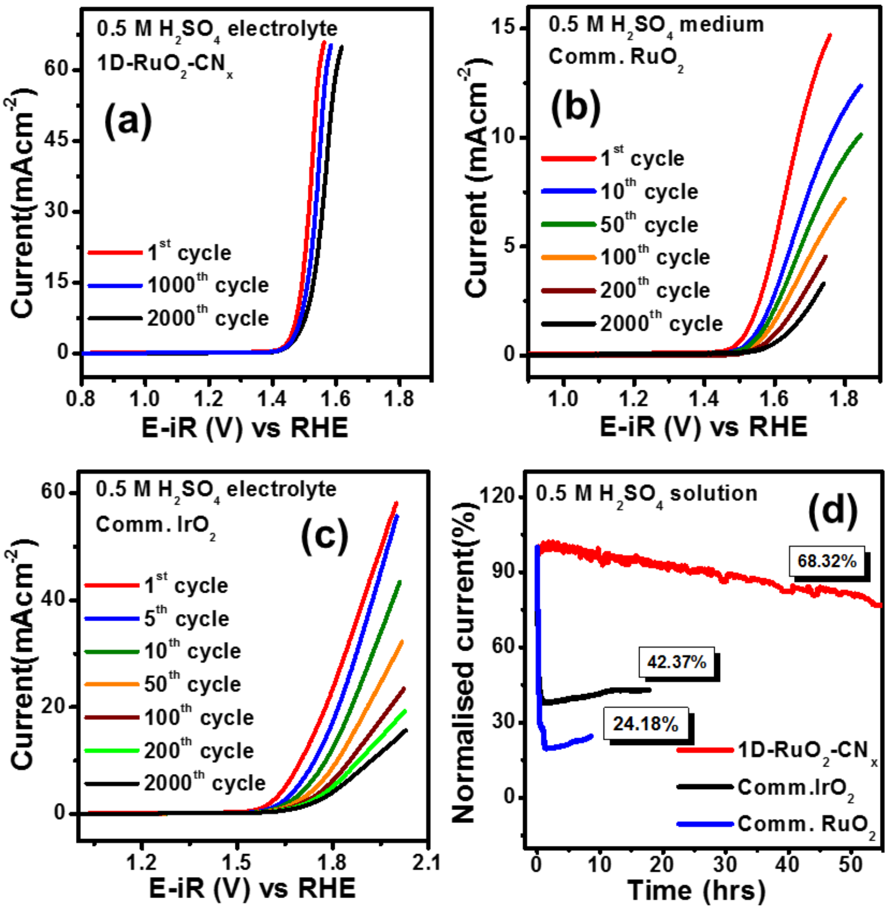

Figure 5.12. 1st and 2000th cycling LSV curves of (a) 1D-RuO$_2$-CN$_x$ composite. (b) comm. RuO$_2$. (c) Comm. IrO$_2$ in 0.5 M H$_2$SO$_4$. (d) Comparison of steady state chronoamperometry of 1D-RuO$_2$-CN$_x$, comm. RuO$_2$ and IrO$_2$ in 0.5 M H$_2$SO$_4$ at constant potential of 1.57 V.

10 mA cm^{-2} increased by only 3 mV for 1D-RuO$_2$-CN$_x$ whereas for state of art catalyst comm. IrO$_2$ and RuO$_2$ $\eta_{10\ \mathrm{mA\ cm^{-2}}}$ increased by 230 mV and > 340 mV respectively. This suggests superior cycling stability of this 1D-RuO$_2$-CN$_x$ catalyst as compare to state-of-art catalysts. As shown in **Figure 5.12.d** (chronoamperometry study), 1D-RuO$_2$-CN$_x$ catalyst lost only ~32% of its initial current after 55 hrs of scan whereas comm.IrO$_2$ and RuO$_2$ losses its ~58% and 76% of its initial current within 1hr of scan under acidic condition. The LSV cycling test and chronometric study clearly demonstrated the superior catalytic activity and long term stability of 1D-RuO$_2$-CN$_x$ in acidic medium which is much better than that of comm. IrO$_2$ and RuO$_2$.

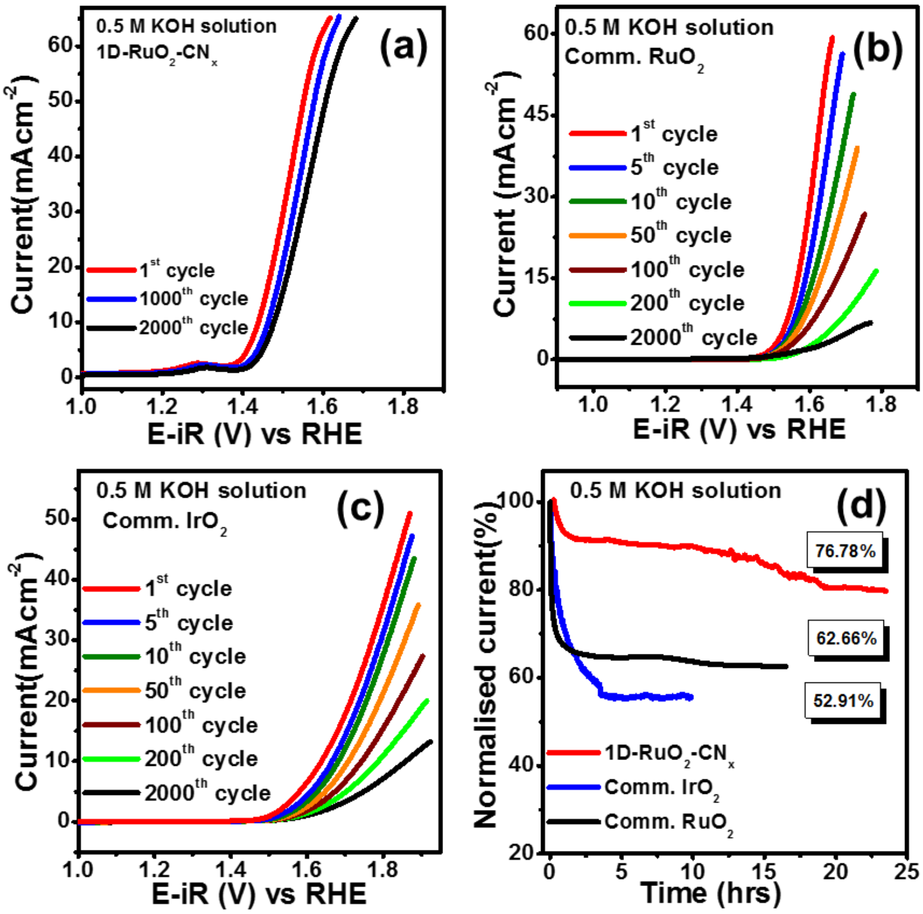

Figure 5.13. 1st and 2000th cycling LSV curves of (a) 1D-RuO_2-CN_x composite, (b) comm. RuO_2, (c) Comm. IrO_2 in 0.5 M KOH.(d) Comparison of steady state chronoamperometry of 1D-RuO_2-CN_x, comm. RuO_2 and IrO_2 in 0.5 M KOH at constant potential of 1.6 V. The RuO_2 oxide loading was 0.012 mg.

This catalyst also displayed excellent durability in basic medium as well. The continuous LSV cycling test and comparative chronoamperometry study (**Figure 5.13.(a-d)**) confirmed that long term stability of this catalyst is much higher than that of comm. IrO_2 and RuO_2 in basic medium. In addition the superior OER stability of 1D-RuO_2-CN_x in neutral media (**Figure 5.14**.(**a-c**)) suggests that outstanding OER activity and excellent stability of 1D-RuO_2-CN_x catalyst in all pH solution.

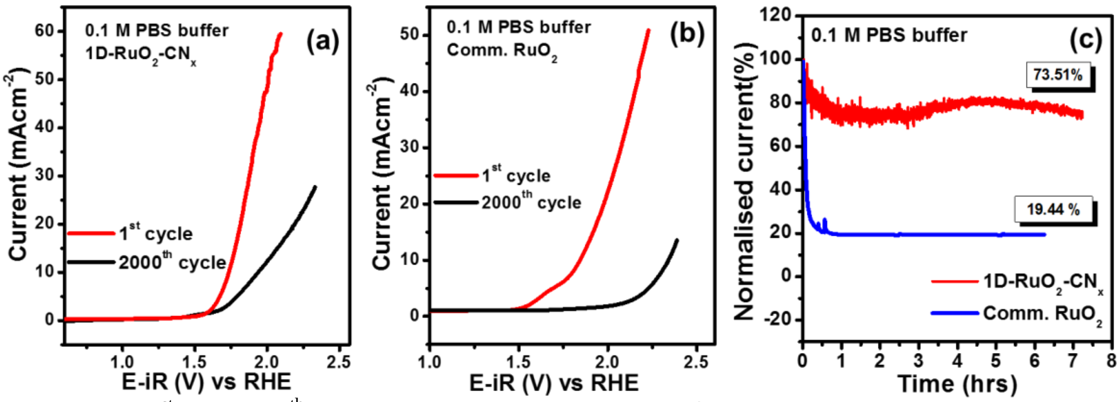

Figure 5.14. 1st and 2000th cycle LSV polarization curves of (a) 1D-RuO$_2$-CN$_x$ (b) Commercial RuO$_2$ in 0.1 M PBS. (c) Chronoamperometry studies of 1D-RuO$_2$-CN$_x$ composite and Pt/C catalyst in 0.1M PBS electrolyte at a constant potentials of 1.6 V.

Electrocatalytic HER on 1D-RuO$_2$-CN$_x$ Composite:

The catalytic activity of 1D-RuO$_2$-CN$_x$ composite towards HER was performed in different pH solutions. The electrochemical HER were studied using a three electrodes setup with a scan speed of 10 mV/Sec at rotation of 1600 rpm. **Figure 5.15.a** show the representative hydrogen evolution linear sweep voltammetry (LSV) polarization (current *vs*. voltage) curves of 1D-RuO$_2$-CN$_x$ and RuNPs-CN$_x$ catalysts in 0.5 M H_2SO_4. The HER activity of commercial Pt/C, g-CN$_x$ and bare GC electrode were also shown for comparison. The bare GC and g-CN$_x$ modified GC electrodes are inactive towards HER in both acid and basic media with high onset potentials (> 0.3 V). In acid media, Pt/C showed excellent HER activity with onset potential of zero volt (0 V). The onset potential of 1D-RuO$_2$-CN$_x$ in acidic media were 14 mV which is close to Pt/C, but smaller than that of and RuNPs-CN$_x$ (40 mV). The small onset potential of 1D-RuO$_2$-CN$_x$ and steady rise of cathodic current beyond onset potential suggested a superior hydrogen evolution activity of 1D-RuO$_2$-CN$_x$ catalyst. To achieve the current density of 10 mA/cm^2, the 1D-RuO$_2$-CN$_x$ required only 93 mV whereas Pt/C and RuNPs-CN$_x$ composite needed 43 mV and 156 mV respectively.

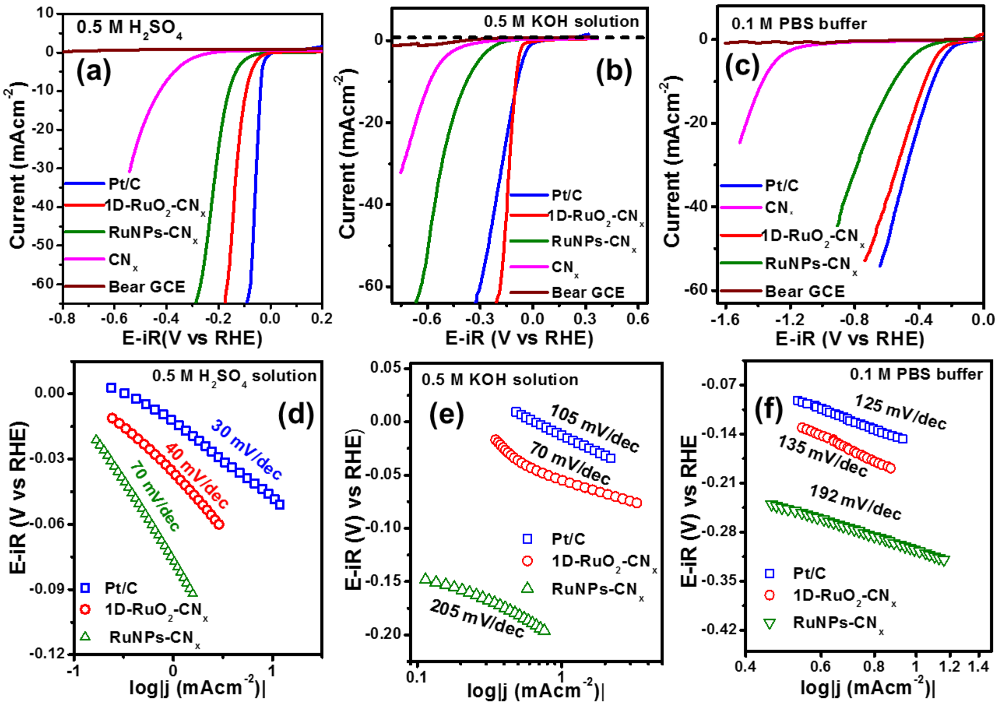

Figure 5.15. (a-c) Linear sweep voltammetry comparison curves of Pt/C, RuNPs-CN_x, 1D-RUO_2-CN_x at 10 mV scan rate, (d-f) Corresponding Tafel plot in N_2 saturated 0.5 M H_2SO_4, 0.5 M KOH and 0.1 PBS electrolyte.

Tafel slope value of Pt/C, 1D-RuO_2-CN_x and RuNPs-CN_x composite in 0.5 M H_2SO_4 medium was 30, 40 and 70 mV/dec respectively as shown in **Figure 5.15.d**. The Tafel slope value of Pt/C catalyst is consistent with reported values and it follows Tafel-Volmer pathway for HER in 0.5 M H_2SO_4 electrolyte. But the Tafel slope value of 1D-RuO_2-CN_x and RuNPs-CN_x suggests that both the catalyst follow Volmer–Heyrovsky mechanism with Heyrovsky is the rate limiting step in 0.5 M H_2SO_4 medium. The HER polarization curves and Tafel slopes of the different catalysts in basic media were shown in **Figure 5.15.b** and **Figure 5.15.e** respectively. The onset potentials of Pt/C and 1D-RuO_2-CN_x were ~0 V and 16 mV respectively. Although 1D-RuO_2-CN_x catalyst showed slightly higher onset potential of 16 mV in compare to value of ~0 V for Pt/C, the cathodic current density for 1D-RuO_2-CN_x catalyst was increased more steeply and outperformed the Pt/C when potential is greater than 95 mV.

Table 5.7. Summarized HER activity of 1D-RuO_2-CN_x and Pt/C in 0.5 M H_2SO_4 and KOH

Electrolyte	**Catalyst**	**$\eta_{J=10\ mA/cm^2}$ (mV)**	**Tafel slope (b mV/dec)**	**Exchange current(J_o) mA/cm^2**
0.5M H_2SO_4	1D-RuO_2-CN_x	93	40	0.22
	Pt/C	43	30	0.54
0.5 M KOH	1D-RuO_2-CN_x	95	70	0.28
	Pt/C	94	105	0.42

The 1D-RuO_2-CN_x and Pt/C catalysts required almost same overpotential of ~95 mV to reach the current density of 10 mA/cm^{-2}; but to reach current density of 40 mA/cm^{-2} , 1D-RuO_2-CN_x needed lower overpotential (149 mv) in compare to that of Pt/C (205 mV). In addition, the Tafel slope of 1D-RuO_2-CN_x was 70 mV/dec which is also lower than Pt/C (105 mV/dec). Exchange current density (J_0) is considered as one of the activity descriptor for HER. The exchange current density of 1D-RuO_2-CN_x composite in acidic and basic medium were found to be 0.22 mA cm^{-2} and 0.28 mA cm^{-2} respectively (**Table 5.7**). The exchange current of 1D-RuO_2-CN_x was very close to Pt/C. The J_o of this catalyst is ~2 times lower than that of Pt/C and is comparable/ better than other recently reported catalysts such as NiP_2/CC,[25] defect rich MoS_2,[72] Co-NRCNT,[28] MoB,[73] Ni_2P hollow nanoparticle,[74] MoC_x nano-octahedrons.[13] The comparison HER performance of this catalyst with other different reported catalyst in 0.5 M H_2SO_4 and 0.5 M KOH electrolyte is given in **Table 5.8** and **5.9** respectively. This suggests that 1D-RuO_2-CN_x composite is one of the best HER catalyst in both acid and basic media. In order to prove the versatility of the catalyst we have also performed HER activity in neutral medium (**Figure 5.15. c and f**).

Table 5.8. Comparison of HER activity of different catalysts with 1D-RuO_2-CN_x on GC electrode in acidic medium.

Catalyst	Electrolyte	Current ($mAcm^{-2}$)	Potential (mV)	Reference
MoS_2/RGO	0.5 M H_2SO_4	10	150	*J. Am. Chem. Soc.* **2011**, *133*, 7296-7299[24].
Co-NRCNTs	0.5 M H_2SO_4	10	260	*Angew. Chem. Int. Ed.* **2014**, *53*, 4372-4376[28].
Ni_5P4-Ni_2P/NF	0.5 M H_2SO_4	10	120	*Angew. Chem. Int. Ed.* **2015**, *54*, 8188-8192[75].
Cu_3P NW/CF	0.5 M H_2SO_4	10	143	*Angew. Chem. Int. Ed.* **2014**, *53*, 9577-9581[76].
Au–aerogel–CN_x	0.5 M H_2SO_4	10	185	*J. Mater. Chem. A* **2015**, *3*, 23120-23135[77].
$Pt_{13}Cu_{73}Ni_{14}$/CNF@CF	1 M H_2SO_4	5	70	*ACS Appl. Mater. Interfaces* **2016**, *8*, 3464-3472[78].
Mo_2C/CNT	0.1 M $HClO_4$	10	152	*Energy Environ. Sci.* **2013**, *6*, 943-951[79].
Porous Pd-CN_x	0.5 M H_2SO_4	10	55	*ACS Catal.* **2016**, *6*, 1929-1941[80]
$Co_{0.6}Mo_{1.4}N_2$	0.1 M $HClO_4$	10	200	*J. Am. Chem. Soc.* **2013**, *135*, 19186-19192[81].
Ru/SiNWs	0.5 M H_2SO_4	10	200	*Electrochem. Commun.* **2015**, *52*, 29-33[37].
Nanoporous MoS_2	0.5 M H_2SO_4	10	270	*Nat Mater* **2012**, *11*, 963-969[50]
1D-RuO_2-CN_x	**0.5 M H_2SO_4**	**10**	**93**	**This work**

The comparison of HER catalytic activity of 1D-RuO_2-CN_x composite with other catalysts under 0.1 M PBS buffer condition (pH=7.4) has shown in **Figure 5.15.c.** Although the catalytic activity of 1D-RuO_2-CN_x composite was relatively lower in neutral medium in comparison the ones at pH=0 and pH=14, its activity in neutral medium is close to Pt/C in **Table 5.10**. The HER catalytic activity of 1D-RuO_2-CN_x composite was also comparable with the different reported catalyst as shown in **Table 5.11**. The Tafel plot of different catalyst in 0.1 M PBS buffer was shown in **Figure 5.15.f.**

Table 5.9. Comparison of HER activity of different catalysts with 1D-RuO_2-CN_x in basic medium.

Catalyst	Electrolyte	Current (mA cm^{-2})	Potential (mV)	Reference
CoP/CC	1 M KOH	10	209	*J. Am. Chem. Soc.* **2014**, *136*, 7587-7590[26].
MoB	1 M KOH	10	225	*Angew. Chem. Int. Ed.* **2012**, *51*, 12703-12706.[73]
Ni-Ag alloy	0.1 M KOH	4	260	*Phys. Chem. Chem. Phys.* **2014**, *16*, 19250-19257[82].
Pt NWs/SL-$Ni(OH)_2$	1 M KOH	4	85.5	*Nat. Commun.* **2015**, *6*, 6430[83].
NiONi-CNT	1 M KOH	10	~ 100	*Nat. Commun.* **2014**, *5*, 4695[84].
CoOx@CN	1 M KOH	10	232	*J. Am. Chem. Soc.* **2015**, *137*, 2688-2694[85].
Amorphous MoS_x	1 M KOH	10	540	*Chem. Sci.* **2011**, *2*, 1262-1267[86]
Porous Pd-CN_x	0.5 M KOH	5	180	*ACS Catal.* **2016**, *6*, 1929-1941[80].
Ni/MWCNT	1 M KOH	10	~ 350	*Journal of Power Sources* **2014**, *266*, 365-373[87].
MnNi	0.1 M KOH	10	360	*Adv. Funct. Mater.* **2015**, *25*, 393-399[88]
Co-NRCNTs	1 M KOH	10	370	*Angew. Chem. Int. Ed.* **2014**, *53*, 4372-4376[28].
1D-RuO_2-CN_x	**0.5 M KOH**	**10**	**95**	**This work**

Table 5.10. Summarization of HER activity of 1D-RuO_2-CN_x in PBS medium.

Electrolyte	**Catalyst**	**η=J_{10} mAcm^{-2} (mV)**	**Tafel slope (b mV/dec)**	**Exchange current(J_o) A/cm^2**
0.1 M PBS buffer electrolyte	**1D-RuO_2-CN_x**	**356**	**135**	**1.8×10^{-4}**
	Pt/C	323	198	2.3×10^{-4}

Table 5.11. Comparison of HER activity of 1D-RuO_2-CN_x with different catalysts in 0.1 M PBS buffer solution.

Catalyst	**electrolyte**	**Current (mA/cm^2)**	**Potential (mV)**	**Reference**
Metallic Co@cobalt-oxo/hydroxophosphate	0.1 M PBS	2	385	*Nat. Mater.* **2012**, *11*, 802-807[89].
MoB	0.1 M PBS	1	250	*Angew. Chem. Int. Ed.* **2012**, *51*, 12703-12706[73].
Co-NRCNTs	0.1 M PBS	2	380	*Angew. Chem. Int. Ed.* **2014**, *53*, 4372-4376[28].
Amorphous MoS_2	0.1 M PBS	2	280	*Chem. Sci.* **2011**, *2*, 1262-1267[86].
$CuMoS_4$ crystals	0.1 M PBS	2	210	*Energy Environ. Sci.* **2012**, *5*, 8912-8916[90].
1D-RuO_2-CN_x	**0.1 M PBS**	**2**	**250**	**This work**

The long term stability is an important characteristic of a good electro-catalyst. We have performed continuous LSV cycling test and chronoamperometry studies in order to access the durability of the catalysts. **Figure 5.16.a** show the 1st cycle and 5000th LSV curves of this catalyst with accelerated scan rate of 100 mV/sec in the potentials range of 0.2 to -0.3 V (RHE) whereas a comparative chronoamperometry study at constant potential of -0.15 V of 1D-RuO_2-CN_x and Pt/C catalysts in 0.5 M H_2SO_4 electrolyte was shown in **Figure 5.16.b**. After 5000 continuous LSV cycles, a very small shift of LSV curve suggests the superior durability of this catalyst in acid media.

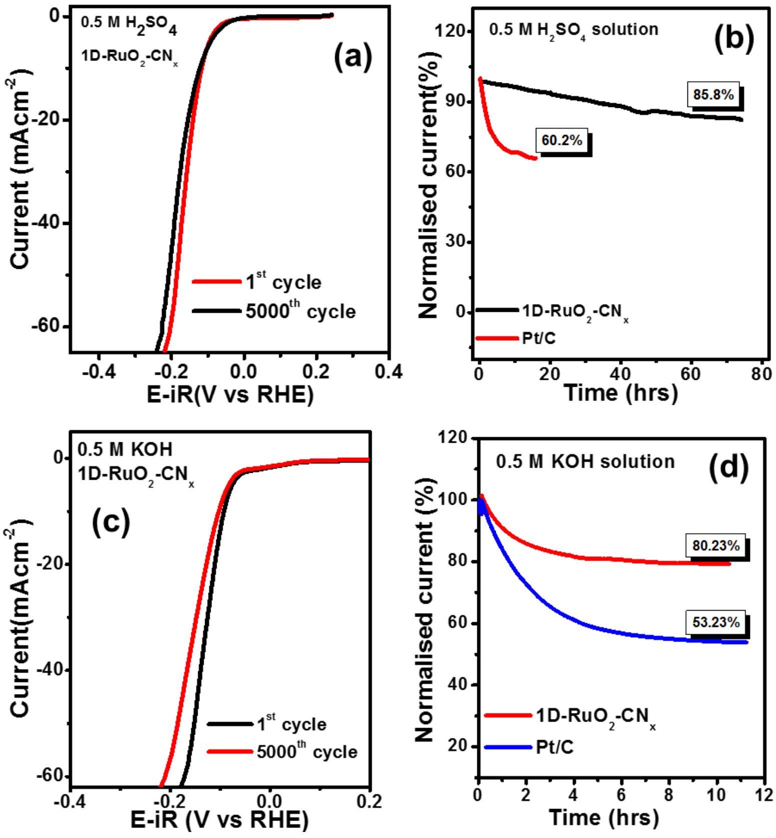

Figure 5.16. Initial and 5000th cycle LSV curve of 1D-$Ru0_2$-CN_x (at 10mV/sec) in (a) 0.5 M H_2SO_4 and (c) 0.5 M KOH medium. Steady state chronoamperometry study of 1D-RuO_2-CN_x and comm. Pt/C in (b) 0.5 M H_2SO_4, (d) 0.5 M KOH at constant potentials of -0.15 V.

The chronoamperometry study shows that the initial current density of this 1D-RuO_2-CN_x catalyst remain unchanged after 12 hrs of scan time and lost only 20% of its initial current even after 70 hrs scan time, whereas Pt/C has lost 40% of its initial current within 12 hrs scan at same potential (-0.15 V). Several group reported electrochemical formation of the hydrous RuO_2 under strong reducing condition and this phase provided enhanced HER activity and durability.[54, 91] The excellent catalytic activity and higher durability of the 1D-RuO_2-CN_x composite towards HER under acidic condition indicate that hydrous RuO_2 phase covering 1D-RuO_2 may be the active phase under electrochemical reduction condition. These stability tests proved that 1D-RuO_2-CN_x catalyst is more stable than Pt/C in acid media. Moreover, stability of this 1D-RuO_2-CN_x composite in basic medium is also excellent as suggested by stability tests (**Figure 5.16.(c,d)**).

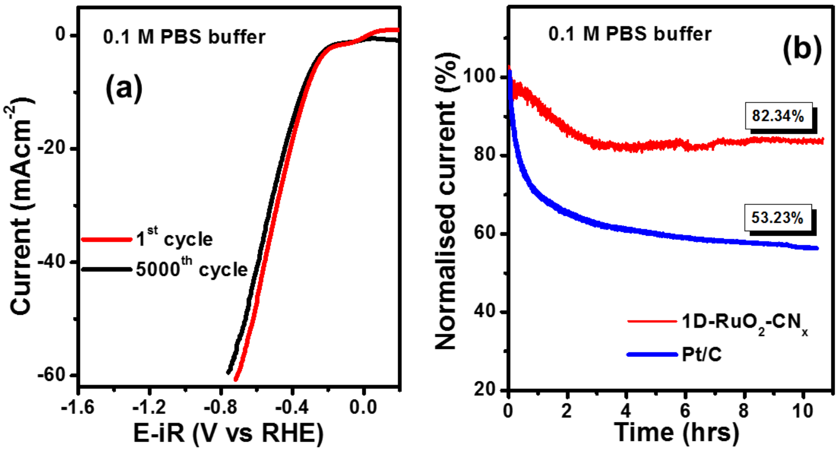

Figure 5.17. (a) 1st and 5000th cycle LSV polarization curves of 1D-RuO_2-CN_xin 0.1 M PBS. (b) Comparison of chronoamperometry studied of 1D-RuO_2-CN_x and Pt/C catalyst in 0.1PBS electrolyte at a constant potentials of -0.4 V.

In PBS buffer solution of 1D-RuO_2-CN_x composite also shows a better stability and long term durability as compared to Pt/C catalyst as shown in **Figure 5.17.(a,b)**. Like acidic and basic medium this catalyst (1D-RuO_2-CN_x composite) is also highly active in neutral medium.

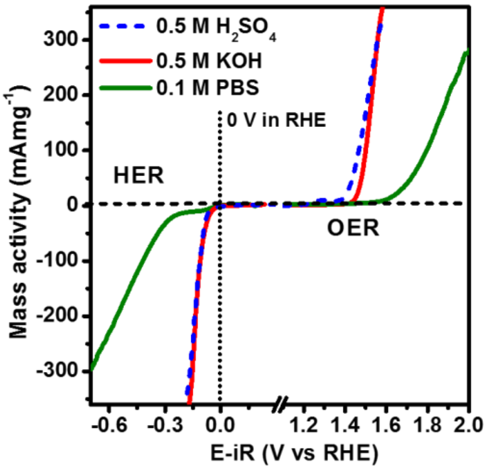

Figure 5.18. Both HER and OER LSV curves of 1D-RuO_2-CN_x at different pH values.

Based on the above experimental observations, we may conclude that 1D-RuO_2-CN_x composite is highly active and durable bi-functional electrocatalyst for HER and OER in wide range of pH solutions (**Figure 5.18**). We have also prepared an electrolyzer in basic media (1 M KOH solution) by applying 1D-RuO_2-CN_x as both cathode and anode for HER and OER as shown in **Figure 5.19.a**. To reach the current density of 20 mA cm^{-2}, 1D-RuO_2-CN_x required only 1.59 V which is comparable to other reported catalysts.[85, 92] Inset **Figure 5.19.a** shows the optical photograph of O_2 and H_2 bubbles formation on the electrodes during water splitting. The durability test of this cell was also performed and it shows a considerable stability at least for 3h (**Figure 5.19.b**).

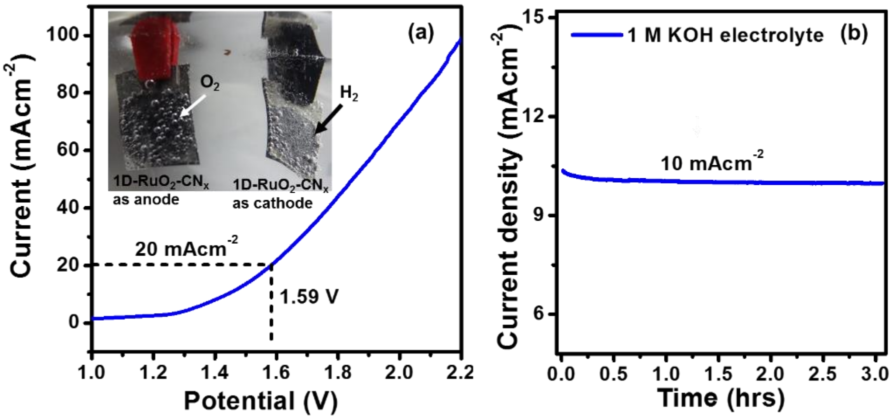

Figure 5.19. (a) LSV polarization curve of overall water splitting in 1M KOH electrolysed using 1D-RuO_2-CN_x as cathode as well anode. In-set: Optical photograph showing the H_2 and O_2 bubbling on cathode and anode respectively during overall water splitting. (b) Chronoamperometry response of 1D-RuO_2-CN_x at 1.53 V in RHE.

Factors Responsible for Superior Electrocatalytic HER and OER Activity:

The remarkably high electro catalytic activity and long term durability of 1D-RuO_2-CN_x towards overall water splitting can be attributed by several factors, such as

(i) The strong interaction between CN_x and RuO_2 could be one of reason for its enhanced activity and enhanced long term durability. The direct growth of RuO_2 on CN_x surface leads to formation of composite with strongly interacting 1D-RuO_2 and support (CN_x). This improves electron transfer through 1D-RuO_2-CN_x composite and interaction between RuO_2 to CN_x sheets provide structural stability for long term electrochemical measurements. The electrochemical impedance spectroscopy (EIS) was done for this purpose. The electrochemical impedance spectroscopy (EIS) was done for this purpose. The EIS spectra of 1D-RuO_2-CN_x at 1.45 V was shown in **Figure 5.20.a**. In-set of **Figure 5.20.a** shows the electrical circuit for Nyquist curve fitting. **Figure 5.20.b** shows the Nyquist plot of commercial RuO_2, 1D-RuO_2-CN_x and comm.RuO_2-CN_x (physical mixture) in 0.5 M KOH at a potentials of 1.45 V (RHE). EIS spectra of g-CN_x in alkaline medium at potential 1.45 V is also shown in **Figure 5.20.c**.

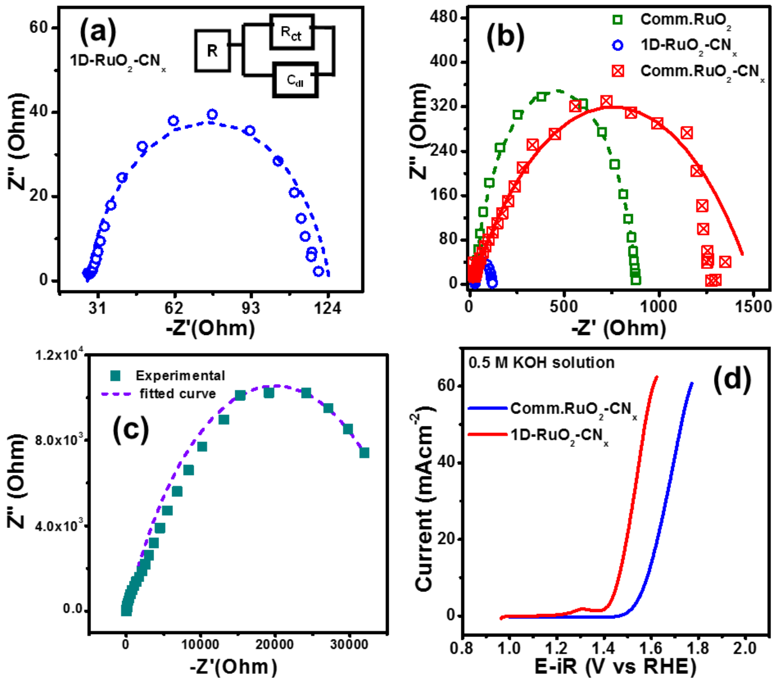

Figure 5.20. (a) Nyquist plot of 1D-RuO_2-CN_x composite in 0.5 M KOH medium at overpotentials of 0.22 V (RHE). Inset: Electronic circuit for fitting the Nyquist plot. (b) Comparison of Nyquist plot of comm. RuO_2, comm. RuO_2-CN_x and 1D-RuO_2-CN_x composite in 0.5 M KOH medium at overpotentials of 0.22 V (RHE) (c) Nyquist plot of free g-C_3N_4 under similar condition.(d) Comparison of OER LSV curve of 1D-RuO_2-CN_x, and comm. RuO_2-CN_x.

All the EIS spectra of different catalysts are semicircle and the diameter gradually decreased from g-CN_x, comm.RuO_2-CN_x, comm. RuO_2 to 1D-RuO_2-CN_x, suggesting decrease of charge transfer resistance in 1D-RuO_2-CN_x. The calculated charge transfer resistance value for g-CN_x, comm.RuO_2, comm. RuO_2-CN_x and 1D-RuO_2-CN_x was 435 Ω, 87 Ω, 147 Ω and 40 KΩ respectively. This low R_{ct} value of 1D-RuO_2-CN_x proves the easy electron transfer through this 1D-RuO_2-CN_x catalyst. The catalytic activity of comm.RuO_2-CN_x is inferior as compared to 1D-RuO_2-CN_x (**Figure 5.20.d**). The interaction between 1D-RuO_2 and g-CN_x, facial electron transfer enhances the activity and durability of this catalyst.

(ii) The high electrochemical surface area of 1D-RuO_2-CN_x composite resulting from large number catalytic sites is another reason for its high catalytic activity. The ECSA of the catalyst was calculated from the double layer capacitance. The specific capacity of RuO_2 was varied from 0.013 mF cm^{-2} to 0.019 mF cm^{-2}.[93] Here we are considered 0.013 mF cm^{-2} to calculate the ECSA value. The CV curves of 1D-RuO_2-CN_x at different scan speeds in 0.5 M KOH solution and corresponding liner plot of current vs scan rate at potential of 0 V (in Ag/AgCl) were shown in **Figure 5.21.a** and **b** respectively. The CV curves of comm. RuO_2 at different scan speeds in 0.5 M KOH solution and corresponding liner plot of current vs scan rate at potential of 0 V (in Ag/AgCl) were shown in **Figure 5.21.c** and **d** respectively. The calculated active surface area of 1D-RuO_2-CN_x was 76.3 cm^2 whereas for comm. RuO_2 it was 9.06 cm^{-2}. The large surface area suggests that the catalyst has large number catalytic sites due to its one dimensional morphology of the catalyst, which is significantly contributing to its high HER and OER activity.

(iii) Thermal method produces tilted RuO_2 nanowires on CN_x support (as confirmed by FE-SEM). The tilted nanowire assembly allows easy pathways for reactant and products[19]. The reactant molecule can thus easily reach to active sites and products can easily come out from its surface. It is known that HER and OER activity strongly depend on the morphology of the catalyst- porous electrode showed better performance than flat electrode.[19, 94-95] The HER and OER activity is thus enhanced due to tilted assembly of RuO_2 nanowires on CN_x surface.

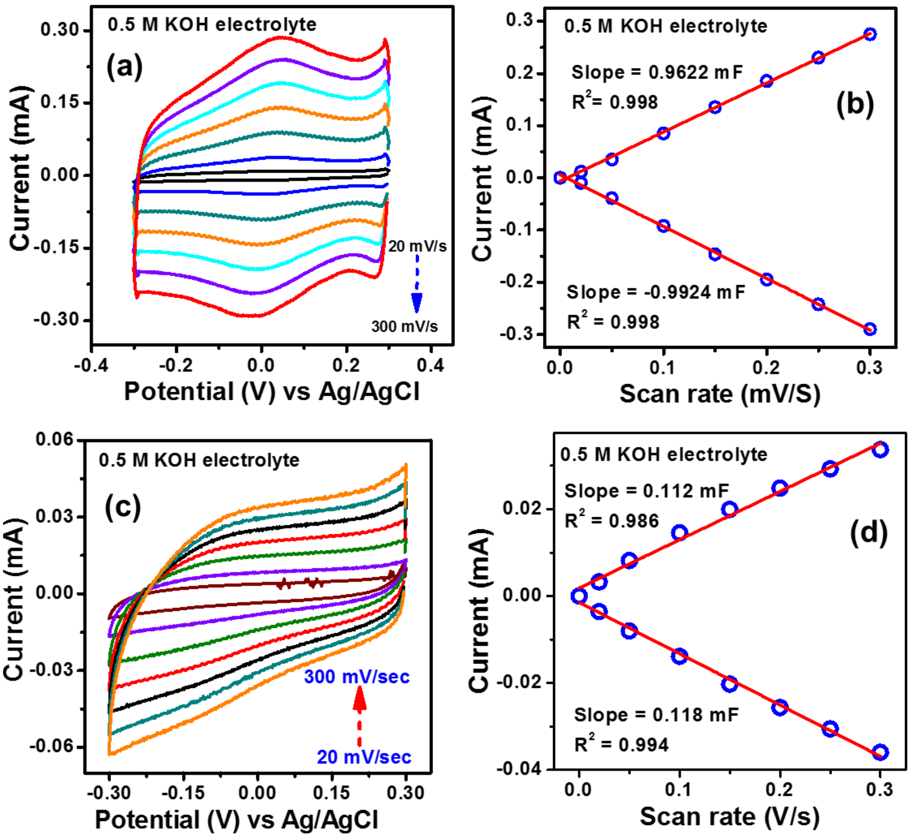

Figure 5.21. CVs curve of (a) 1D-RuO_2-CN_x composite and (b) linear plot between double layer current and scan rate at potential of 0 V in (Ag/AgCl). CVs curve of (c) Comm. RuO_2 in potential range from 0.3 V to -0.3 V (Ag/AgCl) with different scan rate 0f 20, 50, 100, 150, 200, 300 mV/sec. and (d) linear plot between double layer current and scan rate at potential of 0 V in (Ag/AgCl).

(iv)The presence of nitrogen in CN_x support is also helped to improve the activity durability of this catalyst. It is reported[77, 80, 96] by several groups that the presence of nitrogen in carbon matrix of electro-catalyst enhances electrochemical activity and durability. The nitrogen atoms generally interact more easily with reactants and also its presence creates positive charge density on nearest carbon atoms which may then become catalytic active.[28]

(v) The remarkable long term stability of this catalyst is probably due to highly crystalline RuO_2 nanowire with few or no defects. The XRD, HR-TEM, SAED studies confirmed that thermally grown RuO_2 on CN_X are single crystalline. It is reported[42, 45] that thermally prepared rutile RuO_2 with fewer defects has much higher durability than that of electrochemically prepared amorphous RuO_2. The quite large size of RuO_2 nanowire is also another reason for its stability.

5.5 Conclusions

In conclusion, we demonstrated a facile thermal method for direct growth of one dimensional, highly crystalline rutile RuO_2 nanowire on g-carbon nitride (1D-RuO_2-CN_x). This 1D-RuO_2-CN_x catalyst showed excellent catalytic activity for HER and OER at wide pH range. We have shown that HER activity of this catalyst is comparable to Pt/C in acid and is better than Pt/C in base at high overpotential. We have also demonstrated that OER activity of this 1D-RuO_2-CN_x catalyst is better than state of art catalysts (RuO_2 or IrO_2) in terms of onset potential, over-potential for appreciable current density (10 $mAcm^{-2}$), Tafel slope. Most importantly, stability (continuous cycling and chronoamperometry) tests proved OER stability of 1D-RuO_2-CN_x catalyst is much higher that of commercial RuO_2. Although it is general believe that OER activity and its stability are inversely related (e.g. rutile RuO_2 is more stable, but less active whereas amorphous RuO_2 is less stable, but more active), this 1D-RuO_2-CN_x catalyst interestingly showed very high OER active as well as remarkable stability. The outstanding HER and OER activity with excellent long term durability of this catalyst is making them a promising electro-catalyst for various renewable energy storage and conversion devices such as water-splitting devices, metal-air batteries, fuel cells etc.

5.6 References

1. Surendranath, Y.; Bediako, D. K.; Nocera, D. G., *Proc. Natl. Acad. Sci. U.S.A.* **2012,** *109,* 15617-15621.

2. Walter, M. G.; Warren, E. L.; McKone, J. R.; Boettcher, S. W.; Mi, Q.; Santori, E. A.; Lewis, N. S., *Chem. Rev.* **2011,** *111,* 5815-5815.

3. G. W. Crabtree, M. S. D., and M. V. Buchanan., *Physics Today* **2004,** *57,* 39-44.

4. Gasteiger, H. A.; Marković, N. M., *Science* **2009,** *324,* 48-49.

5. Lewis, N. S.; Nocera, D. G., *Proc. Natl. Acad. Sci. U. S. A.***2006,** *103,* 15729-15735.

6. McCrory, C. C. L.; Jung, S.; Ferrer, I. M.; Chatman, S. M.; Peters, J. C.; Jaramillo, T. F., *J. Am. Chem. Soc.* **2015,** *137,* 4347-4357.

7. Fabbri, E.; Habereder, A.; Waltar, K.; Kotz, R.; Schmidt, T. J., *Catal. Sci. Technol.* **2014,** *4,* 3800-3821.

8. Li, X.; Hao, X.; Abudula, A.; Guan, G., *J. Mater. Chem. A* **2016,** *4,* 11973-12000.

9. Chandra, D.; Takama, D.; Masaki, T.; Sato, T.; Abe, N.; Togashi, T.; Kurihara, M.; Saito, K.; Yui, T.; Yagi, M., *Acs Catal.* **2016,** *6,* 3946-3954.

10. Audichon, T.; Napporn, T. W.; Canaff, C.; Morais, C.; Comminges, C.; Kokoh, K. B., *J. Phys. Chem. C* **2016,** *120,* 2562-2573.

11. McCrory, C. C. L.; Jung, S.; Peters, J. C.; Jaramillo, T. F., *J. Am. Chem. Soc.* **2013,** *135,* 16977-16987.

12. Koper, M. T. M., *Nat. Chem.* **2013,** *5,* 255-256.

13. Wu, H. B.; Xia, B. Y.; Yu, L.; Yu, X.-Y.; Lou, X. W., *Nat. Commun.* **2015,** *6,* 6512-6519.

14. Sheng, W.; Myint, M.; Chen, J. G.; Yan, Y., *Energy Environ. Sci.* **2013,** *6,* 1509-1512.

15. Gao, M.; Sheng, W.; Zhuang, Z.; Fang, Q.; Gu, S.; Jiang, J.; Yan, Y., *J. Am. Chem. Soc.* **2014,** *136,* 7077-7084.

16. Sun, T.; Xu, L.; Yan, Y.; Zakhidov, A. A.; Baughman, R. H.; Chen, J., *ACS Catal.* **2016,** *6,* 1446-1450.

17. Zhu, Y.; Zhou, W.; Chen, Y.; Yu, J.; Liu, M.; Shao, Z., *Adv. Mater.* **2015,** *27,* 7150-7155.

18. Gong, M.; Li, Y.; Wang, H.; Liang, Y.; Wu, J. Z.; Zhou, J.; Wang, J.; Regier, T.; Wei, F.; Dai, H., *J. Am. Chem. Soc.* **2013,** *135,* 8452-8455.

19. Ma, T. Y.; Dai, S.; Jaroniec, M.; Qiao, S. Z., *J. Am. Chem. Soc.* **2014,** *136,* 13925-13931.

20. Su, D.; wang, J.; Jin, H.; Gong, Y.; Li, M.; Pang, Z.; Wang, Y., *J. Mater. Chem. A* **2015,** *3,* 11756-11761.

21. Wang, S.; Wang, J.; Zhu, M.; Bao, X.; Xiao, B.; Su, D.; Li, H.; Wang, Y., *J. Am. Chem. Soc.* **2015,** *137,* 15753-15759.

22. Kong, D.; Wang, H.; Lu, Z.; Cui, Y., *J. Am. Chem. Soc.* **2014,** *136,* 4897-4900.

23. Gao, M. R.; Liang, J. X.; Zheng, Y. R.; Xu, Y. F.; Jiang, J.; Gao, Q.; Li, J.; Yu, S. H., *Nat Commun* **2015,** *6,* 5982-5988.

24. Li, Y.; Wang, H.; Xie, L.; Liang, Y.; Hong, G.; Dai, H., *J. Am. Chem. Soc.* **2011,** *133,* 7296-7299.

25. Jiang, P.; Liu, Q.; Sun, X., *Nanoscale* **2014,** *6,* 13440-13445.

26. Tian, J.; Liu, Q.; Asiri, A. M.; Sun, X., *J. Am. Chem. Soc.* **2014,** *136,* 7587-7590.

27. Yan, Y.; Xia, B. Y.; Ge, X.; Liu, Z.; Fisher, A.; Wang, X., *Chem. Euro. J.* **2015,** *21,* 18062-18067.

28. Zou, X.; Huang, X.; Goswami, A.; Silva, R.; Sathe, B. R.; Mikmeková, E.; Asefa, T., *Angew. Chem. Int. Ed.* **2014,** *53,* 4372-4376.

29. Minguzzi, A.; Fan, F.-R. F.; Vertova, A.; Rondinini, S.; Bard, A. J., *Chem. Sci.* **2012,** *3,* 217-229.

30. Kang, M.; Lee, Y.; Jung, H.; Shim, J. H.; Lee, N.-S.; Baik, J. M.; Lee, S. C.; Lee, C.; Lee, Y.; Kim, M. H., *Anal. Chem.* **2012,** *84,* 9485-9491.

31. Wang, W.; Guo, S.; Lee, I.; Ahmed, K.; Zhong, J.; Favors, Z.; Zaera, F.; Ozkan, M.; Ozkan, C. S., *Sci. Rep.* **2014,** *4,* 4452-4460.

32. Maeda, K., *ACS Catal.* **2014,** *4,* 1632-1636.

33. Mamaca, N.; Mayousse, E.; Arrii-Clacens, S.; Napporn, T. W.; Servat, K.; Guillet, N.; Kokoh, K. B., *Appl. Catal. B: Environ.* **2012,** *111–112,* 376-380.

34. Park, J.-e.; Lee, Y.; Lee, J.; Jang, H. S.; Shin, H.-Y.; Yoon, S.; Baik, J. M.; Kim, M. H.; Kim, S.-J., *Crys. Growth Des.* **2012,** *12,* 3829-3833.

35. Lee, Y.; Ye, B.-U.; Yu, H. k.; Lee, J.-L.; Kim, M. H.; Baik, J. M., *J. Phys. Chem. C* **2011,** *115,* 4611-4615.

36. Cheng, J.; Zhang, H.; Ma, H.; Zhong, H.; Zou, Y., *Electrochim. Acta* **2010,** *55,* 1855-1861.

37. Zhu, L.; Cai, Q.; Liao, F.; Sheng, M.; Wu, B.; Shao, M., *Electrochem. Commun.* **2015,** *52,* 29-33.

38. Cherevko, S.; Geiger, S.; Kasian, O.; Kulyk, N.; Grote, J.-P.; Savan, A.; Shrestha, B. R.; Merzlikin, S.; Breitbach, B.; Ludwig, A.; Mayrhofer, K. J. J., *Catalysis Today* **2016,** *262,* 170-180.

39. Kong, X.; Xu, K.; Zhang, C.; Dai, J.; Norooz Oliaee, S.; Li, L.; Zeng, X.; Wu, C.; Peng, Z., *ACS Catal.* **2016,** 1487-1492.

40. Galizzioli, D.; Tantardini, F.; Trasatti, S., *J. Appl. Electrochem.* **1975,** *5,* 203-214.

41. Cherevko, S.; Geiger, S.; Kasian, O.; Kulyk, N.; Grote, J.-P.; Savan, A.; Shrestha, B. R.; Merzlikin, S.; Breitbach, B.; Ludwig, A.; Mayrhofer, K. J. J., *Catal. Today* **2016,** *262,* 170-180.

42. Hodnik, N.; Jovanovič, P.; Pavlišič, A.; Jozinović, B.; Zorko, M.; Bele, M.; Šelih, V. S.; Šala, M.; Hočevar, S.; Gaberšček, M., *J. Phys. Chem. C* **2015,** *119,* 10140-10147.

43. Audichon, T.; Mayousse, E.; Morisset, S.; Morais, C.; Comminges, C.; Napporn, T. W.; Kokoh, K. B., *Int. J. Hydrogen Energy.* **2014,** *39,* 16785-16796.

44. Lee, Y.; Suntivich, J.; May, K. J.; Perry, E. E.; Shao-Horn, Y., *J. Phys. Chem. Lett.* **2012,** *3,* 399-404.

45. Tsuji, E.; Imanishi, A.; Fukui, K.-i.; Nakato, Y., *Electrochim. Acta* **2011,** *56,* 2009-2016.

46. Jirkovský, J.; Makarova, M.; Krtil, P., *Electrochem. Commun.* **2006,** *8,* 1417-1422.

47. Barman, S.; Sadhukhan, M., *J. Mater. Chem.* **2012,** *22,* 21832-21837.

48. Bhowmik, T.; Kundu, M. K.; Barman, S., *Inter. J. Hydrogen Energy* **2016,** *41,* 14768-14777.

49. Kundu, M. K.; Sadhukhan, M.; Barman, S., *J. Mater. Chem. B* **2015,** *3,* 1289-1300.

50. Kibsgaard, J.; Chen, Z.; Reinecke, B. N.; Jaramillo, T. F., *Nat Mater* **2012,** *11,* 963-969.

51. Bhaskar, S.; Dobal, P. S.; Majumder, S. B.; Katiyar, R. S., *J. Appl. Phys.* **2001,** *89,* 2987-2992.

52. Oh, H.-S.; Nong, H. N.; Reier, T.; Gliech, M.; Strasser, P., *Chem. Sci.* **2015,** *6,* 3321-3328.

53. Nong, H. N.; Oh, H.-S.; Reier, T.; Willinger, E.; Willinger, M.-G.; Petkov, V.; Teschner, D.; Strasser, P., *Angew. Chem. Int. Ed.* **2015,** *54,* 2975-2979.

54. Over, H., *Chem. Rev.* **2012,** *112,* 3356-3426.

55. Castelli, P.; Trasatti, S.; Pollak, F. H.; O'Grady, W. E., *J. Electroanal. Chem.* **1986,** *210,* 189-194.

56. Fang, Y.-H.; Liu, Z.-P., *J. Am. Chem. Soc.* **2010,** *132,* 18214-18222.

57. Man, I. C.; Su, H.-Y.; Calle-Vallejo, F.; Hansen, H. A.; Martínez, J. I.; Inoglu, N. G.; Kitchin, J.; Jaramillo, T. F.; Nørskov, J. K.; Rossmeisl, J., *ChemCatChem* **2011,** *3,* 1159-1165.

58. Bernicke, M.; Ortel, E.; Reier, T.; Bergmann, A.; Ferreira de Araujo, J.; Strasser, P.; Kraehnert, R., *ChemSusChem* **2015,** *8,* 1908-1915.

59. Fei, H.; Dong, J.; Arellano-Jimenez, M. J.; Ye, G.; Dong Kim, N.; Samuel, E. L.; Peng, Z.; Zhu, Z.; Qin, F.; Bao, J.; Yacaman, M. J.; Ajayan, P. M.; Chen, D.; Tour, J. M., *Nat. Commun.* **2015,** *6,* 8668-8675.

60. Doyle, R. L.; Godwin, I. J.; Brandon, M. P.; Lyons, M. E. G., *Phys. Chem. Chem. Phys.* **2013,** *15,* 13737-13783.

61. Giordano, L.; Han, B.; Risch, M.; Hong, W. T.; Rao, R. R.; Stoerzinger, K. A.; Shao-Horn, Y., *Catal. Today* **2016,** *262,* 2-10.

62. Gao, M.-R.; Cao, X.; Gao, Q.; Xu, Y.-F.; Zheng, Y.-R.; Jiang, J.; Yu, S.-H., *ACS Nano* **2014,** *8,* 3970-3978.

63. Zhao, Y.; Nakamura, R.; Kamiya, K.; Nakanishi, S.; Hashimoto, K., *Nat. Commun.* **2013,** *4,* 2390-2396.

64. Suntivich, J.; May, K. J.; Gasteiger, H. A.; Goodenough, J. B.; Shao-Horn, Y., *Science* **2011,** *334,* 1383-1385.

65. Zou, X.; Su, J.; Silva, R.; Goswami, A.; Sathe, B. R.; Asefa, T., *Chem. Commun.* **2013,** *49,* 7522-7524.

66. Mao, S.; Wen, Z.; Huang, T.; Hou, Y.; Chen, J., *Energy Environ. Sci.* **2014,** *7,* 609-616.

67. Gao, M.-R.; Xu, Y.-F.; Jiang, J.; Zheng, Y.-R.; Yu, S.-H., *J. Am. Chem. Soc.* **2012,** *134,* 2930-2933.

68. Mendoza-Garcia, A.; Su, D.; Sun, S., *Nanoscale* **2016,** *8,* 3244-3247.

69. Bikkarolla, S. K.; Papakonstantinou, P., *J. Power Sources* **2015,** *281,* 243-251.

70. Liu, X.; Jiang, J.; Ai, L., *J. Mater. Chem. A* **2015,** *3,* 9707-9713.

71. Chen, P.; Xu, K.; Zhou, T.; Tong, Y.; Wu, J.; Cheng, H.; Lu, X.; Ding, H.; Wu, C.; Xie, Y., *Angew. Chem. Int. Ed.* **2016,** *55,* 2488-2492.

72. Xie, J.; Zhang, H.; Li, S.; Wang, R.; Sun, X.; Zhou, M.; Zhou, J.; Lou, X. W.; Xie, Y., *Adv. Mater.* **2013,** *25,* 5807-5813.

73. Vrubel, H.; Hu, X., *Angew. Chem. Int. Ed.* **2012,** *51,* 12703-12706.

74. Popczun, E. J.; McKone, J. R.; Read, C. G.; Biacchi, A. J.; Wiltrout, A. M.; Lewis, N. S.; Schaak, R. E., *J. Am. Chem. Soc.* **2013,** *135,* 9267-9270.

75. Wang, X.; Kolen'ko, Y. V.; Bao, X.-Q.; Kovnir, K.; Liu, L., *Angew. Chem. Int. Ed.* **2015,** *54,* 8188-8192.

76. Tian, J.; Liu, Q.; Cheng, N.; Asiri, A. M.; Sun, X., *Angew. Chem. Int. Ed.* **2014,** *53,* 9577-9581.

77. Kundu, M. K.; Bhowmik, T.; Barman, S., *J. Mater. Chem. A* **2015,** *3,* 23120-23135.

78. Shen, Y.; Lua, A. C.; Xi, J.; Qiu, X., *ACS Appl. Mater. Interfaces* **2016,** *8,* 3464-3472.

79. Chen, W. F.; Wang, C. H.; Sasaki, K.; Marinkovic, N.; Xu, W.; Muckerman, J. T.; Zhu, Y.; Adzic, R. R., *Energy Environ. Sci.* **2013,** *6,* 943-951.

80. Bhowmik, T.; Kundu, M. K.; Barman, S., *ACS Catal.* **2016,** *6,* 1929-1941.

81. Cao, B.; Veith, G. M.; Neuefeind, J. C.; Adzic, R. R.; Khalifah, P. G., *J. Am. Chem. Soc.* **2013,** *135,* 19186-19192.

82. Tang, M. H.; Hahn, C.; Klobuchar, A. J.; Ng, J. W. D.; Wellendorff, J.; Bligaard, T.; Jaramillo, T. F., *Phys. Chem. Chem. Phys.* **2014,** *16,* 19250-19257.

83. Yin, H.; Zhao, S.; Zhao, K.; Muqsit, A.; Tang, H.; Chang, L.; Zhao, H.; Gao, Y.; Tang, Z., *Nat. Commun.* **2015,** *6,* 6430.

84. Gong, M.; Zhou, W.; Tsai, M. C.; Zhou, J.; Guan, M.; Lin, M. C.; Zhang, B.; Hu, Y.; Wang, D. Y.; Yang, J.; Pennycook, S. J.; Hwang, B. J.; Dai, H., *Nat. Commun.* **2014,** *5,* 4695.

85. Jin, H.; Wang, J.; Su, D.; Wei, Z.; Pang, Z.; Wang, Y., *J. Am. Chem. Soc.* **2015,** *137,* 2688-2694.

86. Merki, D.; Fierro, S.; Vrubel, H.; Hu, X., *Chem. Sci.* **2011,** *2,* 1262-1267.

87. McArthur, M. A.; Jorge, L.; Coulombe, S.; Omanovic, S., *Journal of Power Sources* **2014,** *266*, 365-373.

88. Ledendecker, M.; Clavel, G.; Antonietti, M.; Shalom, M., *Adv. Funct. Mater.* **2015,** *25,* 393-399.

89. Cobo, S.; Heidkamp, J.; Jacques, P.-A.; Fize, J.; Fourmond, V.; Guetaz, L.; Jousselme, B.; Ivanova, V.; Dau, H.; Palacin, S.; Fontecave, M.; Artero, V., *Nat. Mater.* **2012,** *11,* 802-807.

90. Tran, P. D.; Nguyen, M.; Pramana, S. S.; Bhattacharjee, A.; Chiam, S. Y.; Fize, J.; Field, M. J.; Artero, V.; Wong, L. H.; Loo, J.; Barber, J., *Energy Environ. Sci.* **2012,** *5,* 8912-8916.

91. Kötz, E. R.; Stucki, S., *J. Appl. Electrochem.* **1987,** *17,* 1190-1197.

92. Wang, X.; Li, W.; Xiong, D.; Petrovykh, D. Y.; Liu, L., *Adv. Funct. Mater.* **2016,** *26,* 4067-4077.

93. Anantharaj, S.; Jayachandran, M.; Kundu, S., *Chem. Sci.* **2016**.

94. Faber, M. S.; Dziedzic, R.; Lukowski, M. A.; Kaiser, N. S.; Ding, Q.; Jin, S., *J. Am. Chem. Soc.* **2014,** *136,* 10053-10061.

95. Maiyalagan, T.; Chemelewski, K. R.; Manthiram, A., *ACS Catal.* **2014,** *4,* 421-425.

96. Negro, E.; Vezzù, K.; Bertasi, F.; Schiavuta, P.; Toniolo, L.; Polizzi, S.; Di Noto, V., *ChemElectroChem* **2014,** *1,* 1359-1369.

Chapter 6

Formic Acid oxidation on Palladium Nanoparticles- Graphitic Carbon Nitride

6.1 Abstract

The electrochemical formic acid oxidation reaction (FAO) is an anodic process of direct formic acid fuel cells (DFAFCs). Carbon supported platinum (Pt/C) and Palladium (Pd/C) catalysts are widely used as anode materials for FAO. The CO poisoning of Pt/C and poor stability of Pd/C are main obstacles for its commercialization. We report here superior electrocatalytic activity of Palladium nanoparticles-carbon nitride composite (PdNPs/CNx) towards formic acid oxidation (FAO) with high mass activity (1640 mAmgPd-1) in acid media which is 7.2 times higher than that of commercial Pd/C catalyst in 0.5 M H_2SO_4 medium. It also exhibited an outstanding stability for FAO (mass activity of this catalyst was 23 times higher than commercial Pd/C after 1000 cycles).

6.2 Introduction

Development of sustainable and renewable energy sources[1] are gaining enormous attentions due to the limited access of natural fossil fuel and the rapid rise of energy demand. The fuel cells are the green energy resources, alternative to fossil fuel.[2] In recent years, Direct Formic Acid Fuel Cells (DFAFCs) have attracted attentions to scientific community due to its unique advantages over hydrogen fuel cell and direct methanol fuel cells (DMFCs).[3] For hydrogen fuel cell, hydrogen storage and transportation are the main limitations for its applications, whereas methanol cross over, toxicity of methanol are the disadvantages of DMFCs. The DFAFCs has been created great attention as a promising alternate to DMFCs due to its higher power density, low fuel crossover, higher energy efficiency and higher electromotive force. The theoretical open circuit potential of DFAFCs is 1.48 V (vs. saturated hydrogen electrode) which is higher than hydrogen and methanol fuel cells.[4] The low fuel crossover in DFAFC is due to dissociation of formic acid to format ions ($HCOO^-$) and their repulsive interaction.[5] The electro-oxidation of formic acid on solid surfaces is known to occur via two different paths – (1) dehydrogenation process, the direct-path involves oxidation of formic acid to carbon dioxide ($HCOOH = CO_2 + 2H^+ + 2e^-$) and (2) the indirect-path (dehydration path) occurs via intermediate formation, oxidation of adsorbed CO species ($HCOOH = CO_{ads} + H_2O = CO_2 + 2H^+ + 2e^-$).[6] The formic acid oxidation through indirect path is easier one since the energy barrier of C-H bond activation is more than that of C-O bond activation. The Pt and Pd based catalysts [7-10] are considered as the most effective electrocatalysts for the oxidation of formic acid. However, Pd catalysts are more suitable than Pt.[11-13] The main disadvantage of Pt catalysts is the CO poisoning since FAO proceeds through indirect-pathway. In contrast, Pd catalysts[14-15] are considered as better electrocatalysts than Pt because of the reaction on Pd surface follows direct-pathway. However, stability of Pd catalysts is main issue since they are less stable for electro-oxidation of formic acid in acid electrolyte than Pt. The formic acid oxidation reaction over Pd surface highly depends on the electronic effect[16], shape[17] and crystal pattern of the surface[18]. Several strategies were adopted by different groups to enhance catalytic activity at low over potentials and increase durability of Pd based catalyst such as by making bimetallic compound[19-20] of Pd, alloying with early transition metal, [21-27] addition of adatoms[28-32] such as Pb, Bi, Sb on the Pd surface.

In recent years, carbon based materials are gaining attentions due to their versatile physical and chemical properties as well as the superior applications towards electrocatalysis. The g-C_3N_4 is one of the promising materials among different carbon based materials due to its unique structure, comprising of large number of carbon-nitrogen coordination nest to stabilize nanoparticle. The g-C_3N_4 supported stabilized metals nanoparticles have different potential applications towards electrochemical sensing,[33] photo catalysis,[34] electro catalysis[35] etc. But low conductivity of g-C_3N_4 moiety obstacles their intrigue application. However, several groups have reported [36-37] that the decrease of nitrogen concentration in carbon nitride support increases conductivity of support and thereby enhances the electrochemical performances. It is still challenging to synthesize electrocatalysts with high conductivity for improved the catalytic activity and high stability under operating condition.

Herein, we report the superior catalytic activity of PdNPs/CN_x catalyst towards electrochemical FAO. The oxidation of formic acid on PdNPs/CN_x occurs via direct pathway and its mass activity is 7.2 time higher than that of commercial Pd/C. Most importantly, this catalyst shows a remarkable durability and long-term stability towards FAO as compare to commercial Pd/C and Pt/C catalyst. The superior catalytic activity of PdNPs/CN_x can be mainly attributed by the lower charge transfer resistance (R_{ct}) due to strong interaction between Pd nanoparticles and CN_x support.

6.3 Experimental Section

Preparation of g-C_3N_4:

The g-CN_x was synthesized[38] by microwave heating of fomamide ($HCONH_2$). In a microwave oven 30 ml $HCONH_2$ was heated at 180°C for 3 hrs. The brownish solution, thus obtained was further evaporated at 180°C to produce a black product. Then the black product was washed with distilled water and dried in vacuum in order to obtain desired g-CN_x.

PdNPs/CN$_x$ Catalyst Synthesis:

The PdNPs/CN$_x$ catalyst was synthesized by ultrasound mediated brohydride reduction method, reported recently by our group.[35] First, aqueous $PdCl_4^{-2}$ solution was prepared by dissolving 0.14 mmol $PdCl_2$ into 8 ml aqueous 0.1% HCl solution. Next g-CN$_x$ (5 mg) was dispersed in de-ionized water (2 ml) and then added 8ml aqueous $PdCl_4^{-2}$ solution into dispersed g-CN$_x$ suspension. After that 0.1 M aqueous solution of $NaBH_4$ (0.7 ml) was added gradually to the previous mixture. The whole solution was sonicated at a constant frequency (28 kHz) using a probe sonicator for 3 hours. Finally the black product was separated by centrifugation and then dried under vacuum.

Preparations of Working Electrode:

First, PdNPs/CN$_x$ catalyst (0.5 mg) was dispersed in Millipure water (1ml) by half an hour sonication at a constant frequency (60 Hz). Then this solution was kept for few days (3 days) before being used for electrode preparation. 10 µL of this aged solution was evaported on polished glassy carbon working electrode of 3 mm diameter at ~50^0C. In this procedure, no polymer binder (nafion) was required for the preparation of PdNPs/CN$_x$, modified GC electrode for FAO activity and stability studies. Although in FAO activity experiment, In order to observe long term stability of Pt/C or Pd/C electrode, polymer binder was required for the immobilization of catalyst on GC electrode. In a typical experiment, 1.5 mg Pt/C or 1 mg of Pd/C catalyst were added to 1ml of water followed by vigorous solication for half an hour. Then the aliquot (20 µl for Pt/C and 10 µl for Pd/C) was drop casted onto the electrode and kept for drying. For Pd/C ,Next, the electrode was charged with 10 µl nafion solution (0.25 wt%) and kept for drying.

6.4 Results and Discussion

In an ultrasound-mediated process, aqueous $PdCl_4^{-2}$ solution containing g-CN_x was reduced by $NaBH_4$ in order to obtain the PdNPs/CN_x catalyst (details in experimental section). Surface structure of PdNPs/CN_x catalyst was investigated by TEM image as shown in **Figure 6.1.a** From TEM image it was clearly observed that the Pd-NPs were decorated on the g-CN_x with particle size distribution in between 5-14 nm (**Figure 6.1.b**).

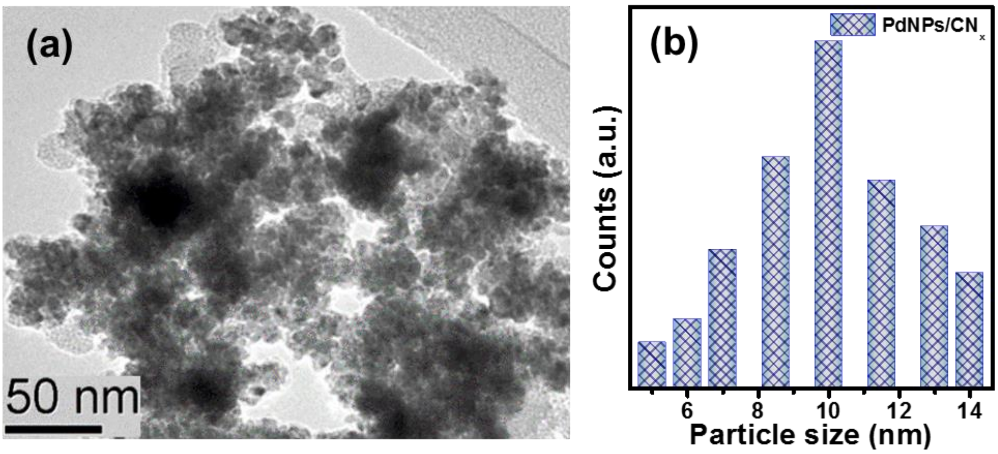

Figure 6.1. (a) TEM image and (b) corresponding particle size distribution plot of PdNPs/CN_x.

For comparisons, we have performed the TEM measurement of comm. Pd/C and Pt/C catalyst (**Figure 6.2.**). The TEM image of comm. Pd/C catalyst and corresponding particle size distribution was shown in **Figure 6.2.(a,b).** The particle size of Pd nanoparticles in comm. Pd/C was found to be within 6-10 nm. The TEM image of comm. Pt/C catalyst was shown in **Figure 6.2.c.** TEM image of Pt/C catalyst clearly shows very small particles are well distributed on the carbon sheets. The sizes of Pt particles in commercial Pt/C were in between 2-5 nm (**Figure 6.2.d**). The morphology of PdNPs/CN_x catalyst was further investigated by FE-SEM measurement as shown in **Figure 6.3.a**. In addition also distribution of the palladium NPs was investigated by

EDX mapping as shown in **Figure 6.3.(b-e).** The FE-SEM mapping clearly shows that Pd, C, N elements are uniformly distributed in the composite materials. The amount of Pd loading in PdNPs/CN_x composite calculated from FE-SEM EDX experiment and it is ~ 61.1 wt. %.

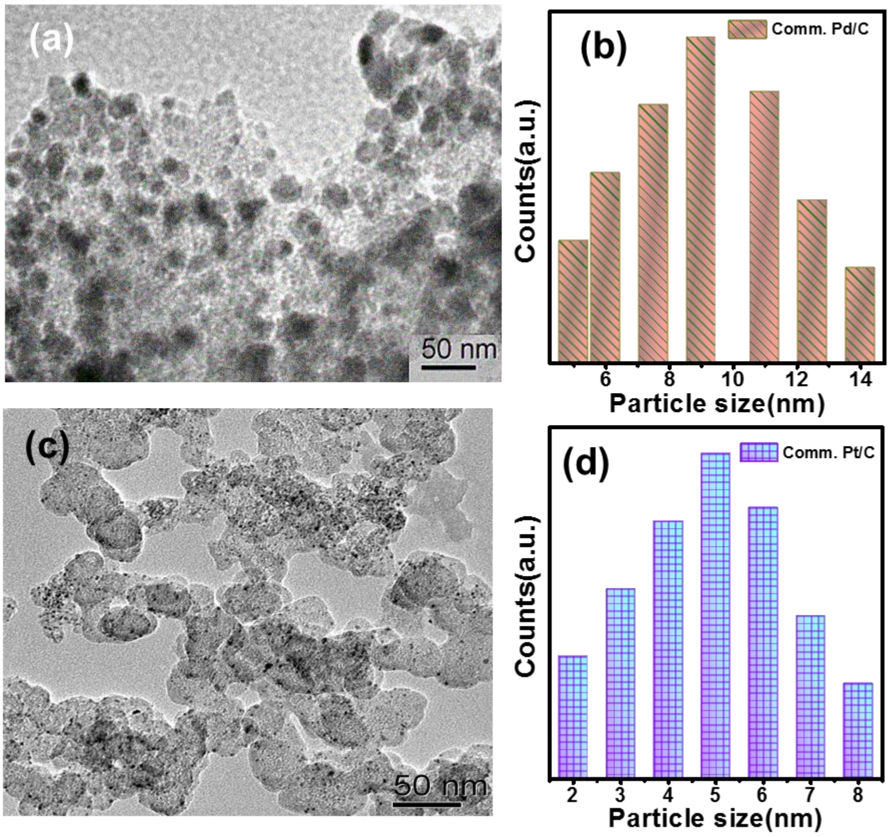

Figure 6.2. TEM image and corresponding particle size distribution plot of (a,b) comm. Pd/C and (c,d) comm. Pt/C.

From these measurements clearly confirmed the formation of Pd-NPs on the g-CN_x moiety by ultrasound assisted $NaBH_4$ reduction methods. Inductively coupled plasma optical emission spectrometry (ICP-OES) was used to measure the amount of Pd loading on PdNPs/CN_x catalyst. The ICP-OES analysis confirmed 59.4 wt.% PdNPs was present in PdNPs/CN_x catalyst. CHN elemental analysis indicated that the N:C ratio in PdNPs/CN_x catalyst was 0.89 where as in free g-C_3N_4 moiety it was 1.1.

The CV curves of PdNPs/CN_x catalyst, comm. Pd/C and Pt/C catalyst collected from N_2 saturated 0.5 M H_2SO_4 medium were shown in **Figure 6.4.(a-c).**

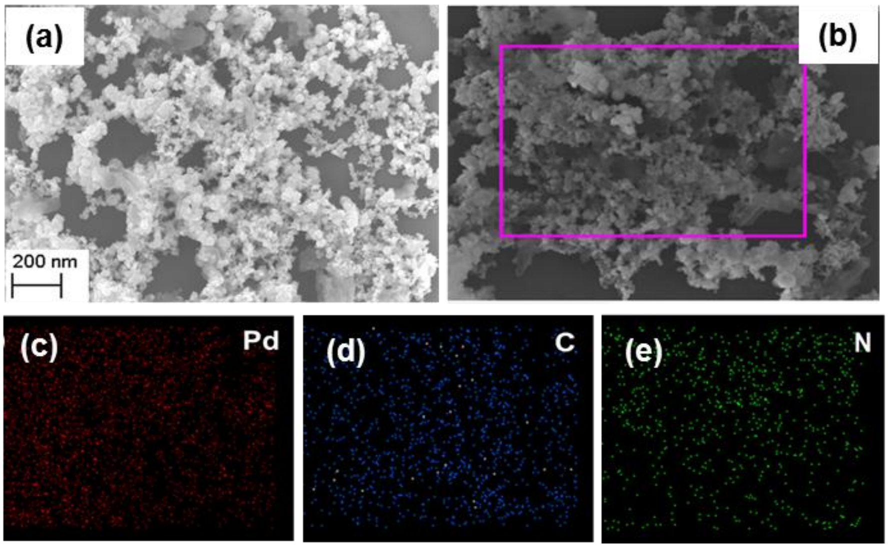

Figure 6.3. (a,b) FESEM images of PdNPs/CN_x composite. EDX elemental mapping of (c) Pd, (d) Carbon and (e) Nitrogen**.**

The electrochemical active surface area was calculate from the H-desorption peak by the formula

$$\text{ECSA (from H-desorption peak)} = \frac{Q_s}{0.21 * M_{Pd}}$$

where Q_s is the average charge calculated from area under the voltragram of the H-desorption CV curve in mC /cm^2 unit shown in **Figure 6.4. (a-c)**,by

$$Q_s = \int \frac{I * dE}{v}$$

Where v is the scan rate.

The electrochemical surface area (ECSA) of PdNPs/CN_x and comm. Pd/C and Pt/C catalyst was extracted from H-adsorption/desorption region of CV curves (**Figure**

6.4.(a-c).The calculated ECSA values of PdNPs/CN$_x$, comm. Pd/C and Pt/C in 0.5 M H_2SO_4 electrolyte were 63 m^{2}g^{-1}, 57.4 m^{2}g^{-1} and 59.2 m^{2}g^{-1} respectively.

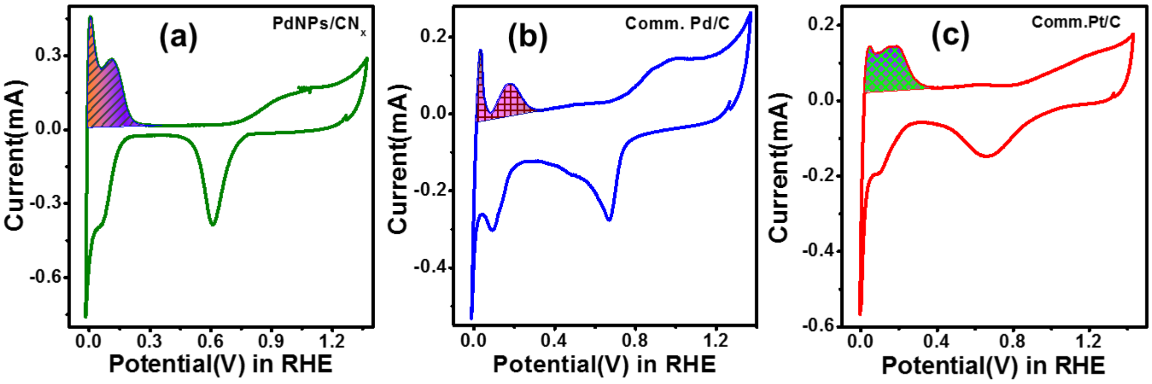

Figure 6.4. CV curves of different catalyst in N_2 saturated 0.5 M H_2SO_4 with 100 mV/sec scan rate (a) PdNPs/CN$_x$, (b) Comm. Pd/C, (c) Comm. Pt/c respectively.

The very good ORR activity[39] of PdNPs/CN$_x$ composite was reported by our group recently. **Figure 6.5.(a-c)** demonstrated the typical CV curves of PdNPs/CN$_x$, comm. Pd/C and Pt/C modified GC electrodes in 0.5 M H_2SO_4 electrolyte with and without 0.3 M HCOOH solution at a scan rate of 50 mV/sec. **Figure 6.5.a** shows both forward and backward scan of PdNPs/CN$_x$ catalyst for FAO. In addition also **Figure 6.5.(a,b)** shows both forward and backward scan of comm. Pd/C and comm. Pt/C catalyst for FAO in 0.5 M H_2SO_4 solution. The forward scan of CV curve of Pt/C catalyst is consist of two separate peaks – peak at 0.52 V can be assigned for FAO through direct-path and peak at 0.94 V can be attributed to FAO through indirect-pathway(**Figure 6.5.c**). But, in case of Pd/C and PdNPs/CN$_x$ catalysts, the forward scan has only single peak at 0.44V and 0.37 V respectively (**Figure 6.5.(a,b)**). This suggested that formic acid oxidation on these Pd catalysts occurred through 2e$^-$ electron transfer direct pathway.[14, 40] The comparisons of CV forward scan for different catalyst in presence of formic acid have also shown in **Figure 6.6.a**.

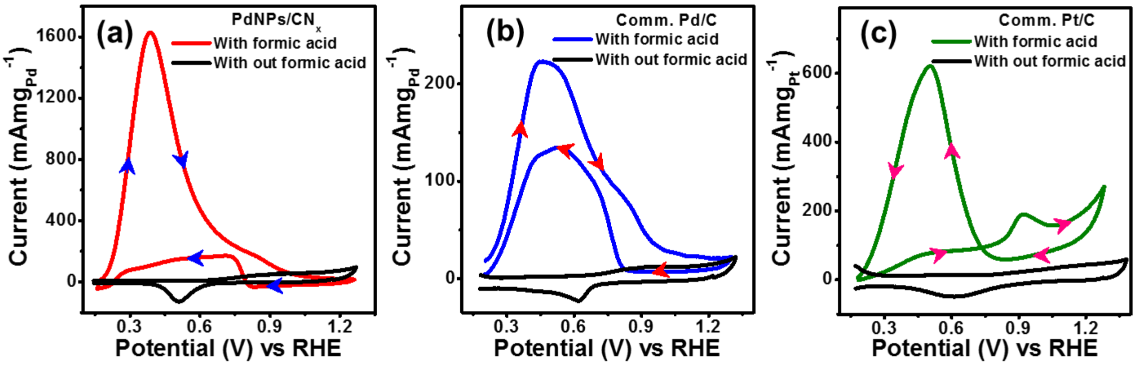

Figure 6.5. Comparison of full CVs of (a) PdNPs/CN$_x$, (b) comm. Pd/C, (c) comm. Pt/C presence and absence of formic acid.

The maximum peak current of forward scan for PdNPs/CN$_x$, comm. Pd/C and Pt/C were appeared at 0.37 V, 0.44 V, and 0.44 V (RHE) respectively. We have calculated the mass and specific activity of different catalyst to measure the efficiency towards FAO. The mass activity (mAmg^{-1}$_{Pd}$) was calculated from the measured current J (mA) at particular overpotential and Pd metal loading m (mg) on the electrode surface using following equation:

$$\text{Mass activity (MA)} = \frac{\text{J (mA)}}{\text{m(mg)}}$$

The specific activity of the catalyst were measured from mass activity (MA), geometrical area of the electrode S (cm^2) and metal loading m (mg) on the electrode:

$$\text{Specific activity (SA)} = \frac{\text{MA} \times \text{m}}{\text{S}}$$

The measured MA of PdNPs/CN$_x$, comm. Pd/C and Pt/C catalyst at peak potential were 1640 mA/mg$_{Pd}$ 227.7 mA/mg$_{pd}$ and 192 mA/mg$_{Pt}$ respectively. In addition, the catalytic activities for different catalysts for FAO was summarized in **Table 6.1**. The PdNPs/CN$_x$ catalyst has 70 mV more negative peak potential and 7.2 times higher mass activity than comm. Pd/C catalyst for FAO reaction.

Table 6.1. Different parameters of different catalysts for FAO reaction in 0.5 M H_2SO_4.

catalyst	**ECSA (m^2g^{-1})**	**Peak potential (V vs RHE)**	**Mass activity ($mAmg_M^{-2}$)**	**Specific activity ($mAcm_{geo}^{-2}$)**
PdNPs/CN_x	42.0	0.37	1640	70.18
Commercial Pd/C	39.4	0.44	227.7	9.76
Commercial Pt/C	36.4	0.94	192	8.23

At 0.4 V (RHE) (the typical working voltage in DFAFC) the current density of PdNPs/CN_x catalyst for formic acid oxidation is ~7.6 times and ~36 times higher than that of comm. Pd/C and Pt/C catalyst respectively. The comparison of the mass activity of PdNPs/CN_x, comm. Pd/C and Pt/C catalysts at different potentials is shown in **Figure 6.6.b**. The porous PdNPs/CN_x catalyst has higher mass activity at any potential, lower to 0.8 V; but at the potential of 0.9 V, the Pt/C has higher mass activity than PdNPs/CN_x catalyst since Pt/C follows dual pathway mechanism.

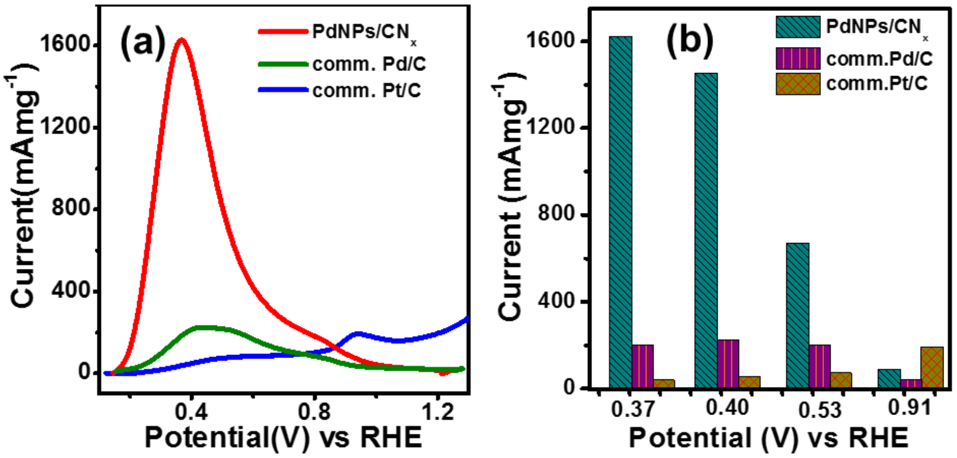

Figure 6.6. (a) Forward scan of CV curves of PdNPs/CN_x, comm. Pd/C, comm. Pt/C. (b) Comparison of M.A. for PdNPs/CN_x,comm. Pd/C, comm. Pt/C catalyst at different potentials.

The long term cycling stability of these catalysts was carried out as shown in **Figure 6.7.a** and **Figure 6.7.b**. The CV cycling stability of PdNPs/CN_x and Pd/C catalyst was performed in the potentials range of 0.14 to 1.24 V (RHE) at scan rate of 50 mV in steady state. Although the mass activity of PdNPs/CN_x decreases to 1100 mA mg_{pd}^{-1}

after 1000 cycles, but it was still much higher than that of Pd/C (48 mA mg_{Pd}^{-1}) and Pt/C catalyst. The long term cycling stability of this PdNPs/CN_x catalyst is excellent since it retains ~ 70% of its initial current density whereas Pd/C and Pt/C retains only 17% and 2.4% of its initial mass activity after 1000 repeated cycles (**Figure 6.7.b**). In addition the catalytic activity and long term stability of PdNPs/CN_x composite was further studied by measuring change of ECSA with cycle number. **Figure 6.7.c** shows the change in ECSA of PdNPs/CN_x in comparison with comm. Pd/C and Pt/C catalyst with CV cycle number. After 1000 cycle, ECSA of Pd-CN_x composite decreases only 15% whereas it decreases 74 and 71% for comm. Pd/C, Pt/C respectively.

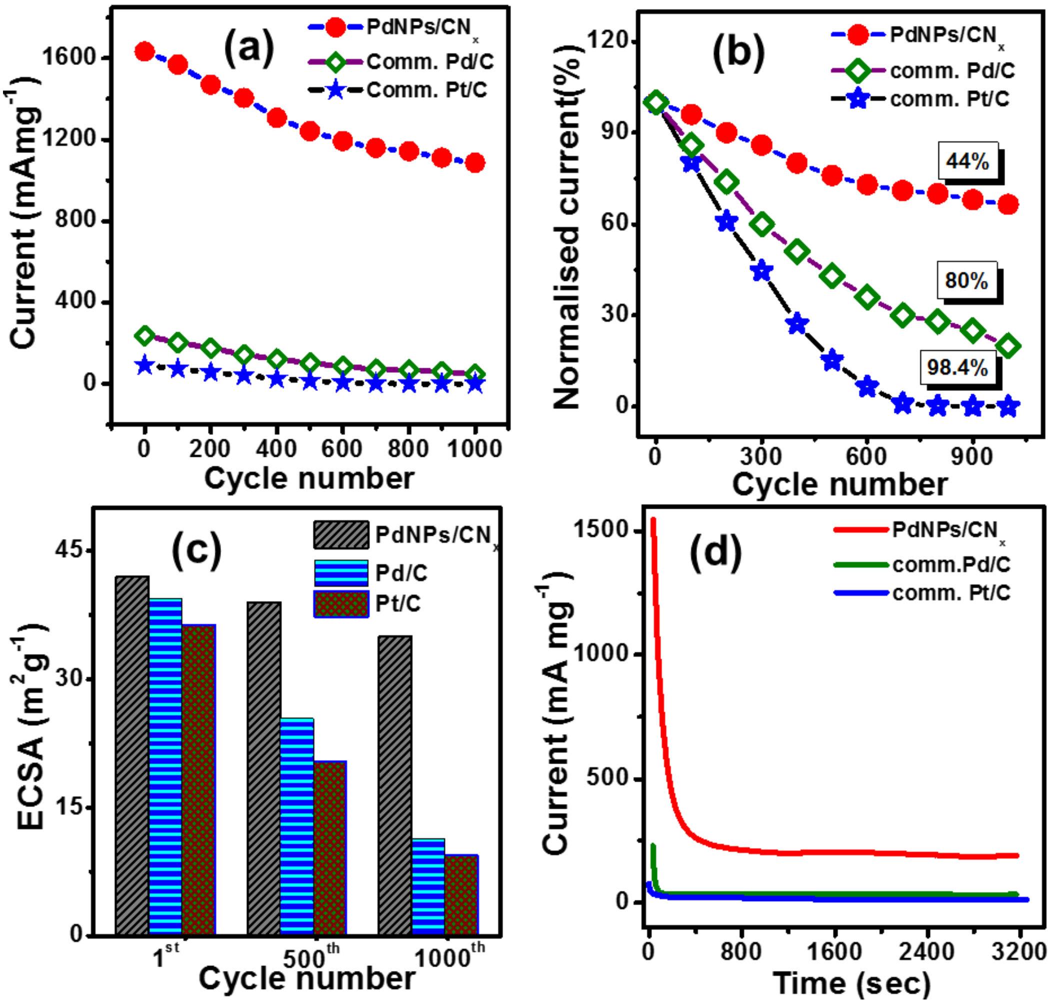

Figure 6.7. Comparative study of (a) absolute M.A. values (b) Normalised M.A. values, (c) ECSA, and (d) Chronoampermetric response of different catalysts with cycle number in 0.5 M H_2SO_4.

Table 6.2. Comparison of mass activity and peak potential of PdNPs/CN_x with reported Pd based catalyst for FAO in 0.5 M H_2SO_4 electrolyte.

Catalyst	**Peak potential (V) (RHE)**	**Mass activity (mA mg_{Pd}^{-1})**	**Ref.**
Pd-graphene	0.45	500	27
Pd-DNA@CNTs	0.44	181.23	28
Pd sheet	0.42	1380	29
Pd cube	0.48	~140	30
$Pd_{57}Ni_{43}$	0.36	~850	12
C-PdCu	0.48	1192.9	32
Pd_6Co	0.43	430.8	16
Pd_1Ni_1-NNs/ RGO	0.58	604.3	33
Pd -tripod	0.48	401.0	31
PdNPs/CN_x	**0.37**	**1640**	**This work**

The comparison of chronoamperometry study of PdNPs/CN_x, Pd/C and Pt/C catalyst at an operating potential of 0.33 V (RHE) in 0.5 M H_2SO_4 + 0.5 M HCOOH solution was shown in **Figure 6.7.d.** This revealed that the current densities of these three electrodes decreases with time and the current density of PdNPs/CN_x catalyst was much higher than that of Pd/C and Pt/C over the entire scan time range. After 3200 sec scan the current density on PdNPs/CN_x electrode was 6.2 and 27 times higher than that of Pd/C and Pt/C respectively. This proves that this PdNPs/CN_x catalyst has much higher durability than that of commercial Pd/C and Pt/C. The comparison of the mass activity as well as the peak potentials of PdNPs/CN_x for FAO with reported Pd and Pt based catalyst was shown in **Table 6.2.** The PdNPs/CN_x catalyst has higher mass activity (1640 mA mg_{Pd}^{-1}) than the different monometallic Pd based electrocatalysts such as Pd-graphene (500 mA mg_{Pd}^{-1}),[41] Pd-DNA@CNT (181.23 mA mg_{Pd}^{-1}),[42] Pd-sheet (1380 $mAmg_{Pd}^{-1}$),[43] Pd cube (140 $mAmg_{Pd}^{-1}$)[44] Pd-tripod (401.0 $mAmg_{Pd}^{-1}$)[45] and also higher or comparable mass activity with respect to different bi- metallic systems such as $Pd_{57}Ni_{43}$ (850 mA mg_{Pd}^{-1}),[19] C-PdCu (1192.8 mA mg_{Pd}^{-1}),[46] Pd_6Co(430.8 mA mg_{Pd}^{-1})[23] and Pd_1Ni_1-NNs/RGO (604.3 mA mg_{Pd}^{-1}).[47] The higher mass activity, more negative peak potentials and long term durability of PdNPs/CN_x as compared to the commercial Pt/C and Pd/C catalyst suggest the intrinsic and excellent catalytic activity towards electrochemical FAO reaction.

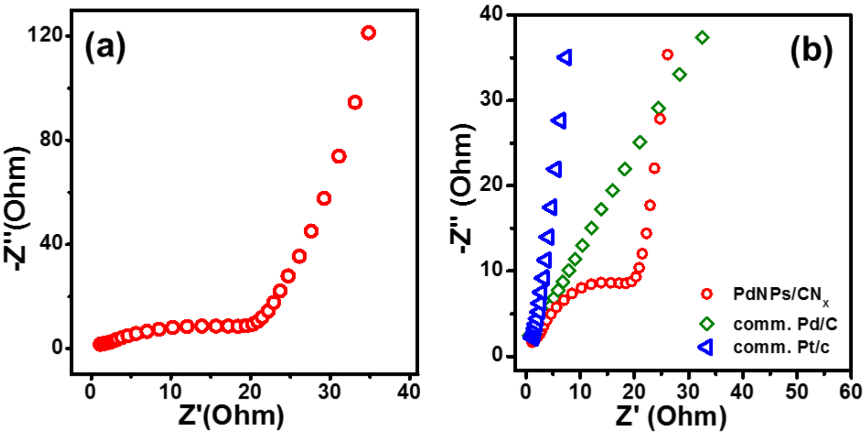

Figure 6.8. (a) EIS spectra of PdNPs/CN_x. (b) Comparison of EIS spectra of PdNPs/CN_x, comm. Pd/C, comm. Pt/C in 0.5 M H_2SO_4.

The strong metal-support interaction also enhances electron transport thorough the catalyst support. In order to find charge transfer resistance of the composite, impedance spectroscopic studies were performed shown in **Figure 6.8.(a,b)**. The charge transfer resistance (R_{ct}) of PdNPs/CN_x, Pd/C and Pt/C are 39.7, 90 and 870 ohm respectively.

The considerably low R_{ct} value in PdNPs/CN_x suggests that the strong synergistic interaction between Pd-NPs and CN_x facilitates electron transfer through the composite thus enhances the electrocatalytic activities of the PdNPs/CN_x catalyst. In addition, presence of N atom in support (CN_x) is also helped to enhance catalytic activity of this PdNPs/CN_x composite.

6.5 Conclusions

Thus, we have demonstrated the superior behavior of PdNPs/CN_x electro-catalyst as compare to the commercial Pt/C or Pd/C for formic acid oxidation in acidic media. The mass activity of PdNPs/CN_x composite for FAO is 7.2 times higher than that of commercial Pd/C and its peak potential is 70 mV more negative as compare to commercial Pd/C. In addition, mass activity of PdNPs/CN_x catalyst became 23 times higher than Pd/C after 1000 continuous LSV cycles confirming an outstanding stability of this catalyst. The excellent catalytic activity and durability of PdNPs/CN_x catalyst is well supported by the decreasing charge transfer resistance of PdNPs/CN_x catalyst. The outstanding performance of PdNPs/CN_x towards formic acid oxidation making them a superior catalyst for FAFCs.

6.6 References

1. G. W. Crabtree, M. S. D., and M. V. Buchanan., *Physics Today* **2004,** *57,* 39-44.
2. Bai, Z.; Shi, M.; Zhang, Y.; Zhang, Q.; Yang, L.; Yang, Z.; Zhang, J., *Green Chem.* **2016,** *18,* 386-391.
3. Wang, Y.; Liu, H.; Wang, L.; Wang, H.; Du, X.; Wang, F.; Qi, T.; Lee, J.-M.; Wang, X., *J. Mater. Chem. A* **2013,** *1,* 6839-6848.
4. Kristian, N.; Yan, Y.; Wang, X., *Chem. Commun.* **2008,** 353-355.
5. Wang, X.; Hu, J.-M.; Hsing, I. M., *J. Electroanal. Chem.* **2004,** *562,* 73-80.
6. Jiang, K.; Zhang, H.-X.; Zou, S.; Cai, W.-B., *Phys. Chem. Chem. Phys.* **2014,** *16,* 20360-20376.
7. Zhang, J.-M.; Wang, R.-X.; Nong, R.-J.; Li, Y.; Zhang, X.-J.; Zhang, P.-Y.; Fan, Y.-J., *Inter. J. Hydrogen Energy* http://dx.doi.org/10.1016/j.ijhydene.2016.05.198.

8. Han, S.-H.; Ji, Y.-G.; Xing, S.-H.; Hui, J.-J.; Guo, Q.; Shi, F.; Chen, P.; Chen, Y., *Inter. J. Hydrogen Energy* http://dx.doi.org/10.1016/j.ijhydene.2016.09.026.

9. Hao, Y.; Shen, J.; Wang, X.; Yuan, J.; Shao, Y.; Niu, L.; Huang, S., *Inter. J. Hydrogen Energy* **2016,** *41,* 3015-3022.

10. Malolepszy, A.; Mazurkiewicz, M.; Stobinski, L.; Lesiak, B.; Kövér, L.; Tóth, J.; Mierzwa, B.; Borodzinski, A.; Nitze, F.; Wågberg, T., *Inter. J. Hydrogen Energy* **2015,** *40,* 16724-16733.

11. Larsen, R.; Ha, S.; Zakzeski, J.; Masel, R. I., *J. Power Sources* **2006,** *157,* 78-84.

12. Wang, R.; Liao, S.; Ji, S., *J. Power Sources* **2008,** *180,* 205-208.

13. Bai, Z.; Yang, L.; Guo, Y.; Zheng, Z.; Hu, C.; Xu, P., *Chem. Commun.* **2011,** *47,* 1752-1754.

14. Zhou, Z.-Y.; Kang, X.; Song, Y.; Chen, S., *Chem. Commun.* **2011,** *47,* 6075-6077.

15. Wang, J.; Yin, G.; Chen, Y.; Li, R.; Sun, X., *Inter. J. Hydrogen Energy* **2009,** *34,* 8270-8275.

16. Hoshi, N.; Kida, K.; Nakamura, M.; Nakada, M.; Osada, K., *J. Phys. Chem. B* **2006,** *110,* 12480-12484.

17. Vidal-Iglesias, F. J.; Aran-Ais, R. M.; Solla-Gullon, J.; Garnier, E.; Herrero, E.; Aldaz, A.; Feliu, J. M., *Phys. Chem. Chem. Phys.* **2012,** *14,* 10258-10265.

18. Shao, M.; Odell, J.; Humbert, M.; Yu, T.; Xia, Y., *J. Phys. Chem. C* **2013,** *117,* 4172-4180.

19. Du, C.; Chen, M.; Wang, W.; Yin, G., *ACS Appl. Mater. Interfaces* **2011,** *3,* 105-109.

20. Hu, S.; Munoz, F.; Noborikawa, J.; Haan, J.; Scudiero, L.; Ha, S., *Appl. Catal. B: Environ.* **2016,** *180,* 758-765.

21. Liu, D.; Guo, Q.; Hou, H.; Niwa, O.; You, T., *ACS Catal.* **2014,** *4,* 1825-1829.

22. Mazumder, V.; Chi, M.; Mankin, M. N.; Liu, Y.; Metin, Ö.; Sun, D.; More, K. L.; Sun, S., *Nano Lett.* **2012,** *12,* 1102-1106.

23. Zhang, L. Y.; Zhao, Z. L.; Yuan, W.; Li, C. M., *Nanoscale* **2016,** *8,* 1905-9.

24. Hu, S.; Scudiero, L.; Ha, S., *Electrochem. Commun.* **2014,** *38,* 107-109.

25. Fathirad, F.; Afzali, D.; Mostafavi, A., *Inter. J. Hydrogen Energy* **2016,** *41,* 13220-13226.

26. Yang, F.; Zhang, Y.; Liu, P.-F.; Cui, Y.; Ge, X.-R.; Jing, Q.-S., *Inter. J. Hydrogen Energy* **2016,** *41,* 6773-6780.

27. Wang, L.; Zhai, J.-J.; Jiang, K.; Wang, J.-Q.; Cai, W.-B., *Inter. J. Hydrogen Energy* **2015,** *40,* 1726-1734.

28. Gong, M.; Li, F.; Yao, Z.; Zhang, S.; Dong, J.; Chen, Y.; Tang, Y., *Nanoscale* **2015,** *7,* 4894-4899.

29. Atkinson, R. W.; St. John, S.; Dyck, O.; Unocic, K. A.; Unocic, R. R.; Burke, C. S.; Cisco, J. W.; Rice, C. A.; Zawodzinski, T. A.; Papandrew, A. B., *ACS Catal.* **2015,** *5,* 5154-5163.

30. Vidal-Iglesias, F. J.; López-Cudero, A.; Solla-Gullón, J.; Feliu, J. M., *Angew. Chem. Int. Ed.* **2013,** *52,* 964-967.

31. Perales-Rondón, J. V.; Ferre-Vilaplana, A.; Feliu, J. M.; Herrero, E., *J. Am. Chem. Soc.* **2014,** *136,* 13110-13113.

32. Qu, W.; Wang, Z.; Sui, X.; Gu, D., *Inter. J. Hydrogen Energy* **2014,** *39,* 5678-5688.

33. Kundu, M. K.; Sadhukhan, M.; Barman, S., *J. Mater. Chem. B* **2015,** *3,* 1289-1300.

34. Bhowmik, T.; Kundu, M. K.; Barman, S., *RSC Adv.* **2015,** *5,* 38760-38773.

35. Bhowmik, T.; Kundu, M. K.; Barman, S., *ACS Catal.* **2016,** *6,* 1929-1941.

36. Negro, E.; Vezzù, K.; Bertasi, F.; Schiavuta, P.; Toniolo, L.; Polizzi, S.; Di Noto, V., *ChemElectroChem* **2014,** *1,* 1359-1369.

37. Kundu, M. K.; Bhowmik, T.; Barman, S., *J. Mater. Chem. A* **2015,** *3,* 23120-23135.

38. Barman, S.; Sadhukhan, M., *J. Mater. Chem.* **2012,** *22,* 21832-21837.

39. Bhowmik, T.; Kundu, M. K.; Barman, S., *Inter. J. Hydrogen Energy* **2016,** 10.1016/j.ijydene.2016.05.295.

40. Mazumder, V.; Sun, S., *J. Am. Chem. Soc.* **2009,** *131,* 4588-4589.

41. Du, C.; Liao, Y.; Hua, X.; Luo, W.; Chen, S.; Cheng, G., *Chem. Commun.* **2014,** *50,* 12843-12846.

42. Zhang, L. Y.; Guo, C. X.; Pang, H.; Hu, W.; Qiao, Y.; Li, C. M., *ChemElectroChem* **2014,** *1,* 72-75.

43. Huang, X.; Tang, S.; Mu, X.; Dai, Y.; Chen, G.; Zhou, Z.; Ruan, F.; Yang, Z.; Zheng, N., *Nat. Nano.* **2011,** *6,* 28-32.

44. Zhang, X.; Yin, H.; Wang, J.; Chang, L.; Gao, Y.; Liu, W.; Tang, Z., *Nanoscale* **2013,** *5,* 8392-8397.

45. St. John, S.; Atkinson, R. W.; Dyck, O.; Sun, C.-J.; Zawodzinski, T. A.; Papandrew, A. B., *Chem. Commun.* **2015,** *51,* 16633-16636.

46. Ho, S. F.; Mendoza-Garcia, A.; Guo, S.; He, K.; Su, D.; Liu, S.; Metin, O.; Sun, S., *Nanoscale* **2014,** *6,* 6970-6973.

47. Bin, D.; Yang, B.; Ren, F.; Zhang, K.; Yang, P.; Du, Y., *J. Mater. Chem. A* **2015,** *3,* 14001-14006.

Chapter 7

CoFe Layered Double Hydroxide Supported on Graphitic Carbon Nitrides as a Bi-functional Electrocatalyst

7.1 Abstract

Herein, we report the synthesis of cobalt iron layered double hydroxide ($Co_{1-\delta}Fe_{\delta}$ LDH) and g-carbon nitride composite ($Co_{1-\delta}Fe_{\delta}$ LDH/g-CN_x) for alkaline water electrolysis. The thin $Co_{1-\delta}Fe_{\delta}$ LDH nano-sheets are successfully impregnated on graphitic carbon nitride surface by one pot co-precipitation method at ambient temperature. The optimal composite, $Co_{0.4}Fe_{0.6}$ LDH/g-CN_x exhibited superior OER activity in 1 M KOH electrolyte with a small overpotential of 0.28 V for 10 mA cm^{-2}, low Tafel slope of 29 mV/dec, 100% faradic efficiency and high TOF of 0.25 s^{-1} which is superior to commercial (comm) IrO_2. Furthermore, the $Co_{0.4}Fe_{0.6}$ LDH/g-CN_x composite also exhibited remarkable HER activity in alkaline media and its HER activity is slightly lower than that of comm. Pt/C at low overpotential but it out-performs Pt/C at high overpotential. The catalyst demonstrated its long term durability and higher stability for HER and OER under alkaline environment. This $Co_{0.4}Fe_{0.6}$ LDH/g-CN_x catalyst can serve as both cathode and anode for overall water-splitting and required the small potential of 1.61 V to achieve a current density of 10 mA cm^{-2}. The superior electrocatalytic activities of the $Co_{0.4}Fe_{0.6}$ LDH/g-CN_x composite are due to the high electrochemical surface area (ECSA), easy access of abundant active sites and easy mass transport owing to 2D sheet morphology of the composite.

7.2 Introduction

It is very important to develop non-precious metal based highly active and durable electro-catalyst for water splitting reactions[1-3]. In recent years, tremendous efforts have been devoted for development of low cost electro catalyst for HER [4-7] and OER [8-12]. Several studies confirmed that first row transition metal dichalogenide[13-14], phosphide[6, 15], nitride[16] and carbide[17] catalysts exhibited superior HER activity whereas transition metal oxide[18-19], hydroxides[12, 20-21] and oxy(hydroxide)[11] based catalysts are active for OER. Generally, most of the good HER catalysts are active in acidic environment[22-23] whereas most of the nonprecious OER catalysts are active under alkaline environment[24-25]. The designing of a bi-functional catalyst [26-30] where the single catalyst is used as a cathode (HER) and anode (OER) under similar electrolyte, is highly desirable because this simple system reduces the cost of the water electrolyser.

The transition metal based layered double hydroxides[31-32] (LDHs) with the general formula of $[M^{2+}_{1-x}\, M^{3+}_{x}\, (OH)_2]^{x+}[A^{n-}_{(x/n)}.\, mH_2O]^{x}$ is considered as promising materials for alkaline water splitting reaction[33-37] because of its layered, open structure and densely distributed active sites. However, the poor electrical conductivity, low specific surface area and inherent corrosion susceptibility of transition metals LDH in the alkaline environment are the main obstacles for their electrochemical applications. For an electrochemical application, the LDH powder catalysts are generally immobilized directly on flat electrode (glassy carbon electrode) by using a polymer binder (e.g., poly tetra fluoro ethylene and Nafion) or conductive agent. But during immobilization of LDH with polymers, a large number of active sites are buried inside polymer and develop a contact resistance (R_{ct}) between the catalyst and current collector to inhibit the electron transfer between catalysts and current collector. In order to resolve these problems, most commonly used strategies are the combination of LDH and conducting supports such as nickel foam,[38] different conducting carbon matrix[39] with their improved charge transfer mobility and high surface area for electrochemical applications. Among different nano carbons grapheme,[40] carbon nanotube,[41] carbon quantum dots[42] etc. have been applied as catalyst supports. In recent years, two dimensional (2D) hetero assymble structure[38] of graphene have great interest of study because of its unique properties such as high electron mobility, large surface area and high mechanical strength. Recently, Yao and his co-workers[20] reported an improved water splitting activity of Ni-Fe hydroxide by making a heterostructure assembly with defective graphene. Furthermore, Ma et al. reported[43] hetero-assembled Ni–Fe hydroxide nano-sheets and graphene for efficient oxygen evolution. Han et al. reported[40] integration of CoFe-LDH with rGO to form sheet-on-sheet CoFe-LDH/r-GO composite with enhanced mass and charge transport behaviors for OER in alkaline media. Graphitic carbon nitride; another 2D material having similar structure like graphene, has been attracted attention as a support materials for various metal nanoparticles and transition metal oxide due to its potential applications in energy conversion,[44-45] organic transformation,[46] and photo-catalysis.[47] Although graphene-LDH based heteroassymble catalyst are known for superior OER activity, but, there are very few reports on LDH based heteroassymble catalyst [48-49] for overall water splitting reaction. Developing a non-precious metal LDH based composite material with improved conductivity and superior catalytic activities with high durability still is a daunting task.

Herein, we report one pot co-precipitation synthesis of cobalt iron layered double hydroxide ($Co_{1-\delta}Fe_{\delta}$ LDH) supported on g-carbon nitride at room temperature. The in situ nucleation and growth on carbon nitride surface leads to the formation of two dimensional composite of $Co_{1-\delta}Fe_{\delta}$ LDH and g-CN_x ($Co_{1-\delta}Fe_{\delta}$ LDH/g-CN_x), where thin

$Co_{1-\delta}Fe_{\delta}$ LDH sheets are dispersed on g-CN_x sheets without aggregation. This composite showed superior activity towards HER and OER in alkaline media. The $Co_{0.4}Fe_{0.6}$ LDH/g-CN_x has superior OER activity and stability in alkaline media with over-potential (η) of 0.28 V at 10 $mAcm^{-2}$ and high TOF value of 0.25 s^{-1} at η = 0.35 V. The OER activity of $Co_{0.4}Fe_{0.6}$ LDH/g-CN_x electrocatalyst is much higher than that of comm. IrO_2 whereas its HER activity is close to that of Pt/C in alkaline media. The amount of gas evolved from HER and OER processes was quantified and gases were produced with 100% faradic efficiency for both HER and OER.

7.3 Experimental Section

Synthesis of Graphitic Carbon Nitride (g-CN_x):

Graphitic carbon nitride (g-CN_x) was synthesised from formamide by microwave heated method recently report by our groups.[50] In a typical a procedure, formamide (30 ml) as precursor, was placed in 100 ml three-neck round bottom flask (RB) fitted with temperature controlled probe and heated at 180 °C by irradiation of 300 watt microwave for 180 min. After the reaction completion, a brown color solution was obtained from colorless formamide and the resulting brownish solution was evaporated at 180 °C in a rotary evaporator to get a solid product. The black solid product was washed 3 to 4 times with de-ionised (DI) water to remove un-reacted formamide and dried in a vacuum to obtain desired solid g-CN_x.

Synthesis of $Co_{1-\delta}Fe_{\delta}$ LDH/g-CN_x Composite:

$Co_{1-\delta}Fe_{\delta}$ LDH/g-CN_x composites (δ= 0.1, 0.17, 0.28, 0.40, 0.50, 0.6, 0.72, 0.83, 0.9) were synthesized by one-pot co-precipitation methods. In a typical synthesis of $Co_{0.4}Fe_{0.6}$ LDH/g-CN_x composite, 15 mg g-carbon nitride was dispersed in 50 ml deionised water by bath sonication in a 250 ml three neck round bottom flask (RB). 100 ml an aqueous solution containing 0.14 mmol of $Co(NO_3)_2.6H_2O$, 0.22 mmol of

$Fe(NO_3)_3.9H_2O$ (total metal ion concentration 0.36 mmol) and 0.125 gm of NH_4F was slowly poured into aqueous dispersion of g-CN_x with continuous magnetic stirring for 1 hr at room temperature. After this, 30 ml of 0.015(M) ammonia solution (25%) was added drop wise into that 250 ml RB at a rate of 5 drops/sec and the reaction was continued for 48 hrs at room temperature. After completion of the reaction, the whole suspension was centrifuged at 1,000 rpm for 4 min and the centrifuged mass were washed with de-ionized water as well ethanol separately for five times and finally, solid products was dried over vacuum. The obtained solid product was named as $Co_{0.4}Fe_{0.6}$ LDH/g-CN_x.

Synthesis of Co Hydroxide or Fe hydroxide g-Carbon Nitride Composite:

$Co(OH)_2$/g-CN_x and FeO(OH)/g-CN_x composite was synthesized by similar procedure as mention above. 0.36 mmol of $Co(NO_3)_2.6H_2O$ and 0.36 mmol of $Fe(NO_3)_3.$ $9H_2O$ were used for the synthesis of $Co(OH)_2$/g-CN_x and FeO(OH)/g-CN_x respectively.

Synthesis of Pure $Co_{0.4}Fe_{0.6}$ LDH:

Pure $Co_{0.4}Fe_{0.6}$ LDH was synthesized without g-CN_x by the similar procedure as mentioned above.

Electrode Preparation:

$Co_{0.4}Fe_{0.6}$ LDH/g-CN_x Coated on Glassy Carbon Electrodes:

As synthesized 2 mg $Co_{0.4}Fe_{0.6}$ LDH/g-CN_x was dispersed into 1ml of mixed solvent of DI-Ionized water/Isopropanol (4:1 V/V) by sonication for 20 min to form a homogeneous suspension. 5 μl of homogeneous suspension of catalyst (metal contained 4.5 μg) was drop casting onto the 0.07 cm^{-2} of glassy electrode surface and dried at 40 ^{0}C. The catalyst loading on GC electrode was 0.14 mg cm^{-2}.

$Co(OH)_2$/g-CN_x and FeO(OH)/g-CN_x Coated on Glassy Carbon Electrodes:

2 mg of synthesized $Co(OH)_2$/g-CN_x or FeO(OH)/g-CN_x was dispersed into 1 ml mixed solvent of DI-Ionized water/Isopropanol (4:1 v/v). After that 5 μl of the homogeneous

suspension was drop casting onto GC surface as similar to above method. Maintain the catalyst loading was 0.14 mg cm^{-2}.

Physical Mixture of $Co_{0.4}Fe_{0.6}$ LDH and g-CN_x Coated on Glassy Carbon Electrodes:

6 mg $Co_{0.4}Fe_{0.6}$ LDH was homogeneously mixed with 4 mg g-C_3N_4 in solid state in a porcelain pot by hand grinding. After that 2 mg of this homogeneous mixture was dispersed and drop caste onto GC electrode as similar methods describes above. The catalyst loading on the GC electrode surface was 0.14 mg cm^{-2}.

7.4 Results and Discussion

The $Co_{1-\delta}Fe_{\delta}$ LDH/g-CN_x composite with different compositions (δ= 0.1, 0.17, 0.28, 0.40, 0.50, 0.6, 0.72, 0.83, 0.9) were synthesised by one pot co-precipitation method at room temperature from $Co(NO_3)_2$.$6H_2O$; $Fe(NO_3)_3$.$9H_2O$ and g-CN_x (details in Experimental section). **Figure 7.1.a** shows the powered X-ray diffraction (p-XRD) pattern of $Co_{0.4}Fe_{0.6}$ LDH/g-CN_x and g-CN_x. The p-XRD pattern of g-CN_x shows a peak at 2θ value 27.3° corresponding to the (002) plane of g-carbon nitride.[50] The p-XRD patterns of $Co_{0.4}Fe_{0.6}$ LDH/g-CN_x has diffraction peaks at 2θ values of 11.05°, 22.66°, 33.43°, 38.25°, 45.55°, 58.82° and 59° are assigned to (003), (006), (012), (015), (018), (110) and (113) planes of pure $Co_{0.4}Fe_{0.6}$ LDH respectively and peak at 27.3° due to graphitic (002) diffraction plane of g-CN_x.

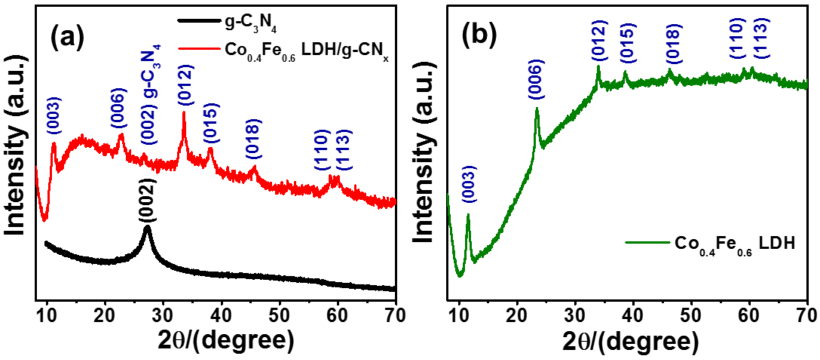

Figure 7.1. p-XRD pattern of (a) g-C_3N_4 and $Co_{0.4}Fe_{0.6}$ LDH/g-CN_x hybrids composite, (b) Pure $Co_{0.4}Fe_{0.6}$ LDH.

The similarity in diffraction pattern of $Co_{0.4}Fe_{0.6}$ LDH/g-CN_x composite and pure $Co_{0.4}Fe_{0.6}$ LDH (**Figure 7.1.b**) clearly demonstrated the consistency of LDH structure in the composite materials. The p-XRD pattern of $Co(OH)_2$/g-CN_x and FeO(OH)/g-CN_x composite was also shown for comparison in **Figure 7.2.(a,b)**.

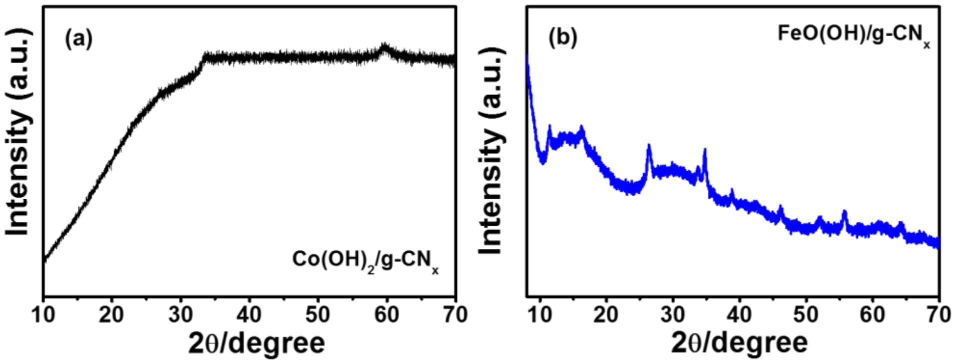

Figure 7.2. p-XRD pattern of (a) $Co(OH)_2$/g-CN_x and (b) FeO(OH)/g-CN_x.

Fourier transform infrared (FT-IR) spectra of pure $Co_{0.4}Fe_{0.6}$ LDH and $Co_{0.4}Fe_{0.6}$ LDH/g-CN_x composite (**Figure 7.3**) has two sharp peaks at 1632 and 1352 cm^{-1} indicating the presence of water and CO_3^{2-} ion at interlayer position. The similar FT-IR spectra of pure LDH and composite materials reveals the intactness of LDH structure over g-CN_x moiety.

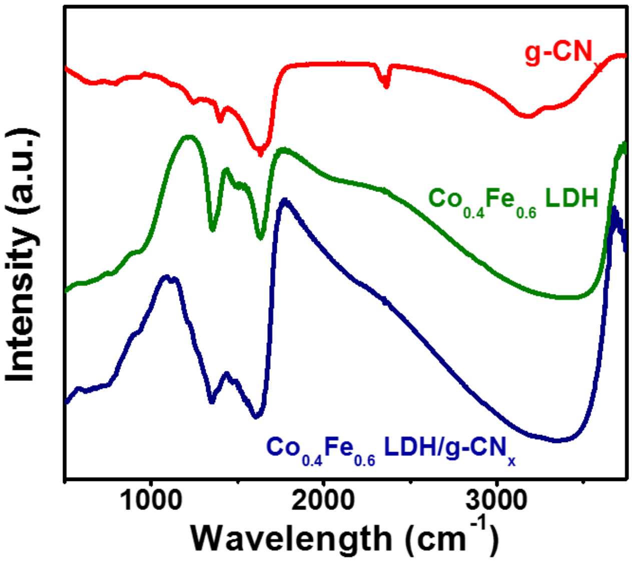

Figure 7.3. FT-IR spectra of g-CN_x, pure $Co_{0.4}Fe_{0.6}$ LDH and $Co_{0.4}Fe_{0.6}$ LDH/g-CN_x composite.

The morphology of the $Co_{0.4}Fe_{0.6}$ LDH/g-CN_x composite was carried out by transmission electron microscopy (TEM) and scanning electron microscopy (SEM). TEM images of the $Co_{0.4}Fe_{0.6}$ LDH/g-CN_x composite was shown in **Figure 7.4.(a-c)** and **Figure 7.5**.(a-c)

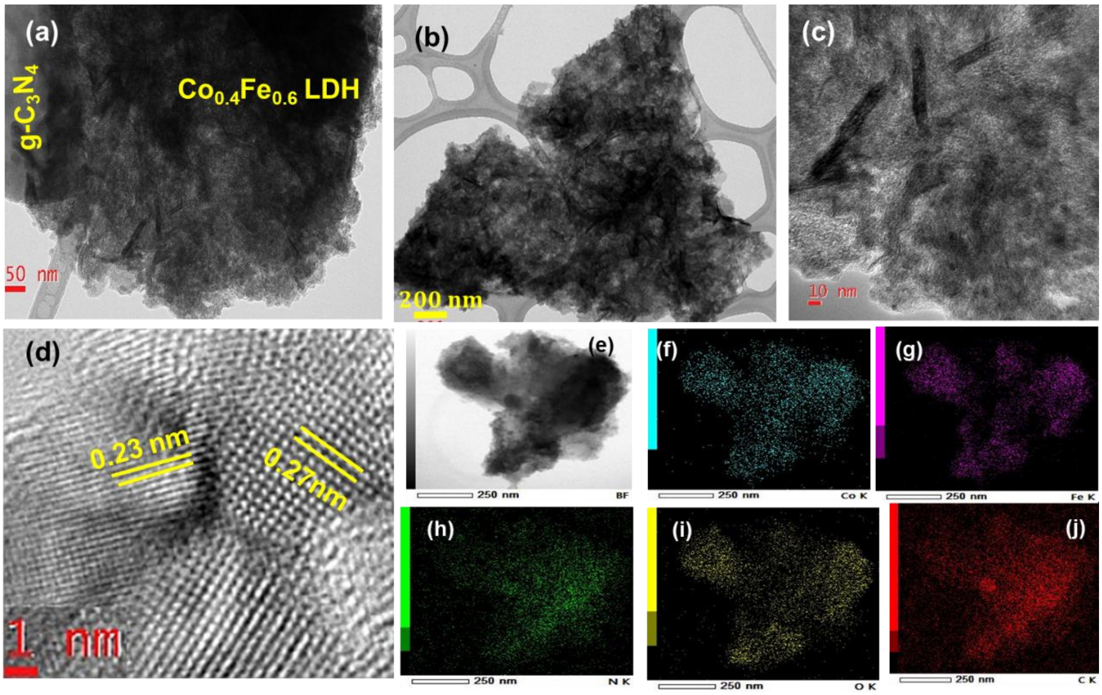

Figure 7.4. (a-c) TEM images of $Co_{0.4}Fe_{0.6}$ LDH/g-CN_x hybrids composite. (d) HRTEM image of $Co_{0.4}Fe_{0.6}$ LDH/g-CN_x. (e) STEM bright field image of $Co_{0.4}Fe_{0.6}$ LDH/g-CN_x hybrids composite and (f-j) corresponding EDX elemental mapping of Co, Fe, N, O, C respectively.

These TEM images clearly showed that thin two dimensional sheets of $Co_{0.4}Fe_{0.6}$ LDH are supported on g-CN_x sheets. As shown in **Figure 7.4.d**, the HRTEM image of the composite showed lattice fringes with the lattice distances of 0.27 and 0.23 nm corresponding to (012) and (015) plane of $Co_{0.4}Fe_{0.6}$ LDH respectively. The HRTEM image confirmed the formation of hetero assembled composite between graphitic carbon nitride and $Co_{0.4}Fe_{0.6}$ LDH. Furthermore, the STEM image and their corresponding EDS mapping of $Co_{0.4}Fe_{0.6}$ LDH/g-CN_x composite confirmed the uniform distribution of Co, Fe, N, O and C in the composite as shown in **Figure 7.4.(e-j)**.

The STEM mapping of Co and Fe with their overlay was shown in **Figure 7.6.(a-d)** which further confirmed that Co and Fe elements are uniformly distributed over the 2D sheets of graphitic carbon nitride.

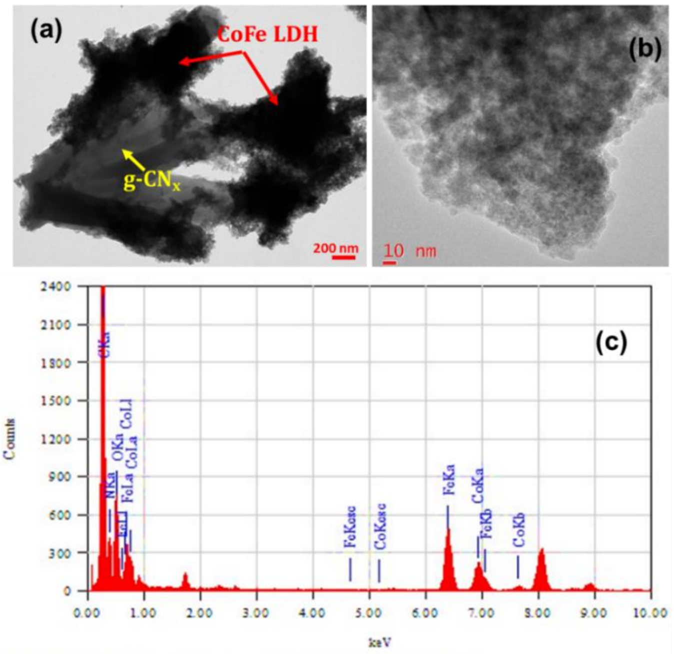

Figure 7.5. (a-b) TEM images and (c) EDX profile taken on Figure S7.3b, of $Co_{0.4}Fe_{0.6}$ LDH/g-CN$_x$.

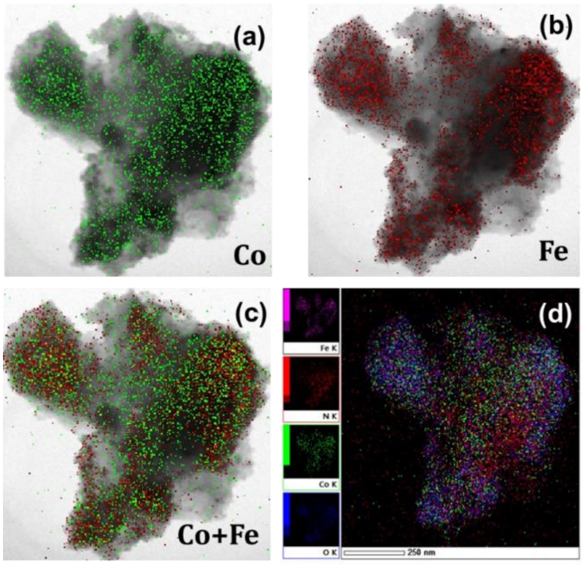

Figure 7.6. STEM mapping of (a) Co, (b) Fe, (c) Co+Fe and (d) Co+Fe+N+O of $Co_{0.4}Fe_{0.6}$ LDH/g-CN$_x$.

The FESEM sample was prepared by evaporation of the aqueous solution of the composite on silicon substrate. The FESEM images and corresponding EDS of $Co_{0.4}Fe_{0.6}$ LDH/g-CN_x composite were shown in **Figure 7.7.(a-c)** where folded sheets of composite are present with Fe:Co atomic ratio of 1.5.

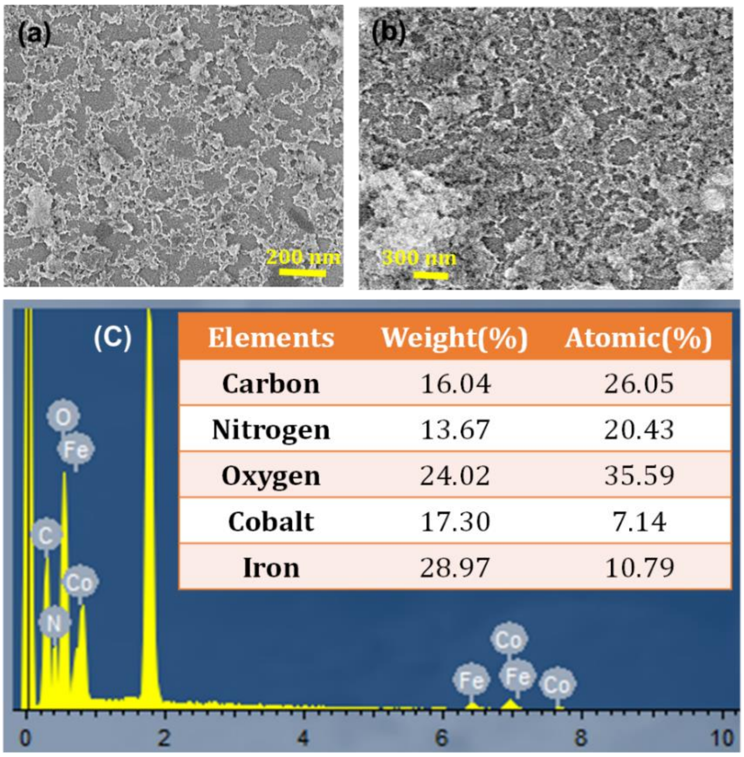

Elements	Weight(%)	Atomic(%)
Carbon	16.04	26.05
Nitrogen	13.67	20.43
Oxygen	24.02	35.59
Cobalt	17.30	7.14
Iron	28.97	10.79

Figure 7.7. (a,b) FESEM images of $Co_{0.4}Fe_{0.6}$ LDH/g-CN_x composite. (c) EDX profile and its corresponding atomic as well as weight percentage of $Co_{0.4}Fe_{0.6}$ LDH/g-CN_x.

The surface oxidation state of Co and Fe in the $Co_{0.4}Fe_{0.6}$ LDH/g-CN_x composite were studied by using X-ray photo electron spectroscopy (XPS). The wide range XPS spectra of $Co_{0.4}Fe_{0.6}$ LDH/g-CN_x composite (**Figure 7.8.a**) confirmed the presence of carbon (C), nitrogen (N), cobalt (Co), iron (Fe) and oxygen (O). The high resolution XPS spectra of Co and Fe appeared as doublet ($2p_{1/2}$ and $2p_{3/2}$) due to spin orbital coupling as shown in **Figure 7.8.b** and **7.8.c**. The $2p_{3/2}$ spectra of Co was deconvulated into four peaks – peaks at 779.6 and 781.9 eV are assigned for Co^{+3} and Co^{+2} species, remaining two peaks at ~785 and 788 eV are assigned to two shake-up satellite peak correspond to Co(II) and Co(III) species.[24, 37]

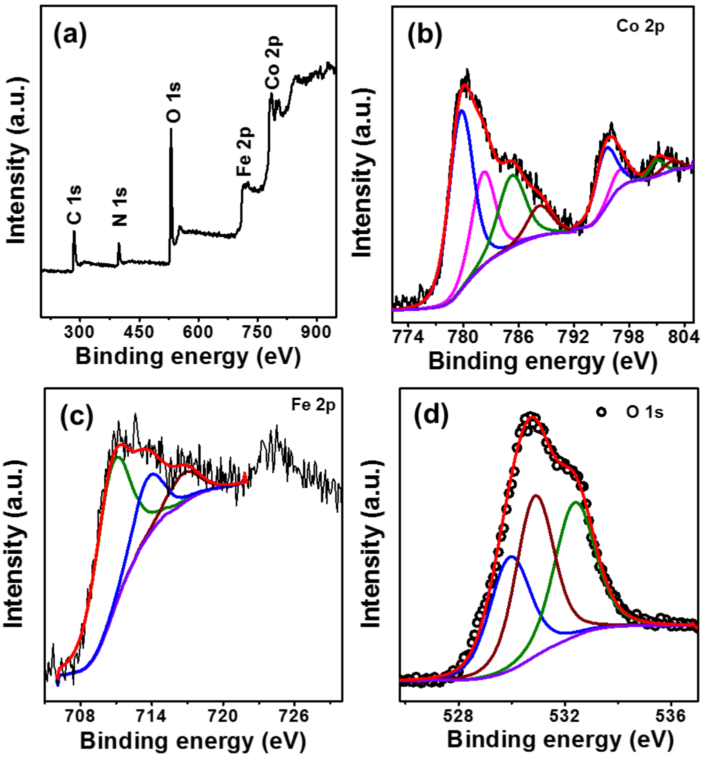

Figure 7.8. XPS spectra of $Co_{0.4}Fe_{0.6}$ LDH/g-CN_x composite (a) wide range XPS spectra and core level XPS spectra of (b) Co 2p, (c) Fe 2p, (d) O 1s.

The atomic ratio of Co^{+2}/Co^{+3} in the the $Co_{0.4}Fe_{0.6}$ LDH/g-CN_x for hybrid composite was found to be 1:2. Similar curve fitting of the high resolution XPS spectra of Fe $2p_{3/2}$ showed two distinct species,[51] peak at 711.1 eV identified as Fe(II) whereas peak at 714.6 eV corresponds to Fe(III). As shown in **Figure 7.8.d**, the O 1s XPS spectrum of $Co_{0.4}Fe_{0.6}$ LDH/g-CN_x also was deconvulated into three peaks. The peaks at 529.6, 530.9 and 533.6 eV are assigned to oxygen atom bound with metal atom, hydroxyl oxygen and oxygen of carbon-oxygen species respectively. The deconvulated C 1s and N 1s spectra were shown in **Figure 7.9** which are similar to the free g-CN_x reported in the literature.[61] The Nitrogen 1s spectra showed the presence of pyridinic and quaternary nitrogen atoms in the g-CN_x moiety which act as coordination sites for metal ions from their salts. As the co-precipitation reaction progress, nucleation followed by growth of $Co_{0.4}Fe_{0.6}$ LDH on the surface of CN_x sheets lead to formation of $Co_{0.4}Fe_{0.6}$ LDH decorated g-CN_x composite.

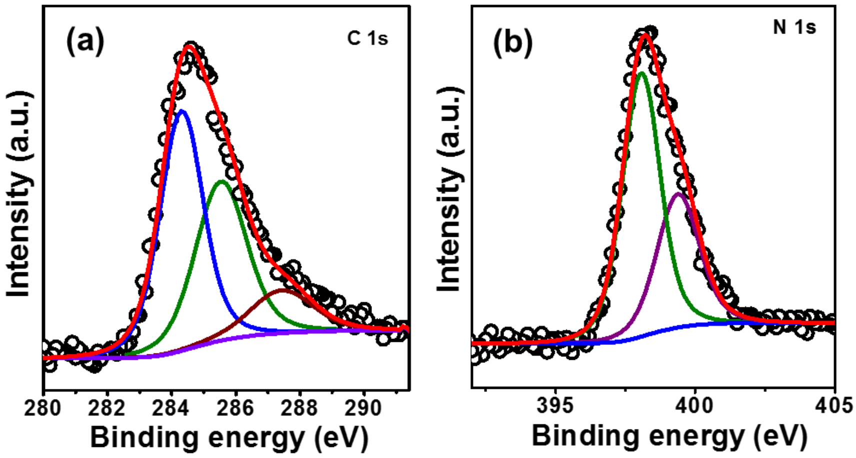

Figure 7.9. (a) C 1s and (b) N 1s XPS spectra of $Co_{0.4}Fe_{0.6}$ LDH/g-CN_x.

The atomic composition of Co and Fe in the various hybrid composite was confirmed through ICP-OES measurements. It is found that $Co_{0.4}Fe_{0.6}$ LDH/g-CN_x composite contained 27.1 wt% of Fe and 18.5 wt% of Co with Fe:Co was 1.46. In addition, amount of carbon and nitrogen present in the $Co_{0.4}Fe_{0.6}$ LDH/g-CN_x composite was measured by using CHN analysis as given in **Table 7.1**. The CHN analysis suggests the N:C in $Co_{0.4}Fe_{0.6}$ LDH/g-CN_x composite was found to be 0.86 whereas in the free g-CN_x N:C ratio is 1.09. The catalytic activity of $Co_{1-\delta}Fe_{\delta}$ LDH/g-CN_x composites with varying ratio of Co and Fe, were evaluated by performing electro-catalytic oxygen evolution reaction (OER) in alkaline electrolyte using a conventional three-electrode setup.

Table 7.1. CHN analysis of free g-C_3N_4 and $Co_{0.4}Fe_{0.6}$ LDH/g-CN_x composite.

Catalyst	**Carbon (wt.%)**	**Nitrogen (wt.%)**	**Oxygen (wt.%)**	**N:C**
g-C_3N_4	43.13	47.3	3.79	1.09
$Co_{0.4}Fe_{0.6}$LDH/g-CN_x	13.66	11.72	3.12	0.86

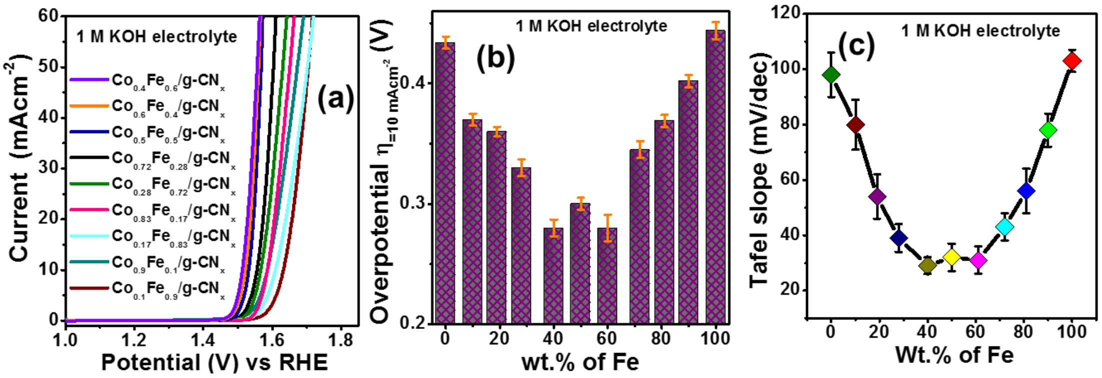

Figure 7.10. (a) OER LSV curves, (b) Overpotentials need for 10 mA cm^{-2}, (c) Tafel plots of $Co_{1-\delta}Fe_{\delta}$ LDH/g-CN_x composite with different composition.

The glassy carbon electrode (GC) was coated with $Co_{1-\delta}Fe_{\delta}$ LDH/g-CN_x catalyst at a constant catalyst loading of 0.14 mg cm^{-2} and was applied as working electrode. The linear sweep voltammetry (LSV) curves for OER were collected between 1.0 to 1.9 V (RHE) potential windows at 5 mV/s scan speed with 1600 rpm rotation in O_2 saturated 1 M KOH electrolyte. The LSV comparisons curves and over-potential, need to reach the current density of 10 mAcm^{-2} of different $Co_{1-\delta}Fe_{\delta}$ LDH/g-CN_x composites in 1 M KOH electrolyte was shown in **Figure 7.10.a** and **7.10.b** respectively. Tafel plots of $Co_{1-\delta}Fe_{\delta}$ LDH/g-CN_x composite with different composition are shown in **Figure 7.10.c**. The optimal catalytic activity was observed with $Co_{0.4}Fe_{0.6}$ LDH/g-CN_x composition. The OER LSV curves of $Co_{0.4}Fe_{0.6}$ LDH/g-CN_x composite, comm. IrO_2 and Pt/C are presented in **Figure 7.11.a**. The OER on-set potential of $Co_{0.4}Fe_{0.6}$ LDH/g-CN_x composite (**Figure 7.11.b**) is 1.46 V (RHE) which is lower than $Co(OH)_2$/g-CN_x (1.56 V) and FeO(OH)/g-CN_x (1.58 V). The $Co_{0.4}Fe_{0.6}$ LDH/g-CN_x catalyst has lower onset potential in comparison with state of art IrO_2 (1.49 V) suggesting very high OER activity.

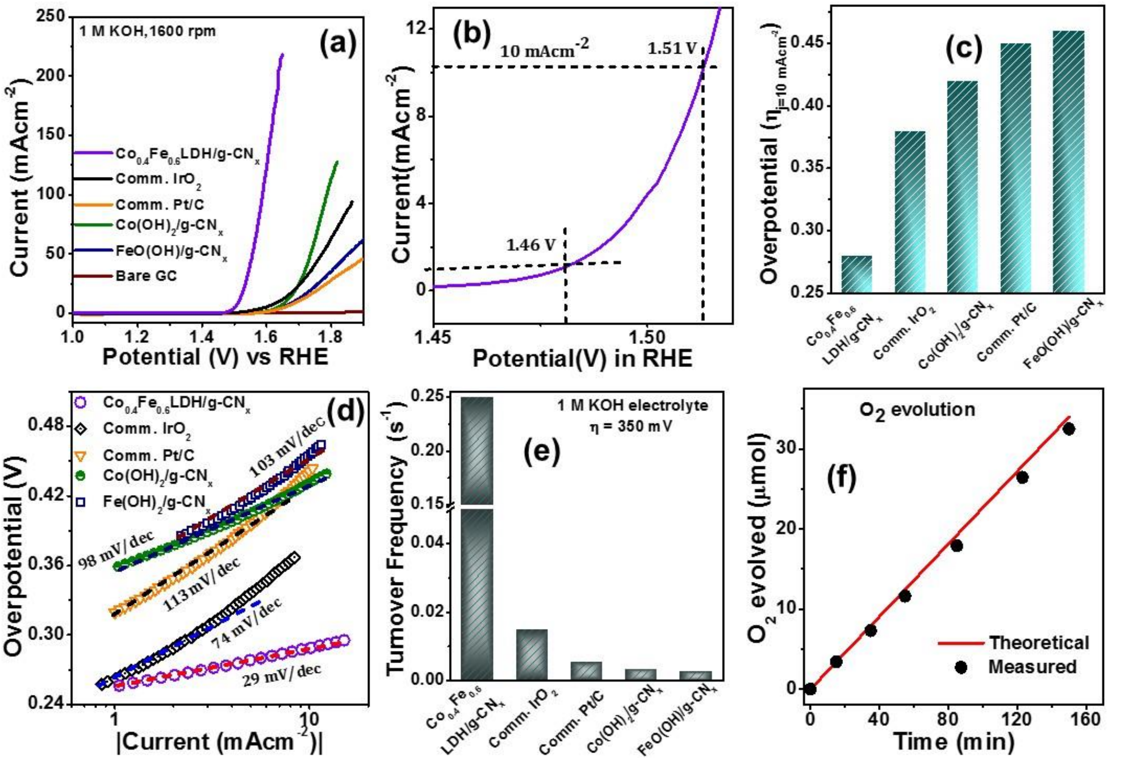

Figure 7.11. (a) LSV curves of $Co_{0.4}Fe_{0.6}$ LDH/g-CN$_x$, Comm. IrO_2, Comm. Pt/C, Co(OH$_2$/g-CN$_x$, FeO(OH) /g-CN$_x$ and bear GC electrode in O_2 saturated 1 M KOH electrolyte (Scan rate: 5 mV/s, 1600 rpm). (b) LSV curve of $Co_{0.4}Fe_{0.6}$ LDH/g-CN$_x$ indicating onset potential and potential required for 10 mAcm^{-2}. (c) Comparison of overpotentials required for 10 mAcm^{-2} ($\eta_{j=10\ mAc\mu}{}^{-2}$). (d)Tafel plot of different catalysts in 1 M KOH electrolyte. (e) Comparison of TOF value at η=0.35 V overpotentials. (f) The theoretical and measured amount of evolved O_2 gas on $Co_{0.4}Fe_{0.6}$ LDH/g-CN$_x$ electrode at current density of ~7mAcm^{-2} in 1 M KOH.

The superior OER catalytic activity of $Co_{0.4}Fe_{0.6}$ LDH/g-CN$_x$ composite was further evaluated by comparing three parameters: (i) the overpotential required to reach current density of 10 mA cm^{-2}($\eta_{\varphi=10\ mA\ cm}{}^{-2}$), (ii) Tafel slope and (iii) turnover frequency (TOF) values at η=0.35 V overpotential. This $Co_{0.4}Fe_{0.6}$ LDH/g-CN$_x$ catalyst needs overpotential of 0.28 V to achieve 10 mA cm^{-2} a current density whereas comm. IrO_2 and Comm. Pt/C catalyst needed 0.37 and 0.45 V respectively (**Figure 7.11.c**). Tafel slope (log J vs V plot) is an intrinsic property of the catalyst that governs the rate limiting step among four step proton/electron couple OER reaction. The Tafel slope value (b) for a chemically reversible multistep proton/electron couple reaction with a single rate determining step was theoretically calculated by

$$b = \frac{\mathrm{RT}\ln 10}{(n-\alpha)\,F}$$

Where R, T and F define their usual meaning, n is the number of electron transfers of the corresponding step and α is the electron transfer coefficient (generally 0.5).

Table 7.2. OER activity parameters of different catalysts in 1 M KOH electrolyte.

Catalyst	**Onset potential (V) in RHE**	**Overpotential (V) at j = 10 mAcm^{-2} ($\eta_{j=10\ \mathrm{mAcm}^{-2}}$).**	**Tafel slope (mV/dec)**	**M.A. at η=0.35 V (mAmg^{-1})**	**TOF (s^{-1})**
$Co_{0.4}Fe_{0.6}$ LDH/g-CN_x	1.45±0.03	0.28±0.009	29±3	1353±4	0.25±0.01
Comm. IrO_2	1.49±0.02	0.37±0.004	74±4	45±2	0.013±0.05
$Co(OH)_2$/g-CN_x	1.56±0.06	0.42±0.007	98±4	21±4	0.0035±0.0009
FeO(OH)/g-CN_x	1.58±0.08	0.46±0.005	103±8	15±6	0.0022±0.001
Comm. Pt/C	1.53±0.05	0.45±0.003	113±2	11±2	0.0056±0.0009

Several reaction mechanisms for multistep OER reaction are available in literatures[51-52]. Recently, J.Rossmeisl and his co-worker[51] found an analogous OER behavior of different oxide based electrocatalyst and proposed general four step reaction mechanism for OER on transition metal oxide electrocatalyst based on DFT calculation. Four steps for OER are described as follows:

The first step is the water adsorption as hydroxyl group on the surface active site (S)-

$$S + {}^{-}OH = S\text{-}OH_{ads} + e^{-} \qquad b = 118\ \mathrm{mV/dec} \qquad (1)$$

The second step is deprotonation of adsorbed hydroxyl group via charge transfer

$$S\text{-}OH_{ads} + {}^{-}OH = S\text{-}O_{ads} + H_2O + e^{-} \qquad b = 39\ \mathrm{mV/dec} \qquad (2)$$

The third step is the formation of intermediated Oxy-hydroxide species

$$S\text{-}O_{ads} + {}^{-}OH = S\text{-}OOH + e^{-} \qquad b = 24\ \mathrm{mV/dec} \qquad (3)$$

Final step is the oxygen evolution from intermediated oxy-hydroxide species

$$S\text{-}OOH + {}^{-}OH = S + O_2 + H_2O + e^- \quad b = 17\ mV/dec \quad (4)$$

The $Co_{0.4}Fe_{0.6}$ LDH/g-CN_x composite has a lower Tafel slope value of 29 mV/dec as compared to comm IrO_2 (74 mV/dec) and comm. Pt/C (113 mV/dec) catalyst **(Figure 7.11.d**). The low Tafel value of $Co_{0.4}Fe_{0.6}$ LDH/g-CN_x catalyst suggests that the third step is the rate determine step for OER.

Table 7.3. Comparison of OER activity of $Co_{0.4}Fe_{0.6}$ LDH/g-CN_x composite with recently reported different OER catalyst in alkaline medium.

Catalyst	**Electrolyte**	**Overpotential at 10 mA cm^{-2} (V)**	**Tafel slope(mV /dec)**	**Current collector**	**Reference**
CoMn LDH	1 M KOH	0.324	43	Glassy carabon	*J. Am. Chem. Soc.* **2014,** 13, 16481[53].
NiCo LDH	1 M KOH	0.334	41	Glassy carbon	*Nat. Commun.* **2014,** 5, 4477[35]
Ni0.9Fe0.1/NC	1 M KOH	0.330	45	Glassy carabon	*ACS Catal.* **2016,** 6, 580[48]
Ultrathin $NiCo_2O_4$ nanosheets	1 M KOH	0.320	30	Glassy carbon	*Angew. Chem. Int.* Ed. **2015,** 54, 7399[54]
rGO@$CoNiO_x$	0.1 M KOH	0.320	45	Glassy carbon	*Adv.Funct.Mater.* **2017,** 27, 1606325[55].
CoFe-LDH/rGO	0.1 M KOH	0.325	N.A	Glassy carbon	*Adv.Mater.Interfaces* **2016,** 3, 1500782[40].
NiCo-LDH-NS	1M KOH	0.334	45	Ni foam	*J. Power Sources* **2015,** 278, 445[56]
NiFe LDH/oGSH	0.1M KOH	0.350	54	Glassy carbon	*J. Mater. Chem. A* **2015,** 3, 24540[57]
Ni-Fe LDH/CNT	1 M KOH	0.250	31	Glassy carbon	*J. Am. Chem. Soc.* **2013,** 135, 8452[34]
CoFe LDH-C	1 M KOH	0.415	47	Glassy carbon	*ACS Appl. Mater. Interfaces* **2016,** 8, 34474[37]
$NiCo_{2.7}(OH)_x$ amorp.nanocage	1 M KOH	0.350	65	Glassy carbon	*Adv. Energy Mater.* **2015,** 5, 1401880[58]
Co_5Mn-LDH/MWCNT	1 M KOH	0.300	73.6	Glassy carbon	*ACS Appl. Mater. Interfaces 2016,* 8, 14527[41]
$LiCo_{0.8}Fe_{0.2}O_2$ (LCF0.2)	0.1 M KOH	0.340	50	Glassy carbon	*Adv. Mater.* **2015,** 27, 7150[59]
NiCo LDH	1 M KOH	0.367	N.A	Carbon paper	*Nano Lett.* **2015,** 15, 1421[60]
$Co_{2.25}$ $Cr_{0.75}$ O_4	1 M NaOH	0.350	52	Glassy carbon	*ACS Catal.* **2017**, 7, 443−451[61]
$Co_{0.4}Fe_{0.6}$ LDH/g-CN_x	1 M KOH	0.280	29	Glassy carbon	**This work**

Furthermore, the catalyst has higher mass activity at $\eta_{0.35\ V}$ than state of art IrO_2 catalyst as shown in **Table 7.2**. The catalyst has mass activity of 1353 $mAmg^{-1}$ at η=0.35 V, which was ~ 30 times higher than the comm. IrO_2 catalyst (45 mA mg^{-1}). The fundamental origin and trends in the activity of the catalysts were quantified by assessing the intrinsic activity, turnover frequency (TOF). The $TOF_{Total,\ OER}$ value of different catalyst is shown in **Figure 7.11.e**. The $TOF_{Total,\ OER}$ value of $Co_{0.4}Fe_{0.6}$ LDH/g-CN_x catalyst was 0.25 s^{-1} which is found to be 18 times of the comm IrO_2 catalyst. Furthermore, TOF value of $Co_{0.4}Fe_{0.6}$ LDH/g-CN_x composite was much higher than that of only Co and Fe hydroxide/g-CN_x composite, implies the enhanced OER catalytic activity of the $Co_{0.4}Fe_{0.6}$ LDH/g-CN_x composite due to a synergistic interaction between Fe and Co atoms. The comparison of different parameters for electrocatalytic OER activity of $Co_{0.4}Fe_{0.6}$ LDH/g-CN_x catalyst with other catalyst comm. IrO_2, comm. Pt/C, $Co(OH)_2$/g-CN_x and FeO(OH)/g-CN_x are provided in **Table 7.2**.

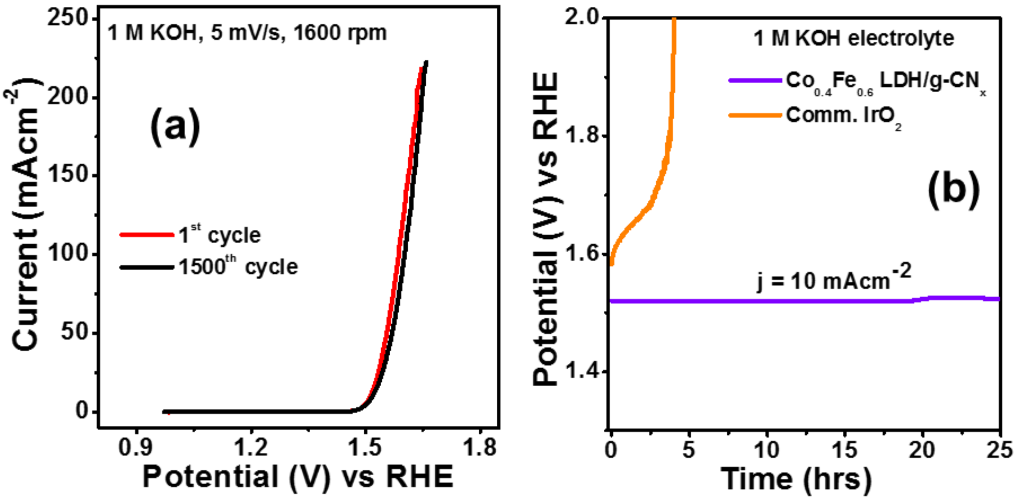

Figure 7.12. (a) Chronopotentiometry study of Comm. IrO_2 and $Co_{0.4}Fe_{0.6}$ LDH/g-CN_x composite at 10 $mAcm^{-2}$ current density (b) LSV cycling stability of $Co_{0.4}Fe_{0.6}$ LDH/g-CN_x composite.

The electrocatalytic OER activity of $Co_{0.4}Fe_{0.6}$LDH/g-CN_x composite is compared with different benchmark transition metal based catalysts **(Table 7.3.)**. The $Co_{0.4}Fe_{0.6}$

LDH/g-CN_x composite has high or comparable OER activity as compared to other transition metal based catalysts such as, CoFe-LDH/rGO,[52] NiCo LDH,[47] Fe_1Co_1-ONS.[30] Based on **Table 7.2** and **Table 7.3**, it may be concluded that the $Co_{0.4}Fe_{0.6}$ LDH/g-CN_x is one of the best Co based electrocatalysts for oxygen evolution in alkaline media. Furthermore, the amount of O_2 gas evolved during OER was quantified and compared with the amount expected during 100% faradic efficiency as shown in **Figure 7.11.f**. The theoretical amount of O_2 was calculated from accumulated charge during galvanostatic electroly-sis by assuming 100% faradic efficiency. **Figure 7.11.f** shows that the experimentally evolved O_2 amount was very close to 100% faradic efficiency during 150 min. The accelerated degradation study (ADS) of the composite was measured by performing LSV study before and after repeated accelerated CV cycling test of $Co_{0.4}Fe_{0.6}$ LDH/g-CN_x catalyst as shown in **Figure 7.12.a.** The composite showed very high cycling stability after 1500 cycles. In addition long term durability and higher stability are essential parameters for a superior electro-catalyst. The long term durability of the $Co_{0.4}Fe_{0.6}$ LDH/g-CN_x composite was investigated by chronopotentiometric response at a constant current density of 10 mA cm^{-2} (**Figure 7.12.b**). This shows that $Co_{0.4}Fe_{0.6}$ LDH/g-CN_x composite needs almost unchanged overpotential (~0.28 V) for oxygen evolution at 10 mA cm^{-2} for 24 hrs. The chronopotentiometry response for commercial IrO_2 at 10 mA cm^{-2} was performed under similar condition and compared in **Figure 7.12.b**. The over-potentials for commercial IrO_2 catalyst increases drastically from 0.35 V to 0.80 V within 4 hrs, suggesting the easy degradation of the comm. IrO_2 catalyst. Thus, the chronopotentiometric study confirmed the superior stability of the $Co_{0.4}Fe_{0.6}$ LDH /g-CN_x catalyst during the OER performance.

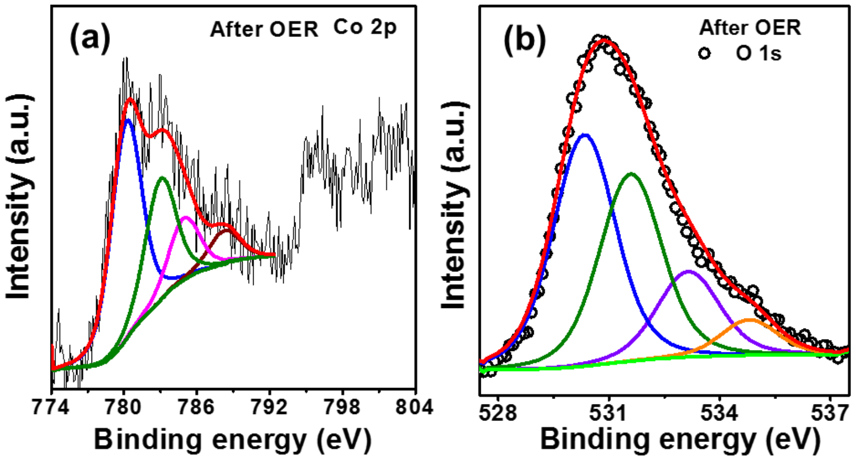

Figure 7.13. High resolution XPS spectra of (a) Co 2p and (b) O 1s of $Co_{0.4}Fe_{0.6}$ LDH/g-CN_x composite after OER stability.

We have performed XPS measurement of the catalyst after OER stability measurement to know the physical structure of the catalyst after long term durability study. After 20 hrs, chronopotentiometry measurement at a constant current of 10 mA cm^{-2}, the catalyst sample was collected from GC electrode surface for XPS measurements. The high resolution XPS spectrum of Co 2p and O 1s of the catalyst after OER stability was provided in **Figure 7.13.(a,b)**. No significant change is observed in XPS spectra and Co^{+2}/Co^{+3} ratio remains same as fresh catalyst, further confirming the higher stability and unaltered physical state of the catalyst under OER experimental condition.

To evaluate the HER activity of these catalysts, we have recorded LSV curves of $Co_{1-\delta}Fe_{\delta}$ LDH/g-CN_x modified GC electrode in H_2 saturated 1 M KOH solution at 5 mV/s scan rate with 1600 rpm rotation. Like OER performance, $Co_{0.4}Fe_{0.6}$ LDH/g-CN_x composite has higher HER activity among different $Co_{1-\delta}Fe_{\delta}$ LDH/g-CN_x composite materials as shown in **Figure 7.14.(a-c)**. The comparison of LSV curves of $Co_{1-\delta}Fe_{\delta}$ LDH/g-CN_x composites with different composition and comparison of overpotential to reach 10 mA cm^{-2} current density are shown in **Figure 7.14.(a,b)**.

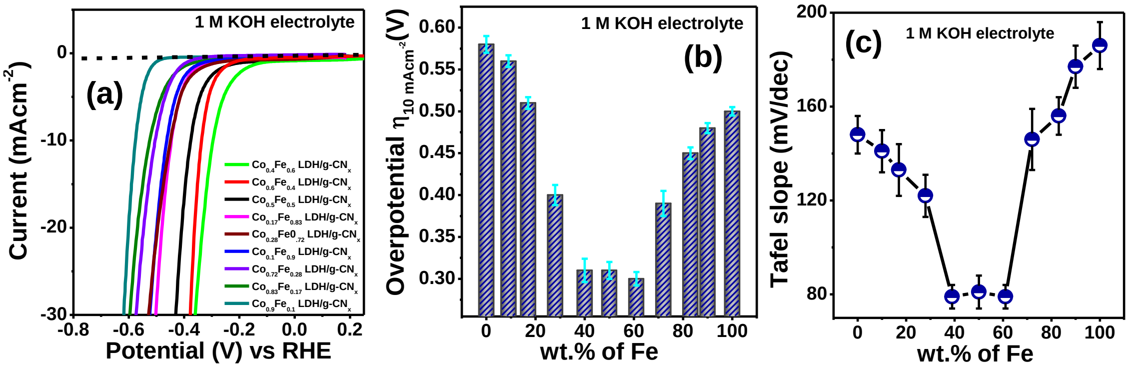

Figure 7.14. (a) HER LSV curves, (b) Overpotentials need for 10 mA cm^{-2}, (c) Tafel plots of $Co_{1-\delta}Fe_{\delta}$ LDH/g-CN_x composite with different composition.

Figure 7.15.a represents the HER LSV curves of $Co_{0.4}Fe_{0.6}$ LDH/g-CN_x, commercial Pt/C, and other catalysts in 1 M KOH electrolyte. The $Co_{0.4}Fe_{0.6}$ LDH/g-CN_x composite has much lower onset-potential than that of $Co(OH)_2$/g-CN_x and FeO(OH)/g-CN_x catalysts. The state of the art Pt/C catalyst exhibited small onset potential of 0 V in RHE whereas $Co_{0.4}Fe_{0.6}$ LDH/g-CN_x composite showed slightly higher onset potentials of ~0.12 V but $Co_{0.4}Fe_{0.6}$ LDH/g-CN_x catalyst outperforms the HER activity of Pt/C catalyst at an overpotential above 0.32 V.

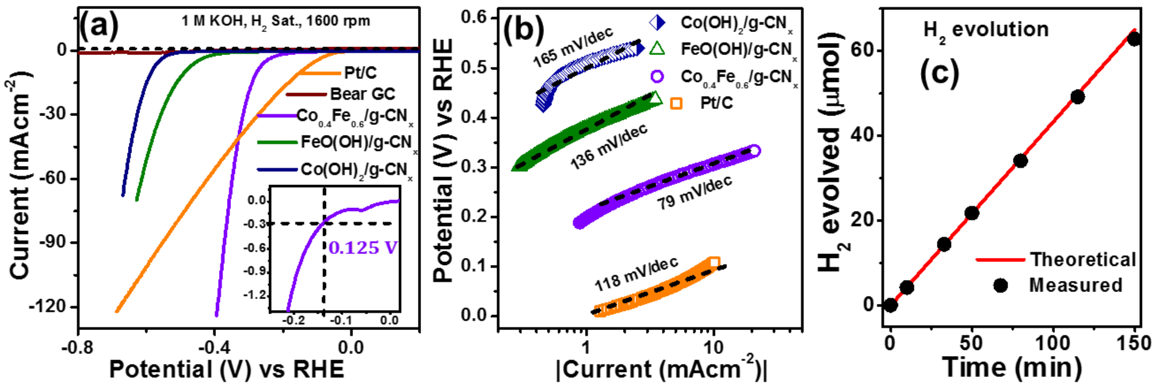

Figure 7.15. (a) LSV curves of $Co_{0.4}Fe_{0.6}$ LDH/g-CN_x, Comm. Pt/C, Co(OH$_2$/g-CN_x, FeO(OH) /g-CN_x and bear GC electrode in H_2 saturated 1 M KOH electrolyte (Scan rate: 5 mV/s, 1600 rpm). In-set: LSV curve $Co_{0.4}Fe_{0.6}$ LDH/g-CN_x indicating onset-potentials. (b) Tafel plot of different catalyst. (c) The theoretical and measured amount of evolved H_2 gas on $Co_{0.4}Fe_{0.6}$ LDH/g-CN_x electrode at current density of ~7mAcm^{-2} in 1 M KOH.

The rapid increase in cathodic current of $Co_{0.4}Fe_{0.6}$ LDH/g-CN_x composite indicates the fast HER reaction kinetics in alkaline medium. **Figure 7.15.b** exhibited the Tafel plot of $Co_{0.4}Fe_{0.6}$ LDH/g-CN_x, comm. Pt/C, $Co(OH)_2$/g-CN_x and $Fe(OH)_2$/g-CN_x catalysts. The $Co(OH)_2$/g-CN_x and $Fe(OH)_2$/g-CN_x has Tafel value of 165 and 136 mV/dec respectively whereas $Co_{0.4}Fe_{0.6}$LDH/g-CN_x catalyst exhibits low Tafel value of 79 mV/dec. It was reported in literature[17] that in alkaline medium comm. Pt/C catalyst has a Tafel slope value of 120 mV/dec, following Volmer-Tafel mechanism with Volmer is the rate determine step. Here comm. Pt/C catalyst exhibited a Tafel value of 118 mV/dec which is close to reported the value.

Table 7.4. Comparison of HER activity parameter of different catalysts in 1 M KOH solution.

Catalyst	**Overpotential (V)**		**Tafel slope (mV/dec)**	**Exchange current ($mAcm^{-2}$)**
	10 $mAcm^{-2}$	**60 $mAcm^{-2}$**		
$Co_{0.4}Fe_{0.6}$ LDH/g-CN_x	0.270±0.008	0.342±0.008	79 ± 3	0.157±0.003
Comm.Pt/C	0.135±0.004	0.40±0.004	118±2	N.A.
$Co(OH)_2$/g-CN_x	0.586±0.01	0.661±0.01	165±6	0.015±0.008
$Fe(OH)_2$/g-CN_x	0.489±0.005	0.609±0.005	136±8	0.051±0.005

The low HER Tafel slope (79 mV/dec) of $Co_{0.4}Fe_{0.6}$ LDH/g-CN_x catalyst suggests that it follows the Volmer- Heyrovsky mechanism in alkaline medium where Heyrovsky is the rate determine step. Furthermore, $Co_{0.4}Fe_{0.6}$ LDH/g-CN_x composite has the exchange current density of 0.157 $mAcm^{-2}$ which was much higher as compared to 0.015 mA cm^{-2} for pure $Co(OH)_2$/g-CN_x and 0.05 mA cm^{-2} for FeO(OH)/g-CN_x (**Table 7.4**). The HER activity of this catalyst is better or comparable with that of the other reported transition metal based catalyst as given in **Table 7.5**. The amount of evolved H_2 during galvanostatic electrolysis at 7 mA cm^{-2} current was quantified and compared with theoretical amount with 100% faradic efficiency.

Table 7.5. Comparison of HER activity of $Co_{0.4}Fe_{0.6}$ LDH/g-CN_x composite with recently reported different HER catalyst in alkaline medium.

Catalyst	Electrolyte	Overpotential at 10 mA cm^{-2}	Tafel slope	References
Ni1Mn1	0.1 M KOH	0.360	N.A	*Adv. Funct. Mater.* **2015**, *25*, 393[30]
Ni wire	1.0 M NaOH	0.350	N.A	*ACS Catal.* **2013**, 3,166[62]
FeP NAs/CC	1.0 M KOH	0.218	146	ACS Catal. 2014, 4, 4065[6].
Ni/C NFs	2.0 M KOH	0.170	105	*Electrochim. Acta,* **2015,** 159, 1[63].
Co-NRCNTs	1.0M KOH	0.375	NA	*Angew. Chem. Int. Ed.* **2014,** 53, 4372[7].
MoB	1 M KOH	0.225	59	*Angew. Chem. Int. Ed.* **2012**, 51, 12703[64].
CoO_x@CN	1 M KOH	0.232	115	*J. Am. Chem. Soc.* **2015**, *137*, 2688[65].
Amorp. MoS_x	1 M KOH	0.540	NA	*Chem. Sci.* **2011,** 2, 1262[66]
cobalt-sulfide	1 M KOH	0.480	NA	*J.Am.Chem.Soc.* **2013,**135, 17699[67].
Ni/MWCNT	1 M KOH	~ 350	102	*Journal of Power Sources* **2014**, *266*, 365[68]
$Co_{0.4}Fe_{0.6}$ LDH/g-CN_x	1 M KOH	0.270	79	**This work**

The $Co_{0.4}Fe_{0.6}$ LDH/g-CN_x catalyst has ~100% faradic efficiency during 150 min of electrolysis as shown in **Figure 7.15.c**. The long term durability and stability of $Co_{0.4}Fe_{0.6}$ LDH/g-CN_x composite was evaluated by Chronopotentiometry and repeated LSV cycling measurement.

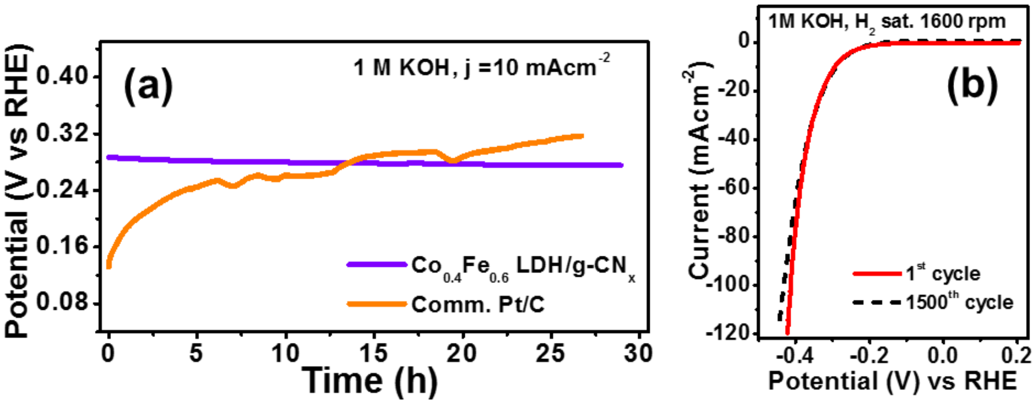

Figure 7.16. (a) Chronopotentiometry comparison of comm. Pt/C catalyst and $Co_{0.4}Fe_{0.6}$ LDH/g-CN_x composite at 10 $mAcm^{-2}$.(b) LSV cycling stability of $Co_{1-\delta}Fe_{\delta}$ LDH/g-CN_x composite for HER.

Figure 7.16.a shows outstanding HER stability of $Co_{0.4}Fe_{0.6}$ LDH/g-CN_x catalyst at constant current of 10 mA cm^{-2}.The $Co_{0.4}Fe_{0.6}$ LDH/g-CN_x catalyst need an overpotential of ~0.30 V for 10 mA cm^{-2} and remains almost unchanged for 24 hrs whereas for comm. Pt/C catalyst overpotential increases from 0.1 V to 0.3 V. In addition, the HER LSV curves of 1st and after 1500 CV cycles are shown in **Figure 7.16.b** which reveals almost identical LSV curves suggesting excellent cycling stability of this $Co_{0.4}Fe_{0.6}$ LDH/g-CN_x catalyst.

Based on above superior HER and OER activities of this Co0.4Fe0.6 LDH/g-CNx catalyst, we expected that this supported catalyst should act as a suitable bifunctionalised catalyst for over all water splitting in basic media. In order to show bi-functionality of this catalyst, we have applied a two electrode configuration where $Co_{0.4}Fe_{0.6}$ LDH/g-CN_x catalyst are used as both cathode and anode catalysts. The LSV curve of $Co_{0.4}Fe_{0.6}$ LDH/g-CN_x composite for overall water splitting clearly shows that this catalyst requires a potential of 1.61 V to drive current density of 10 mA cm^{-2} (**Figure 7.17.a**).

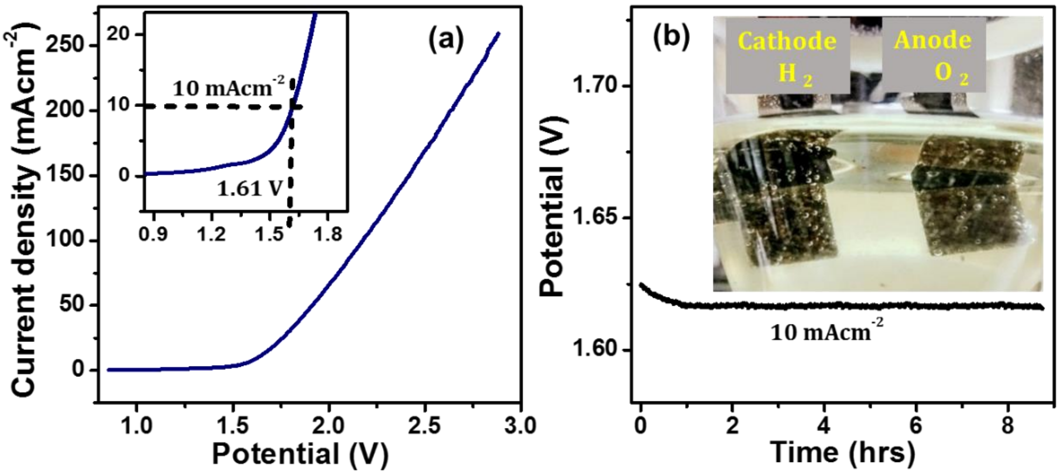

Figure 7.17. (a) LSV polarization curve of overall water splitting in 1M KOH electrolyte at 5 mV/s scan rate using $Co_{0.4}Fe_{0.6}$ LDH/g-CN_x as cathode as well anode. Inset: Indicating potential required for 10 $mAcm^{-2}$. (b) Chronopotentiometry response of $Co_{0.4}Fe_{0.6}$ LDH/g-CN_x at 10 $mAcm^{-2}$. Inset: Photography of cathode and anode electrode.

Furthermore, $Co_{0.4}Fe_{0.6}$ LDH/g-CN_x composite showed long term stability with only slight change of overpotential at 10 $mAcm^{-2}$ over 9 hrs time periods as shown in **Figure 7.17.b**. Thus, these results clearly suggest that $Co_{0.4}Fe_{0.6}$ LDH/g-CN_x catalyst could be a promising bi-functional electro-catalyst for alkaline water electrolysis. The superior electro-catalytic activity and excellent stability of the $Co_{0.4}Fe_{0.6}$ LDH/g-CN_x catalyst towards OER, and HER in alkaline electrolyte may be elucidated by several factors such as:

a) The in situ growth of LDH on a solid conducting support improves the electrochemical performances of LDH based electrode[31] because of enhanced conductivity and efficient exposure of active sites. The superior electrochemical activities of $Co_{0.4}Fe_{0.6}$ LDH supported on g-CN_x could be attributed due to the enhanced conductivity and decrease in the charge transfer resistance (R_{ct}) of this catalyst resulting from the synergistic coupling between $Co_{0.4}Fe_{0.6}$ LDH and g-CN_x support. To measure the R_{ct} value, we have studied the electrochemical impedance spectroscopy (EIS) of different catalysts as shown in **Figure 7.18.(a,b)**. **Figure 7.18.a** shows the EIS of $Co_{0.4}Fe_{0.6}$ LDH/g-CN_x composite with different potentials varying from 1.37 to 1.50 V. The radii of the semicircle gradually decreases as moving towards the onset potentials of OER and it has charge transfer resistance of 14.8 ohm at 1.50 V (detailed in **Table 7.6**). We have compared the EIS of $Co_{0.4}Fe_{0.6}$ LDH/g-CN_x composite with pure $Co_{0.4}Fe_{0.6}$ LDH and physical mixture ($Co_{0.4}Fe_{0.6}$ LDH + g-CN_x) at $\eta_{0.27\ V}$ as shown in **Figure 7.18.b**. The smaller semicircle as well as lower charge transfer resistance of this $Co_{0.4}Fe_{0.6}$ LDH/g-CN_x composite as compared to $Co_{0.4}Fe_{0.6}$ LDH and physical mixture in **Table 7.7**) may be due to the larger contact, strong synergistic interaction between $Co_{0.4}Fe_{0.6}$ LDH and g-CN_x support.

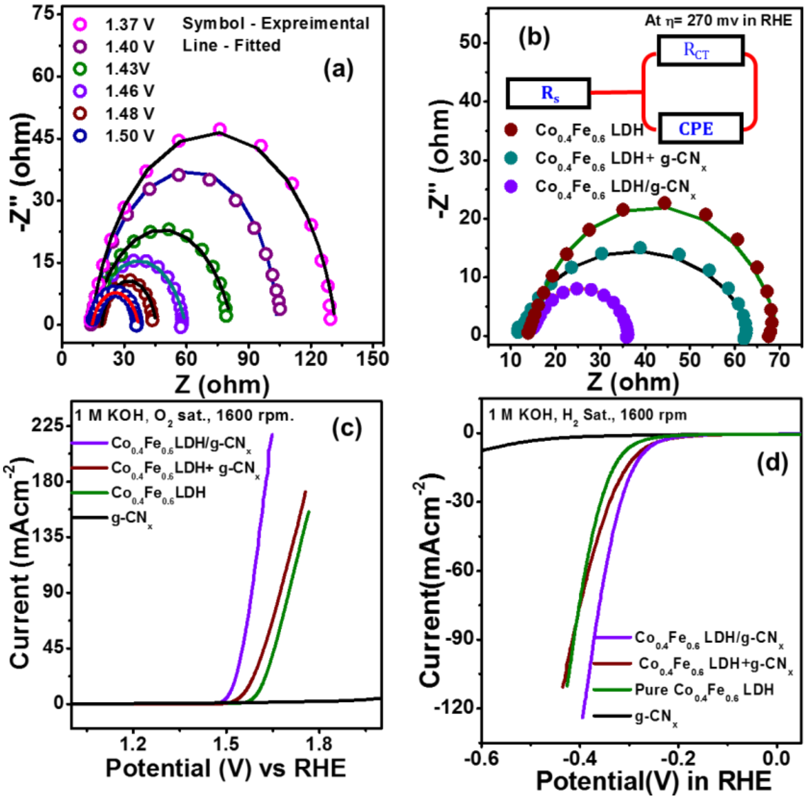

Figure 7.18. (a) Nyquist plot of $Co_{0.4}Fe_{0.6}$ LDH/g-CN_x composite in 1 M KOH at different overpotentials. (b) Comparison of Nyquist plot of $Co_{0.4}Fe_{0.6}$ LDH/g-CN_x, $Co_{0.4}Fe_{0.6}$ LDH and physical mixture of $Co_{0.4}Fe_{0.6}$ LDH and g-CN_x at 0.55 V in RHE under similar condition. Inset: Electronic circuit for fitting the Nyquist plot. (c) OER and (d) HER activity comparison of $Co_{0.4}Fe_{0.6}$ LDH/g-CNx composite, pure Co0.4Fe0.6 LDH, physical mixture (Co0.4Fe0.6 LDH+g-CNx) and g-CN_x.

All EIS consist of one semicircle and fitted with simplified randles cell equivalent circuit as given in in-set of **Figure 7.18.b**. Furthermore, the higher electrochemical OER and HER activities of $Co_{0.4}Fe_{0.6}$ LDH/g-CN_x catalyst as compare to pure $Co_{0.4}Fe_{0.6}$ LDH, physical mixture of $Co_{0.4}Fe_{0.6}$ LDH+g-CN_x and g-CN_x (**Figure 7.18.c** and **7.18.d** respectively) suggests a strong synergistic interaction between g-CN_x moiety and $Co_{0.4}Fe_{0.6}$ LDH. The in-situ growth of $Co_{0.4}Fe_{0.6}$ LDH on a two dimensional g-CN_x makes the rigid two dimensional sheets morphology of the composite which further allows the easy access of reactant to highly abundant active sites in entire composite and allows the products to come out easily from the active sites.

Table 7.6. EIS fitting parameter of $Co_{0.4}Fe_{0.6}$ LDH/g-CN_x composite at different over potentials.

Potentials / Parameter	η=270 mV	η=250 mV	η=230 mV	η=200 mV	η=170 mV	η=140 mV
R_s (ohm)	14.8	14.6	14.0	14.8	14.4	14.0
R_p (ohm)	16.1	25.5	42.1	65.9	91.4	118
CPE (μMho)	316	345	297	306	309	328

Table 7.7. EIS fitting parameter of different potential catalyst at η=270 mV potentials.

Parameter / Catalyst	R_s (ohm)	R_p (ohm)	CPE (μMho)
$Co_{0.4}Fe_{0.6}$ LDH/g-CN_x	14.8	16.1	316
$Co_{0.4}Fe_{0.6}$ LDH + g-CN_x mixture	18.1	47.2	657
$Co_{0.4}Fe_{0.6}$ LDH	18.4	55.5	702

b) The structure of $Co_{0.4}Fe_{0.6}$ LDH sheets on thin carbon nitrides could play a crucial role for the excellent electrochemical activities of $Co_{0.4}Fe_{0.6}$ LDH/g-CN_x catalyst. The XPS studies (Figure 3) revealed the presence of large amount of high oxidation state of cobalt (Co^{+3}) in $Co_{0.4}Fe_{0.6}$ LDH/g-CN_x composite. It is known[69] that highly oxidized transition metal redox couple such as $Ni^{+3/+4}$ and $Co^{+3/+4}$ are the active centres for OER. In addition, electronic configuration of Co^{2+} is $t_{2g}^6e_g^1$ and electronic configuration of Co^{3+} most likely is $t_{2g}^5e_g^1$. These electronic configurations are in good agreement with the intrinsic activity of transition metals showing maximum activity when an e_g orbital occupancy is close to unity.[70] The high oxidation state of these transition metals may enhance to form adsorbed -O- atom because of their high electrophilicity and it accelerates the reaction between -OH and –O- in Co and Fe atoms to form -OOH species and there by enhanced OER activity was observed. Since the oxidation state and chemical composition of $Co_{0.4}Fe_{0.6}$ LDH/g-CN_x composite remain unaltered on long term OER stability measurements, the outstanding stability of this composite is expected due to stable structure/oxidation state of the transition metals.

c) The large active surface area is one of the important parameter required for a good electrocatalyst. The electrocatalytic activity of an electro-catalyst enhances with increasing number of the active site. The active surface area of $Co_{0.4}Fe_{0.6}$ LDH/g-CN_x and $Co_{0.4}Fe_{0.6}$ LDH catalyst was evaluated by measuring the double layer capacitance (C_{dl}) and roughness factor (R_f) as these are directly proportional to active surface area (**Figure 7.19**). **Figure 7.19.(a-e)** shows the CV curves of the $Co_{0.4}Fe_{0.6}$ LDH/g-CN_x composite, pure $Co_{0.4}Fe_{0.6}$ LDH, $Co(OH)_2$/g-CN_x, FeO(OH)/g-CN_x and bare GC in non-Faradic regions respectively. The linear plot of current vs scan rate of corresponding CV curves was given in **Figure 7.19.f.** The C_{dl} and R_f values of $Co_{0.4}Fe_{0.6}$ LDH/g-CN_x were 7.3 mF cm^{-2} and 84 respectively which are much higher than 1.5 $mFcm^{-2}$ and 20.73 for pure $Co_{0.4}Fe_{0.6}$ LDH (details in **Table 7.8**).

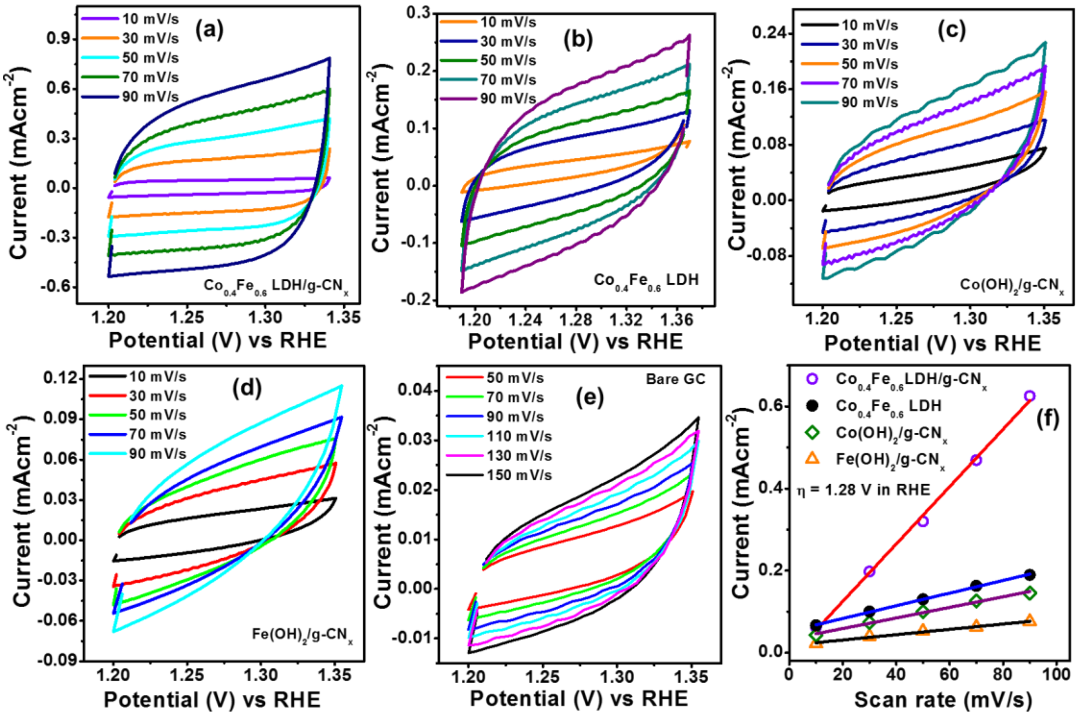

Figure 7.19. CV curves of (a) $Co_{0.4}Fe_{0.6}$ LDH/g-CN_x composite, (b) pure $Co_{0.4}Fe_{0.6}$ LDH, (c) $Co(OH)_2$/g-CN_x, (d) FeO(OH)/g-CN_x, and (e) Bare GC electrode in potential range from 1.20 V to 1.35 V in RHE with different scan rate of 10, 30, 50, 70, 90 mV/s. (f) Linear plot of double layer current vs scan rate in 1 M KOH electrolyte at potential of 1.28 V in RHE.

Table 7.8. Value of double layer capacitance and roughness factors of different catalyst.

Catalyst	**Double layered capacitance (C_{dl}) ($mFcm^{-2}$) at 1.28 V in RHE**	**Electrochemical surface area (ECSA) in cm^2**	**Roughness factor(R_f) (a.u.)**
$Co_{0.4}Fe_{0.6}$ LDH/g-CN_x	7.3	6.2	89
$Co_{0.4}Fe_{0.6}$ LDH	1.7	1.4	20
$Co(OH)_2$/g-CN_x	1.2	1.02	14
FeO(OH)/g-CN_x	0.65	0.55	0.79

These results demonstrated that catalytically active surface area increased due to high dispersion of $Co_{0.4}Fe_{0.6}$ LDH nano-sheets on g-CN_x surface.

d) The presence of nitrogen in carbon support enhances the activity of the composite. The hetero atoms such as N, P, S etc generally modify the electronic properties. The tertiary and pyridinic N species in g-CN_x generates an asymmetric charge separation with highly positive charge density on the nearby sp^2-hybridized carbon atoms due to their electronegativity difference. The positively polarized carbon atom favor the adsorption of reactant ($-OH^-$ for OER and H* for HER) that facilitates the charge transportation between reactant and catalysts surface.[45] Thus, the presence of N in the composite is contributing to enhancing its catalytic activity towards various electrochemical reactions. In addition, less amount of nitrogen in the support of composite in compared to free g-CN_x advantageous for electrochemical activity due to the improved conductivity of the catalyst.[71]

7.5 Conclusions

In summary, a method for preparation of thin $Co_{1-\delta}Fe_{\delta}$ LDH nano-sheets decorated g-carbon nitride composite was demonstrated. The superior electrocatalytic activity and stability of $Co_{1-\delta}Fe_{\delta}$ LDH/g-CN_x towards OER and HER under alkaline electrolyte has been demonstrated. The $Co_{0.4}Fe_{0.6}$ LDH/g-CN_x composite has 100% faradic efficiency for both OER and HER. The bi-functional catalytic activity of $Co_{0.4}Fe_{0.6}$ LDH/g-CN_x composite was demonstrated – it can serve as both cathode and anode; required 1.61 V to reach 10 mA cm^{-2} current density. The $Co_{0.4}Fe_{0.6}$ LDH/g-CN_x composite can be used as promising electro-catalyst for various renewable energy storage and conversion devices such as water-splitting devices, fuel cells, metal-air batteries, etc.

7.7 References

1. Li, X. M.; Hao, X. G.; Abudula, A.; Guan, G. Q., *J. Mater. Chem.* **2016,** *4,* 11973-12000.
2. Eftekhari, A., *Mater. Today Energy* **2017,** *5,* 37-57.
3. Gao, M.; Sheng, W.; Zhuang, Z.; Fang, Q.; Gu, S.; Jiang, J.; Yan, Y., *J. Am. Chem. Soc.* **2014,** *136,* 7077-7084.
4. Tong, X.; Wu, D.; Zhang, C.; Lian, K.; Xiong, D.; Xu, S.; Zhu, Y.; Qi, R.; Huang, R.; Wang, L.; Chu, P. K., *J. Mater. Chem. A* **2017,** *5,* 2629-2639.
5. Yan, X.; Tian, L.; He, M.; Chen, X., *Nano Lett.* **2015,** *15,* 6015-6021.
6. Liang, Y.; Liu, Q.; Asiri, A. M.; Sun, X.; Luo, Y., *ACS Catal.* **2014,** *4,* 4065-4069.
7. Zou, X.; Huang, X.; Goswami, A.; Silva, R.; Sathe, B. R.; Mikmeková, E.; Asefa, T., *Angew. Chem. Int. Ed.* **2014,** *53,* 4372-4376.
8. Blasco-Ahicart, M.; Soriano-López, J.; Carbó, J. J.; Poblet, J. M.; Galan-Mascaros, J. R., *Nature Chemistry* **2017,** *10,* 24.
9. Gong, M.; Zhou, W.; Tsai, M.-C.; Zhou, J.; Guan, M.; Lin, M.-C.; Zhang, B.; Hu, Y.; Wang, D.-Y.; Yang, J.; Pennycook, S. J.; Hwang, B.-J.; Dai, H., *Nature Communications* **2014,** *5,* 4695.
10. Lyons, M. E. G.; Brandon, M. P., *J. Electroanal. Chem.* **2010,** *641,* 119-130.
11. Burke, M. S.; Enman, L. J.; Batchellor, A. S.; Zou, S.; Boettcher, S. W., *Chem. Mater.* **2015,** *27,* 7549-7558.
12. Liu, S.; Luo, H.; Li, Y.; Liu, Q.; Luo, J.-L., *Nano Energy* **2017,** *40,* 115-121.
13. Wang, F.; Shifa, T. A.; Zhan, X.; Huang, Y.; Liu, K.; Cheng, Z.; Jiang, C.; He, J., *Nanoscale* **2015,** *7,* 19764-19788.
14. Kong, D.; Cha, J. J.; Wang, H.; Lee, H. R.; Cui, Y., *Energy Environ. Sci.* **2013,** *6,* 3553-3558.
15. Tian, L.; Yan, X.; Chen, X.; Liu, L.; Chen, X., *J. Mater. Chem. A* **2016,** *4,* 13011-13016.

16. Zhang, Y.; Ouyang, B.; Xu, J.; Jia, G.; Chen, S.; Rawat, R. S.; Fan, H. J., *Angew. Chem. Int. Ed.* **2016,** *55,* 8670-8674.

17. Wu, H. B.; Xia, B. Y.; Yu, L.; Yu, X.-Y.; Lou, X. W., *Nat. commun.* **2015,** *6,* 6512-6519.

18. Zhuang, L.; Ge, L.; Yang, Y.; Li, M.; Jia, Y.; Yao, X.; Zhu, Z., *Adv. Mater.* **2017,** *29,* 1606793.

19. Hua, B.; Li, M.; Sun, Y.-F.; Zhang, Y.-Q.; Yan, N.; Chen, J.; Thundat, T.; Li, J.; Luo, J.-L., *Nano Energy* **2017,** *32,* 247-254.

20. Jia, Y.; Zhang, L.; Gao, G.; Chen, H.; Wang, B.; Zhou, J.; Soo, M. T.; Hong, M.; Yan, X.; Qian, G.; Zou, J.; Du, A.; Yao, X., *Adv. Mater.* **2017,** *29,* 1700017.

21. Tahir, M.; Mahmood, N.; Pan, L.; Huang, Z. F.; Lv, Z.; Zhang, J. W.; Butt, F. K.; Shen, G. Q.; Zhang, X. W.; Dou, S. X.; Zou, J. J., *J. Mater. Chem. A* **2016,** *4,* 12940-12946.

22. Liu, Q.; Tian, J.; Cui, W.; Jiang, P.; Cheng, N.; Asiri, A. M.; Sun, X., *Angew. Chem. Int. Ed.* **2014,** *126,* 6828-6832.

23. Fei, H.; Dong, J.; Arellano-Jimenez, M. J.; Ye, G.; Dong Kim, N.; Samuel, E. L.; Peng, Z.; Zhu, Z.; Qin, F.; Bao, J.; Yacaman, M. J.; Ajayan, P. M.; Chen, D.; Tour, J. M., *Nat. commun.* **2015,** *6,* 8668-8675.

24. Zhang, C.; Zhao, J. W.; Zhou, L.; Li, Z. H.; Shao, M. F.; Wei, M., *J. Mater. Chem. A* **2016,** *4,* 11516-11523.

25. Suen, N.-T.; Hung, S.-F.; Quan, Q.; Zhang, N.; Xu, Y.-J.; Chen, H. M., *Chem. Soc. Rev.* **2017,** *46,* 337-365.

26. Tahir, M.; Mahmood, N.; Pan, L.; Huang, Z.-F.; Lv, Z.; Zhang, J.; Butt, F. K.; Shen, G.; Zhang, X.; Dou, S. X.; Zou, J.-J., *Journal of Materials Chemistry A* **2016,** *4,* 12940-12946.

27. Ma, T. Y.; Dai, S.; Qiao, S. Z., *Materials Today* **2016,** *19,* 265-273.

28. Zhu, Y.; Zhou, W.; Zhong, Y.; Bu, Y.; Chen, X.; Zhong, Q.; Liu, M.; Shao, Z., *Adv. Energy Mater.* **2017,** *7,* 1602122.

29. Ouyang, C.; Wang, X.; Wang, C.; Zhang, X.; Wu, J.; Ma, Z.; Dou, S.; Wang, S., *Electrochimica Acta* **2015,** *174,* 297-301.

30. Ledendecker, M.; Clavel, G.; Antonietti, M.; Shalom, M., *Adv. Funct. Mater.* **2015,** *25,* 393-399.

31. Shao, M.; Zhang, R.; Li, Z.; Wei, M.; Evans, D. G.; Duan, X., *Chem. Commun.* **2015,** *51,* 15880-15893.

32. Long, X.; Wang, Z.; Xiao, S.; An, Y.; Yang, S., *Mater. Today* **2016,** *19,* 213-226.

33. Ma, Y.; Dai, X.; Liu, M.; Yong, J.; Qiao, H.; Jin, A.; Li, Z.; Huang, X.; Wang, H.; Zhang, X., *ACS Appl. Mater. Interfaces* **2016,** *8,* 34396-34404.

34. Gong, M.; Li, Y.; Wang, H.; Liang, Y.; Wu, J. Z.; Zhou, J.; Wang, J.; Regier, T.; Wei, F.; Dai, H., *J. Am. Chem. Soc.* **2013,** *135,* 8452-8455.

35. Song, F.; Hu, X., *Nat. commun.* **2014,** *5,* 4477.

36. Liu, Y.; Bai, Y.; Han, Y.; Yu, Z.; Zhang, S.; Wang, G.; Wei, J.; Wu, Q.; Sun, K., *ACS Appl. Mater. Interfaces* **2017,** 10.1021/acsami.7b12474.

37. Liu, P. F.; Yang, S.; Zhang, B.; Yang, H. G., *ACS Appl. Mater. Interfaces* **2016,** *8,* 34474-34481.

38. Tang, C.; Wang, H.-S.; Wang, H.-F.; Zhang, Q.; Tian, G.-L.; Nie, J.-Q.; Wei, F., *Adv. Mater.* **2015,** *27,* 4516-4522.

39. Li, M.; Liu, T. T.; Bo, X. J.; Zhou, M.; Guo, L. P., *J. Mater. Chem. A* **2017,** *5,* 5413-5425.

40. Han, X. T.; Yu, C.; Yang, J.; Zhao, C. T.; Huang, H. W.; Liu, Z. B.; Ajayan, P. M.; Qiu, J. S., *Adv. Mater. Interfaces* **2016,** *3,* 10.1002/Admi.201500782.

41. Jia, G.; Hu, Y.; Qian, Q.; Yao, Y.; Zhang, S.; Li, Z.; Zou, Z., *ACS Appl. Mater. Interfaces* **2016,** *8,* 14527-14534.

42. Tang, D.; Liu, J.; Wu, X.; Liu, R.; Han, X.; Han, Y.; Huang, H.; Liu, Y.; Kang, Z., *ACS Appl. Mater. Interfaces* **2014,** *6,* 7918-7925.

43. Ma, W.; Ma, R.; Wang, C.; Liang, J.; Liu, X.; Zhou, K.; Sasaki, T., *ACS Nano* **2015,** *9,* 1977-1984.

44. Bhowmik, T.; Kundu, M. K.; Barman, S., *ACS Appl. Mater. Interfaces* **2016,** *8,* 28678-28688.

45. Bhowmik, T.; Kundu, M. K.; Barman, S., *ACS Catal.* **2016,** *6,* 1929-1941.

46. Wang, Y.; Wang, X.; Antonietti, M., *Angew. Chem. Int. Ed.* **2012,** *51,* 68-89.

47. Bhowmik, T.; Kundu, M. K.; Barman, S., *RSC Adv.* **2015,** *5,* 38760-38773.

48. Zhang, X.; Xu, H. M.; Li, X. X.; Li, Y. Y.; Yang, T. B.; Liang, Y. Y., *ACS Catal.* **2016,** *6,* 580-588.

49. Hou, Y.; Lohe, M. R.; Zhang, J.; Liu, S.; Zhuang, X.; Feng, X., *Energy Environ. Sci.* **2016,** *9,* 478-483.

50. Barman, S.; Sadhukhan, M., *J. Mater. Chem.* **2012,** *22,* 21832-21837.

51. Man, I. C.; Su, H.-Y.; Calle-Vallejo, F.; Hansen, H. A.; Martínez, J. I.; Inoglu, N. G.; Kitchin, J.; Jaramillo, T. F.; Nørskov, J. K.; Rossmeisl, J., *ChemCatChem* **2011,** *3,* 1159-1165.

52. Giordano, L.; Han, B.; Risch, M.; Hong, W. T.; Rao, R. R.; Stoerzinger, K. A.; Shao-Horn, Y., *Catal. Today* **2016,** *262,* 2-10.

53. Song, F.; Hu, X., *J. Am. Chem. Soc.* **2014,** *136,* 16481-16484.

54. Bao, J.; Zhang, X.; Fan, B.; Zhang, J.; Zhou, M.; Yang, W.; Hu, X.; Wang, H.; Pan, B.; Xie, Y., *Angew. Chem. Int. Ed.*

2015, *54,* 7399-7404.

55. Li, P.; Zeng, H. C., *Adv. Funct. Mater.* **2017,** *27,* 1606325-n/a.

56. Jiang, J.; Zhang, A.; Li, L.; Ai, L., *J. Power Sources* **2015,** *278,* 445-451.

57. Zhu, X.; Tang, C.; Wang, H.-F.; Zhang, Q.; Yang, C.; Wei, F., *J. Mater. Chem. A*

2015, *3,* 24540-24546.

58. Nai, J.; Yin, H.; You, T.; Zheng, L.; Zhang, J.; Wang, P.; Jin, Z.; Tian, Y.; Liu, J.; Tang, Z.; Guo, L., *Adv. Energy Mater.* **2015,** *5,* 1401880-n/a.

59. Zhu, Y.; Zhou, W.; Chen, Y.; Yu, J.; Liu, M.; Shao, Z., *Adv. Mater.* **2015,** *27,* 7150-7155.

60. Liang, H.; Meng, F.; Cabán-Acevedo, M.; Li, L.; Forticaux, A.; Xiu, L.; Wang, Z.; Jin, S., *Nano Letters* **2015,** *15,* 1421-1427.

61. Lin, C.-C.; McCrory, C. C. L., *ACS Catal.*

2017, *7,* 443-451.

62. McKone, J. R.; Sadtler, B. F.; Werlang, C. A.; Lewis, N. S.; Gray, H. B., *ACS Catalysis* **2013,** *3,* 166-169.

63. Ding, Q.; Liu, M.; Miao, Y.-E.; Huang, Y.; Liu, T., *Electrochimica Acta* **2015,** *159,* 1-7.

64. Vrubel, H.; Hu, X., *Angew. Chem. Int. Ed.* **2012,** *51,* 12703-12706.

65. Jin, H.; Wang, J.; Su, D.; Wei, Z.; Pang, Z.; Wang, Y., *J. Am. Chem. Soc.* **2015,** *137,* 2688-2694.

66. Merki, D.; Fierro, S.; Vrubel, H.; Hu, X., *Chem. Sci.* **2011,** *2,* 1262-1267.

67. Sun, Y.; Liu, C.; Grauer, D. C.; Yano, J.; Long, J. R.; Yang, P.; Chang, C. J., *Journal of the American Chemical Society* **2013,** *135,* 17699-17702.

68. McArthur, M. A.; Jorge, L.; Coulombe, S.; Omanovic, S., *J. Power Sources* **2014,** *266,* 365-373.

69. Maiyalagan, T.; Jarvis, K. A.; Therese, S.; Ferreira, P. J.; Manthiram, A., *Nat. commun.* **2014,** *5,* 3949.

70. Suntivich, J.; May, K. J.; Gasteiger, H. A.; Goodenough, J. B.; Shao-Horn, Y., *Science* **2011,** *334,* 1383-1385.

71. Negro, E.; Vezzù, K.; Bertasi, F.; Schiavuta, P.; Toniolo, L.; Polizzi, S.; Di Noto, V., *ChemElectroChem* **2014,** *1,* 1359-1369.

Chapter 8

$Co_1Al_2(OH)_m$ LDH and g-Carbon Nitride Composite Nanostructure for Water Oxidation Reactions

8.1 Abstract

Designing of an inexpensive efficient electrocatalyst for oxygen evolution reaction (OER) is very much important for the development of various renewable energy storage and conversion technologies. The commercial RuO_2 and IrO_2 based catalysts are highly active towards OER; but their high price and poor stability under different operating conditions are the main obstacles for their commercialization. Herein, we report the cobalt aluminium hydroxide ($Co_1Al_\delta(OH)_m$) supported on graphitic carbon nitride (g-CN_x) composite materials for superior OER activity in alkaline condition. One pot microwave heating of aqueous solution of $Co(NO_3)_2.6H_2O$ and $Al(NO_3)_3.9H_2O$ in presence of g-CN_x successfully produced $Co_1Al_\delta(OH)_m$ nanosheet impregnated on the g-CN_x. The composite catalyst required small overpotential of 0.31 V to reach the current density 10 mA cm^{-2} with low Tafel slope of 34 mV/dec. The catalyst has very high mass activity and TOF value of 1211 mA mg^{-1} and 0.61 s^{-1} at 0.35 V which are ~ 10 higher as compared to comm. IrO_2 (Comm. IrO_2) respectively. Most importantly catalyst shows remarkable high stability as compare to comm. IrO_2 in alkaline medium. Synergistic effect between binary metal (Co and Al), two dimensional sheet morphology, high electrochemical surface area (ECSA) and strong interaction between support and $CoAl(OH)_m$ nanosheet may attributed the superior activity of the composite materials.

8.2 Introduction

Due to the ever increasing energy demand and environmental concern causes importance towards renewable intermittent energy resources.[1] Electrocatalytic water splitting into molecular H_2 and O_2 is one of best suitable technologies to generate and store the electricity from intermittent sources.[2] Water electrolysis consists of two half-cell reactions such as cathodic hydrogen evolution reaction (HER) to produce molecular hydrogen and anodic oxygen evolution reaction (OER) to form molecular oxygen.[3] But the lower efficiency of the water oxidation has restricted their world wide applications.[4] The cathodic HER process is a two electron transfer process whereas anodic OER is the multistep four electron-proton couple process. Due to the multistep processes, OER has a very sluggish kinetics and is the bottleneck process of the water electrolysis.[5] To improve the overall rate and efficiency of water electrolysis, developing of an efficient electrocatalyst for OER is a challenging task. Till to date, Ir-based[6-8] and Ru-based[6, 8-9] materials have been considered as excellent OER catalysts for both acidic and alkaline solutions. However, scarcity and very expensive nature of these materials, reduces their practical applications on a large scale. Now a day, several efforts have been exploited to design a non-precious metal based electrocatalyst for OER application.[10-13] Recently, X. Sun and his co-workers reported[14] nickel-substituted cobalt-borate nanowire as an earth abundant electrocatalyst for oxygen evolution reaction. C. L. McCrory and his co-worker reported[15] cobalt-chromium spinel for efficient water oxidation reaction. Several literature reports[16-21] suggest the improved electrocatalytic activity of Co or Ni hydroxide by incorporation of Fe^{+3} ion. Burke et al. reported[22] Cobalt−Iron (Oxy) hydroxide and Nickel−Iron Oxyhydroxide[23] electrocatalyst with improved OER activity as compare Cobalt or nickel (Oxy) hydroxide in alkaline medium. The OER activity of Cobalt or nickel (Oxy)hydroxide with iron incorporation increases up to a certain limit and has a maximum activity with a certain composition *i.e.* $Co_{0.54}Fe_{0.46}(OOH)$ composite shows highest activity among all other composite of $Co_{1-x}Fe_x(OOH)$. But till now the actual origin of improved activity as well as the active site for OER is not clear. Literature reports[21, 24-25] suggested that both Co and Fe hydroxide are moderately active for OER in alkaline medium. Recently, several efforts have been given to improve the OER activity of a moderately active electrocatalyst by incorporation of a material of feebly active. X.Hu and his co-worker reported[26] an improved OER activity of CoO_x by incorporation of VO_x. Recently, Qiao et al. also reported[27] Zn-Cobalt layered double hydroxide for OER activity. Most of the literature reports deal with $Co(OH)_x$ materials with the incorporation of transition metals for improvement of OER activity. But there is highly urge to know the OER activity of $Co(OH)_x$ materials by incorporation of any low cost main group materials.[28]

Herein, we report a one pot microwave heating method for the growth of $Co_1Al_\delta(OH)_m$ nanosheets on carbon nitride support ($Co_1Al_\delta(OH)_m$/g-CN_x). The in situ nucleation and growth of $Co_1Al_\delta(OH)_m$ on carbon nitride surface that leads to the formation of two dimensional composite nanostructures. The composite materials showed improved OER activity as compared to only $Co(OH)_m$/g-CN_x and/or $Al(OH)_m$/g-CN_x composite in alkaline medium. It has an overpotentials of 0.31 V for 10 $mAcm^{-2}$ current density and much higher TOF value of 0.61 s^{-1} at 0.35 V. More importantly, evolved gas from OER was quantified and measured the faradic efficiency (FE). The composite catalyst showed ~ 99% faradic efficiency for OER over 20 min of reaction time.

8.3 Experimental Section

Synthesis of $Co_1Al_\delta(OH)_m/g\text{-}CN_x$ Composites:

One pot microwave heating methods were used for synthesis of $Co_1Al_\delta(OH)_m/g\text{-}CN_x$ composites ($\delta = 0.2, 0.6, 0.8, 1, 2, 3, 4$). In a typical synthesis of $Co_1Al_2(OH)_m/g\text{-}CN_x$ composite, 35 mg g-carbon nitride was taken in a 100 ml three neck round bottom (RB) and dispersed in 20 ml deionised water by bath sonication for 15 min. An 30 ml aqueous solution contains 0.28 mmol of $Co(NO_3)_2 \cdot 6H_2O$, 0.52 mmol of $Al(NO_3)_3 \cdot 9H_2O$ (total metal ion concentration 0.80 mmol), 0.600 gm of hexamethylenetetramine (HMT) and 0.100 gm of NH_4F was added into the aqueous g-C_3N_4 dispersion with continuous starring for 30 min at room temperature. After this, whole mixture solution was microwave heated at 85^o C with continuous stirring for 5 hrs. After the reaction was completed, whole suspension was centrifuge at 1,000 rpm for 4 min and the centrifuged product was washed with deionised water as well ethanol separately for five times and finally solid products was dried over vacuumed. As obtained solid product was termed as $Co_1Al_2(OH)_m/g\text{-}CN_x$.

Synthesis of $Co(OH)_m$ or $Al(OH)_m$- g-carbon nitride Composite:

The monometallic hydroxide composite, $Co(OH)_m/g\text{-}CN_x$ and $Al(OH)_m/g\text{-}CN_x$ was synthesised by similar procedure as mention above where 0.8 mmol of $Co(NO_3)_2 \cdot 6H_2O$ was used for $Co(OH)_m/g\text{-}CN_x$ and 0.8 mmol of $Al(NO_3)_3 \cdot 9H_2O$ for $Al(OH)_m/g\text{-}CN_x$.

Pure $Co_1Al_\delta(OH)_m$ Synthesis:

Pure $Co_1Al_\delta(OH)_m$ was synthesised by Similar procedure as mentioned above without the addition of $g\text{-}CN_x$.

8.4 Results and Discussion

The nanocomposite of g-CN_x and binary metal hydroxide made of Co, Al was synthesised by one pot microwave heating method (details in experimental section). The control samples were synthesised by similar method with individual metal salt of Co and Al to obtained the nanocomposite, $Co(OH)_m$/g-CN_x and $Al(OH)_m$/g-CN_x. The crystallinity pattern of selected nanocomposite and controlled sample were analysed by p-XRD pattern as shown in **Figure 8.1.(a-e)**. The p-XRD pattern of controlled composite materials, $Al(OH)_m$/g-CN_x and $Co(OH)_x$/g-CN_x (**Figure 8.1.a** and **8.1.e**) has crystalline diffraction pattern for cubic $Al(OH)_3$ and β-$Co(OH)_2$ with an addition peak at 2θ value at 27.3° corresponding to the (002) plane of g-carbon nitride.[29] The sharp XRD peaks of $Al(OH)_m$/g-CN_x and $Co(OH)_m$/g-CN_x suggested high crystallinity and large grain size of the composite materials. But the p-XRD pattern of $Co_1Al_2(OH)_m$/g-CN_x has identical crystalline pattern with $Al(OH)_m$/g-CN_x with broadening crystalline pattern (**Figure 8.1.b**).

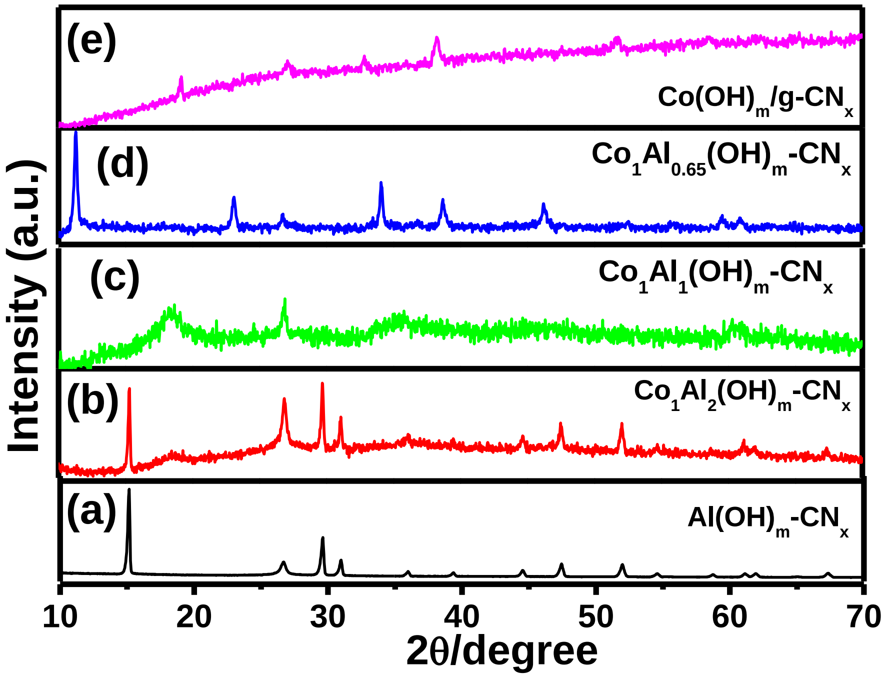

Figure 8.1. p-XRD pattern of (a) $Al(OH)_m$/g-CN_x, (b) $Co_1Al_2(OH)_m$/g-CN_x, (c)$Co_1Al_1(OH)_m$/g-CN_x, (d) $Co_1Al_{0.6}(OH)_m$/g-CN_x and (e) $Co(OH)_m$/g-CN_x.

With increasing amount of Co, the diffraction pattern getting broaden and intensity decreases gradually. At $Co_1Al_1(OH)_m/CN_x$ composition, composite materials loss it's crystallinity and has an amorphous nature as shown in **Figure 8.1.c**. This behaviour suggested Co incorporation decreases the grain size of the composite materials. Moreover, after a certain ratio of Co/Al, the structure of the composite materials changes and $Co_1Al_{0.5}(OH)_m$/g-CN_x composite materials has a layered double hydroxide (LDH) structure (**Figure 8.1.d**). The p-XRD pattern of LDH composition has diffraction peaks at 2θ values of 11.05°, 22.66°, 33.43°, 38.25°, 45.55°, 58.82° and 59° are assigned to (003), (006), (012), (015), (018), (110) and (113) planes of CoAl LDH. For comparisons, we have prepared the pure CoAl LDH materials by microwave mediated heating methods without addition of CN_x materials and its p-XRD pattern was shown in **Figure 8.2.**

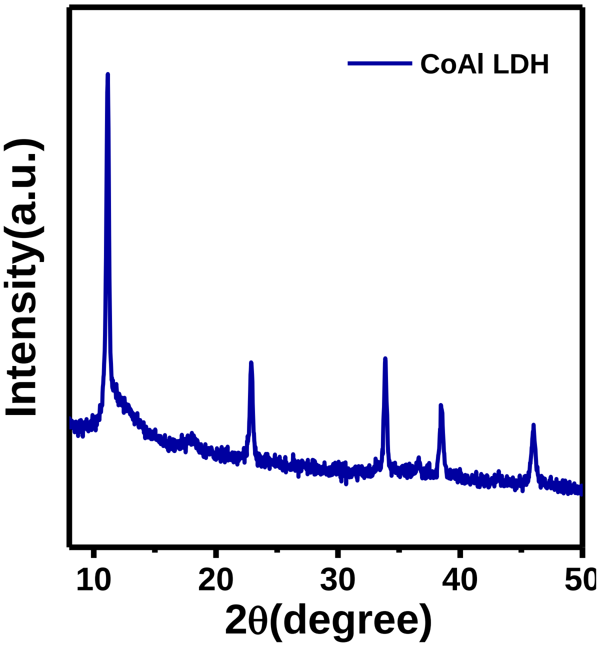

Figure 8.2. p-XRD pattern of CoAl LDH only.

The similar p-XRD pattern of composite materials and blank sample confirmed the intactness of the binary hydroxide structure after composition. Fourier transform infrared (FT-IR) spectra of pure $Co_1Al_2(OH)_m$ and $Co_1Al_2(OH)_m$/g-CN_x composite has two sharp peak at 1632 and 1352 cm^{-1} indicating presence of interlayered water and CO_3^{2-} ion as shown in **Figure 8.3**. The similar FT-IR spectra of pure hydroxide and composite materials reveals the intactness of structure over g-CN_x moiety.

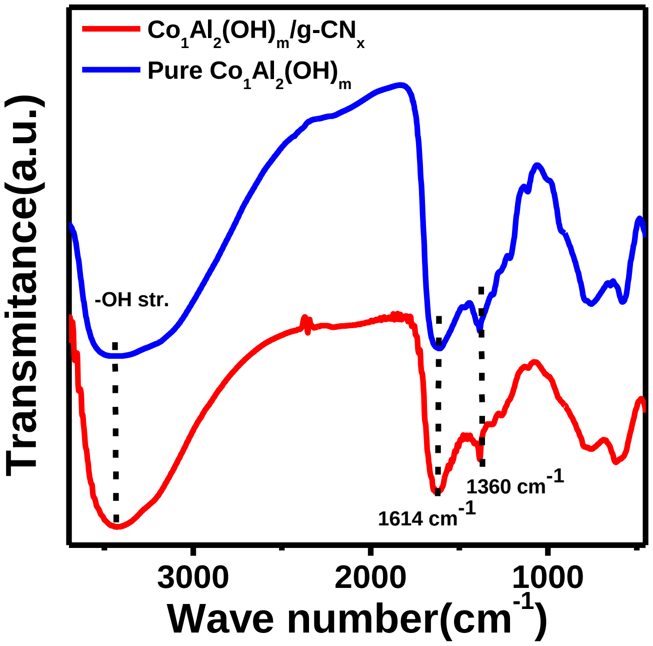

Figure 8.3. Comparison of FT-IR for $Co_1Al_2(OH)_m$ and $Co_1Al_2(OH)m$/g-CN_x composite.

The surface structure of the synthesized $Co_1Al_2(OH)_m$/g-CN_x composite was carried out by scanning electron microscopy (SEM) and transmission electron microscopy (TEM). The TEM sample was prepared by evaporation of the aqueous solution of the composite on copper grid substrate. TEM images of the $Co_1Al_2(OH)_m$/g-CN_x composite was shown in **Figure 8.4.(a-c)**. These TEM images clearly showed that very thin flooded two dimensional $Co_1Al_2(OH)_m$ nanosheets are impregnated on g-CN_x. The homogeneity of Co and Al in the composite materials was studied through STEM mapping as shown in **Figure 8.4.(d-i)**. The STEM bright field image and their corresponding mapping for different component elements of $Co_1Al_2(OH)_m$/g-CN_x composite confirmed the uniformly distribution of Co, Al, N, O and C in the composite.

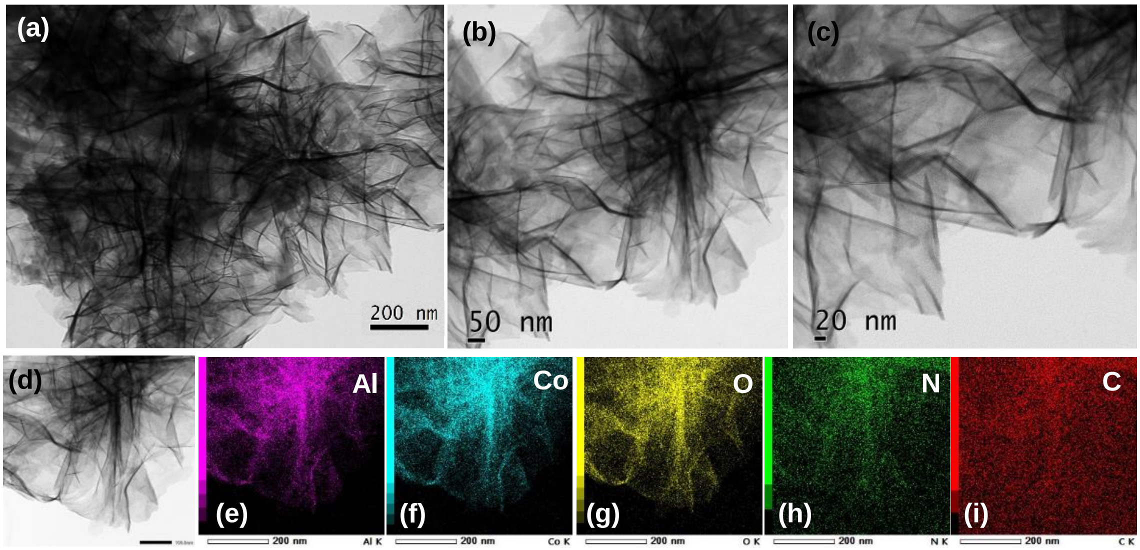

Figure 8.4. (a-c) TEM images, (d) STEM and corresponding mapping of element (e) Al, (f) Co, (g) O, (h) N, (i) C of $Co_1Al_2(OH)_m/g\text{-}CN_x$ composite.

The HR-TEM image of the composite was shown in **Figure 8.5.(a-c)**. It showed lattice fringes with the lattice distances of 0.24 nm corresponding to (015) plane of CoAl hydroxide.

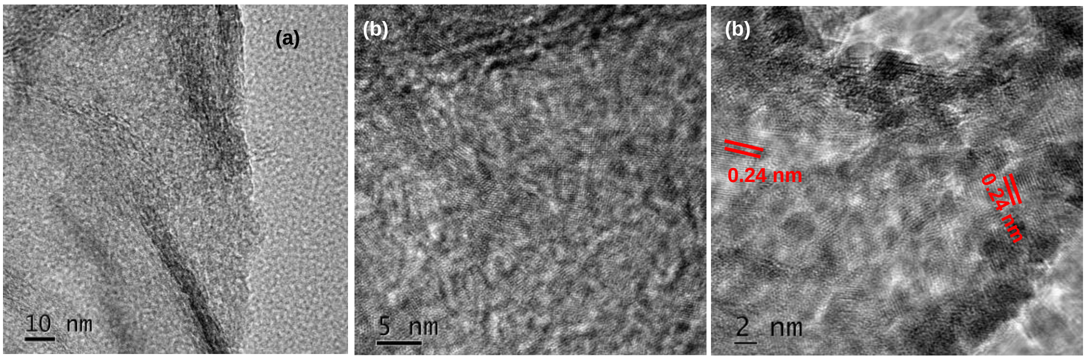

Figure 8.5. (a-c) HRTEM images of $Co_1Al_2(OH)_m/g\text{-}CN_x$ composite.

We also performed the Fe-SEM measurement of the composite materials as shown in **Figure 8.6.(a-b)**. It is also clearly shown the two dimensional sheet morphology. In addition, **Figure 8.6.c** represents FE-SEM EDS spectra of the $Co_1Al_2(OH)_m/g\text{-}CN_x$ composite showing the presence of Al to Co with an atomic ratio 1.68 along with carbon, nitrogen and oxygen. The atomic composition of Co and Al in the various hybride composite was confirmed through ICP-OES measurements. The

$Co_1Al_2(OH)_m$/g-CN_x composite contained 15.1 wt.% of Al and 9.2 wt% of Co with their atomic ratio 1.64:1. In addition, amount of carbon and nitrogen, presented in the $Co_1Al_2(OH)_m$/g-CN_x composite was measured by using CHN analysis. The CHN analysis suggests that the N:C ratio in $CoAl(OH)_m$/g-CN_x is 0.77 whereas in the free g-CN_x N:C ratio is 1.1.

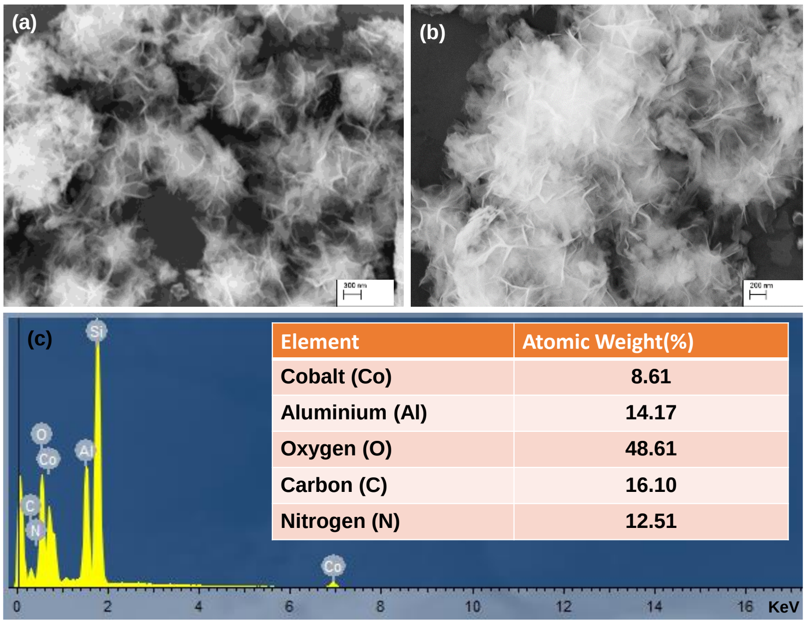

Element	Atomic Weight(%)
Cobalt (Co)	8.61
Aluminium (Al)	14.17
Oxygen (O)	48.61
Carbon (C)	16.10
Nitrogen (N)	12.51

Figure 8.6. (a-b) FESEM images of $Co_1Al_2(OH)_m$/g-CN_x composite. (c) FE-SEM EDS profile and atomic percentage of different elements.

The x-ray photoelectron spectroscopy (XPS) was carried out to know the chemical oxidation state of the element present in the $Co_1Al_2(OH)_m$/g-CN_x composite materials. The XPS survey scan spectrum is shown in **Figure 8.7.a**. which clearly shows the presence of cobalt (Co), aluminium (Al), oxygen (O), carbon (C) and nitrogen (N) in the composite materials. The high resolution XPS spectra of cobalt 2p orbital was shown in **Figure 8.7.b**. The high resolution Co 2p spectra was appeared as doublet ($2p_{1/2}$, $2p_{3/2}$) with spin orbital coupling value of 4.5 eV. The $2p_{1/2}$ $2p_{3/2}$ spectra of Co was deconvulated into three peaks – peaks at 779.8 and 782 eV correspond to Co^{3+} and Co^{2+} whereas the additional peak at 783.6 eV was assigned for shake-up satellite peak.[30] The Co^{2+} to Co^{3+} atomic ratio in the composite materials was 1:3. The high resolution 2p spectra of Al was appeared as singlet with peak centred at 74.3 eV assigned to Al oxide (**Figure 8.7.c**). The high resolution 1s XPS spectrum of oxygen was deconvulated into three peaks and it was shown in **Figure 8.7.d**. The peaks at 532.7, 531.4 and 528.6 eV were assigned for C-O, adsorbed H_2O and metal-hydroxyl bond respectively.

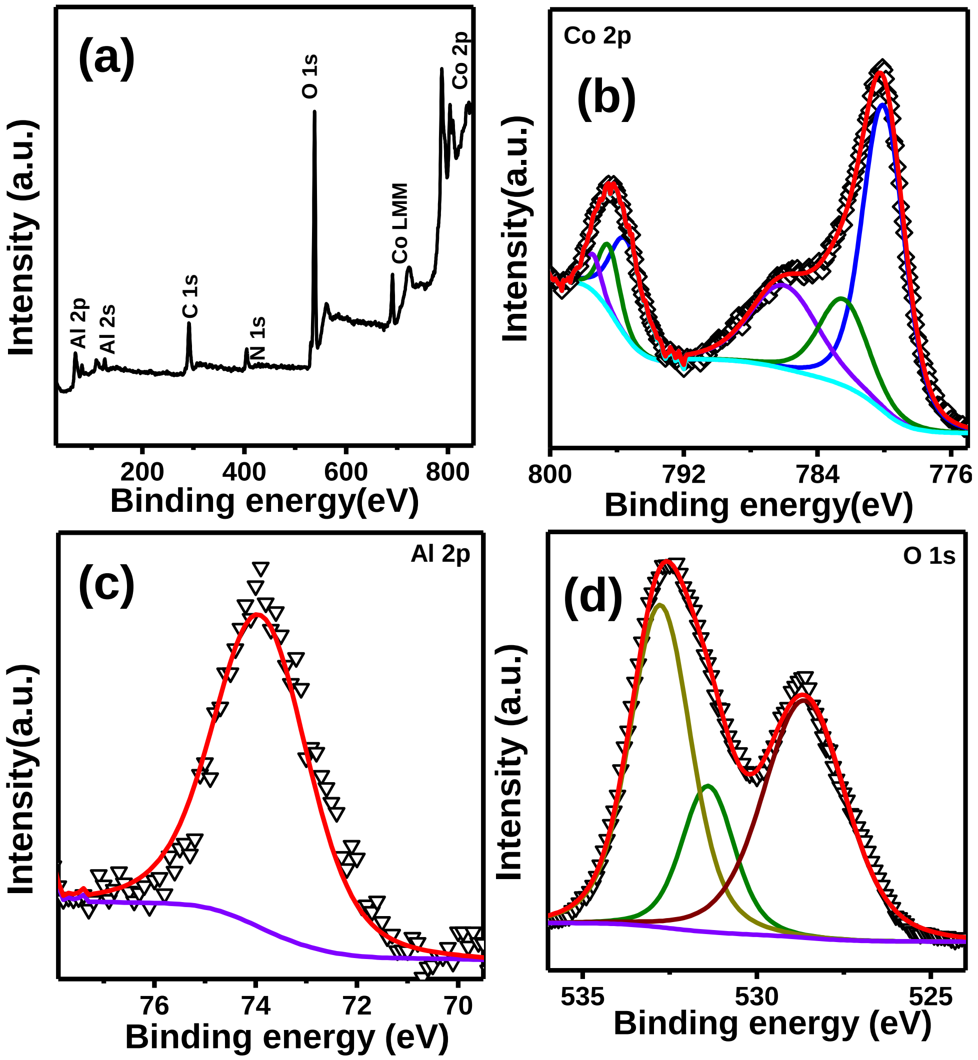

Figure. 8.7. (a) XPS survey scan spectra, high resolution (b) Co 2p, (c) Al 2p and (d) O 1s spectra of $Co_1Al_2(OH)_m$/g-CN_x

The high resolution 1s XPS spectra of carbon and nitrogen were shown in Figure **8.8.a** and **b**. The 1s high resolution spectra of C and N were deconvulated into three and two peaks as similar to free g-CN_x reported in the literature.[31-32] This results further revealed that carbon nitride moiety was remained intact even after composite the formation. In addition that, we have calculated the atomic ratio of Co and Al into the composite materials and it is found to be 0.59.

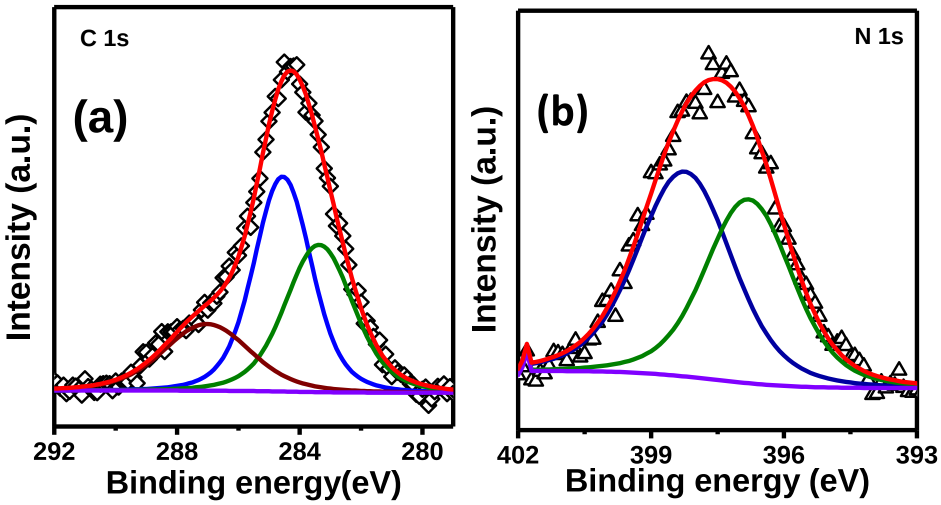

Figure 8.8. High resolution XPS spectra of (a) C 1s and (b) N 1s of $Co_1Al_2(OH)m/g-CN_x$ composite

The catalytic activity of composites with varying ratio of Co and Al, were evaluated by performing electro-catalytic oxygen evolution reaction (OER) on a glassy carbon as working electrode in 1 M KOH using a conventional three-electrode setup. Varying the amount of Co, Al ratio, a series of composite materials was prepared and optimized the catalytic activity. The OER LSV curve of different composition was shown in **Figure 8.9.a**. The overpotential (η) to reach 10 mA cm^{-2} current density for different composite materials was shown in **Figure 8.9.b**. Tafel slope value of different composite materials was observed in **Figure 8.9.c**. The highest catalytic activity was observed for the composite of Co:Al ratio to be 1:2. The LSV comparison curves of composite, controlled sample $Co(OH)_m/g-CN_x$, $Al(OH)_m/g-CN_x$ and stat-of art catalyst comm. IrO_2 in 1 M KOH with 5 mV/s scan rate was shown in **Figure 8.10.a**. The superiority of OER catalytic activity on different composite materials was evaluated by comparing three parameters: (i) the overpotentials required to reach current density of 10 $mAcm^{-2}$($\eta_{j=10\ mAcm^{-2}}$), (ii) Tafel slope and (iii) turnover frequency (TOF) values at η=0.35 V overpotentials. The OER LSV curve of optimized $Co_1Al_2(OH)_m$/g-CN_x composite, control samples $Co(OH)_m$/g-CN_x, $Al(OH)_x$/g-CN_x and state-of-art IrO_2 catalyst in Fe free 1 M KOH at 5 mV/s scan rate with 1600 rpm was shown in **Figure 8.10.a**. **Figure 8.10.a** shows poor OER activities of bare GC, and $Al(OH)_m$/g-CN_x electrodes. The $Co(OH)_m$/g-CN_x and comm. IrO_2 catalyst showed moderate OER activity, but $Co_1Al_2(OH)_m$/g-CN_x composite catalyst exhibited much improved OER activity. The $Co_1Al_2(OH)_m$/g-CN_x composite exhibited a low onset potential of 1.48 V which was 60 mV lower than that of comm. IrO_2. The OER activity of these catalysts were further evaluated by comparing the overpotential required to obtain a current density of 10 mA cm^{-2}($\eta_{10\ mAcm-2}$) as shown in **Figure 8.10.b**. The Tafel plots of different catalyst in 1 M KOH was shown in **Figure 8.10.c**.

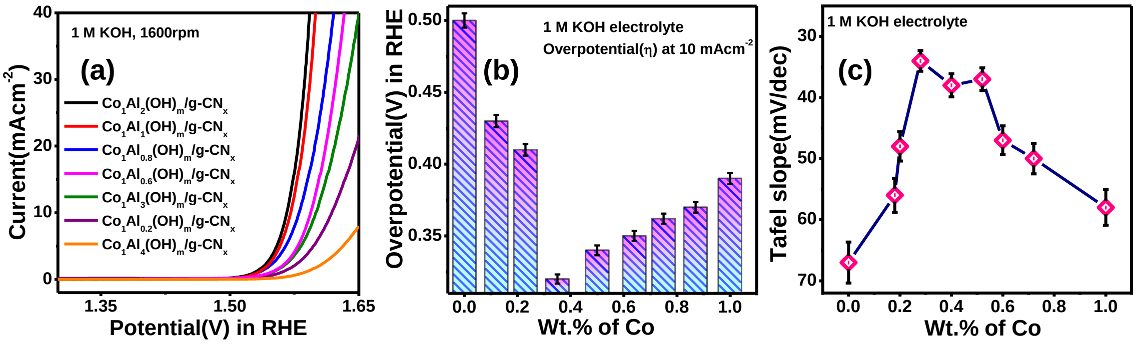

Figure 8.9. (a) OER LSV curve, (b) overpotentials required to reach 10 $mAcm^{-2}$ current density and (c) Tafel slope value of different composite materials.

The Tafel slope value of $Co_1Al_2(OH)_m$/g-CN_x composite was 36 mV/dec whereas Tafel slope value for Comm. IrO_2, $Co(OH)_m$/g-CN_x and $Al(OH)_x$/g-CN_x were 64, 56, and 67 mV/dec respectively. Several reaction mechanisms for multistep OER reaction are available in the literature. Recently, J.Rossmeisl and his co-worker[33] found an analogous OER behaviour of different oxide based electrocatalyst and proposed general four step reaction mechanism for OER on transition metal oxide electrocatalyst based on DFT calculation. Four steps for OER are describes as

The first step is the water adsorption as hydroxyl group on the surface active site (S)-

$$S + {}^{-}OH = S\text{-}OH_{ads} + e^{-} \qquad (1)$$

$$S\text{-}OH_{ads} + {}^{-}OH = S\text{-}O_{ads} + H_2O + e^{-} \qquad (2)$$

$$S\text{-}O_{ads} + OH = S\text{-}OOH + e^{-} \qquad (3)$$

$$S\text{-}OOH + {}^{-}OH = S + O_2 + H_2O + e^{-} \qquad (4)$$

The Tafel slope value (b) for a chemically reversible multistep proton/electron couple reaction with a single rate determine step was theoretically calculated by

$$b = \frac{\mathrm{RT}\ \ln 10}{(n - \alpha)\ F}$$

Where R, T and F is defined as their usual meaning, n is the number of electron transfers of the corresponding step and α is the electron transfer coefficient (0.5).

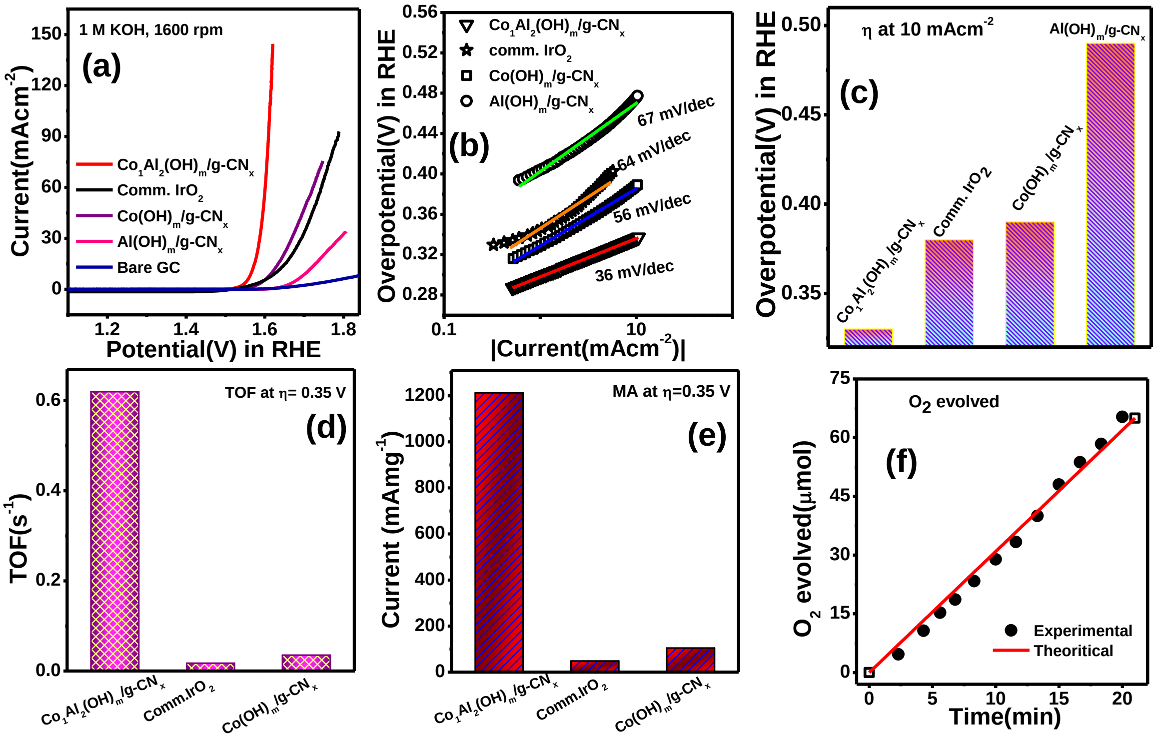

Figure 8.10. (a) LSV comparison curve of $Co_1Al_2(OH)_m/g\text{-}CN_x$, comm. IrO_2, $Co(OH)_m/g\text{-}CN_x$ and $Al(OH)_m/g\text{-}CN_x$. (b) $\eta_{j=10\ mAcm\text{-}2}$ values of different composite materials. (c) Tafel plot of $Co_1Al_2(OH)_m/g\text{-}CN_x$, comm. IrO_2, $Co(OH)_m/g\text{-}CN_x$ and $Al(OH)_m/g\text{-}CN_x$. Comparison of (d) TOF and (e) MA values of different catalyst at 0.35 V overpotential. (f) The theoretical and measured amount of evolved O_2 gas on $Co_1Fe_2\,(OH)_m/g\text{-}CN_x$ electrode in 1 M KOH.

The low Tafel value of $Co_1Al_2(OH)_m$/g-CN_x catalyst suggests the second step *i.e.* hydroxide to oxide formation is the rate determine step for OER. In general mass activity (MA) and turn over frequency (TOF) are considered as the parameter for the intrinsic activity of the catalyst. For these purpose we have calculated the TOF and MA values for different catalyst at 0.35 V overpotentials and they are shown in **Figure 8.10.d** and **8.10.e** respectively. $Co_1Al_2(OH)_m$/g-CN_x composite catalyst has very high TOF value of 0.61 s^{-1} which is 27 times higher than comm. IrO_2 (0.021 s^{-1}) catalyst. Furthermore, the composite catalyst has much improved MA activity of 1211 mA mg^{-1} which is ~ 25 times higher than that of comm. IrO_2 catalyst. We have compare the OER activity of $Co_1Al_2(OH)_m$/g-CN_x with other reported OER catalyst and shown in **Table 8.1**. This result displays that $Co_1Al_2(OH)_m$/g-CN_x has higher or comparable OER activity with different reported catalyst.

The long term stability of OER performance is an important parameter for its practical application. We have determined the operational durability of samples by comparing the LSV cycling curve before and after 2000 continuous repeated accelerated CV cycling test at a 10 mV s^{-1} scan rate. The LSV cycling stability of $Co_1Al_2(OH)_m$/g-CN_x composite was shown in **Figure 8.11.a**. Although IrO_2 is considered as the state-of-art catalyst for OER but their low thermodynamical stability under alkaline medium obstacle its practical utilization. For comparison, we have also performed the OER LSV cycling stability of comm. IrO_2 under similar condition as mentioned for $Co_1Al_2(OH)_m$/g-CN_x catalyst. The LSV cycling stability curve of comm. IrO_2 was shown in **Figure 8.11.b**. The $Co_1Al_2(OH)_m$/g-CN_x catalyst shows only 20% decrease of current density at 0.35 V after 2000 continuous cycling whereas comm. IrO_2 losses 82% of its initial current density even after only 1500 cycles.

Table 8.1. Comparison of OER activity of $Co_1Al_2(OH)_m$/g-CN_x composite with recently reported different OER catalyst in alkaline medium on glassy carbon electrode

Catalyst	**Electrolyte**	**Overpotential at 10 $mAcm^{-2}$ (V)**	**Tafel slope(mV/ dec)**	**Reference**
CoMn LDH	1 M KOH	0.324	43	*J. Am. Chem. Soc.* **2014,** 13, 16481[1].
$Zn_xCo_{3-x}O_4$	1 M KOH	0.32	51	*Chem. Mater. 2014, 26, 1889−1895.*[2]
NiCo LDH	1 M KOH	0.334	41	*Nat. Commun.* **2014,** 5, 4477[3]
Ni0.9Fe0.1/NC	1 M KOH	0.330	45	*ACS Catal.* **2016,** 6, 580[4]
Ultrathin $NiCo_2O_4$ nanosheets	1 M KOH	0.320	30	*Angew. Chem. Int.* Ed. **2015,** 54, 7399[5]
rGO@$CoNiO_x$	0.1 M KOH	0.320	45	*Adv.Funct.Mater.* **2017,** 27, 1606325[6].
ZnCo2O4	1 M KOH	0.40 V	46	J. Phys. Chem. Lett. **2014,** *5*, 2370−2374.[7]
NiFe LDH/oGSH	0.1M KOH	0.350	54	*J. Mater. Chem. A* **2015,** 3, 24540[8]
$Mn_3O_4/CoSe_2$	0.1 M KOH	0.45		*J.Am.Chem.Soc.* **2012**, *134,* 2930−2933.[9]
CoFe LDH-C	1 M KOH	0.415	47	*ACS Appl. Mater. Interfaces* **2016,** 8, 34474[10]
$NiCo_{2.7}(OH)_x$ amorp.nanocage	1 M KOH	0.350	65	*Adv. Energy Mater.* **2015,** 5, 1401880[11]
Co_5Mn-LDH/MWCNT	1 M KOH	0.300	73.6	*ACS Appl. Mater. Interfaces 2016*, 8, 14527[12]
$Co_{2.25}Cr_{0.75}O_4$	1 M NaOH	0.350	52	*ACS Catal.* **2017**, 7, 443−451[13]
$CoVO_x$	1 M KOH	0.366	49	*ACS Catal.* **2018**, *8*, 644−650.[14]
$Co_1Al_2(OH)_m$/g-CN_x	1 M KOH	0.32	36	**This work**

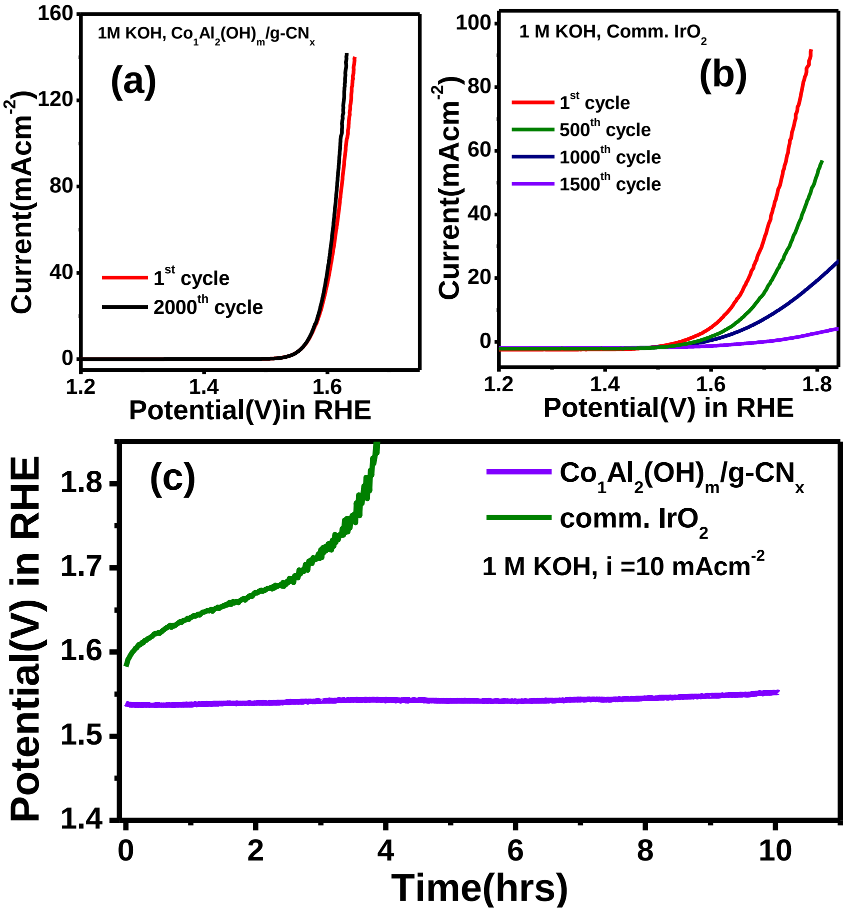

Figure 8.11. LSV cycling stability study of (a) $Co_1Al_2(OH)_m/g\text{-}CN_x$ composite, (b) comm. IrO_2. (c) Chronopotentiometry study of Comm. IrO_2 and $Co_1Al_2(OH)_m/g\text{-}CN_x$ composite at 10 mAcm^{-2} current density.

This behaviour suggested the superior OER stability of $Co_1Al_2(OH)_m/g\text{-}CN_x$ composite as compare to comm. IrO_2 catalyst in alkaline medium. Furthermore, the long term durability of the catalyst was also investigated by chronoamperometry study at a particular current density.A comparative chronoamperometry study at 10 mA cm^{-2} current density for $Co_1Al_2(OH)_m/g\text{-}CN_x$ composite and comm. IrO_2 was performed under similar condition and shown in **Figure 8.11.c**. The over-potentials for comm. IrO_2 catalyst increases drastically from 0.35 to 0.8 V within 4 hrs time periods whereas for $Co_1Al_2(OH)_m/g\text{-}CN_x$ composite, there was almost no change of overpotential after 10 hrs time periods. This result further demonstrated the easy degradation, desolation and surface oxidation of the IrO_2 catalyst, whereas, $Co_1Al_2(OH)_m/g\text{-}CN_x$ catalyst showed strong durability under alkaline working condition. It is important task for a superior electrocatalyst to intact its chemical composition, structure and morphology even after long term durability. For these purposes, we have performed post characterisations of the composite catalyst through XPS, FE-SEM and EDS measurements. The high resolution XPS spectra of Co 2p, Al 2p and O 1s of composite catalyst after chronoamperometry stability was shown in **Figure 8.12.a-c.** No significant change was observed in XPS pattern. This result suggested that the catalyst was very stable under operational condition.

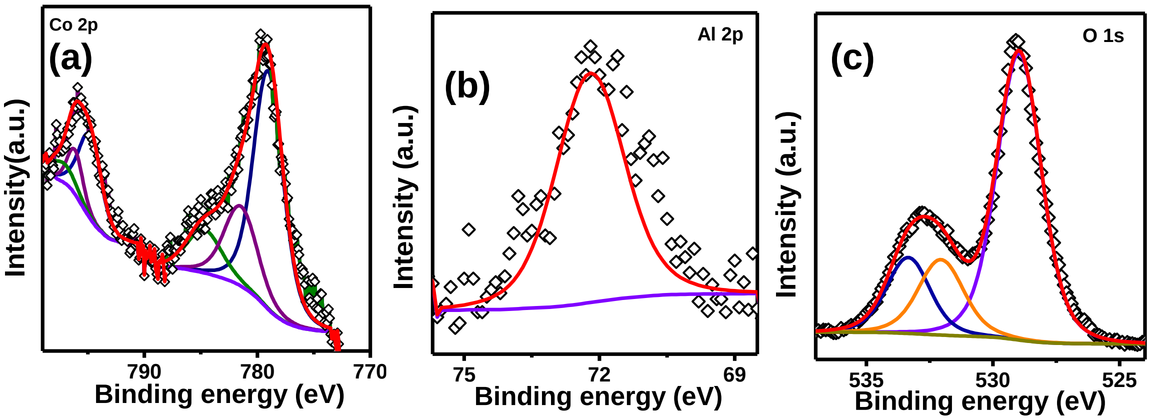

Figure 8.12. High resolution XPS spectra of (a) Co 2p, (b) Al 2p and (c) O 1s of of $Co_1Al_2(OH)m/g\text{-}CN_x$ catalyst after stability study.

Furthermore, we have also studied the morphology of the catalyst after stability test and shown in **Figure 8.13.a.** The EDS spectra of FE-SEM image was shown in **Figure 8.13.b.** It has clearly showed the presence of Co, Al, O, C and N. This result further confirmed the higher stability and unaltered structure as well as chemical composition of the catalyst under OER experimental condition.

The superior electro-catalytic activity and excellent stability of the Co_1Al_2 $(OH)_m/g\text{-}CN_x$ catalyst towards OER in alkaline electrolyte may be elucidated by several factors such as:

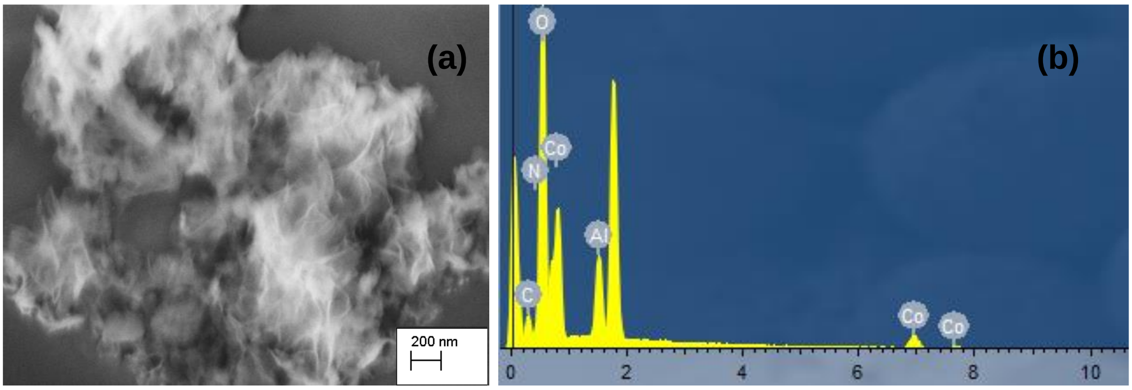

Figure 8.13. (a) FESEM image and (b) corresponding EDS spectra of $Co_1Al_2(OH)m/g-CN_x$ catalyst after stability study.

(a) It is well kown[34-35] that highly oxidized transition metal redox couple such as $Ni^{+3/+4}$ and $Co^{+3/+4}$ are the active centres for OER. In literature, Co based materials[36-37] have two type redox natures : (i) 1.2 and 1.3 V corresponds to Co^{2+}/Co^{3+} and (ii) in the range of 1.3 to 1.6 V which corresponds to Co^{3+}/Co^{4+}. The cyclic voltammetry (CV) patterns of $Co(OH)_m/g-CN_x$, $Al(OH)_m/g-CN_x$ and different $Co_1Al_\delta(OH)_m/g-CN_x$ composite in 1 M KOH (Fe free) at 10 mV/s scan rate was shown in **Figure 8.14**.

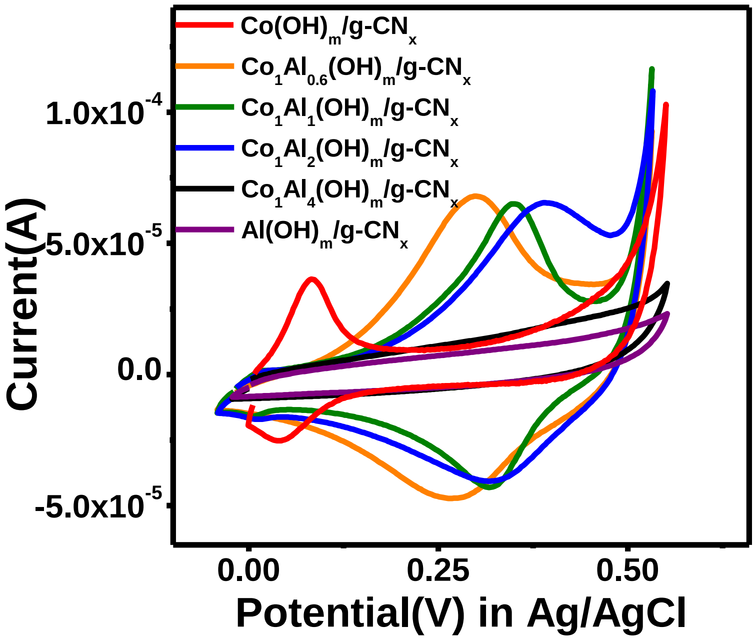

Figure 8.14. CV comparison curves of different composite materials.

$Al(OH)_m$/g-CN_x composite does not have any redox peaks in 1 to 1.6 V region where as $Co(OH)_m$/g-CN_x composite have a anodic peak at 1.2 V assigned for $Co^{2+/}Co^{3+}$ redox transition. But when incorporation of Al^{3+} occoured into $Co(OH)_m$ moiety, the anodic peak shows an anodic shifting of Co^{2+}/Co^{3+} redox wave, indicating strong electronic interactions between Co, Al and substitution of Co by Al. Smith et al. reported[22] the anodic peak shifting of Co^{2+}/Co^{3+} redox wave for incorporation of Fe and Ni into $Co(OH)_2$ moiety. **Figure 8.14** shows that the $Co_1Al_q(OH)_m$-CN_x with Al wt.% of 30 to 60, has a anodic CV peak at 1.5 V corresponding to Co^{+3}/Co^{+4} redox wave. The previous literature reports suggested[35] that Oh Co^{3+} sites are indeed the real active sites of cobalt based materials for the OER. Moreover, several groups suggested[35, 38] that Oh Co^{3+} forms Co^{4+} species during OER and enhances the electrophilicity of the adsorbed O which further assists the formation of O–OH facilitating the deprotonation of –OOH. The CV curve of $Co_1Al_2(OH)_m$/g-CN_x composite has peak at 1.45 V that confirms the predominate surface active Co^{3+} sites. Therefore, superior OER activity of $Co_1Al_2(OH)_m$-CN_x composite may be attributed due to the presence of greater number of electrochemically accessible active Oh Co^{3+} site which enhances –OH adsorption onto the Co^{3+}.

b) The strong interaction between $Co_1Al_2(OH)_m$ and supported materials g-CN_x could be one of reason for its enhanced activity and enhanced long term durability. The direct growth of $Co_1Al_2(OH)_m$ on g-CN_x surface leads to the formation of composite with strong interaction between $Co_1Al_2(OH)_m$ and support (CN_x). This increases the conductivity by improving electron transfer through CoAl composite. The electrochemical impedance spectroscopy (EIS) study was performed for this purpose. **Figure 8.15.a s**hows the Nyquist plot of Co_1Al_2 $(OH)_m$/g-CN_x composite at different potential. At all the potentials Nyquist plot of Co_1Al_2 $(OH)_m$/g-CN_x composite consist with a semicircle and radii of the semicircle gradually decreases as one approaches towards onset potentials. The charge transfer resistance (R_{ct}) of the catalyst was calculated by fitting the experimental curve with an electrical circuit as shown in in-set of **Figure 8.15.a**.

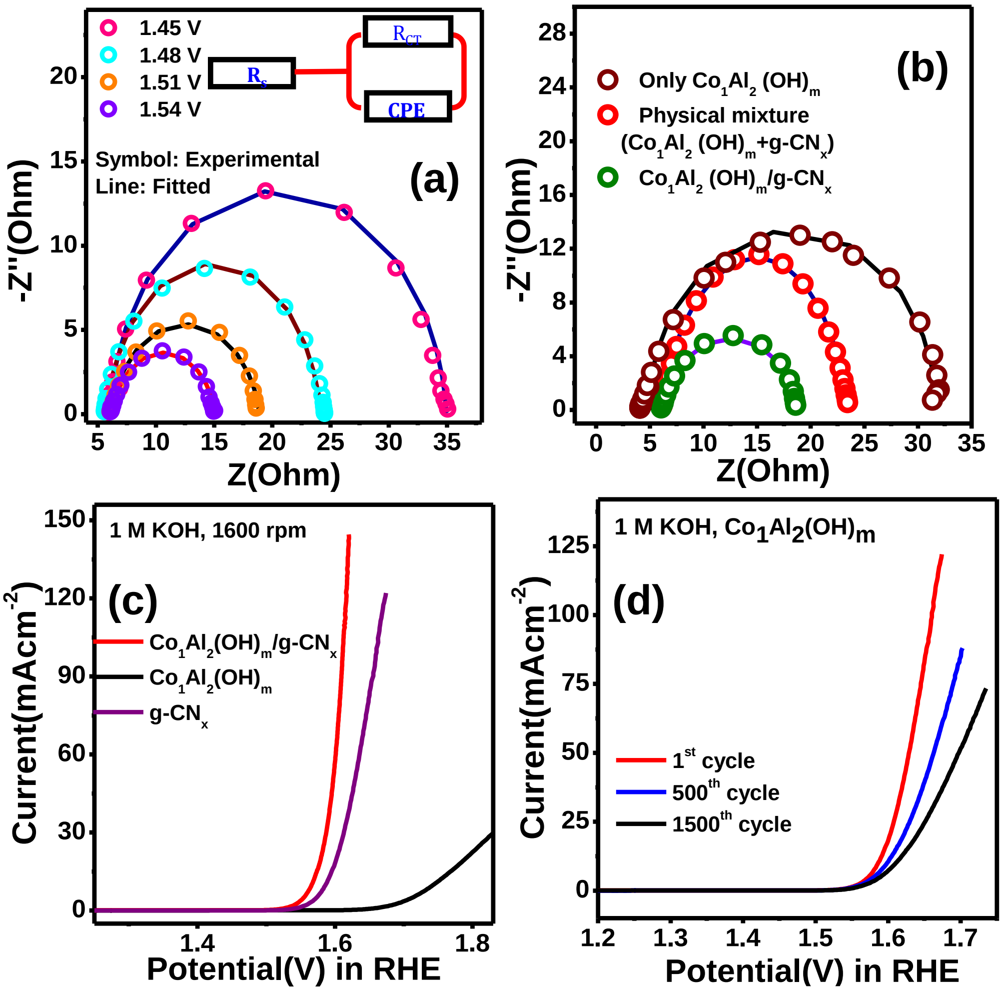

Figure 8.15. (a) Nyquist plot of $Co_1Al_2\ (OH)_m/g\text{-}CN_x$ composite in 1 M KOH at different overpotentials. Inset: Electronic circuit for fitting the Nyquist plot. (b) Comparison of Nyquist plot of $Co_1Al_2(OH)_m/g\text{-}CN_x$, only $Co_1Al_2(OH)_m$ and physical mixture of $Co_1Al_2\ (OH)_m$ and g-CN_x at 1.54 V in RHE under similar condition. (c) Comparison of OER LSV curve of $Co_1Al_2\ (OH)_m/g\text{-}CN_x$, g-$CN_x$ and physical mixture of $Co_1Al_2\ (OH)_m$ and g-CN_x. (d) 1^{st} and 1500^{th} LSV curve of physical mixture of $Co_1Al_2\ (OH)_m$ and g-CN_x..

The $Co_1Al_2\ (OH)_m/g\text{-}CN_x$ composite has the lower R_{ct} value of 5 ohm^{-1} at 1.54 V in RHE. Furthermore we have performed the Nyquist plot of $Co_1Al_2\ (OH)_m/g\text{-}CN_x$, only $Co_1Al_2(OH)_m$ and physical mixture of $Co_1Al_2\ (OH)_m$ and g-CN_x at 1.51 V in RHE and shown in **Figure 8.15.b**. The R_{ct} value of $Co_1Al_2\ (OH)_m/g\text{-}CN_x$, physical mixture and only Co_1Al_2 $(OH)_m$ are 8 ohm^{-1}, 18 ohm^{-1} and 26.7 ohm^{-1} respectively. This results reveals that the composition improve the interfacial charge transfer and enhanced the electrocatalytic OER activity. Moreover, we have compared the OER activity of free g-CN_x, physical mixture (Co_1Al_2 $(OH)_m$ + g-CN_x) and Co_1Al_2 $(OH)_m$/g-CN_x as shown in **Figure 8.15.c**. These results showed that the free g-CN_x has very low OER activity whereas the physical mixture has a moderate activity but on composition results an improved OER activity.

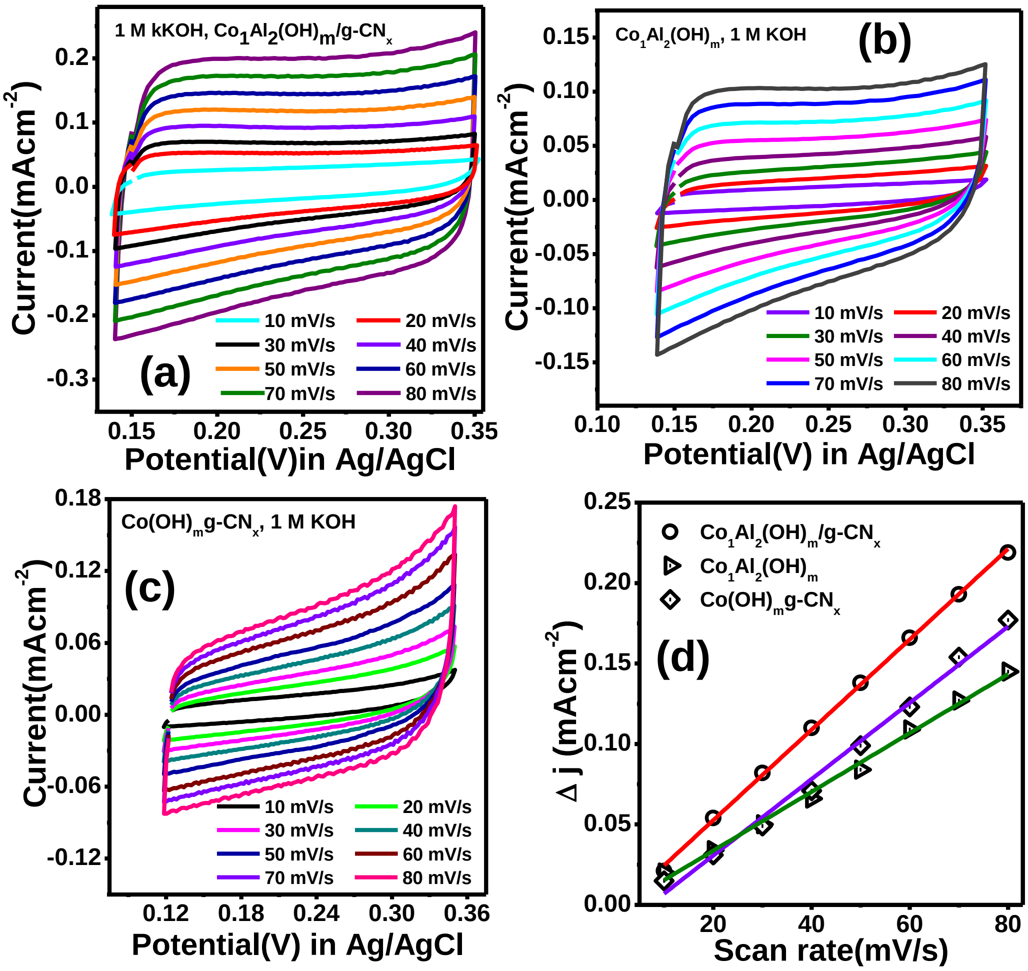

Figure 8.16. CV curves of (a) Co_1Al_2 $(OH)_m$/g-CN_x, (b) only Co_1Al_2 $(OH)_m$ and (c) $Co(OH)_m$/g-CN_x composite in the potential range of 0.1 to 0.35 V in Ag/AgCl under variable scan rate. (d) Linear plot of dJ vs scan rate at particular potentials of 0.3 V in Ag/AgCl of different catalyst.

This confirmed the strong interaction between Co_1Al_2 $(OH)_m$ and g-CN_x in composite materials helps to improve the catalytic activity. In addition, an interaction between $Co_1Al_2(OH)_m$ to CN_x sheets provide structural stability for long term electrochemical measurements of the catalyst. The OER LSV cycling stability of physical mixture (Co_1Al_2 $(OH)_m$ + g-CN_x) shows that it have poor stability as compare the composite materials(**Figure 8.15.d**).

c) The high electrochemical surface area of Co_1Al_2 $(OH)_m$/g-CN_x composite resulting from large number catalytic sites is another reason for its high catalytic activity. The active surface area of $Co_1Al_2(OH)_m$/g-CN_x, $Co_1Al_2(OH)_m$ and $Co(OH)_m$/g-CN_x catalyst was evaluated by measuring the double layer capacitance (C_{dl}) of the catalyst. The CV curves of $Co_1Al_2(OH)_m$/g-CN_x, $Co_1Al_2(OH)_m$ and $Co(OH)_m$/g-CN_x catalyst at different scan speeds in 1 M KOH solution in 0.1 to 0.35 V potential window was shown in **Figure 8.16.a**, **b** and **c** respectively. The corresponding liner plot of current vs scan rate at potential of 0.25 V (in Ag/AgCl) were shown in **Figure 8.16.d**. The C_{dl} value of a catalyst was directly proportional to ECSA value. The higher C_{dl} value of Co_1Al_2 $(OH)_m$/g-CN_x of 2.9 mF cm^{-2} which is higher as compared to Co_1Al_2 $(OH)_m$ (1.9 mF cm^{-2}) and $Co(OH)_m$/g-CN_x (1.6 mF cm^{-2}). The large surface area suggests that the catalyst has large number catalytic sites due to its two dimensional morphology of the catalyst, which is significantly contributing to its high OER activity.

8.5 Conclusions:

In conclusion, we have demonstrated a facile microwave heating method for the development of thin Co_1Al_δ(OH)m nano-sheets and composite formation with g-carbon nitride. A highly folded $Co_1Al_\delta(OH)_m$ two dimensional naosheets was synthesized which is highly dispersed on the g-CN_x sheet. The $Co_1Al_2(OH)_m$/g-CN_x composite showed a superior electrocatalytic water oxidation activity in alkaline medium. The $Co_1Al_2(OH)_m$/g-CN_x composite exhibited a small overpotential of 0.31 V for 10 mA cm^{-2}, low Tafel slope of 34 mV/dec and very high TOF value of 0.61 s^{-1} at 0.35 V. The catalyst has enhanced cycling stability as well as long term durability with constant current density of 10 $mAcm^{-2}$ for 10 hrs. The enhanced electrocatalytic OER activity and long term stability of the composite materials may be due to the synergistic interaction between Co and Al, high surface area, easy mass and electron transportation from two dimensional morphology, strong interaction between support materials and catalytic active $Co_1Al_2(OH)_m$ sites. The superior OER activity with long term durability of $Co_1Al_2(OH)m$/g-CN_x composite makes it as a promising catalyst for water-splitting devices.

8.6 References

1. Lewis, N. S.; Nocera, D. G., *Proceedings of the National Academy of Sciences of the United States of America* **2006,** *103,* 15729-35.
2. Stamenkovic, V. R.; Strmcnik, D.; Lopes, P. P.; Markovic, N. M., *Nat. Mater.* **2017,** *16,* 57-69.
3. Fabbri, E.; Habereder, A.; Waltar, K.; Kotz, R.; Schmidt, T. J., *Catal. Sci. Technol.* **2014,** *4,* 3800-3821.
4. Dresselhaus, M. S.; Thomas, I. L., *Nature* **2001,** *414,* 332-337.
5. Goodenough, J. B.; Manthiram, A., *MRS Commun.* **2014,** *4,* 135-142.
6. Mamaca, N.; Mayousse, E.; Arrii-Clacens, S.; Napporn, T. W.; Servat, K.; Guillet, N.; Kokoh, K. B., *Appl. Catal. B: Environ.* **2012,** *111–112,* 376-380.
7. Nong, H. N.; Oh, H.-S.; Reier, T.; Willinger, E.; Willinger, M.-G.; Petkov, V.; Teschner, D.; Strasser, P., *Angew. Chem. Int. Ed.* **2015,** *54,* 2975-2979.
8. Danilovic, N.; Subbaraman, R.; Chang, K. C.; Chang, S. H.; Kang, Y.; Snyder, J.; Paulikas, A. P.; Strmcnik, D.; Kim, Y. T.; Myers, D.; Stamenkovic, V. R.; Markovic, N. M., *Angew. Chem. Inter. Ed.* **2014,** *53,* 14016-14021.
9. Kong, X.; Xu, K.; Zhang, C.; Dai, J.; Norooz Oliaee, S.; Li, L.; Zeng, X.; Wu, C.; Peng, Z., *ACS Catal.* **2016,** 1487-1492.
10. Eftekhari, A., *Mater. Today Energy* **2017,** *5,* 37-57.

11. Han, L.; Dong, S.; Wang, E., *Adv. Mater.* **2016,** *28,* 9266-9291.

12. Chen, D.; Chen, C.; Baiyee, Z. M.; Shao, Z.; Ciucci, F., *Chem. Rev.* **2015,** *115*, 9869-9921.

13. Hunter, B. M.; Gray, H. B.; Müller, A. M., *Chem. Rev.* **2016,** *116*, 14120-14136.

14. Ma, M.; Qu, F.; Ji, X.; Liu, D.; Hao, S.; Du, G.; Asiri, A. M.; Yao, Y.; Chen, L.; Sun, X., *Small* **2017,** *13,* 1700394-n/a.

15. Lin, C.-C.; McCrory, C. C. L., *ACS Catal.* **2017,** *7,* 443-451.

16. Jin, H.; Mao, S.; Zhan, G.; Xu, F.; Bao, X.; Wang, Y., *J. Mater. Chem. A* **2017,** *5,* 1078-1084.

17. Sun, F.; Li, L.; Wang, G.; Lin, Y., *J. Mater. Chem. A,* **2017**.

18. Zhu, K.; Liu, H.; Li, M.; Li, X.; Wang, J.; Zhu, X.; Yang, W., *J. Mater. Chem. A,* **2017**.

19. Feng, Y.; Zhang, H.; Fang, L.; Mu, Y.; Wang, Y., *ACS Catal.***2016,** *6,* 4477-4485.

20. Zhang, X.; Xu, H. M.; Li, X. X.; Li, Y. Y.; Yang, T. B.; Liang, Y. Y., *ACS Catal.* **2016,** *6,* 580-588.

21. Friebel, D.; Louie, M. W.; Bajdich, M.; Sanwald, K. E.; Cai, Y.; Wise, A. M.; Cheng, M.-J.; Sokaras, D.; Weng, T.-C.; Alonso-Mori, R.; Davis, R. C.; Bargar, J. R.; Nørskov, J. K.; Nilsson, A.; Bell, A. T., *J. Am. Chem. Soc.* **2015,** *137,* 1305-1313.

22. Burke, M. S.; Kast, M. G.; Trotochaud, L.; Smith, A. M.; Boettcher, S. W., *J. Am. Chem. Soc.* **2015,** *137,* 3638-3648.

23. Trotochaud, L.; Young, S. L.; Ranney, J. K.; Boettcher, S. W., *J. Am. Chem. Soc.* **2014,** *136*, 6744-6753.

24. Görlin, M.; Chernev, P.; Ferreira de Araújo, J.; Reier, T.; Dresp, S.; Paul, B.; Krähnert, R.; Dau, H.; Strasser, P., *J. Am. Chem. Soc.* **2016,** *138,* 5603-5614.

25. Görlin, M.; Ferreira de Araújo, J.; Schmies, H.; Bernsmeier, D.; Dresp, S.; Gliech, M.; Jusys, Z.; Chernev, P.; Kraehnert, R.; Dau, H.; Strasser, P., *J. Am. Chem. Soc.* **2017,** *139,* 2070-2082.

26. Liardet, L.; Hu, X., *ACS Catal.* **2018,** *8,* 644-650.

27. Qiao, C.; Zhang, Y.; Zhu, Y.; Cao, C.; Bao, X.; Xu, J., *J. Mater. Chem. A* **2015,** *3,* 6878-6883.

28. Ping, J.; Wang, Y.; Lu, Q.; Chen, B.; Chen, J.; Huang, Y.; Ma, Q.; Tan, C.; Yang, J.; Cao, X.; Wang, Z.; Wu, J.; Ying, Y.; Zhang, H., *Adv. Mater.* **2016,** *28,* 7640-7645.

29. Barman, S.; Sadhukhan, M., *J. Mater. Chem.* **2012,** *22,* 21832-21837.

30. Li, S.; Peng, S.; Huang, L.; Cui, X.; Al-Enizi, A. M.; Zheng, G., *ACS Appl. Mater. Interfaces* **2016,** *8,* 20534-20539.

31. Fang, J.; Fan, H.; Li, M.; Long, C., *J. Mater. Chem. A* **2015,** *3,* 13819-13826.

32. Barman, S.; Sadhukhan, M., *J. Mater. Chem.* **2012,** *22,* 21832-21837.

33. Man, I. C.; Su, H.-Y.; Calle-Vallejo, F.; Hansen, H. A.; Martínez, J. I.; Inoglu, N. G.; Kitchin, J.; Jaramillo, T. F.; Nørskov, J. K.; Rossmeisl, J., *ChemCatChem* **2011,** *3*, 1159-1165.

34. Maiyalagan, T.; Jarvis, K. A.; Therese, S.; Ferreira, P. J.; Manthiram, A., *Nat. commun.* **2014,** *5*, 3949.

35. Suntivich, J.; May, K. J.; Gasteiger, H. A.; Goodenough, J. B.; Shao-Horn, Y., *Science* **2011,** *334,* 1383-1385.

36. Liu, X.; Chang, Z.; Luo, L.; Xu, T.; Lei, X.; Liu, J.; Sun, X., *Chem. Mater.* **2014,** *26,* 1889-1895.

37. Han, S.; Liu, S.; Wang, R.; Liu, X.; Bai, L.; He, Z., *ACS Appl. Mater. Interfaces* **2017,** *9,* 17186-17194.

38. Menezes, P. W.; Indra, A.; Bergmann, A.; Chernev, P.; Walter, C.; Dau, H.; Strasser, P.; Driess, M., *J. Mater. Chem. A* **2016,** *4,* 10014-10022.

Chapter 9

Selective Hydrogenation of Nitro Compounds and Ullmann Coupling Reaction by Palladium Nanoparticles Supported on Graphitic Carbon Nitride.

9.1 ABSTRACT

Improved catalytic activity with enhanced stability is an important criterion for the utilization of a noble metal based nano-composite catalyst. Herein we report a facile synthesis of highly dispersed palladium nanoparticles embedded on graphitic carbon nitride (Pd@CN$_x$) by ultrasound assisted method without aid of any external reducing agent. The Pd@CN$_x$ composite was well characterized by different techniques. This Pd@CN$_x$ shows effective catalytic activity towards easy dehydrogenation of sodium borohydride (NaBH$_4$) and ammonia borane (AB) in aqueous medium and also can easily hydrogenate 4-Nitrophenol to 4-aminophenlo with fast kinetics. The catalyst is highly selective towards nitro groups in presence of other reducible groups with good stability. Furthermore, the catalyst exhibits superior catalytic activity towards ullmann coupling reaction of different aryl halides with broad range of substrates scope with easy recovery of the catalyst and high recycling property.

9.2 Introduction

In recent years, noble metal nanoparticles (MNPs) have attracted a lot of attention due to their intriguing potential applications in verious fields such as in catalysis,[1-3]photoreaction,[4] fuel cell,[5-6] energy conversion.[7] Size and shape dependent selectivity and reactivity [8-9] makes the nanocatalyst versatile, but the easy aggregation of NPs in solution, reduces surface tension, reactivity, selectivity and recycling property of the catalyst.[10] To prevent aggregation of nanoparticles several methods are generally used, such as capping the NPs with different capping agents[11] or immobilizing the NPs on solid supports.[12] Metal oxide,[13] porous compound,[14] carbon black,[15] polymer,[16] metal organic framework (MOF)[17] and 2D graphene[18] are extremely used as a support for metal nanoparticles. The presence of heteroatoms in grapheme, such as nitrogen as electron donor[19] or boron as electron acceptor,[20] can further modify catalytic property of the 2D grapheme.[21-22] Another 2D material graphitic carbon nitride, create attention due to its higher thermal and chemical stability,[23] and their potential applications in sensing,[24] photocatalytic reaction[25] and different organic transformation.[26] Graphitic carbon nitride,[19] consists of repetitive s-triazine units[20] and consider as a good support material for metal NPs due to presence of large number active binding sites.

The remediation of aromatic nitro compounds is highly important as the aromatic nitro moiety is one the most characteristic of anthropogenic contaminants.[27] Conventional water purification treatment is not effective for the removal of 4-NP due to its high stability and solubility in water. The reduction of 4-NP to 4-AP is one of the the best idea for remediation of nitro compounds, since 4-AP is also a starting material in various industrial synthesis. Recently scientific communities have given lot of attentions to develop catalyst for the reduction of 4-NP to 4-AP.[28-30] There are various synthetic methods for nitro to amine transformation such as molecular hydrogen as hydrogenating agent,[31] and using stoichiometric reducing agent.[32-33] $NaBH_4$ and ammonia borane are the two promising hydrogen storage materials.[34-35] In aqueous medium, hydrolysis of $NaBH_4$ can easily release hydrogen at room temperature whereas ammonia borane releases hydrogen by thermal decomposition (generally at 85° C).[36]Among different hydride materials ammonia borane (AB) is one of the best promising hydrogen storage materials due higher gravimatric hydrogen storage capacity (19.5 wt.%).[37] In aqueous medium, ammonia borane releases hydrogen at 85°

C.[36] So, there is a requirement of catalyst(s) which can liberate the hydrogen from AB in aqueous medium at room temperature.[38-42]

Metal catalyzed carbon–carbon bond formation[43] reaction is one of the most important reaction for the construction of symmetrical and unsymmetrical biaryl moiety in complex molecule such as pharmaceutical reagent and alkaloid.[44] In 1901, F. Ullmann first reported copper catalyzed ullmann reaction for the formation of symmetrical biaryl.[45] High reaction temperature (200 °C) makes this process ineffective for the synthesis of biaryl compound containing thermo sensitive groups.[46] Different metals [47-49] *i.e.* palladium[50-54] (Pd), Nickel (Ni) and gold (Au) etc. have been introduced as homogeneous or heterogeneous catalysts. Recently PdNPs have been used enormously for different types of cross coupling reactions,[55] but there is very few reports on Pd catalysed ullmann reaction.[56] Although there are several reports for palladium catalysed ullmann reaction under heterogeneous condition[57-59] but most of the cases requires some reductive conditions; presence of formate ion (HCO_2^-)[57] or electoreductive conditions[60] or supercritical carbon dioxide (CO_2).[61] This may limited the practical utility of the reaction due to contamination with products.

In this study, we describe a facile preparation of PdNPs embedded on carbon nitride by ultrasonic method without using any external reducing agent. The carbon nitride provides a solid support for stabilizing (1-4 nm size) PdNPs. The Pd@CN_x composite has shown excellent catalytic activity towards the reduction of 4-NP in presence of aqueous $NaBH_4$ solution with fast kinetic as well as good reusability. It reduces 4-NP within 18 sec. The selective reduction of nitro groups in presence of other reducible groups has been performed in aqueous medium using ammonium borane as hydrogenating agent at room temperature. In addition, this catalyst is also equally effective towards ullmann C-C coupling reaction in ethanol medium at 80 ^{o}C with high reusability.

9.3. Experimental Section

Preparation of Pd@CN$_x$ Composite:

First, 5 ml of 1 mg/ml aqueous suspension of g-CN$_x$ was prepared by dispersing required amount of g-CN$_x$ in water by sonication for 10 min. Then 5 ml of 0.028 M aqueous PdCl$_2$ solution was injected in one spell. The resultant suspension was further sonicated by probe sonicator operating at 28 kHz frequency (power 420 watt) for 180 minutes. The initial black suspension gradually turned orange to dark brown, indicating formation of metallic PdNPs. Finally Pd@CN$_x$ composite was separated by centrifugation at 10,000 rpm for 30 minutes followed by washing with de-ionised water and dried in vacuum.

Reduction of 4-nitrophenol by NaBH$_4$ in Water Medium:

In a typical procedure, 4 ml of 0.1 mM aqueous freshly prepared 4-nitrophenol (4-NP) was taken in a glass vial and then 1 ml of 0.3 M freshly prepared aqueous NaBH$_4$ solution was injected into 4-NP solution. After that 3 mg of Pd@CN$_x$ was immediately added to 4-NP solution and progress of the reaction was monitor by measuring the absorbance spectra of the solution with time using the UV-vis spectrophotometer. The reaction kinetics of 4-NP reduction was monitored by observing the decrease of absorbance at 400 nm.

Selective Nitro Group Reduction by AB in Water at Room Temperature:

Nitro compounds **1a-l** (1mmol, 1 equiv.), ammonium borane (3 mmol, 3 equiv.), were taken in a 10 ml reaction vial, 3 ml water was added and stirred for 10 minutes at room temperature. Then Pd@CN$_x$ (4mg) catalyst was injected into solution mixture and closed the vial. The reaction was continued with vigorous stirring up to complication time (9-30 min). The reaction was monitored by thin layered chromatography (TLC) using hexane/ethyl acetated as eluting. After completion of the reaction, catalyst was directly removed by centrifugation with 16,000 rpm for 10 min. After that NH_4Cl was added to supernatant to neutralise the solution. The organic phase was extracted by using 3x10 ml ethyl acetated. The combined organic phase was dried over anhydrous Na_2SO_4. After that reaction mixture was evaporated under reduced pressure and residue was purified by column chromatography technique using hexane/ethyl acetated as eluting. The products was characterized by ^{1}H-NMR and ^{13}C-NMR.

Ullmann Coupling Reaction by Pd@CN$_x$ in Ethanol Solution:

In typical procedure, an oven dried two neck round bottom (rb) flask fitted with condenser was charged with aryl halide, **3a-n** (1 mmol,1 equiv.), potassium carbonate (1.5 mmol, 1.5 equiv., 207 mg) in ethanol and Pd@CN$_x$ catalyst (5 mg) was added to solution mixture. The resultant reaction mixture was allowed to stire at 80 ^{o}C. The reaction was monitored by thin layered chromatography (TLC) using hexane/ethyl acetated as eluting. After the completion of the reaction, mixture was cooled to room temperature and catalyst was separated by centrifugation at 16,000 rpm for 10 min. The organic phase was extracted by using 3x10 ml dichloromethane. The combined organic phase was dried over anhydrous Na_2SO_4. The combined organic phase was evaporated under reduced pressure and residue was purified by Silica gel column chromatography using hexane and ethyl acetate as eluting to get pure homocoupling products. The products were characterised by ^{1}H-NMR, ^{13}C-NMR .

9.4. Results and Discussion

The carbon nitride supported PdNPs were prepared by two steps: First, graphitic carbon nitride was obtained by microwave heating[62] of formamide ($HCONH_2$) at 180 °C (details in experimental section); second, PdNPs were synthesized on the surface of carbon nitride by ultrasonication of aqueous solution containing g-carbon nitride and Pd^{2+} ions. The UV-Vis absorption spectra of aqueous palladium chloride ($PdCl_2$) solution showed peaks at 305 nm and 420 nm (**Figure 9.1.a**) due to metal to ligand charge transfer.

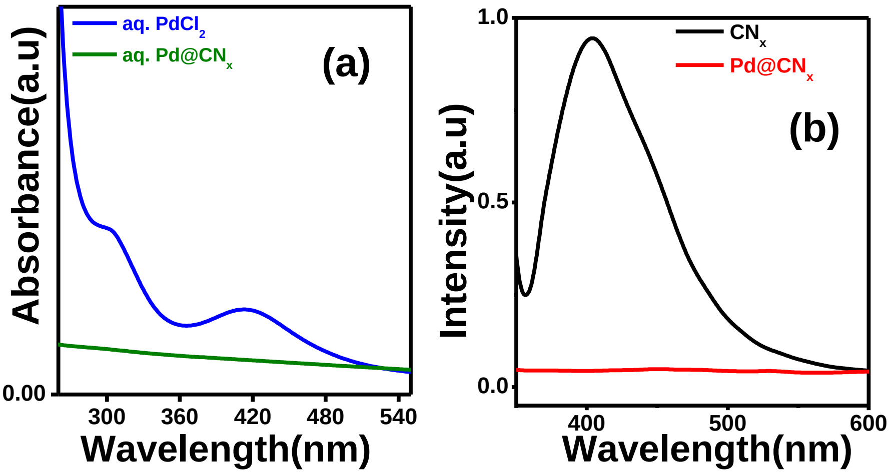

Figure 9.1. (a) UV-vis absorbance spectra of $PdCl_2$ and $Pd@CN_x$ water. (b) Comparison of fluorescence spectra of g-CN_x and $Pd@CN_x$ composite. Excitation wavelength is 340 nm.

But the peaks were disappeared after ultasonication of $PdCl_2$ in presence of aqueous dispersion of carbon nitride indicating the strong interaction between g-C_3N_4 moieties and Pd (**Figure 9.1.a**).[63] In addition, the strong fluorescence emission of aqueous dispersion of carbon nitride was quenched gradually upon the addition of aqueous Pd^{+2} solution and completely disappeared after ultrasonication indicating strong interaction between g-C_3N_4, Pd^{+2} ions and after ultrasonication Pd was loaded on g-C_3N_4 moiety (**Figure 9.1.b**). Formation of PdNPs was further confirmed by powder x-ray diffraction pattern (pXRD) and XPS analysis. **Figure 9.2.a** shows the powder x-ray diffraction pattern of g-C_3N_4 and Pd@CN_x composite. Both the curve has a common diffraction peak at 2θ value of 27.2^0 with interlayer spacing of 3.3 Å corresponds to (002) reflection plane of carbon nitride.[62] In addition, Pd@CN_x composite has extra diffraction peaks at 40.1^0, 46.7^0, 68.7^0, 80.9^0, 86.7^0 correspond to the (111), (200), (220), (311), (222) planes respectively of face centred cubic palladium (PDF No #00-046-1043).

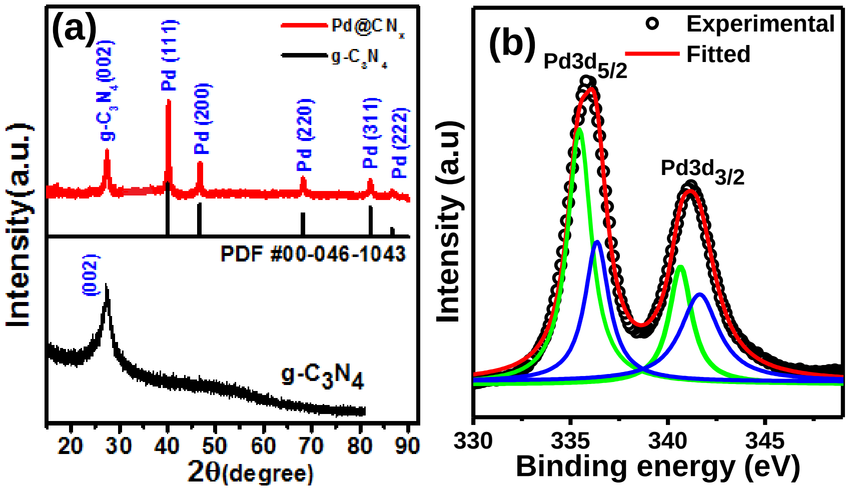

Figure 9.2. (a) XRD pattern of Pd@CN_x. composite. (b) XPS spectra of palladium 3d orbitals.

These clearly suggest the formation of PdNPs on carbon nitride after ultrasound treatment. The Fourier transform infrared (FT-IR) spectra of carbon nitride and Pd@CN_x composite have shown in **Figure 9.3**.

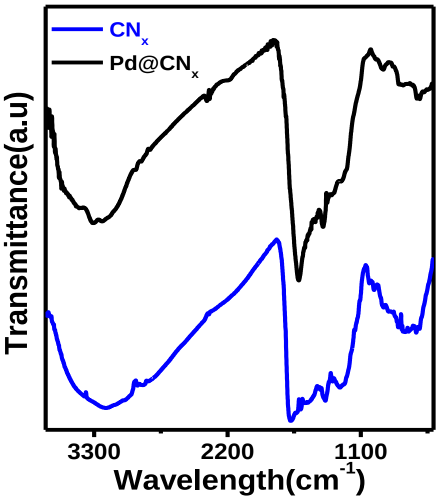

Figure. 9.3. Comparison of FT-IR spectra of g-CN_x and Pd@CN_x.

Both the spectra showed four strong bands between 1213 to 1408 cm^{-1} assigned to secondary (2C-N) and tertiary (3C-N) amine fragment. In addition to peak at 1600 cm^{-1} correspond to C=N stretch frequency associated s-triazine unit. The FT-IR spectra of carbon nitride and Pd@CN$_x$ composite suggest that carbon nitride framework remains unaltered after loading of PdNPs. The X-ray Photo Electron Spectroscopy (XPS) was performed to characterize the Pd@CN$_x$ composite. The 3d XPS spectra of palladium always appeared as doublet (3d$_{5/2}$ and 3d$_{3/2}$) due to spin-orbital coupling.[64-65] It is reported in literature[57, 66-67] by several groups that 3d5/2 and 3d3/2 peaks of Pd(0) generally appeared at ~335.3 eV and 340.7 eV respectively. The Pd 3d XPS spectra of Pd@CN$_x$ composite was consisted of two asymmetric, assigned as 3d$_{5/2}$ (lower eV) and 3d$_{3/2}$ (higher eV) as shown in **Figure 9.2.b**. The 3d core spectra were deconvoluted into two doublets for two species. The peaks at 335.5 eV and 340.7 eV corresponds to the metallic Pd(0) state which is good agreement with the literature. Another pair of peak located at 336.6 and 341.8 eV corresponds to the Pd(II) species. In addition also calculated contribution for Pd(0) is 62% which is the major phase in Pd@CN$_x$ composite. The de-convoluted carbon, nitrogen 1s XPS spectra of graphitic carbon nitride was shown in **Figure 9.4**.(**a,b**) for comparison.

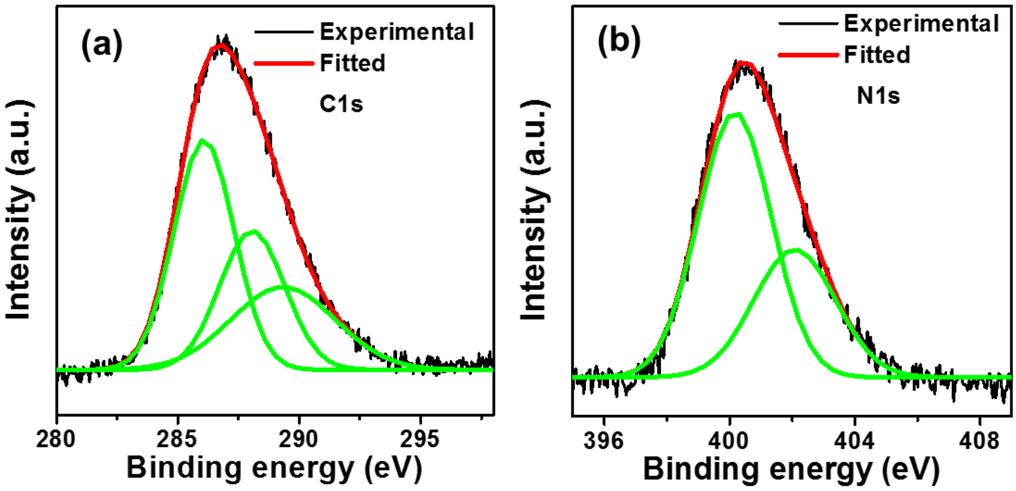

Figure. 9.4. Deconvulated XPS spectra of (a) C 1s and (b) N 1s of carbon nitride

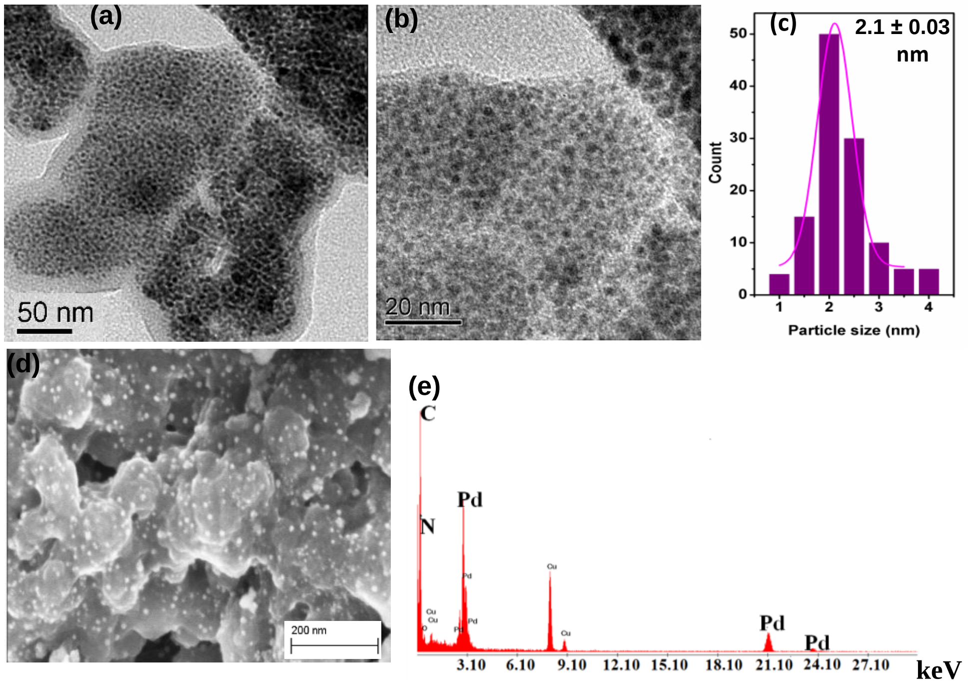

Figure 9.5. (a,b) TEM images of Pd@CN$_x$ catalyst are showing the formation of PdNPs on carbon nitride. (c) Particle size distribution of Pd@CN$_x$ catalyst calculated from Figure (b). (d) FESEM image of Pd@CN$_x$ composite. (e) EDX spectra of highly dispersed PdNPs on carbon nitride taken from Figure (a).

The morphology of the g-C$_3$N$_4$ and Pd@CN$_x$ composite was established by TEM analysis. The TEM images of PdNPs on carbon nitride surface are shown in **Figure 9.5.(a,b)**. It shows that PdNPs are uniformly distributed on carbon nitride sheet. The size distribution of PdNPs is given in Figure 9.3 c showing that that their size varies from 1 nm to 4 nm and their average size is ~2 nm with standard deviation of 0.03 nm from the Gaussian fitting. **Figure 9.5.d** displays the FESEM image of Pd@CN$_x$ composite which further reveals the formation of 2-5 nm spherical PdNPs on carbon nitride sheets. The EDS spectrum of Pd@CN$_x$ composite (**Figure 9.5.e**), taken from the image of **Figure 9.5.a**, shows the presence of carbon, nitrogen and Pd confirming the deposition of PdNPs on carbon nitride sheets. In addition; EDX spectra were used to measure the total loading of Pd in Pd@CN$_x$ composite. The result shows that Pd@CN$_x$ composite contains ~ 31 wt% Pd. The TEM image of g-C$_3$N$_4$ was shown in **Figure 9.6.** which clearly displayed 2D sheet like morphology.

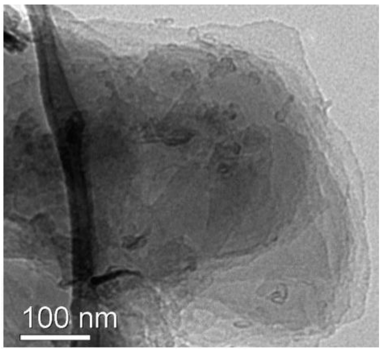

Figure 9.6. TEM image of graphitic carbon nitride.

The TGA comparison curve of g-C_3N_4 and Pd@CN_x composite was shown in **Figure 9.7** and the Pd loading calculated from TGA was 31.2 wt%. The exact loading of PdNPs in Pd@CN_x composite was measured by inductively coupled plasma optical emission spectrometry (ICP-OES) and calculated Pd loading is found to be 30.7 wt% in the composite. The EDS and TGA results were in good agreement with ICP-OES data.

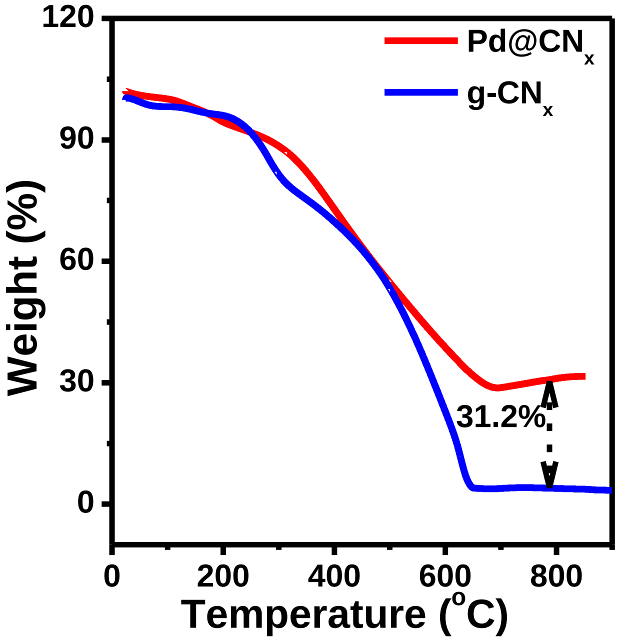

Figure 9.7. TGA curve of g-CN_x and Pd@CN_x composite.

The catalytic activity of freshly prepared Pd@CN_x composite was evaluated by 4-NP reduction with an aqueous solution of $NaBH_4$. The reduction of 4-NP to 4-AP was monitored by observing the change of UV-Vis absorption spectra as well as the colour change of the reaction mixture in the presence of Pd@CN$_x$. Freshly prepared 4-NP solution has absorption peak centred at 316 nm (**Figure 9.8.a**) whereas upon addition of aqueous NaBH$_4$ solution the peak immediately red-shifted to 400 nm (**Figure 9.8.a**) due to the formation of 4-nitrophenolate ions in basic condition.[28, 68]

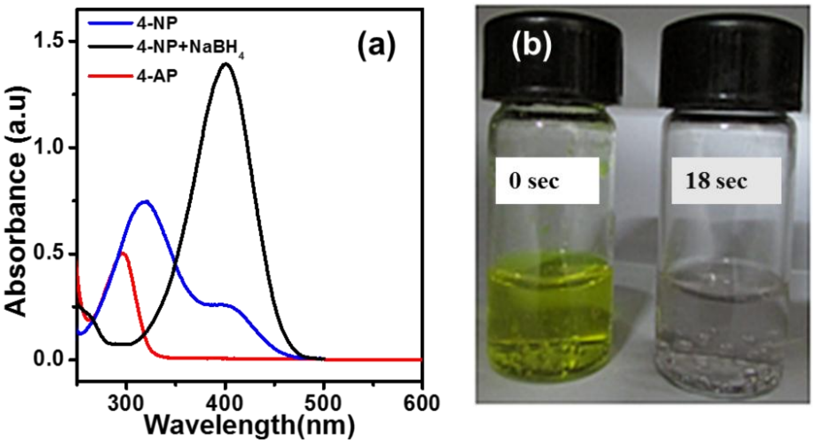

Figure. 9.8 (a) UV-vis spectra of aqueous solution of 4-NP (blue) where brown curve is UV-vis spectrum of NaBH$_4$ containing 4-NP in absence of Pd@CN$_x$ composite and red curve represents 4-AP. (b) The colour changes due to transformation of 4-NP to 4-AP.

When Pd@CN$_x$ composite was added to the reaction mixture, the yellow colour immediately faded and ultimately bleached within 18 sec and a new absorption peak centered at 298 nm was appeared which indicates the formation of 4-AP. The colour of the initial and final solution was shown in **Figure 9.8.b**.

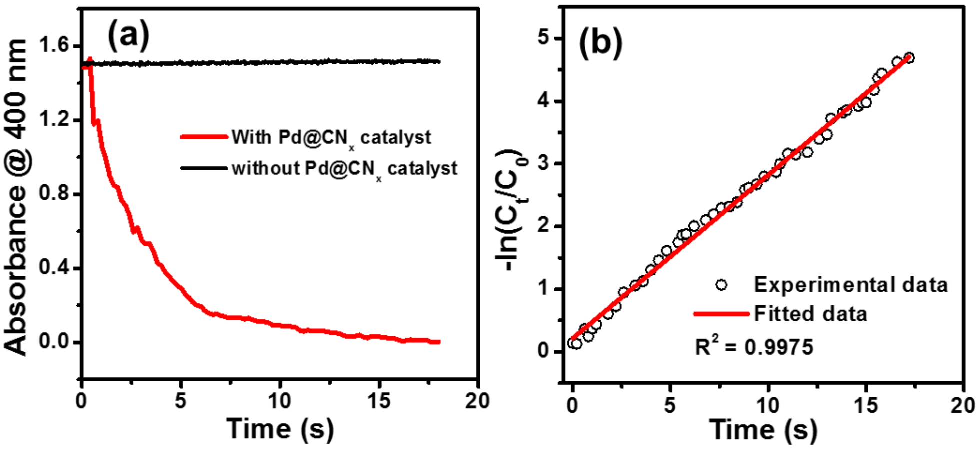

Figure. 9.9. (a) Change of absorbance at 400 nm of (4NP +NaBH$_4$) solution with time in presence and absence of Pd@CN$_x$ catalyst. (b) Linear plots of –ln(C$_t$/C$_0$) vs time of Pd@CN$_x$ catalyst.

Although recently Xu and his co-workers reported bimetallic Au-Pt and Au-Pd system, which took 12 sec for 100% reduction of 4-NP but in case of monometallic AuNPs time increases to 80 sec.[69] The Pd@CN$_x$ composite has displayed better catalytic activity than other monometallic NPs systems. Due to the presence of excess NaBH$_4$, it has been assumed that the 4-NP reduction reaction kinetic is independent of NaBH$_4$ and follows the pseudo first order kinetics. The pseudo first order kinetics was applied to determine the 4-NP reduction kinetics on Pd@CN$_x$ composite. **Figure 9.9.a** shows the change of absorption at 400 nm in presence of Pd@CN$_x$ catalyst. ln(C$_t$/C$_o$) versus reaction time (sec) plot for 4-NP reduction on Pd@CN$_x$ composite also shown in **Figure 9.9.b**, where C$_0$ and C$_t$ is initial and different time interval concentration of 4-NP. The rate constant (K) value of 4-NP reduction was 0.38 s^{-1} which calculated from the slope of ln(C$_t$/C$_o$) vs time plot (**Figure 9.9.b**). Furthermore the intrinsic activity parameters (κ) of the catalyst, defined as K/m where m is either total mass of catalyst or total mass of PdNPs was calculated. The intrinsic activity parameter (κ) of Pd@CN$_x$ composite were 12.7 s^{-1} g$_{cat}^{-1}$ and 31.6 s^{-1} g$_{Pd}^{-1}$.In addition we have calculated the turn over frequency (TOF) of Pd@CN$_x$ catalyst (Details calculation in ESI).

Table 9.1. Comparison studies of 4-NP reduction with NaBH$_4$ in presence of different palladium nanoparticle based catalytic systems.

Catalyst	**Amount of catal. (mg)**	**Amount of 4-NP (mmol)**	**Amount of NaBH$_4$ (mmol)**	**Conv. time (s)**	**Ref.**
Pd@CN$_x$	3	4x10^{-4}	3x10^{-2}	18	**This work**
Porous Au-Pd	-	5x10^{-4}	2x10^{-2}	12	69
Pd/CNTs	-	1x10^{-4}	5x10^{-2}	420	70
RGO@Pd@C	5	3x10^{-4}	3x10^{-2}	30	71
Pd-mpg C$_3$N$_4$	5	3x10^{-4}	3x10^{-1}	300	28
Pd–rGO-CNT	5	3x10^{-4}	3x10^{-2}	20	72

The calculated TOF value of Pd-CN$_x$ catalyst for reduction of 4-NP with NaBH$_4$ is 9.8 h^{-1} .Table 9.1 describes a compression of different condition for 4-NP reduction with existing literature. The reduction rate with Pd@CN$_x$ composite was comparable and also for some cases it is even better than other reported PdNPs based catalytic systems such as porous Au-Pd,[69] Pd/CNTs,[70] RGO@Pd@C,[71] Pd-mpg C_3N_4,[28] Pd-rGO-CNT.[73] The better catalytic activity of Pd@CN$_x$ catalyst for 4-NP reduction is probably due to the facile adsorption of acceptor molecule (4-NP) on the carbon nitride surface as well as fast electron transfer from donor molecule BH_4^- to 4-NP. The catalytic stability and durability was one of the important properties of the catalyst for the liquid phase reaction. The catalyst was recovered from solution for next cycle by direct centrifugation of the solution and wash with water. Herein we have evaluated the stability and durability of the catalyst under same reaction conditions. **Figure 9.10.a** reveals the conversion time of 4-NP to 4-AP vs. cycle numbers. The catalyst has been reused up to six cycles with slight increment of the reaction time. The characterization of the six times reused Pd@CN$_x$ catalyst was performed by investigating of TEM analysis as shown in **Figure 9.10.b**.

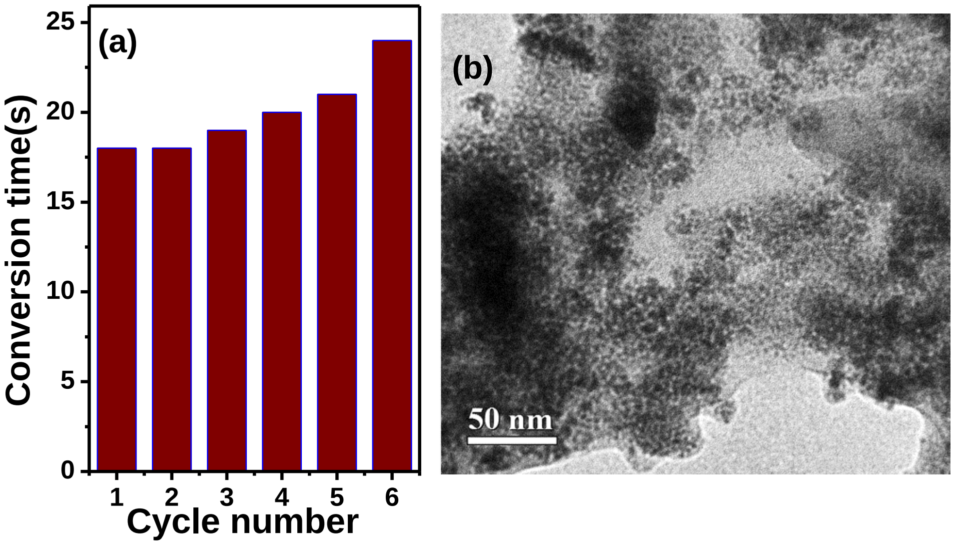

Figure 9.10. (a) Recycling profile of Pd@CN$_x$ catalyst for 4-NP reduction reaction in water medium with AB which shows catalyst was highly active upto six cycles.(b) TEM images of six times reused Pd@CN$_x$ catalyst.

The TEM image clearly shows that small PdNPs (1-4 nm) are decorated on g-carbon nitride sheet with presence of few slight larger PdNPs (3-6 nm). The ICP-OES analysis of reaction solution further confirmed that only 2.4 % Pd was leached after six cycle. The TEM and ICP-OES analysis thus demonstrated the superior catalytic with high stability of the Pd@CN_x catalyst.

Selective reduction of nitro group in presence of other reducible groups in aqueous medium was important pathway in synthetic chemistry for producing functional amino groups[74-78]. We have explored the catalyst for selective nitro reduction with different hydride donor. The details study of 4-nitroobenzonitrile reduction with different hydride donor is summarized in **Table 9.2**. In typical reaction, 4-Nitrobenzonitrile (**1l**) was reduced by $NaBH_4$ in aqueous medium with 91% yields (**Table. 9.2**). Whereas in water-methanol and water-ethanol yields was slightly decreased due to fast hydrolysis of $NaBH_4$ in aqueous medium in presence of PdNPs.

Table 9.2. Comparison of 4-Nitrobenzonitrile reduction with different hydride sources.

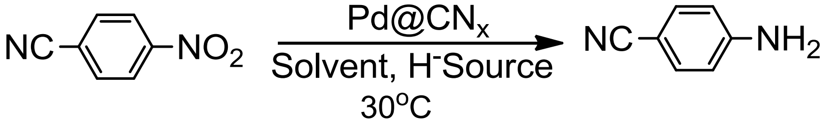

Entry	Hydride source	Solvent	Time(min)	Yields(%)[a]
1	$NaBH_4$	H_2O	7	91
2	$NaBH_4$	H_2O:EtOH	9	84
3	$NaBH_4$	H_2O:MeOH	10	87
4	H_3B-NH_3	H_2O	10	99
5	H_3B-NH_3	H_2O:EtOH	15	83
6	H_3B-NH_3	H_2O:MeOH	10	88

Reaction condition: 4-Nitrobenzonitrile (1 mmol), hydride (3 equiv.), solvents (3 ml),Catalyst (4 mg), [a] isolated yields.

The Pd@CN$_x$ catalyst was equally effective for selective reduction of nitro groups using both NaBH$_4$ and AB as the reducing agent but we have reported the selective reduction of nitro groups in aqueous medium using AB as hydride donor[79] due to its less toxicity and high volume/mass hydrogen density than NaBH$_4$. In **Table 9.2** represent the optimization for selective reduction of nitro group. Nitro compound (1 mmol), H$_3$B-NH$_3$ (3 equiv.), Pd@CN$_x$ (4 mg), H$_2$O (3 ml) at room temperature give the best result. The selective nitro group reduction with Pd@CN$_x$ catalyst was summarized in **Table 9.3.** Nitrobenzene (**1a**) was easily reduced to aniline (2a) with 88% yield. Amino benzene with electron donating group at para position (2b, 2c, 2e), ortho position (2d) as well as meat position (2f) was obtained with good yield. The nitrobenzene containing halogen group also easily and selectively reduced to halo amine (2g, 2h) with moderate TOF values.

Table 9.3. Selective nitro groups reduction of different nitro arenes with Pd@CN$_x$ catalyst

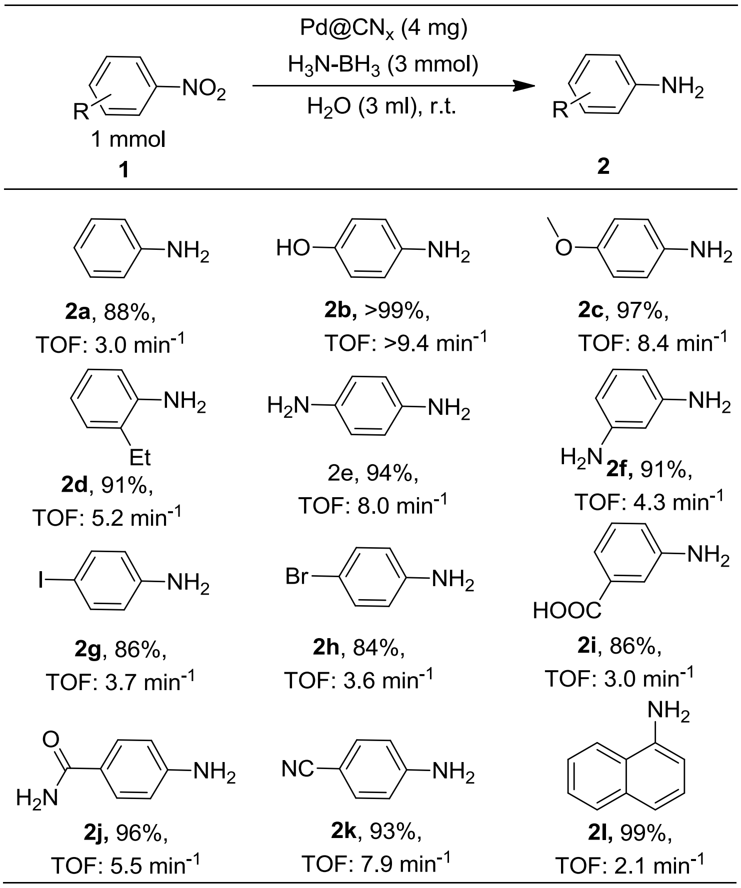

Furthermore amino benzene containing electron withdrawing group (2i, 2j, 2k) also obtained efficiently with excellent yields. The reaction was also extended to 1-Nitronapthalene in order to obtained desired product (2l) with TOF value 2.1 min^{-1}.

The moderate yields for few amine compounds might be justified by the possibility of formation of trace amount of azoxy compounds or dehaloganated amine (halogen containing reactant).So, **Table 9.3** demonstrates that Pd@CN$_x$ catalyst can reduce nitro group selectively in presence of other reducible functional groups like –OH, -OMe, halogens, -COOH, -CONH$_2$, -CN with good TOF values (2.1 to 9.4 min^{-1}) in aqueous medium. There are few reports for selective reduction of nitro groups with hydride donor but in all cases long time and higher equivalent hydride donor is required in order to obtained good yields[80]. Recently, S. Sun and his co-workers reported reduction of nitro group with using AB.[81] So our catalyst is highly effective for nitro group reduction in aqueous medium at room temperature. The catalytic stability and durability was one of the important properties of the catalyst for the liquid phase reaction. Catalyst was recovered from solution for next cycle by direct centrifugation of solution and wash with water. Herein we examined the stability and durability of the catalyst under same reaction conditions with 4-NP.

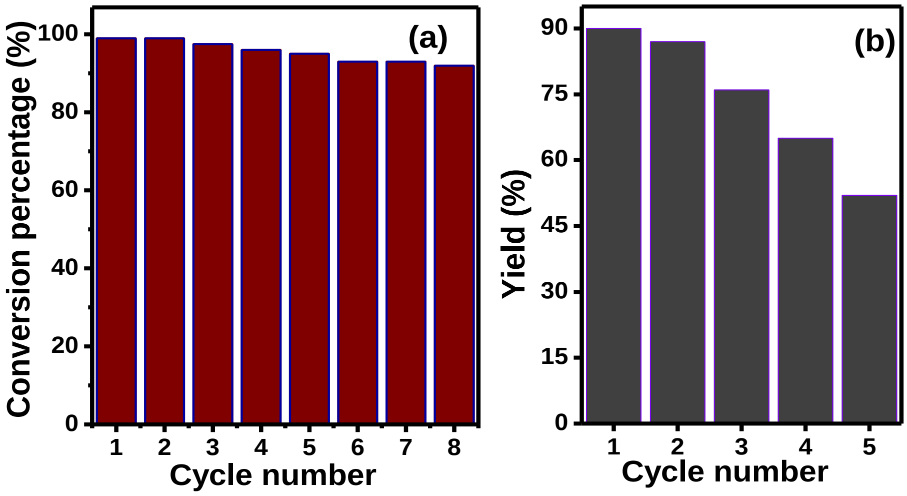

Figure 9.11. Recycling profile of Pd@CN$_x$ catalyst for (a) Nitro reduction with AB and (b) ullmann coupling reaction in ethanol.

Figure 9.11.a shows the recycling profile of 4-NP reduction with AB in aqueous medium. The catalyst has high stability with good yields after six cycles (**Figure 9.11.b**).

We have also investigated the catalytic property of prepared Pd@CN_x by monitoring the ullmann homocoupling reaction of 4-methoxybromobenzene (1 mmol) **(3i)** in ethanol medium using Na_2CO_3 (1.5 equiv) as base at 80 ^{0}C under air, we got moderate yield of the desired coupling product 4,4-dimethoxybyphenyl (4i) with high selectivity. This result encouraged us to validate the efficiency of the catalyst. For optimized the reaction condition we have screened several conditions which are summarized in **Table 9.4.** As the support material has no catalytic activity towards the ullmann coupling reaction under the same reaction conditions (**Table 9.4**, entry 1), so the well dispersed PdNPs actually provided the active site for ullmann reaction. In the absence of base no desired products were obtained (**Table 9.4**, entry 2); concluded the crucial role of base in coupling reaction. After that, we monitored the reaction with different bases (**Table 9.4**). Reaction was smoothly occurred under inorganic carbonate bases (**Table.9.4**, entries 3 to 6). At the same time organic bases such as NaOEt, NEt_3 also gave moderate yield of the corresponding products (**Table 9.4**, entries 8 and 9). But in case of K_3PO_4 yield of the product was drastically reduced to 35% (**Table 9.4**, entry 7). From the several screening, best result was obtained by using K_2CO_3 (1.5 equiv) as base (**Table 9.4**, entry 5). There was no distinguishable change of yields under nitrogen atmosphere which clearly indicated the feasible nature of the reaction under aerobic condition. Halo-benzene (1 mmol), K_2CO_3 (1.5 mmol), EtOH (5 ml), Pd@CN_x (5 mg) at 80 ^oC reaction condition give the best yield of biphenyl product. Having optimized reaction condition, the broad applicability of Pd@CN_x was illustrated by extending the protocol for different substituted haloarenes which were summarized in **Table 9.5**.

Table 9.4. Optimization of ullmann coupling reaction of 4-bromoanisole.

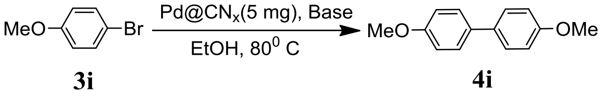

Entry	Catalyst	Base	Time(h)	Yield[a](%)
1	CN_x	K_2CO_3	24	0
2	Pd@CN_x	-	24	0
3	Pd@CN_x	Na_2CO_3	8	70
4	Pd@CN_x	Cs_2CO_3	8	64
5	Pd@CN_x	K_2CO_3	8	93
6	Pd@CN_x	$NaHCO_3$	8	67
7	Pd@CN_x	K_3PO_4	8	35
8	Pd@CN_x	NaOEt	8	52
9	Pd@CN_x	NEt_3	8	24
10[b]	Pd@CN_x	K_2CO_3	8	91

Reaction condition: 4-methoxybromobenzene (1 mmol), base (1.5 mmol), ethanol (5 ml), catalyst (5 mg). [a]Isolated yield . [b]N_2 atmosphere .

This catalytic system was broadly applicable for iodo, bromo and chlorobenzene systems to obtain desired biphenyl products (4a, 4b, 4c). The Haloarens with electron donating group (4d, 4e) at para and also meta position (4f, 4g) were coupled easily to give desired biaryl products with excellent yields. In the case of different flouro and chloro substituted iodoaren, selectively coupled occurred from more reactive iodo sides to form corresponding products (4h, 4i, 4j). The electron withdrawing groups (-CN, -CHO) at para position were also equally activated towards the coupling reaction to give desired biaryl products (4k, 4l). The catalytic system was not only effective for benzene moiety but also extended for napthyl and heterocylic moiety effectively. The 2-bromonapthalene gave corresponding coupled product (4m) with good yield in 24 hours. There were very few studies on the homo coupling of heterohaloarene due to its inertness.[58] In addition, 2-bromopyridin formed 2,2'-bipyridine (4n) with 54% yield in 24 hours. So this catalytic system was equally applicable for a broad range of substrates with high yield and selectivity. The most important properties of the heterogeneous catalysts in liquid phase reaction were its stability and reusability. Here in we recycled the catalyst for the reaction of 4-iodotoluene in ethanol solution (**Figure 9.11.b**). The catalysed was reused up to five cycles with slight decrease of yields of desired product. Catalyst was separated from the reaction mixture by direct centrifugation of the solution followed by washed with ethanol and dried at 80 ^{0}C for overnight.

Table 9.5. Ullmann coupling reaction of different aryl halides with Pd@CN$_x$.

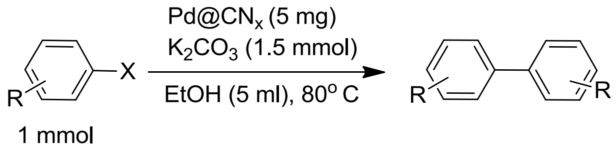

3

4

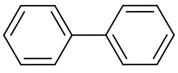

4a, X=I, 8 h, 93%
4b, X=Br, 8 h, 95%
4c, X=Cl, 8 h, 71%

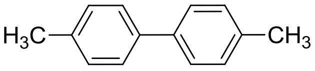

4d, X=I, 8 h, 96%

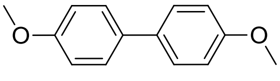

4e, X=I, 8 h, 90%

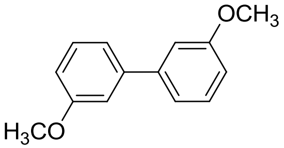

4f, X=Br, 8 h, 89%

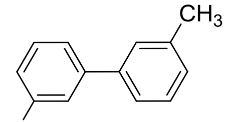

4g, X=Br, 8 h, 88%

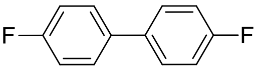

4h, X=I, 8 h, 95%

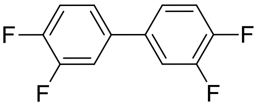

4i, X=I, 8 h, 94%

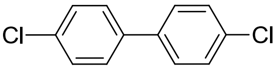

4j, X=I, 8 h, 86%

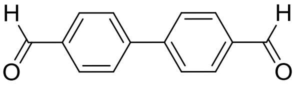

4k, X=Br, 8 h, 81%

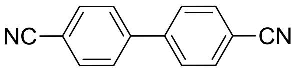

4l, X=Br, 8 h, 74%

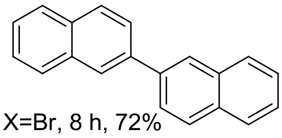

4m, X=Br, 8 h, 72%

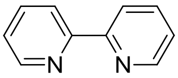

4n, X=Br, 8 h, 54%

9.5. Conclusions

In conclusion, we have successfully demonstrated a green facile approach to synthesize 1-4 nm sized PdNPs immobilized in carbon nitride by ultrasonic methods without using any reducing agents. Due to small particle size, catalyst is highly active towards the dehydrogenation of $NaBH_4$ and AB in aqueous medium. It also hydrogenated the different nitro groups with high good TOF values (9.4 to 2.1 min^{-1}). In addition the Pd@CN_x catalyst is highly active towards ethanol mediated ullmann coupling reaction to synthesize the biaryl compound at 80^0C with a broad range of substrate scope. This catalyst shows satisfactory yield of biaryl product up to five cycles with less leaching of PdNPs.

9.6. References

1. Fihri, A.; Bouhrara, M.; Nekoueishahraki, B.; Basset, J.-M.; Polshettiwar, V., *Chem.Soc.Rev.* **2011,** *40,* 5181-5203.
2. Polshettiwar, V.; Varma, R. S., *Green Chem.* **2010,** *12,* 743-754.
3. Saha, K.; Agasti, S. S.; Kim, C.; Li, X.; Rotello, V. M., *Chem. Rev.* **2012,** *112,* 2739-79.
4. Zhang, N.; Fu, X.; Xu, Y.-J., *J. Mater. Chem.* **2011,** *21,* 8152-8158.
5. Debe, M. K., *Nature* **2012,** *486,* 43-51.
6. Bhowmik, T.; Kundu, M. K.; Barman, S., *ACS Catal.* **2016,** *6,* 1929-1941.
7. Lim, B.; Jiang, M.; Camargo, P. H.; Cho, E. C.; Tao, J.; Lu, X.; Zhu, Y.; Xia, Y., *Science* **2009,** *324,* 1302-5.
8. Burda, C.; Chen, X.; Narayanan, R.; El-Sayed, M. A., *Chem. Rev.* **2005,** *105,* 1025-1102.
9. Hua, Q.; Cao, T.; Gu, X. K.; Lu, J.; Jiang, Z.; Pan, X.; Luo, L.; Li, W. X.; Huang, W., *Angew.Chem.Int.Ed.* **2014,** *53,* 4856-61.
10. Narayanan, R.; El-Sayed, M. A., *J. Am. Chem. Soc.* **2003,** *125,* 8340-8347.
11. Mazumder, V.; Sun, S., *J. Am. Chem. Soc.* **2009,** *131,* 4588-4589.
12. Campelo, J. M.; Luna, D.; Luque, R.; Marinas, J. M.; Romero, A. A., *ChemSusChem* **2009,** *2,* 18-45.

13. Abad, A.; Concepción, P.; Corma, A.; García, H., *Angew. Chem. Int. Ed.* **2005,** *44,* 4066-4069.

14. Han, P.; Wang, X.; Qiu, X.; Ji, X.; Gao, L., *J. Mol. Catal. A: Chem.* **2007,** *272,* 136-141.

15. Zhou, Z. Y.; Huang, Z. Z.; Chen, D. J.; Wang, Q.; Tian, N.; Sun, S. G., *Angew.Chem.Int.Ed.* **2010,** *49,* 411-4.

16. Gallon, B. J.; Kojima, R. W.; Kaner, R. B.; Diaconescu, P. L., *Angew.Chem.Int.Ed.* **2007,** *46,* 7251-4.

17. Pan, Y.; Yuan, B.; Li, Y.; He, D., *Chem. Commun.* **2010,** *46,* 2280-2.

18. Yu, C.; Fu, J.; Muzzio, M.; Shen, T.; Su, D.; Zhu, J.; Sun, S., *Chem. Mater.* **2017,** *29,* 1413-1418.

19. Algara-Siller, G.; Severin, N.; Chong, S. Y.; Björkman, T.; Palgrave, R. G.; Laybourn, A.; Antonietti, M.; Khimyak, Y. Z.; Krasheninnikov, A. V.; Rabe, J. P.; Kaiser, U.; Cooper, A. I.; Thomas, A.; Bojdys, M. J., *Angew.Chem.Int.Ed.* **2014,** *53,* 7450-7455.

20. kumar, N.; Moses, K.; Pramoda, K.; Shirodkar, S. N.; Mishra, A. K.; Waghmare, U. V.; Sundaresan, A.; Rao, C. N. R., *J. Mater. Chem. A* **2013,** *1,* 5806-5826.

21. Geim, A. K., *Science* **2009,** *324,* 1530-1534.

22. Scheuermann, G. M.; Rumi, L., Steurer,P,; Bannwarth, W.; Mulhaupt, R., *J. Am. Chem. Soc.* **2009,** *131,* 8262–8270.

23. Gillan, E. G., *Chem. Mater.* **2000,** *12,* 3906-3912.

24. Sadhukhan, M.; Barman, S., *J. Mater. Chem. A* **2013,** *1,* 2752-2756.

25. Wang, X.; Maeda, K.; Thomas, A.; Takanabe, K.; Xin, G.; Carlsson, J. M.; Domen, K.; Antonietti, M., *Nat. Mater.* **2009,** *8,* 76-80.

26. Wang, Y.; Wang, X.; Antonietti, M., *Angew. Chem. Int. Ed.* **2012,** *51,* 68-89.

27. Lai, T.-L.; Yong, K.-F.; Yu, J.-W.; Chen, J.-H.; Shu, Y.-Y.; Wang, C.-B., *J. Hazard. Mater.* **2011,** *185,* 366-372.

28. Li, X.-H.; Wang, X.; Antonietti, M., *Chem. Sci.* **2012,** *3,* 2170-2174.

29. Pradhan, N.; Pal, A.; Pal, T., *Colloids Surf., A: Physicochem. Eng. Aspects* **2002,** *196,* 247-257.

30. Ye, W.; Yu, J.; Zhou, Y.; Gao, D.; Wang, D.; Wang, C.; Xue, D., *Appl. Catal. B: Environ.* **2016,** *181,* 371-378.

31. Corma, A.; Serna, P.; Concepcion, P.; Calvino, J. J., *J. Am. Chem. Soc.* **2008,** *130,* 8748-53.

32. Saha, A.; Ranu, B., *J. Org. Chem.* **2008,** *73,* 6867-6870.

33. Rahaim, R. J.; Maleczka, R. E., *Org. Lett.* **2005,** *7,* 5087-5090.

34. Rossin, A.; Peruzzini, M., *Chem. Rev.* **2016,** *116,* 8848-8872.

35. Zhan, W.-W.; Zhu, Q.-L.; Xu, Q., *ACS Catal.* **2016,** *6,* 6892-6905.

36. Demirci, U. B.; Miele, P., *Eneregy Environ. Sci.* **2009,** *2,* 627-637.

37. Kılıç, B.; Şencanlı, S.; Metin, Ö., *J. Mol. Catal. A: Chem* **2012,** *361–362,* 104-110.

38. Akbayrak, S.; Kaya, M.; Volkan, M.; Özkar, S., *Appl. Catal B: Environ.* **2014,** *147,* 387-393.

39. Gulcan, M.; Zahmakiran, M.; Özkar, S., *Appl. Catal B: Environ.* **2014,** *147,* 394-401.

40. Tonbul, Y.; Akbayrak, S.; Özkar, S., *Int. J. Hydrogen Energy* **2016,** *41,* 11154-11162.

41. Zhou, Q.; Xu, C., *Chem. Asian J.* **2016,** *11,* 705-712.

42. Ma, X.; Zhou, Y. X.; Liu, H.; Li, Y.; Jiang, H. L., *Chem. Commun.* **2016,** *52,* 7719-22.

43. Astruc, D.; Lu, F.; Aranzaes, J. R., *Angew. Chem. Int. Ed.* **2005,** *44,* 7852-7872.

44. Bringmann, G.; Walter, R.; Weirich, R., *Angew. Chem. Inl. Ed. Engl.* **1990,** *29,* 977-991.

45. Ullmann, F.; Bielecki, J., *Ber. dtsch. chem. Ges.* **1901,** *34*, 2174-2185.

46. Fanta, P. E., *Chem. rev.* **1964,** *64,* 613.

47. Nelson, T. D.; Crouch, R. D., Cu, Ni, and Pd Mediated Homocoupling Reactions in Biaryl Syntheses: The Ullmann Reaction. In *Organic Reactions*, John Wiley & Sons, Inc.: **2004**.

48. Karimi, B.; Esfahani, F. K., *Chem. Commun.* **2011,** *47,* 10452-4.

49. Calò, V.; Nacci, A.; Monopoli, A.; Cotugno, P., *Chem. Eur. J.* **2009,** *15,* 1272-1279.

50. Quan, P. B. P. M., *Synthesis* **1978,** *1978,* 537-538.

51. Venkatraman, S.; Li, C.-J., *Org. Lett.* **1999,** *1,* 1133-1135.

52. Mukhopadhyay, S.; Rothenberg, G.; Joshi, A.; Baidossi, M.; Sasson, Y., *Adv. Synth. Catal.* **2002,** *344,* 348-354.

53. Mukhopadhyay, S.; Rothenberg, G.; Gitis, D.; Sasson, Y., *Org. Lett.* **2000,** *2,* 211-214.

54. Mukhopadhyay, S.; Yaghmur, A.; Baidossi, M.; Kundu, B.; Sasson, Y., *Org. Process Res. Dev.* **2003,** *7,* 641-643.

55. Molnár, Á., *Chem. Rev.* **2011,** *111,* 2251-2320.

56. Dhital, R. N.; Kamonsatikul, C.; Somsook, E.; Bobuatong, K.; Ehara, M.; Karanjit, S.; Sakurai, H., *J. Am. Chem. Soc.* **2012,** *134,* 20250-3.

57. Li, H.; Chen, J.; Wan, Y.; Chai, W.; Zhang, F.; Lu, Y., *Green Chem.* **2007,** *9,* 273-280.

58. Karimi, B.; Behzadnia, H.; Vali, H., *ChemCatChem* **2014,** *6,* 745-748.

59. Yuan, B.; Pan, Y.; Li, Y.; Yin, B.; Jiang, H., *Angew.Chem.Int.Ed.* **2010,** *49,* 4054-8.

60. Pachón, L. D.; Elsevier, C. J.; Rothenberg, G., *Adv. Synth. Catal.* **2006,** *348,* 1705-1710.

61. Cheng, J.; Zhang, G.; Du, J.; Tang, L.; Xu, J.; Li, J., *J. Mater. Chem.* **2011,** *21,* 3485-3494.

62. Barman, S.; Sadhukhan, M., *J. Mater. Chem.* **2012,** *22,* 21832-21837.

63. Sharma, S.; Kim, B.; Lee, D., *Langmuir* **2012,** *28,* 15958-15965.

64. Wagner, C. D.; Muilenberg, G. E., *Handbook of x-ray photoelectron spectroscopy: a reference book of standard data for use in x-ray photoelectron spectroscopy*. Physical Electronics Division, Perkin-Elmer Corp.: **1979**.

65. Militello, M. C.; Simko, S. J., *Surface Science Spectra* **1994,** *3,* 402-409.

66. Wang, Y.; Yao, J.; Li, H.; Su, D.; Antonietti, M., *J. Am. Chem. Soc.* **2011,** *133,* 2362-5.

67. Amali, A. J.; Rana, R. K., *Chem.Commun.* **2008,** 4165-4167.

68. Zhang, C.; Zhang, R.; He, S.; Li, L.; Wang, X.; Liu, M.; Chen, W., *ChemCatChem* **2016,** 10.1002/cctc.201601364.

69. Ma, A.; Xu, J.; Zhang, X.; Zhang, B.; Wang, D.; Xu, H., *Sci Rep* **2014,** *4,* 4849.

70. Gu, X.; Qi, W.; Xu, X.; Sun, Z.; Zhang, L.; Liu, W.; Pan, X.; Su, D., *Nanoscale* **2014,** *6,* 6609-6616.

71. Zhang, Z.; Xiao, F.; Xi, J.; Sun, T.; Xiao, S.; Wang, H.; Wang, S.; Liu, Y., *Sci Rep* **2014,** *4,* 4053.

72. Liang, M.; Su, R.; Huang, R.; Qi, W.; Yu, Y.; Wang, L.; He, Z., *ACS Appl. Mater. Interfaces.* **2014,** *6,* 4638-4649.

73. Sun, T.; Zhang, Z.; Xiao, J.; Chen, C.; Xiao, F.; Wang, S.; Liu, Y., *Sci Rep* **2013,** *3,* 2527.

74. Aditya, T.; Pal, A.; Pal, T., *Chem. Commun.* **2015,** *51,* 9410-9431.

75. Li, Y.; Zhou, Y.-X.; Ma, X.; Jiang, H.-L., *Chem. Commun.* **2016,** *52,* 4199-4202.

76. Göksu, H.; Can, H.; Şendil, K.; Gültekin, M. S.; Metin, Ö., *Appl. Catal. A: General* **2014,** *488,* 176-182.

77. Byun, S.; Song, Y.; Kim, B. M., *ACS Appl. Mater. Interfaces* **2016,** *8,* 14637-14647.

78. Metin, O.; Mendoza-Garcia, A.; Dalmzrak, D.; Gultekin, M. S.; Sun, S., *Catal. Sci. Technol.* **2016,** *6,* 6137-6143.

79. Cao, N.; Su, J.; Hong, X.; Luo, W.; Cheng, G., *Chem. Asian J.* **2014,** *9,* 562-571.

80. Tamiolakis, I.; Fountoulaki, S.; Vordos, N.; Lykakis, I. N.; Armatas, G. S., *J. Mater. Chem. A* **2013,** *1,* 14311-14319.

81. Göksu, H.; Ho, S. F.; Metin, Ö.; Korkmaz, K.; Mendoza Garcia, A.; Gültekin, M. S.; Sun, S., *ACS Catal.* **2014,** *4,* 1777-1782.

NMR data of different amine compounds:

Aniline (2a): ^{1}H NMR (400 MHz, DMSO) δ 7.02 (t, *J* = 7.8 Hz, 2H), 6.58 (d, *J* = 7.8 Hz, 2H), 6.51 (t, *J* = 7.2 Hz, 1H), 4.98 (s, 2H). ^{13}C NMR (100 MHz, DMSO) δ 148.61, 128.88, 115.80, 113.99.

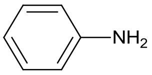

4-aminophenol (2b): ^{1}H NMR (400 MHz, DMSO) δ 8.38 (s, 1H), 6.49 (d, *J* = 8.8 Hz, 2H), 6.43 (d, *J* = 8.8 Hz, 2H), 4.41 (s, 2H). ^{13}C NMR (100 MHz, DMSO) δ 148.28, 140.71, 115.60, 115.33.

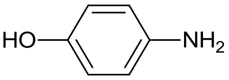

4-methoxyaniline (2c): ^{1}H NMR (400 MHz, DMSO) δ 6.65 (d, *J* = 8.8 Hz, 2H), 6.54 (d, *J* = 8.8 Hz, 2H), 4.56 (s, 2H), 3.62 (s, 3H). ^{13}C NMR (100 MHz, DMSO) δ 150.54, 142.62, 115.07, 114.55, 55.32.

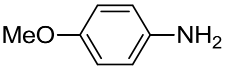

2-ethylaniline (2d): ^{1}H NMR (400 MHz, DMSO) δ 6.88 (dd, *J* = 16.6, 7.6 Hz, 2H), 6.59 (d, *J* = 7.3 Hz, 1H), 6.49 (t, *J* = 7.3 Hz, 1H), 4.75 (s, 2H), 2.42 (q, *J* = 7.5 Hz, 2H), 1.11 (t, *J* = 7.5 Hz, 3H). ^{13}C NMR (100 MHz, DMSO) δ 145.89, 127.96, 126.81, 126.36, 116.37, 114.47, 23.48, 13.28.

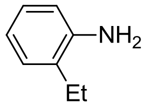

Benzene-1,4-diamine (2e): ^{1}H NMR (400 MHz, DMSO) δ 6.37 (s, 4H). ^{13}C NMR (100 MHz, DMSO) δ 138.99, 115.93.

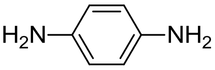

Benzene-1,3-diamine (2f): ^{1}H NMR (400 MHz, D_2O) δ 7.04 (t, *J* = 7.9 Hz, 1H), 6.31 (dd, *J* = 7.9, 2.1 Hz, 2H), 6.28 (s, 1H). ^{13}C NMR (100 MHz, D_2O) δ 147.29, 130.35, 107.72, 104.15.

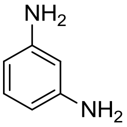

4-iodoaniline (2g): ^{1}H NMR (400 MHz, DMSO) δ 7.26 (d, *J* = 8.6 Hz, 2H), 6.41 (d, *J* = 8.6 Hz, 2H), 5.25 (s, 2H). ^{13}C NMR (100 MHz, DMSO) δ 148.95, 137.55, 116.99, 76.20.

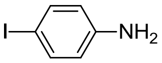

4-bromoaniline (2h): ^{1}H NMR (400 MHz, DMSO) δ 7.11 (d, *J* = 8.7 Hz, 2H), 6.51 (d, *J* = 8.7 Hz, 2H), 5.21 (s, 1H). ^{13}C NMR (100 MHz, DMSO) δ 148.16, 131.51, 116.03, 106.33.

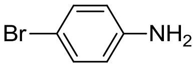

3-aminobenzoic acid (2i): ^{1}H NMR (400 MHz, DMSO) δ 7.20 – 7.09 (m, 3H), 6.77 (d, *J* = 7.1 Hz, 1H). ^{13}C NMR (100 MHz, DMSO) δ 168.04, 148.89, 131.41, 129.03, 118.18, 116.84, 114.56.

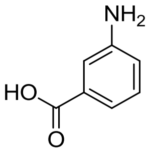

4-aminobenzamide (2j): ^{1}H NMR (400 MHz, DMSO) δ 7.57 (d, *J* = 8.6 Hz, 2H), 6.81 (s, 1H), 6.58 (s, 1H), 6.52 (d, *J* = 8.6 Hz, 2H), 5.58 (s, 2H). ^{13}C NMR (100 MHz, DMSO) δ 168.63, 151.96, 129.41, 120.98, 112.81.

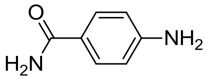

4-aminobenzonitrile (2k): ^{1}H NMR (400 MHz, DMSO) δ 7.37 (d, *J* = 13.4 Hz, 2H), 6.61 (d, *J* = 11.1 Hz, 2H), 6.11 (s, 2H). ^{13}C NMR (100 MHz, DMSO) δ 153.47, 133.72, 121.07, 113.42, 95.97.

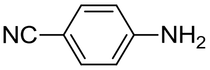

Naphthalen-1-amine (2l): ^{1}H NMR (400 MHz, $CDCl_3$) δ 7.87 - 7.83 (m, 2H), 7.54 – 7.44 (m, 2H), 7.34 (dt, *J* = 15.1, 7.7 Hz, 2H), 6.80 (m, 1H), 3.40-3.97(2H). ^{13}C NMR (100 MHz, $CDCl_3$) δ 142.20, 134.54, 128.65, 126.44, 125.92, 124.93, 123.81, 120.91, 119.07, 109.80.

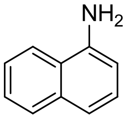

NMR data of different biaryl compounds:

1,1'-biphenyl (4a, 4b, 4c): ^{1}H NMR (400 MHz, $CDCl_3$) δ 7.60 (d, *J* = 7.7 Hz, 4H), 7.45 (t, *J* = 7.6 Hz, 2H), 7.36 (d, *J* = 7.5 Hz, 4H). ^{13}C NMR (100 MHz, $CDCl_3$) δ 141.39, 128.90, 127.39, 127.32.

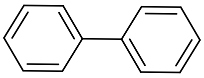

4,4'-dimethyl-1,1'-biphenyl (4d): ^{1}H NMR (400 MHz, $CDCl_3$) δ 7.47 (d, 4H), 7.23 (d, 4H).), 2.38 (s, 6H). ^{13}C NMR (100 MHz, $CDCl_3$) δ 138.43, 136.83, 129.57, 126.95, 21.22.

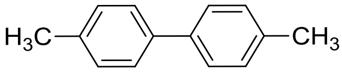

4,4'-dimethoxy-1,1'-biphenyl (4e): ^{1}H NMR (400 MHz, $CDCl_3$) δ 7.48 (d, *J* = 8.5 Hz, 4H), 6.96 (d, *J* = 8.5 Hz, 4H), 3.85 (s, 6H). ^{13}C NMR (100 MHz, $CDCl_3$) δ 158.84, 133.64, 127.88, 114.31, 55.49.

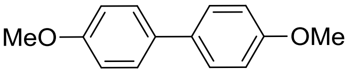

3,3'-dimethoxy-1,1'-biphenyl (4f) : ^{1}H NMR (400 MHz, $CDCl_3$) δ 7.36 (t, *J* = 7.9 Hz, 2H), 7.19 (d, *J* = 7.6 Hz, 2H), 7.14 (s, 2H), 6.91 (d, *J* = 8.2 Hz, 2H), 3.87 (s, 6H). ^{13}C NMR (100 MHz, $CDCl_3$) δ 160.03, 142.77, 129.86, 119.84, 113.09, 112.95, 55.44.

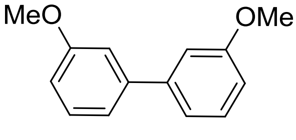

3,3'-dimethyl-1,1'-biphenyl (4g): ^{1}H NMR (400 MHz, CDCl$_3$) δ 7.39 (d, *J* = 8.8 Hz, 4H), 7.32 (t, *J* = 7.5 Hz, 2H), 7.16 (d, *J* = 7.4 Hz, 2H), 2.42 (s, 6H). ^{13}C NMR (100 MHz, CDCl$_3$) δ 141.49, 138.39, 128.74, 128.12, 128.05, 124.42, 21.69.

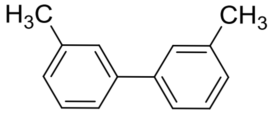

4,4'-difluoro-1,1'-biphenyl (4h): ^{1}H NMR (400 MHz, CDCl$_3$) δ 7.49 (dd, *J* = 8.8, 5.3 Hz, 4H), 7.12 (t, *J* = 8.7 Hz, 4H). ^{13}C NMR (100 MHz, CDCl$_3$) δ 163.66 (s), 161.21 (s), 136.41 (d, *J* = 3.3 Hz), 128.58 (d, *J* = 8.1 Hz), 115.69 (d, *J* = 21.5 Hz).

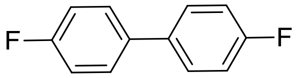

3,3',4,4'-tetrafluoro-1,1'-biphenyl (4i): ^{1}H NMR (400 MHz, CDCl$_3$) δ 7.31 (t, *J* = 7.7 Hz, 2H), 7.21-7.24 (m, 4H). ^{13}C NMR (100 MHz, CDCl$_3$) δ 151.65 (dd, *J* = 29.7, 15.5 Hz), 149.16 (dd, *J* = 34.9, 14.3 Hz), 136.24 (s), 122.97 (s), 117.80 (d, *J* = 17.8 Hz), 116.01 (d, *J* = 18.1 Hz).

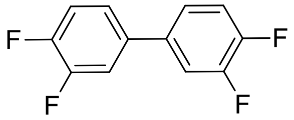

4,4'-dichloro-1,1'-biphenyl (4j): ^{1}H NMR (400 MHz, CDCl$_3$) δ 7.48 (d, *J* = 8.5 Hz, 4H), 7.41 (d, *J* = 8.5 Hz, 4H). ^{13}C NMR (100 MHz, CDCl$_3$) δ 138.45, 133.76, 129.05, 128.23.

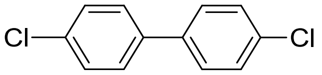

[1,1'-biphenyl]-4,4'-dicarbaldehyde (4k): ^{1}H NMR (400 MHz, CDCl$_3$) δ 9.71 (s, 2H), 7.57 (d, *J* = 8.2 Hz, 4H), 7.43 (d, *J* = 7.9 Hz, 4H). ^{13}C NMR (100 MHz, CDCl$_3$) δ 193.51, 151.24, 132.56, 129.93, 125.85.

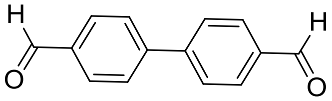

[1,1'-biphenyl]-4,4'-dicarbonitrile (4l): ^{1}H NMR (400 MHz, CDCl$_3$) δ 7.78 (d, *J* = 8.5 Hz, 4H), 7.69 (d, *J* = 8.5 Hz, 4H). ^{13}C NMR (100 MHz, CDCl$_3$) δ 143.68, 133.04, 128.09, 118.54, 112.62.

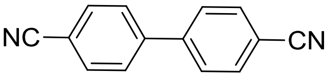

2,2'-binaphthalene (4m): ^{1}H NMR (400 MHz, CDCl$_3$) δ 8.18 (s, 2H), 7.96 (t, *J* = 9.2 Hz, 4H), 7.90 (d, *J* = 8.5 Hz, 4H), 7.56 – 7.48 (m, 4H). ^{13}C NMR (100 MHz, CDCl$_3$) δ 138.58, 133.90, 132.82, 128.67, 128.39, 127.83, 126.51, 126.27, 126.16, 125.89.

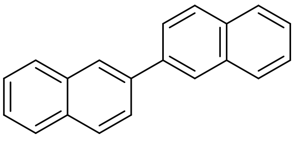

2,2'-bipyridine (4n): ^{1}H NMR (400 MHz, CDCl$_3$) δ 8.68 (d, *J* = 4.8 Hz, 2H), 8.39 (d, *J* = 8.0 Hz, 2H), 7.81 (t, *J* = 7.7 Hz, 2H), 7.30 (dd, *J* = 7.5, 4.8 Hz, 2H). ^{13}C NMR (100 MHz, CDCl$_3$) δ 156.27, 149.31, 137.07, 123.85, 121.23.

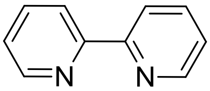

Summary and Future Prospect

Summary

This dissertation discussed the synthesis of graphitic carbon nitride supported various nanocomposite to utilize their catalytic activities in organic reaction and electrochemical reaction related with fuel cell.

The first chapter describes a brief overview of the current and future energy demands and explored the importance of renewable energy conversions and storage techniques. The history and development of fuel cell as well as water electrolyser are highlighted. The general description of different fuel cell reactions such as hydrogen oxidation reaction (HOR), oxygen reduction reaction (ORR) and water electrolyser reaction namely hydrogen evolution reaction (HER), oxygen evolution reaction (OER) has been discussed in this chapter. A brief description of theoretical backgrounds to develop the efficient electro catalysts for different renewable process also has been demonstrated. This chapter also records an account of current literatures pertaining to different nanocarbon materials graphene, carbon nanotube (CNTs), carbon nitride based precious and non-precious metal nanostructure materials, used for various fuel cell reactions. The different synthesis methods, properties and electrochemical applications of transition metals layered double hydroxides (LDHs) structure also discussed in this chapter. Moreover, NPs based heterogeneous catalyst for various organic conversions has been briefly discussed in the last section of this chapter. Finally, at the end of this chapter presented the objective of this dissertation work.

Chapter 2 demonstrated the various experimental procedures and suitable characterization techniques adopted for this whole dissertation work briefly.

In chapter 3 and 4 represented the synthesis, characterization of porous palladium nanoparticles-carbon nitride composite (Pd-CN_x) for superior electrochemical HER, HOR and ORR activity in both acidic and alkaline media. The porous structure of the nanocomposite from an optimized precursor composition and reaction time. This chapter demonstrated that Pd-CN_x nanocomposite showed relatively high electrocatalytic activity compare to commercially available Pt/C and Pd/C catalyst. The long term stability of the nanocomposite was explained by the carbon nitride hybridization which could improve the stability by intimate contact with Pd NPs.

Chapter 5 described synthesis, characterization and efficient hydrogen and oxygen evolution reactions over all pH values of one dimensional highly crystalline RuO_2 nanowires on carbon nitride (1D-RuO_2-CN_x). Moreover the growth mechanism of the nanowire on g-CNx also demonstrated here. The 1D-RuO_2-CN_x, as an OER catalyst, exhibits low onset overpotential of ~ 200 mV in both acidic and basic media whereas Tafel slopes are 52 and 56 mV/dec respectively. This catalyst requires low overpotential of 250 mV and 260 mV to drive the current density of 10 $mAcm^{-2}$ in acidic and basic media respectively. In addition the mass activity of 1D-RuO_2-CN_x is ~14 time higher than that of comm. RuO_2. Most importantly, the 1D-RuO_2-CN_x catalyst has remarkably higher stability in compare to comm. RuO_2 and IrO_2. The superior HER activity of 1D-RuO_2-CN_x with current density of 10 $mAcm^{-2}$ at ~93 and 95 mV in acidic and basic media. The 1D-RuO_2-CN_x composite showed improved HER and OER activity as compared to the state-of-the-art catalyst in 0.1 M PBS buffer electrolyte.

Chapter 6, demonstrated the electrocatalytic activity of palladium nanoparticles-carbon nitride composite (PdNPs/CN_x) towards the formic acid oxidation (FAO) with high mass activity (1640 $mAmg_{Pd}^{-1}$) in acid electrolyte. This chapter also demonstrated that the current density of PdNPs/CN_x catalyst for FAO is ~7.6 times and ~36 times higher than that of the commercial Pd/C and Pt/C catalyst respectively.

Chapter 7, concentrated on finding of non-precious metal based highly active and durable bi-functional electrocatalysts for overall water-splitting. This chapter describes the synthesis, characterization of cobalt iron layered double hydroxide ($Co_{1-\delta}Fe_{\delta}$ LDH) and g-carbon nitride composite ($Co_{1-\delta}$ Fe_{δ} LDH/g-CN_x). He optimized the LDH structure of the nanocomposite from various precursor composition and reaction time. He showed that thin $Co_{1-\delta}Fe_{\delta}$ LDH nano-sheets are successfully impregnated on graphitic carbon nitride surface by one pot co-precipitation method at ambient temperature. The optimal composite, $Co_{0.4}Fe_{0.6}$ LDH/g-CN_x exhibited superior OER activity in 1 M KOH electrolyte with a small overpotential of 0.28 V for 10 mAcm^{-2}, low Tafel slope of 29 mV/dec, 100% faradic efficiency and high TOF of 0.25 s^{-1} which is superior to comm. IrO_2. Furthermore, the catalyst demonstrated its long term durability and higher stability for HER and OER under alkaline environment.

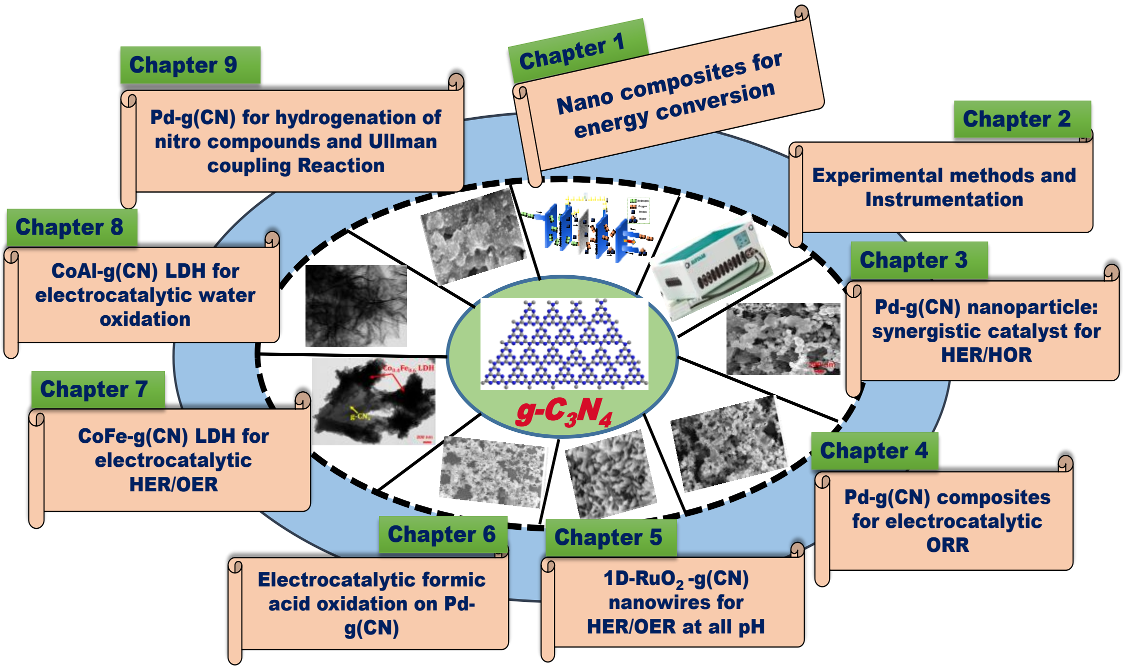

Chapter 8, describes the synthesis of composite cobalt aluminium layered double hydroxide-carbon nitride ($Co_1Al_\delta(OH)_m$-CN_x) by simple microwave heating method and their potential applications towards water oxidation reaction in alkaline medium. He synthesized a series of $Co_1Al_\delta(OH)_m$-CN_x composite materials by varying the amount of Co and Al precursors. It demonstrated that among those different compositions, highest catalytic activity was observed for $Co_1Al_2(OH)_x$-CN_x composite materials with a small overpotentials of 0.31 V to achieve 10 mA cm^{-2} current density, low Tafel slope of 36 mV/dec and ~99% Faradic efficiency. The superior activity of $Co_1Al_2(OH)_x$-CN_x composite was explained with the help of the strong synergestic effect betwwen support and $Co_1Al_{\square}(OH)_m$ LDH or improved ECSA of the composite materials.

Chapter 9, described the synthesis of highly dispersed ultra-small palladium nanoparticles embedded on graphitic carbon nitride (Pd@CN_x) by ultrasound assisted method without aid of any external reducing agent. The chapter showed the efficient catalytic activity towards easy dehydrogenation of sodium borohydride ($NaBH_4$) and ammonia borane (AB) in aqueous medium and also easy hydrogenation of 4-Nitrophenol to 4-aminophenlo with fast kinetics. This chapter exhibited the superior catalytic activity of this catalyst towards ullmann coupling reaction of different aryl halides with broad range of substrates scope with easy recovery of the catalyst and high recycling property.

Future prospect:

The ultra sound mediated sodium borohydride reduction methods synthesised a porous Pd nanoparticle graphitic carbon nitride composite having electrocatalytic activity towards hydrogen oxidation reaction, oxygen reduction reaction and formic acid oxidation reaction. This simple process could create an avenue for the synthesis of porous nanocomposite for catalysis of different Fuel cell reactions. This concept could have an enormous impact in field of energy conversion devices.

Demonstration of bifunctional activity of one dimensional RuO_2 nanorod and g-carbon nitride nanocomposite for HER and OER at all pH values makes them interesting catalytic systems. Further investigation of reaction mechanism on RuO_2 will deepen the understanding of the particular structural properties that are involved in oxygen and hydrogen evolution reaction contribute to the eventual development of catalysts which approach the behaviour of an ideal water electrolyser.

One pot simple co-precipitation methods were used to imprecate the transition metal based LDH material on the g-carbon nitride. This facile process could create an avenue for the synthesis of different LDH and 2D support materials for low price alkaline water electrolyser. Those composite can be used as promising electro-catalyst for various renewable energy storage and conversion devices such as water-splitting devices, fuel cells, metal-air batteries, etc.

Another extension of the work in thesis could be Ultrasound mediated synthesis of small aggregation free metal nanoparticle on the g-carbon nitride sheet. Highly dispersed Pd NPs on g-carbon nitride has very high surface area and shows excellent catalytic activity towards nitro phenol reduction and ullmann coupling reaction. This novel concept could have a great impact for heterogeneous catalysis applications.

Reprints First page
of Published Papers

ACS Catalysis
Research Article
pubs.acs.org/acscatalysis

Palladium Nanoparticle–Graphitic Carbon Nitride Porous Synergistic Catalyst for Hydrogen Evolution/Oxidation Reactions over a Broad Range of pH and Correlation of Its Catalytic Activity with Measured Hydrogen Binding Energy

Tanmay Bhowmik, Manas Kumar Kundu, and Sudip Barman*

School of Chemical Science, National Institute of Science Education and Research, Bhubaneswar 751005, India

Supporting Information

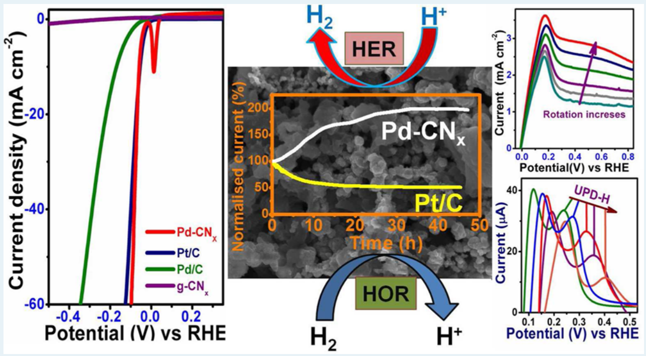

ABSTRACT: The hydrogen evolution reaction (HER) and hydrogen oxidation reaction (HOR) in aqueous medium are two fundamental reactions for the development of non-fossil energy storage and conversion devices. In the polymer electrolyte membrane fuel cell (PEMFC) carbon supported platinum (Pt/C) based catalysts are universally used in cathodes and anodes; however, the poor durability of Pt/C due to degradation of the catalyst in the strongly oxidizing environment prevents its widespread applications. It remains a great challenge to develop new electrocatalysts with superior activity and very high durability for the HER/HOR. Here, we report the synthesis of a porous palladium nanoparticle–carbon nitride composite (Pd-CN$_x$) for its superior activity and high durability toward the HER/HOR in acidic and alkaline media. The Pd-CN$_x$ composites exhibited high catalytic activity for hydrogen evolution in acidic media with a small onset potential of −12 mV and a Tafel slope of 35 mV dec^{-1}. At a small Pd loading of 0.043 mg cm^{-2}, this catalyst also exhibits a current density of 10 mA cm^{-2} at a low overpotential of −55 mV with an excellent stability. The HER activity on Pd-CN$_x$ composite is comparable to that of commercial Pt/C in acid media. The stability tests of this catalyst were done through a large number of repeated potential cycles and long-term electrolysis. These confirm the exceptional durability of this catalyst, which is much better than that of Pt/C catalysts. Furthermore, this catalyst has also displayed superior HOR activity, measured by a rotating-disk experiment with a broad range of pH (0−14) in different buffer solutions. The HER/HOR activities of porous Pd-CN$_x$ composite in different buffer solutions were correlated with the hydrogen binding energy (HBE) of the catalyst surface. The HER/HOR activity gradually decreases with an increase in the HBE as the solution pH increases. The superior HER/HOR activities and very high durability at porous Pd-CN$_x$ composite are due to strong bonding between Pd and carbon (Pd−C bond), the porous morphology, and synergistic interactions between Pd-NPs and the carbon nitride (CN$_x$) support.

KEYWORDS: *palladium nanoparticle, graphitic carbon nitride, hydrogen evolution and oxidation reaction, underpotential deposition, hydrogen binding energy*

■ INTRODUCTION

The rapid depletion of fossil fuels and also various environmental problems arising from the use of fossil fuels are the driving force for developing technologies for energy conversion and storage.[1] Fuel cells and electrolyzers are the most significant renewable energy conversion and storage techniques, respectively. Among the different type of fuel cells, proton exchange membrane fuel cells/polymer electrolyte fuel cells (PEMFCs) are known to be a clean and renewable energy resource due to their high energy conversion efficiency, high energy and power density, and better environmental compatibility.[2,3] The hydrogen evolution reaction (HER) and hydrogen oxidation reaction (HOR) in aqueous medium are two fundamental reactions for the development of non-fossil energy storage and conversion devices.[4] The main applicability of the HOR is predominantly in fuel cells, where chemical energy in hydrogen is converted into electrical energy. The HER is used in electrolyzers, which store the energy in chemical form by liberating the hydrogen. In fuel cells, the anodic hydrogen oxidation reaction (HOR) and cathodic hydrogen evolution reaction (HER) have been catalyzed by the noble metal Pt.[5,6] In practice, large-scale electrochemical hydrogen production is generally restricted by two main problems: (1) dependence on the precious metal platinum and (2) lack of stability of the electrode materials under the strongly acidic conditions of PEM cells. Research efforts are ongoing to

Received: November 5, 2015
Revised: December 9, 2015
Published: February 5, 2016

DOI: 10.1021/acscatal.5b02485
ACS Catal. 2016, 6, 1929−1941

ACS APPLIED MATERIALS & INTERFACES

Research Article

www.acsami.org

Growth of One-Dimensional RuO_2 Nanowires on g-Carbon Nitride: An Active and Stable Bifunctional Electrocatalyst for Hydrogen and Oxygen Evolution Reactions at All pH Values

Tanmay Bhowmik, Manas Kumar Kundu, and Sudip Barman*

School of Chemical Science, National Institute of Science Education and Research, HBNI, Bhubaneswar 751005, India

S Supporting Information

ABSTRACT: Development of highly efficient and durable bifunctional electrocatalyst for hydrogen and oxygen evolution reactions (HER and OER) is essential for efficient solar fuel generation. The commercial RuO_2 or RuO_2-based catalysts are highly active toward OER, but their poor stability under different operating conditions is the main obstacle for their commercialization. Herein, we report growth of one-dimensional highly crystalline RuO_2 nanowires on carbon nitride (1D-RuO_2-CN_x) for their applications in HER and OER at all pH values. The 1D-RuO_2-CN_x, as an OER catalyst, exhibits a low onset overpotential of ~200 mV in both acidic and basic media, whereas Tafel slopes are 52 and 56 mV/dec in acidic and basic media, respectively. This catalyst requires a low overpotential of 250 and 260 mV to drive the current density of 10 mA cm^{-2} in acidic and basic media, respectively. The mass activity of 1D-RuO_2-CN_x catalyst is 352 mA mg^{-1}, which is ~14 times higher than that of commercial RuO_2. Most importantly, the 1D-RuO_2-CN_x catalyst has remarkably higher stability compared to commercial RuO_2. This catalyst also exhibits superior HER activity with a current density of 10 $mAcm^{-2}$ at ~93 and 95 mV in acidic and basic media. The HER Tafel slopes of this catalyst are 40 mV/dec in acidic condition and 70 mV/dec in basic condition. The HER activity of this catalyst is slightly lower than Pt/C in acidic media, whereas in basic media it is comparable or even better than that of Pt/C at higher overpotentials. The HER stability of this catalyst is also better than that of Pt/C in all pH solutions. This superior catalytic activity of 1D-RuO_2-CN_x composite can be attributed to catalyst−support interaction, enhanced mass and electron transport, one-dimensional morphology, and highly crystalline rutile RuO_2 structure.

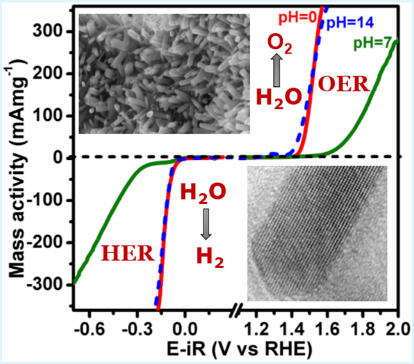

KEYWORDS: *graphitic carbon nitride, one-dimensional RuO_2 nanowire, hydrogen evolution, oxygen evolution, bifunctional*

INTRODUCTION

To solve the energy crisis and environmental problems, worldwide efforts are going on to find renewable energy sources as alternatives to fossil fuels.[1,2] Hydrogen is considered as one of cleanest renewable energy sources as an alternative to fossil fuel.[3,4] Overall, water splitting to produce molecular hydrogen is a promising method to store solar/electric energy into chemical fuels[5] as H_2. The water splitting consists of two half-cell reactions[6] such as hydrogen evolution reaction (HER) and oxygen evolution reaction (OER). Without any suitable catalyst both processes are very slow. Apart from H_2 storage application, HER/OER catalysts are also directly coupled with various renewable energy conversion and storage systems[7,8] such as metal−air batteries, fuel cells, solar cells, etc. OER is a bottleneck process for water splitting because of its sluggish kinetics due to a multistep proton couple electron transfer process.[9] Although RuO_2 and IrO_2 are highly active electrocatalysts for the OER reaction, IrO_2 is preferred as a state-of-the-art catalyst for OER.[10] The both state-of-the-art catalysts[11] still show quite large OER overpotentials as compared to the theoretical value of 1.23 V. The reduction of a large overpotential to reach an appreciable current density for OER is the major challenge of electrochemical water splitting, which is an obstacle for development of renewable energy conversion devices. Carbon-supported platinum (Pt/C) is a state-of-the-art catalyst for HER. Although Pt/C is highly active in acidic media, its activity in basic media is two orders less as compared to acidic media.[12] The slow kinetics of Pt/C toward HER in basic media restricted fuel efficiency, and a large amount of Pt catalyst is needed in basic media.[13,14] In addition, the long-term durability of Pt/C catalyst in strong oxidizing condition is another obstacle for its commercialization. The catalysis of HER as well as OER processes in the same medium is attractive, since only one catalyst can be used for their integration. It is known that almost all good OER[15−19] catalysts are active mainly in basic media, whereas good HER catalysts[20−24] work well in acidic media. Some HER catalysts[25−28] are active in acidic, basic, and neutral medium, but OER catalysts,[29] which are active in all pH, are relatively very rare. It is thus highly desirable to find superior bifunctional

Received: August 19, 2016
Accepted: October 4, 2016
Published: October 4, 2016

DOI: 10.1021/acsami.6b10436
ACS Appl. Mater. Interfaces 2016, 8, 28678−28688

INTERNATIONAL JOURNAL OF HYDROGEN ENERGY 41 (2016) 14768–14777

Available online at www.sciencedirect.com

ScienceDirect

journal homepage: www.elsevier.com/locate/he

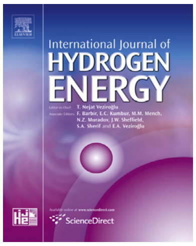

Highly active and durable Pd nanoparticles-porous graphitic carbon nitride composite for electrocatalytic oxygen reduction reaction

Tanmay Bhowmik, Manas Kumar Kundu, Sudip Barman[*]

School of Chemical Science, National Institute of Science Education and Research, Institute of Physics Campus, Bhubaneswar, Odisha, 751 005, India

ARTICLE INFO

Article history:
Received 20 April 2016
Received in revised form
30 May 2016
Accepted 31 May 2016
Available online 20 June 2016

Keywords:
Graphitic carbon-nitride
Palladium nanoparticle
Oxygen reduction
d-band center band
Durability
Synergistic interaction

ABSTRACT

The electrochemical oxygen reduction reaction (ORR) is a cathodic process of fuel cells. The carbon supported Platinum, Pt/C catalyst is universally used as cathode materials; but poor durability of Pt/C due to degradation of catalyst prevent its wide spread applications. It is thus important to develop new cathode material(s) with high activity and stability. We report here, superior electrocatalytic activity of palladium nanoparticles-carbon nitride (Pd-CN_x) composite towards ORR in both alkaline and acidic media. The ORR activity on Pd-CN_x catalyst is better (half wave potential $E_{1/2}$ of 60 mV more positive) than that of Pt/C in 0.5 M KOH solution and is almost comparable in acid media. Moreover, this porous composite display excellent methanol tolerance and has much better long term durability than that of commercial Pt/C in both acidic and alkaline media. Only 4 and 6 mV positive shift of $E_{1/2}$ after 1500 potential cycles in basic medium and acid media respectively prove the excellent durability of this catalyst. The superior electrocatalytic activity and excellent stability of porous Pd-CN_x composite can be attributed to unique synergistic interaction between CN_x support and Pd nanoparticles (Pd-NPs), lower the d-band center of Pd, easy mass transport, and surface structure of Pd-NPs.

Introduction

The oxygen reduction reaction (ORR) is one of the important redox reaction [1] for development of proton exchange membrane fuel cell (PEMFCs), direct liquid fuel cells (DLFCs) and alkaline fuel cells (AFCs). Without any assistance of suitable catalyst, ORR kinetics becomes very sluggish. Platinum is known to be the universal catalyst for the ORR process. In practice, commercialization is restricted mainly by two major problems: (1) the precious platinum metal dependency and (2) lack of stability of the electrode materials under strong acidic condition of PEM cells. It is thus important to develop non platinum based highly active and durable ORR catalyst for commercialization of fuel cell. The palladium, another noble metal which has similar crystal structure, surface structure, has created enormous attention as fuel cell catalyst because Pd is more abundance than Pt and has similar activity with Pt [2]. The ORR reaction is highly depended on the size, shape and crystallinity of the electrode materials and also the electrolyte solution [3–5]. Generally, ORR proceeds on the noble metal through two steps process – (a) adsorption or electron transfer to O–O molecule and breaking the O–O bond

---

[*] *Corresponding author*. Tel: +91 (674) 2304061; fax: +91 (674) 2304070.
E-mail address: sbarman@niser.ac.in (S. Barman).

http://dx.doi.org/10.1016/j.ijhydene.2016.05.295
0360-3199/

ACS APPLIED ENERGY MATERIALS

Article

Cite This: ACS Appl. Energy Mater. 2018, 1, 1200−1209

www.acsaem.org

CoFe Layered Double Hydroxide Supported on Graphitic Carbon Nitrides: An Efficient and Durable Bifunctional Electrocatalyst for Oxygen Evolution and Hydrogen Evolution Reactions

Tanmay Bhowmik, Manas Kumar Kundu, and Sudip Barman*

School of Chemical Science, National Institute of Science Education and Research (NISER), HBNI, Bhubaneswar, Bhimpur-Padanpur, Via Jatni, Khurda, Odisha 752050, India

Supporting Information

ABSTRACT: Finding nonprecious metal based highly active and durable bifunctional electrocatalysts for overall water-splitting is essential for the development of various renewable energy storage and conversion technologies. Herein, we report the synthesis of cobalt iron layered double hydroxide ($Co_{1-\delta}Fe_{\delta}$ LDH) and g-carbon nitride composite ($Co_{1-\delta}Fe_{\delta}$ LDH/g-CN_x) for alkaline water electrolysis. The thin $Co_{1-\delta}Fe_{\delta}$ LDH nanosheets are successfully impregnated on graphitic carbon nitride surface by one pot co-precipitation method at ambient temperature. The optimal composite, $Co_{0.4}Fe_{0.6}$ LDH/g-CN_x exhibited superior OER activity in 1 M KOH electrolyte with a small overpotential of 0.28 V for 10 mA cm^{-2}, low Tafel slope of 29 mV/dec, 100% faradic efficiency, and high TOF of 0.25 s^{-1} which is superior to commercial (comm) IrO_2. Furthermore, the $Co_{0.4}Fe_{0.6}$ LDH/g-CN_x composite also exhibited remarkable HER activity in alkaline media and its HER activity is slightly lower than that of comm Pt/C at low overpotential but it outperforms Pt/C at high overpotential. The catalyst demonstrated its long-term durability and higher stability for HER and OER under alkaline environment. This $Co_{0.4}Fe_{0.6}$ LDH/g-CN_x catalyst can serve as both cathode and anode for overall water-splitting and required the small potential of 1.61 V to achieve a current density of 10 mA cm^{-2}. The superior electrocatalytic activities of the $Co_{0.4}Fe_{0.6}$ LDH/g-CN_x composite are due to the high electrochemical surface area (ECSA), easy access of abundant active sites, and easy mass transport owing to 2D sheet morphology of the composite.

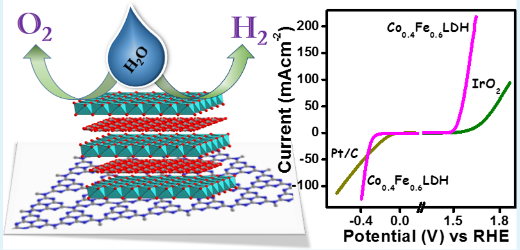

KEYWORDS: *$Co_{0.4}Fe_{0.6}$ LDH, g-carbon nitride, oxygen evolution reaction (OER), hydrogen evolution reaction (HER), overall water splitting.*

INTRODUCTION

With increasing concern over rapid depletion of fossil fuels and negative impact on the environment due to excessive use of fossil fuels, there is urgent need of renewable energy resource and storage techniques alternative to the fossil fuels.[1,2] Hydrogen is considered as a green fuel[3] (energy carrier) alternative to fossil fuel due to its high storage density and environment friendliness. The high purity hydrogen (99.6% purity) is mainly produced from chloroalkali industry during the electrocatalytic formation of chlorine and caustic soda.[4] In recent years, electrolysis of water[4,5] into molecular hydrogen (H_2) and oxygen (O_2) offers one of most viable alternative approaches for the replacement of fossil fuels. Water electrolysis consists of two half-cell[6] reactions such as cathodic hydrogen evolution reaction (HER) to produce molecular hydrogen and anodic oxygen evolution reaction (OER) to form molecular oxygen. Both HER and OER kinetics are sluggish without any suitable catalysts. HER is a simple two-step process occurring at low overpotential on noble metal surfaces,[7] whereas OER is a more complex multielectron process leading to sluggish kinetics of oxygen evolution from water and thus requires large overpotential.[8] The Pt/C is considered as highly active, best electrocatalyst[9,10] for HER, whereas noble metal oxide IrO_2 and RuO_2 are considered as state-of-art electrocatalyst[11,12] for OER. But the widespread applications of these noble metal based electrocatalysts are limited because of their scarcity and high cost. Thus, it is very important to develop nonprecious metal based highly active and durable electrocatalyst for water-splitting reactions.[13−15] In recent years, tremendous efforts have been devoted for development of low cost electrocatalyst for HER[16−19] and OER.[20−24] Several studies confirmed that first row transition metal dichalogenide,[25,26] phosphide,[18,27] nitride,[28] and carbide[29] catalysts exhibited superior HER activity whereas transition metal oxide,[30,31] hydroxides,[24,32,33] and oxy(hydroxide)[23] based catalysts are active for OER. Generally, most of the good HER catalysts are active in acidic environment[34,35] whereas most of the nonprecious OER catalysts are active under alkaline environment.[36,37] The designing of a bifunctional catalyst,[38−42] where the single catalyst is used as a cathode (HER) and anode

Received: December 19, 2017
Accepted: February 22, 2018
Published: February 22, 2018

DOI: 10.1021/acsaem.7b00305
ACS Appl. Energy Mater. 2018, 1, 1200−1209

Available online at www.sciencedirect.com

ScienceDirect

journal homepage: www.elsevier.com/locate/he

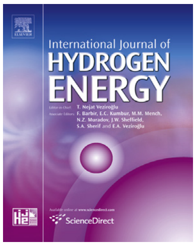

Highly efficient electrocatalytic oxidation of formic acid on palladium nanoparticles-graphitic carbon nitride composite

*Tanmay Bhowmik, Manas Kumar Kundu, Sudip Barman**

School of Chemical Science, National Institute of Science Education and Research, HBNI, Bhubaneswar,
Odisha 751 005, India

ARTICLE INFO

Article history:
Received 24 June 2016
Received in revised form
5 November 2016
Accepted 13 November 2016
Available online 9 December 2016

Keywords:
Graphitic carbon-nitride
Palladium nanoparticle
Formic acid oxidation
Electrocatalyst
Synergistic interaction

ABSTRACT

The electrochemical formic acid oxidation reaction (FAO) is an anodic process of direct formic acid fuel cells. Carbon supported platinum (Pt/C) and Palladium (Pd/C) catalysts are widely used as anode materials for FAO. The CO poisoning of Pt/C and poor stability of Pd/C are main obstacles for its commercialization. We report here superior electrocatalytic activity of Palladium nanoparticles-carbon nitride composite (PdNPs/CN_x) towards formic acid oxidation (FAO) with high mass activity (1640 mAmg$_{Pd}^{-1}$) in acid media (0.5 M H_2SO_4) which is 7.2 times higher than that of commercial Pd/C catalyst. It also exhibited an outstanding stability for FAO (mass activity of this catalyst was 23 times higher than commercial Pd/C after 1000 cycles).

Introduction

Development of sustainable and renewable energy sources [1] are gaining enormous attentions due to the limited access of natural fossil fuel and the rapid rise of energy demand. The fuel cells are the green energy resources, alternative to fossil fuel [2]. In recent years, Direct Formic Acid Fuel Cells (DFAFCs) have attracted attentions to scientific community due to its unique advantages over hydrogen fuel cell and Direct Methanol Fuel Cells (DMFCs) [3]. For hydrogen fuel cell, hydrogen storage and transportation are the main limitations for its applications, whereas methanol cross over, toxicity of methanol are the disadvantages of DMFCs. The DFAFCs has been created great attention as a promising alternate to DMFCs due to its higher power density, low fuel crossover, higher energy efficiency and higher electromotive force. The theoretical open circuit potential of DFAFCs is 1.48 V (vs. saturated hydrogen electrode) which is higher than hydrogen and methanol fuel cells [4]. The low fuel crossover in DFAFC is due to dissociation of formic acid to format ions ($HCOO^-$) and their repulsive interaction [5]. The electro-oxidation of formic acid on solid surfaces is known to occur via two different paths – (1) dehydrogenation process, the direct-path involves oxidation of formic acid to carbon dioxide ($HCOOH = CO_2 + 2H^+ + 2e^-$) and (2) the indirect-path (dehydration path) occurs via intermediate formation, oxidation of adsorbed CO species ($HCOOH = CO_{ads} + H_2O = CO_2 + 2H^+ + 2e^-$) [6]. The formic acid

---

* *Corresponding author*. Fax: +91 674 2304070.
E-mail address: sbarman@niser.ac.in (S. Barman).

http://dx.doi.org/10.1016/j.ijhydene.2016.11.095

Journal of
Materials Chemistry A

PAPER

View Article Online
View Journal | View Issue

Cite this: *J. Mater. Chem. A*, 2015, **3**, 23120

Gold aerogel supported on graphitic carbon nitride: an efficient electrocatalyst for oxygen reduction reaction and hydrogen evolution reaction†

Manas Kumar Kundu, Tanmay Bhowmik and Sudip Barman*

Received 26th August 2015
Accepted 1st October 2015

DOI: 10.1039/c5ta06740e

www.rsc.org/MaterialsA

Fabrication of a high surface area interconnected porous network of metallic nanomaterials is important for their applications in various fields such as catalysis, sensors, and electrochemistry. Here we report a facile bottom up synthesis of high surface area and porous gold aerogel supported on carbon nitride sheets (CN_x). The reduction of $HAuCl_4$ in the presence of carbon nitride nanosheets using sodium borohydride and ultrasonic treatment produces gold aerogel supported on carbon nitride (Au–aerogel–CN_x). When the reduction of $HAuCl_4$ in the presence of CN_x nanosheets was performed using only ultrasonication, highly dispersed ultrasmall (∼2 nm) gold nanoparticles on CN_x sheets (AuNPs–CN_x) were formed. The Au aerogel supported on CN_x sheets was well characterized by powder X-ray diffraction, tunneling electron microscopy, selected area electron diffraction, energy dispersive X-ray spectroscopy, scanning electron microscopy, UV-visible and X-rayphotoelectron spectroscopic methods. The Au–aerogel–CN_x and AuNPs–CN_x composites exhibited superior electrocatalytic activity towards oxygen reduction reaction (ORR) in alkaline and acidic media. The Au–aerogel–CN_x composite showed ORR onset potentials at 0.92 V and 0.43 V (*vs.* RHE) in 0.5 M KOH and H_2SO_4 solution. The four electron oxygen reduction process occurred at these supported catalysts in both alkaline and acidic media. In alkaline (KOH) medium the onset potential at Au–aerogel–CN_x was more positive (∼30 mV) than that of commercial Pt/C catalyst. The composites displayed excellent methanol tolerance and comparable durability with commercial Pt/C. Furthermore, the Au–aerogel–CN_x composites exhibited high catalytic activity for the hydrogen reduction reaction (HER) with a small onset potential of −30 mV and a Tafel slope of 53 mV dec^{-1} in acidic medium. At a small Au loading of 0.130 mg cm^{-2}, this catalyst also exhibits a current density of 10 mA cm^{-2} at a low overpotential of −185 mV with excellent stability. The ORR and HER performances on porous Au–aerogel–CN_x composites were better than those of the AuNPs–CN_x catalyst and commercial flat gold electrode. The superior ORR and HER activities at the Au–aerogel–CN_x composite originated from the unique synergistic effects between the porous Au network and carbon nitride (CN_x) support.

Introduction

Porous materials have attracted tremendous attention in the last few years due to their exceptionally high catalytic activity,[1–3] electrical conductivity[4] and mechanical properties.[5] These properties arise due to their ability to interact with the atoms or ions or molecules throughout the bulk of the material, and not only on their surfaces. In the last decade porous metallic network structures have gained tremendous attention for their various kinds of biological sensing applications[6,7] and catalytic[3] and electrocatalytic applications.[8] Metal aerogels are a new type of porous solid materials that have extremely low density, high porosity, high surface area, high electrical conductivity and catalytic properties. The properties of nanoparticles such as catalytic activities are retained in the metal aerogel and it may thus bridge the gap between nanomaterials and macro-materials. It was reported that the properties of some of the metal aerogels are superior to those of metal nanoparticles because of the combined effects of nanoparticles in the aerogel.[9] Since the discovery of aerogels in 1963 by Kistler,[10] enormous efforts have been taken to synthesise various aerogels. Several approaches are available in the literature for the synthesis of different non-metal aerogels such as carbon aerogels[11] and silica aerogels,[12] organic–inorganic hybrid aerogels,[13] metal oxide aerogels,[14] and metal chalcogenide aerogels.[15] But only few methods are available for the production of metal aerogels.[8,16–18] For example, Eychmüller and coworkers[8,16] have

---

School of Chemical Sciences, National Institute of Science Education and Research (NISER), Bhubaneswar, Orissa 751 005, India. E-mail: sbarman@niser.ac.in; Fax: +91 674 2304070; Tel: +91 674 2304061

† Electronic supplementary information (ESI) available: TEM images, TGA analysis, IR spectra, deconvoluted XPS spectra of CVs of ORR in acidic medium. See DOI: 10.1039/c5ta06740e

ChemPubSoc Europe

DOI: 10.1002/cssc.201800856

CHEMSUSCHEM
Full Papers

Platinum Nanostructure/Nitrogen-Doped Carbon Hybrid: Enhancing its Base Media HER/HOR Activity through Bi-functionality of the Catalyst

Manas Kumar Kundu, Tanmay Bhowmik, Ranjit Mishra, and Sudip Barman*[a]

The design and synthesis of an active catalyst for the hydrogen evolution reaction/hydrogen oxidation reaction (HER/HOR) are important for the development of hydrogen-based renewable technologies. The synthesis of a hybrid of platinum nanostructures and nitrogen-doped carbon [Pt-(PtO_x)-NSs/C] for HER/HOR applications is reported herein. The HER activity of this Pt-(PtO_x)-NSs/C catalyst is 4 and 6.5 times better than that of commercial Pt/C in acids and bases, respectively. The catalyst exhibits a current density of 10 mA cm^{-2} at overpotentials of 5 and 51 mV, with Tafel slopes of 29 and 64 mV dec^{-1} in 0.5 M H_2SO_4 and 0.5 M KOH. This catalyst also showed superior HOR activity at all pH values. The HER/HOR activity of Pt-(PtO_x)-NSs/C and PtO_x-free Pt-nanostructures on carbon (PtNSs/C) catalysts are comparable in acid. The presence of PtO_x in Pt-(PtO_x)-NSs/C makes this Pt catalyst more HER/HOR-active in basic media. The activity of the Pt-(PtO_x)-NSs/C catalyst is fivefold higher than that of the PtNSs/C catalyst in basic medium, although their activity is comparable in acid. The hydrogen-binding energy and oxophilicity are two equivalent descriptors for HER/HOR in basic media. A bifunctional mechanism for the enhanced alkaline HER/HOR activity of the Pt-(PtO_x)-NSs/C catalyst is proposed. In the bifunctional Pt-(PtO_x)-NSs/C catalyst, PtO_x provides an active site for OH^- adsorption to form OH_{ads}, which reacts with hydrogen intermediate (H_{ads}), present at neighbouring Pt sites to form H_2O; this leads to enhancement of the HOR activity in basic medium. This work may provide an opportunity to develop catalysts for various renewable-energy technologies.

Introduction

The rapid rise of global energy demand and environmental problems associated with the use of fossil fuels are the driving force for exploring renewable energy sources and energy storage.[1,2] Water electrolyzers and fuel cells are two important renewable techniques for energy storage and conversion.[2,3] Hydrogen is considered to be one of the best clean energy carriers, with high mass density, and the hydrogen evolution reaction (HER) is featured in water electrolyzers that store energy in chemical form by generating molecular hydrogen.[4] The hydrogen oxidation reaction (HOR) is mainly used in fuel cells, in which chemical energy from hydrogen is converted into electrical energy.[5] The hydrogen fuel cell consists of two half-cell reactions, such as the HOR at the anode and the oxygen reduction reaction (ORR) at the cathode. Water electrolyzers are based on two reactions: HER at the cathode and the oxygen evolution reaction (OER) at the anode.[6] Among the various fuel cells, proton exchange membrane fuel cells (PEMFCs) are one of the best renewable energy sources due to better environmental friendliness, high energy conversion efficiency, and high energy and power density.[2] Platinum is the most active catalyst for both HER/HOR processes in acid media,[7] but poor stability of commercial Pt/C under strongly acidic conditions is one of the main obstacles for the commercialization of PEMFCs.[8] Thus, it is highly desirable to find new highly active and highly durable HER/HOR catalysts. In recent years, alkali membrane fuel cells (AMFCs) and alkaline electrolyzers have been considered as suitable alternatives to PEMFCs and water electrolyzers, respectively, because earth-abundant, transition-metal-based nonprecious-metal catalysts are available for the ORR and OER in alkaline media.[9] Another advantage of AMFCs over PEMFCs is the high stability of the electrocatalyst in alkaline medium. Although Pt is also the best catalyst for the HER and the HOR in alkaline medium, the HER/HOR activity of commercial Pt/C in basic media is two orders of magnitude lower than that in an acid.[10] Because of sluggish HER/HOR kinetics at commercial Pt/C catalysts in alkaline media, a very high Pt loading ($\approx$0.5 mg cm^{-2}) is required at the anode of AMFCs, in comparison to the low Pt loading ($\approx$0.05 mg cm^{-2}) for PEMFCs.[11] Therefore, an effective HOR/HER catalyst is highly desirable for the development of AMFCs or alkaline electrolyzers.

Understanding the mechanism of the HOR/HER in alkaline media is important for designing efficient alkaline HOR/HER electrocatalysts. In acidic media, the HOR/HER occurs through either Tafel–Volmer or Heyrovsky–Volmer mechanisms [Eqs. (1)–(3)]:[10a,11,12]

---

[a] M. K. Kundu, T. Bhowmik, R. Mishra, Dr. S. Barman
School of Chemical Sciences
National Institute of Science Education and Research (NISER)
Bhubaneswar, HBNI, Orissa-751 005 (India)
E-mail: sbarman@niser.ac.in

Supporting Information and the ORCID identification number(s) for the author(s) of this article can be found under: https://doi.org/10.1002/cssc.201800856.

RSC Advances

PAPER

View Article Online
View Journal | View Issue

Cite this: *RSC Adv.*, 2015, **5**, 38760

Ultra small gold nanoparticles–graphitic carbon nitride composite: an efficient catalyst for ultrafast reduction of 4-nitrophenol and removal of organic dyes from water†

Tanmay Bhowmik,‡ Manas Kumar Kundu‡ and Sudip Barman*

Received 19th March 2015
Accepted 20th April 2015

DOI: 10.1039/c5ra04913j

www.rsc.org/advances

Synthesis of supported ultra small gold particles is important for their unusual properties and catalytic applications. We report a facile method for synthesis of ultra small gold nanoparticles supported on carbon nitride sheets (Au–CN$_x$). The ultrasonication was used to form Au–CN$_x$ composite from carbon nitride quantum dots and HAuCl$_4$ without any aid of external reducing agent. The Au–CN$_x$ composite was well characterized by tunneling electron microscopy, selected area electron diffraction, energy dispersive X-ray spectroscopy, powder X-ray diffraction, X-ray photo electron spectroscopy methods. Electron microscopic measurements confirm that thin graphitic carbon nitride sheets provided two dimensional supports to stabilize ultra small, 1–3 nm sized gold nanoparticles (AuNPs). The Au–CN$_x$ composite showed excellent catalytic activity towards the reduction of 4-nitrophenol in aqueous medium in presence of sodium borohydride (NaBH$_4$) with very fast kinetics and good stability. The Au–CN$_x$ catalyst can be used as an absorbent for the removal of organic dye [Rhodamine B (RhB), methylene blue (MB), and methyl red (MR)] from water. It showed excellent adsorption capacity for RhB and MB due to electrostatic interaction between anionic catalyst and cationic organic dye molecules. The catalyst can easily be reused after removing adsorbed dye from the catalyst simply by changing pH of the solution. In addition, Au–CN$_x$ composite exhibited superior photo catalytic degradation of various dyes (RhB, MB and MR) on irradiation of UV, visible light and natural sunlight. Excellent photodegradation rate constants for RhB (0.024 min^{-1}), MB (0.024 min^{-1}) and MR (0.02 min^{-1}) were observed although high concentration of dyes were used for degradation. Au–CN$_x$ is one of the best adsorbent for RhB adsorption with maximum adsorption capacity of 400 mg g^{-1} and catalyst for nitrophenol reduction. We hope that this Au–CN$_x$ composite will find its application as an effective catalyst for water purification.

Introduction

In recent years, noble metal nanoparticles have attracted tremendous attention due to their potential applications in various fields such as catalysis,[1] sensors,[2–6] optics,[6] fuel cell.[7] For example, gold nanoparticles[8] are being used for a long time in drug delivery, different biological application and catalysis. Silver and platinum nanoparticles show promising capabilities in biosensors[9] and in fuel cell.[10] Very small metal NPs has an interesting size and shape dependent reactivity[11] due to the increase of volume to surface ratio. The reduction in size of metal nanoparticles causes a significant change in reduction potential of metal nanoparticles as compared to bulk materials because their Fermi potential becomes more negative. This typical important property helps them in electron transfer in various catalysis reactions. But synthesis of ultra small metal nanoparticle is a very challenging task due its high agglomeration property, arises from its high surface energy. In order to avoid aggregation, nanoparticles should be stabilized by using organic molecules or polymer as a capping agent. But their catalytic activity greatly reduced due to the presence of organic or polymer molecules around nanoparticles. Another alternative available method is to stabilize them on the surface of a solid support.[12] Two dimensional (2D) graphene, due to its unique properties[13] such as high specific surface area, excellent electrical conductivity, high charge carrier mobility, high mechanical strength, became a promising candidate as a support for different nanoparticles. The graphene containing metal or semiconductor nanoparticles have confirmed to be effective nano-composite materials for photovoltaic,[14,15] catalysis and biosensor applications.[16] In recent year another two

---

School of Chemical Sciences, National Institute of Science Education and Research (NISER), Bhubaneswar, Orissa-751 005, India. E-mail: sbarman@niser.ac.in; Fax: +91 674 2304070; Tel: +91 674 2304061

† Electronic supplementary information (ESI) available: Materials details, and additional data. See DOI: 10.1039/c5ra04913j

‡ Tanmay Bhowmik and Manas Kumar Kundu equally contributed to this manuscript.

RSC Advances

PAPER

View Article Online
View Journal | View Issue

Cite this: *RSC Adv.*, 2014, 4, 4998

Facile synthesis of carbon quantum dots and thin graphene sheets for non-enzymatic sensing of hydrogen peroxide†

Mriganka Sadhukhan, Tanmay Bhowmik, Manas Kumar Kundu and Sudip Barman*

Received 20th September 2013
Accepted 4th November 2013

DOI: 10.1039/c3ra46050a

www.rsc.org/advances

Carbon quantum dots (CQDs) and two dimensional (2D) graphene sheets were prepared from formic acid by microwave mediated thermal method. Microwave irradiation followed by thermal evaporation of formic acid produces fluorescent CQDs. The fluorescence emission of CQDs in water can be tuned between 310 and 820 nm by changing the excitation wavelengths. These quantum dots are found to be sensitive towards hydrogen peroxide in aqueous medium due to quenching of fluorescence. The large area graphene sheets are formed on a solid substrate due to self assembly and 2D growth of CQDs. Graphene sheets modified glassy carbon electrode showed fast electron transfer kinetics for $Fe(CN)_6^{3-/4-}$ couple. Moreover, these modified electrodes can be used as a highly sensitive and selective metal free, non-enzymatic electrochemical sensor for hydrogen peroxide. The low detection limit was found to be 300 nM.

Introduction

Since the discovery of the single plane layer of honeycomb network of sp^2 hybridized carbon atoms, graphene by Andrew Geim *et al.*[1] it has attracted enormous amount of interest from the scientific community due to its unique properties.[1,2] The interesting properties of graphene reported in the literature include ballistic electron transport, integer and fractional quantum hall effect, extremely high carrier mobility and ability to sustain very high current densities. Thus, it is considered as a next-generation material for nano-electronics, spintronics, sensors, energy storage. However, the synthesis of large-area graphene on different substrate is hindering its applications. Several methods[1–5] such as mechanical exfoliation of graphite, chemical exfoliation, synthesis from solid carbon sources, chemical vapor deposition (CVD) of hydrocarbons on metal substrates, sublimation of silicon from silicon carbide (SiC) wafers *etc.* are available to synthesize a single or few layers of graphene. Although mechanical exfoliation of graphite provides excellent quality graphene, it is not suitable for large scale production of graphene. The main difficulty in producing high quality of graphene from graphite is especially due to the high van der Waals energy adhering graphene layers to one another. The most popular solution based approach is the chemical exfoliation from graphite which involves chemical oxidation of graphite into graphite oxide, followed by exfoliation of graphite oxide in water to form graphene oxide by ultrasonication.[3] Chemical oxidation induces defects[3,6] into the sheets due to presence of oxygenated functional groups such as carboxyl, hydroxyl, epoxy *etc.* Although reduction of graphene oxide by different reducing agent leads to increasing the π-conjugation of graphene,[6] the restoration of complete π-conjugation is not possible to achieve and hence it has low conductivity. Although chemical vapor deposition (CVD) produces high quality graphene on metal surfaces, there is a need for reliable method(s) for the production of high yield, high quality and large surface area graphene on silicon (Si) substrate. Moreover, compared to 2D graphene less attention has been paid to carbon quantum dots. They are more suitable for various applications as compared to small organic fluorescent molecules and inorganic semiconductor quantum dots, because of their high resistance to photo bleaching, low cytotoxicity and superior biocompatibility. Common methods[7] for the production of carbon quantum dots include pyrolysis of citric acid, ethylene diamine tetraacetic acid salts, the hydrothermal synthesis from grass and graphene sheets. Highly sensitive and selective determination of hydrogen peroxide is important[8] since it is the product of several biological enzyme-catalyzed reactions and also plays an active role in food, pharmaceutical, clinical, industrial, and environmental analyses. Several analytical methods[9] such as titration, chromatographic, fluorometric, colorimetric, chemiluminescent, electrochemical methods are available for determination of H_2O_2. Among these methods, fluorescence and electrochemical methods for determination of H_2O_2 are the best methods because of their low costs, high sensitivity and portability.

School of Chemical Sciences, National Institute of Science Education and Research (NISER), Bhubaneswar, Orissa - 751 005, India. E-mail: sbarman@niser.ac.in; Fax: +91 (674)2304070; Tel: +91 (674)2304061

† Electronic supplementary information (ESI) available: Details of the experimental techniques, quantum yield measurements, fluorescence lifetimes of CQDs. Additional Table S1 and Figures (Fig. S1–S9). See DOI: 10.1039/c3ra46050a

INTERNATIONAL JOURNAL OF HYDROGEN ENERGY 42 (2017) 9371–9383

Available online at www.sciencedirect.com

ScienceDirect

journal homepage: www.elsevier.com/locate/he

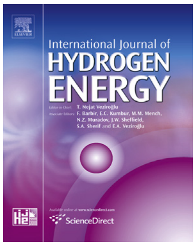

Highly dispersed platinum nanoparticles on graphitic carbon nitride: A highly active and durable electrocatalyst for oxidation of methanol, formic acid and formaldehyde

Mriganka Sadhukhan, Manas Kumar Kundu, Tanmay Bhowmik, Sudip Barman[*]

School of Chemical Sciences, National Institute of Science of Education and Research (NISER), Bhubaneswar, HBNI, Orissa, India

ARTICLE INFO

Article history:
Received 25 July 2016
Received in revised form
11 March 2017
Accepted 15 March 2017
Available online 4 April 2017

Keywords:
Electrocatalyst
Onset potential
Tolerance
Durability
Long term stability

ABSTRACT

Finding efficient electrocatalyst for oxidation of small organic molecules such as methanol (CH_3OH), formic acid (HCOOH), formaldehyde (HCHO) etc. is essential for the development of their respective direct fuel cells. We report here highly dispersed platinum nanoparticles (PtNPs) on carbon nitride (CN_x) were successfully synthesized by the ultrasound mediated sodium borohydride reduction of H_2PtCl_6 in presence of CN_x nanosheets. This platinum–carbon nitride (Pt/CN_x) composite exhibited superior electrocatalytic activity towards oxidation of CH_3OH, HCOOH and HCHO in acid media. The mass activity, onset potential, tolerance to carbon monoxide (CO) poisoning and long term durability for the catalytic oxidation of CH_3OH, HCOOH, HCHO on Pt/CN_x catalyst in acid media is much higher than that of commercial Pt/C catalyst. The mass activity of Pt/CN_x catalyst at ~0.64 V (forward scan) is 310 mA/mg_{Pt} which is 2.7 time higher than that of commercial Pt/C for methanol oxidation. The electrooxidation of HCOOH on Pt/CN_x occurs via dual mechanism with greatly enhanced oxidation through dehydrogenation pathway in comparison with commercial Pt/C. The mass activity on Pt/CN_x at 0.3 V (vs. NHE) is 25 times higher than that of Pt/C for oxidation of HCOOH. The superior catalytic activity and durability of this Pt/CN_x catalyst can be attributed to high dispersion of PtNPs and strong catalyst support interaction.

Introduction

The use of fossil fuel as well as environmental pollution is rising. Therefore, there is a need of green alternate and sustainable energy source. The fuel cells are considered as alternative green energy sources, transforms the chemical energy of fuel to electrical energy due to electrochemical oxidations of fuel molecule. High efficiency, low cost and low pollutant emission are the main advantages of fuel cells [1]. The electrochemical oxidation of small organic molecules such as methanol (CH_3OH), formic acid (HCOOH) and

---

[*] *Corresponding author.*
E-mail address: sbarman@niser.ac.in (S. Barman).

http://dx.doi.org/10.1016/j.ijhydene.2017.03.097

Journal of
Materials Chemistry A

PAPER

View Article Online
View Journal | View Issue

Check for updates

Cite this: *J. Mater. Chem. A*, 2018, **6**, 23531

Rhodium metal–rhodium oxide (Rh–Rh_2O_3) nanostructures with Pt-like or better activity towards hydrogen evolution and oxidation reactions (HER, HOR) in acid and base: correlating its HOR/HER activity with hydrogen binding energy and oxophilicity of the catalyst†

Manas Kumar Kundu,‡ Ranjit Mishra,‡ Tanmay Bhowmik and Sudip Barman *

Design and synthesis of HER/HOR catalysts are of crucial importance for the development of polymer fuel cells and water electrolyzers. We report the synthesis of Rh–Rh_2O_3 nanoparticles/nitrogen-doped carbon composite (Rh–Rh_2O_3-NPs/C) for HER/HOR applications. The HER activity of this catalyst is ~2.2 times and 1.43 times better than that of commercial Pt/C in base and acid, respectively. Rh–Rh_2O_3-NPs/C exhibited 10 mA cm^{-2} current density at an overpotential of 63 mV and 13 mV with Tafel slopes of 70 mV dec^{-1} and 32 mV dec^{-1} in base and acid, respectively. The catalyst showed superior HOR activity at all pH values. The exchange current densities were ~0.425 mA ${cm_{Rh}}^{-2}$ and ~0.43 mA ${cm_{Rh}}^{-2}$ in base and acid, respectively. In base, the HOR and HER activities of Rh–Rh_2O_3-NPs/C are 50-fold and 10-fold higher, respectively, in comparison with those of the Rh_2O_3-free RhNPs/C catalyst, although the HER/HOR activity of both the catalysts is comparable in acid. In base, the adsorption of OH^- species (OH_{ads}) on Rh_2O_3 sites increases the reactivity of hydrogen intermediate (H_{abs}), which leads to the enhancement of HOR activity of Rh–Rh_2O_3-NPs/C. For HER in base, the adsorptive dissociation of water occurs on the Rh_2O_3 sites to form H_{ads} on the neighboring Rh sites and then, the recombination of H_{ads} results in the formation of hydrogen molecules. This study may provide an opportunity to develop an efficient catalyst for hydrogen-based renewable energy technologies.

Received 10th August 2018
Accepted 24th October 2018

DOI: 10.1039/c8ta07028h

rsc.li/materials-a

1. Introduction

With the increase in energy demand and environmental problems due to the use of fossil fuels, there is an urgent need for alternative energy conversion and storage devices.[1,2] Electrolysis of water and fuel cells are the two important renewable technologies for energy conversion and energy storage.[3,4] Hydrogen is considered as one of the greenest fuels and energy carriers,[4] but production of pure hydrogen is a challenging task. Electrocatalytic water splitting is one of the renewable ways to produce pure H_2.[5] Hydrogen evolution reaction (HER) is a cathodic process of electrolysis and hydrogen oxidation reaction (HOR) is generally applied at the anode of fuel cells.[6,7] Pt is the most active catalyst for both processes in acidic media.[8,9] The high price, scarcity and poor stability of Pt-based catalysts in acidic media are the main drawbacks for its commercialization.[10] In proton exchange membrane fuel cells (PEMFCs), hydrogen and oxygen are used as reactants for HOR at the anode and oxygen reduction reaction (ORR) at the cathode, respectively, in strong acidic conditions. PEMFCs have high power efficiency and are environment-friendly due to their ability to convert hydrogen into water.[5,11] Pt is also used as ORR catalyst. However, its commercialization is limited because of the very slow kinetics of ORR at the cathode and to overcome this, large amount of Pt is required.[12] Compared with acidic PEMFC-based technologies, alkali membrane fuel cells (AMFCs) or alkaline electrolyzers, which operate in alkaline media, are highly attractive since highly active earth abundant cheap transition metal-based catalysts are available for ORR and OER in alkaline media.[13–16] However, the main obstacle of AMFCs is that the HER and HOR activity of Pt in basic media is 2–3 orders of magnitude lower than the activity in acidic media.[9,17,18] Thus, highly efficient HER and HOR catalysts are desirable for the development of AFCs and alkali electrolyzers. The

---

School of Chemical Sciences, National Institute of Science Education and Research (NISER), HBNI, Bhubaneswar, Orissa-751 005, India. E-mail: sbarman@niser.ac.in; Tel: +91 6742494183

† Electronic supplementary information (ESI) available: Details of materials synthesis, extended characterization, ECSA calculation, electrochemical HER/HOR study, stability test, activity comparison table. See DOI: 10.1039/c8ta07028h

‡ Authors with equal contributions.